FIGURE CAPTIONS

Figure 3.1.1.1.3.1.2-1 Sketch Map of the Walker Lane Belt [INN 3.1.1.1.3.1.2-1]

Figure 3.1.1.2.3.5-1. Digital Satellite Image Showing the Location of the Potential Yucca Mountain site and the Distribution of Quaternary Volcanic Centers in the Yucca Mountain Region. The Yucca Mountain region (YMR) is defined as the area of the irregular polygon that encloses the potential Yucca Mountain site and the distribution of Pliocene and Quaternary basaltic volcanic centers in the region. Yucca Mountain is a linear range located on the southwest edge of the Nevada Test Site, about 160 km northwest of Las Vegas, Nevada. The mountain extends from Highway 95 on the south to Yucca Wash on the north, a distance of about 25 km. The mountain is bounded on the east by Jackass Flat (the western boundary of Jackass Flat is defined by Fortymile Wash), on the west by Crater Flat, and on the south by the Amargosa Valley. An approximately 6 km2 area in the center part of Yucca Mountain has been identified as the exploratory block (DOE, 1988). It is surrounded by the controlled area, about 86 km2. There are seven Quaternary basaltic volcanic centers in the Yucca Mountain area (< 1.8 Ma). These centers are noted by the special symbol on Figure 3.1.1.2.3.5-1.

Figure 3.1.1.2.3.5.2.1-1 Caldera-related Volcanic Activity of the Ring-Fracture Zone of the Timber Mountain Caldera Complex

Figure 3.1.1.2.3.5.1-2 Migration of Volcanism in Southern Nevada and the Amazmatic Gap [INN 3.1.1.2.3.5.1-1]

Figure 3.1.1.2.3.5.2.1.2-1 Post-Caldera Basalt of the Yucca Mountain Region. Shaded areas are the Older Post-Caldera Basalt (OPB) including: RW: basalt of Rocket Wash, PM: Basalt of Pahute Mesa, SC: basalt of Scarp Canyon, NC: basalt of Nye Canyon, FF: buried basalt of Frenchman Flat. Stippled areas are the Younger Post-Caldera Basalt (YPB) including: TM: basalt of Thirsty Mesa, AV: basalt of Amargosa Valley, PCF: Pliocene basalt of southeast Crater Flat, BB: basalt of Buckboard Mesa, QCF: Quaternary basalt of Crater Flat, SB: basalt of Sleeping Butte, LW: basalt of Lathrop Wells. Asterisks mark aeromagnetic anomalies identified as potential buried basalt centers or intrusions (Kane and Bracken, 1983, Crowe et al. 1986). Dashed line encloses the area of the Crater Flat Volcanic Zone (CFVZ). Numbers associated with the symbols for the volcanic units of the OPB and YPB are the age of the volcanic centers in million years. Modified from Crowe and Perry (1989).

Figure 3.1.1.2.3.5.2.2-2 Generalized Geologic Map of the Basalt of Southeast Crater Flat [INN 3.1.1.2.3.5.2.2-1]

Figure 3.1.1.2.4.1-1 Map of Regional Seismicity [INN 3.1.1.2.4.1-1]

Figure 3.1.1.2.4.2.2-1. Location of Seismic Recording Stations of the Southern Great Basin Seismic Network. Source: Sheehan et al. (1993) [INN 3.1.1.2.4.2.2-1]

Figure 3.1.1.2.4.2.2-2. Stations Recording the Little Skull Mountain, Nevada Earthquake of 29 June 1992 in Southern Nevada. Source: URS/Blume & Assoc. (1992) [INN 3.1.1.2.4.2.2-2]

Figure 3.1.1.2.4.2.2-3. Attenuation of Peak Acceleration and Peak Velocity of the Little Skull Mountain, Nevada Earthquake of 29 June 1992 in Southern Nevada, Compared with the Average of the Estimates Derived from Joyner and Boor (1988) and Campbell (1990). Data Source: URS/Blume & Assoc. (1992) [INN 3.1.1.2.4.2.2-3]

Figure 3.1.1.2.4.2.2-5. Locations of the Little Skull Mountain Earthquake, the Rock Valley Earthquake, and the Recording Station at Midway Valley. Source: Sheehan et al. (1993)

Figure 3.1.1.2.4.2.2-7. Velocity Seismograms of the Eureka Valley Aftershock of June 8, 1993 (magnitude 3.9, depth 5.9 km). Source: Sheehan et al. (1993) [INN 3.1.1.2.4.2.2-5]

Figure 3.1.1.2.4.2.2-8. Velocity Seismograms of the Eureka Valley Aftershock of June 8, 1993 (magnitude 4.0, depth 1.7 km). Source: Sheehan et al. (1993) [INN 3.1.1.2.4.2.2-6]

Figure 3.1.1.2.4.2.2-11. Ratios of Measured PSRV at Station W-14 to Average Values for NTS Sites. Source: Phillips (1991) [INN 3.1.1.2.4.2.2-8]

Figure 3.1.1.2.4.2.2-12. Ratios of Measured PSRV at Station W-23 to Average Values for NTS Sites. Source: Phillips (1991) [INN 3.1.1.2.4.2.2-9]

Figure 3.1.1.2.4.2.2-13. Ratios of Measured PSRV at Station W-22 to Average Values for NTS Sites. Source: Phillips (1991) [INN 3.1.1.2.4.2.2-10]

Figure 3.1.1.2.4.2.2-14. Ratios of Measured PSRV at Station W-21 to Average Values for NTS Sites. Source: Phillips (1991) [INN 3.1.1.2.4.2.2-11]

Figure 3.1.1.2.4.2.2-15. Location Map of Strong Motion Stations That Recorded the Pipkin Nuclear Explosion at Pahute Mesa. Source: Weetman et al. (1970) [INN 3.1.1.2.4.2.2-12]

Figure 3.1.1.2.4.2.2-16. Profile of Radial Velocity Time Histories of the Pipkin Nuclear Explosion at Pahute Mesa Recorded to the South at Stations Shown in Figure 15. Source: Weetman et al. (1970) [INN 3.1.1.2.4.2.2-13]

Figure 3.1.1.2.4.3.4-1. Seismograms Recorded in a Downhole Array at Jackass Flats (Station 10, Well J-11) From a Nuclear Explosion at Pahute Mesa. Top row: accelerations; middle row; velocity; bottom row; displacement. Left column: surface station on alluvium; middle column: -61 meters near the base of alluvium; right column: -356 meters in tuff. Source: Vortman and Long (1982) [INN 3.1.1.2.4.3.4-1]

Figure 3.1.1.2.4.3.4-2. Location Map of Downhole Ground Motion Recordings Stations at Yucca Mountain and Regional Topography. Source: Phillips (1991) [INN 3.1.1.2.4.3.4-2]

Figure 3.1.1.2.7.6.2.1-1. Selection Process for Mechanical Numerical Models [INN 3.1.1.2.7.6.2.1-1]

Figure 3.1.2.2.7-1 Former High Levels of the Water Table in the South-Central Great Basin during trhe Quaternary Period [INN 3.1.2.2.7-1]

Figure 3.1.2.2.7-2 Variations in Flow-Path Length for the Ash Meadows Area in Response to Different Water Table Levels [INN 3.1.2.2.7-2]

Figure 3.1.2.3.9-1. Decline in the Water Level with Well J-13 in Continuous Service [INN 3.1.2.3.9-1]

Figure 3.1.4.1.1-1 Locations of the Climatological Data Stations in the Yucca Mountain Region [INN 3.1.4.1.1-1]

Figure 3.1.4.1.1-2 Locations of Site Specific Monitoring Sites at Yucca Mountain [INN 3.1.4.1.1-1]

Figure 3.1.4.1.1.1.2-1. Average Position of the Polar Front in January. A dashed line indicates the front is not well defined. Air masses are also indicated. (After Gedzelman, 1985) [INN 3.1.4.1.1.1.2-1]

Figure 3.1.4.1.1.1.2-2. Winter Weather Type A. Successive Time-Lapse Positions of the Low-Pressure Cyclone are Shown as the System Develops and Matures (Elliott, 1943). [INN 3.1.4.1.1.1.2-2]

Figure 3.1.4.1.1.1.2-3. Winter Weather Type B. Shown are the Successive Time-Lapse Positions of the Low-Pressure System as it Develops. The System Remains Well to the North of the U.S., as High Pressure Dominates the Southwest (Elliott, 1943). [INN 3.1.4.1.1.1.2-2]

Figure 3.1.4.1.1.1.2-4. Winter Weather Type C. Shown is the Belt of High Pressure which is Displaced Northwest from its Normal Position. The Low-Pressure Centers Develop in the Gulf of Alaska and off the Coast of San Diego. Then they move inland as depicted in this time-lapse sequence (Elliott, 1943). [INN 3.1.4.1.1.1.2-2]

Figure 3.1.4.1.1.1.2-5. Winter Weather Type D. Depicted are Time-Lapse Positions of the Low-Pressure Center as it Tracks Across the Northern U.S. (Elliott, 1943). [INN 3.1.4.1.1.1.2-2]

Figure 3.1.4.1.1.1.2-6. Winter Weather Type E. The Strong Canadian High-Pressure Ridge is Depicted. This Ridge forces Developing Low-Pressure Systems Southward into the Great Basin. These Pacific Storms cross the Sierra-Nevada, Weaken, then Redevelop on Lee side of the Mountain Range (Elliott, 1943). [INN 3.1.4.1.1.1.2-2]

Figure 3.1.4.1.1.1.2-7. Summer Southwest Monsoon. Shown is a lobe of the Bermuda High over the four-corners region. The Resulting Pressure Gradient causes a Gentle Flow of Moisture to begin from the Tropical Eastern Pacific Ocean. The Gulf of Mexico Contributes only an Insignificant Amount of Moisture to the Southwestern U.S. (Elliott, 1943). [INN 3.1.4.1.1.1.2-3]

Figure 3.1.4.1.1.1.3-1. Dominant Summer and Winter Moisture Sources for the Southern Nevada Area [INN 3.1.4.1.1.1.3-1]

Figure 3.1.4.1.1.1.3-2. Regression Curves Relating Annual Average Precipitation (mm) with Precipitation Gage Elevation (ft). Also included are the data from 42 precipitation stations used to obtain the regression curve by Hevesi [INN 3.1.4.1.1.1.3-3]

Figure 3.1.4.1.1.2.2-1 Precipitation Amounts [INN 3.1.4.1.1.2.2-2]

Figure 3.1.4.1.1.2.4-1 to -n Wind Rose Plot (1 - n) [INN 3.1.4.1.1.2.4-1]

Figure 3.1.4.1.1.2.5.1-1. Seasonal and Annual Wind Distribution at 1.524 m Above Mean Sea Level (328 m Above Ground Level) for Yucca Flat (1957 to 1964). Note: Scale is not the same for all distributions. Based on data from Quiring (1968). [INN 3.1.4.1.1.2.5.1-1]

Figure 3.1.4.1.1.2.5.1-2. Seasonal and Annual Wind Distributions at 6,000 ft. (1,829 m) Above Mean Sea Level (633 m Above Ground Level) for Yucca Flat (1957 to 1964). Note: Scale is not the same for all distributions. Based on data from Quiring (1968). [INN 3.1.4.1.1.2.5.1-2]

Figure 3.1.4.1.1.2.5.1-3 Upper Air Data [INN 3.1.4.1.1.2.5.1-3]

Figure 3.1.4.1.1.2.6-1. Monthly Mean Atmospheric Pressure [INN 3.1.4.1.1.2.6-1]

Figure 3.1.4.1.1.2.6-2. Hourly Mean Atmospheric Pressure [INN 3.1.4.1.1.2.6-1]

Figure 3.1.4.1.1.2.8-1 Pattern of Detected Lightening [INN 3.1.4.1.1.2.8-3]

Figure 3.1.4.1.1.2.8-2 Spatial Relationships Between Lightening-Strike Data and Rainfall-Runoff Data [INN 3.1.4.1.1.2.8-5]

Figure 3.1.4.1.3-1 Wind Rose Plots [INN 3.1.4.1.3-1]

Figure 3.1.4.1.3-2 Wind Rose Plots [INN 3.1.4.1.3-1]

Figure 3.1.4.1.3-3 Wind Rose Plots [INN 3.1.4.1.3-1]

Figure 3.1.4.1.3-4 Wind Rose Plots [INN 3.1.4.1.3-1]

Figure 3.1.4.1.3-5 Wind Rose Plots [INN 3.1.4.1.3-1]

Figure 3.1.4.1.3-6 Wind Rose Plots [INN 3.1.4.1.3-1]

Figure 3.1.4.1.3-7 Wind Rose Plots [INN 3.1.4.1.3-1]

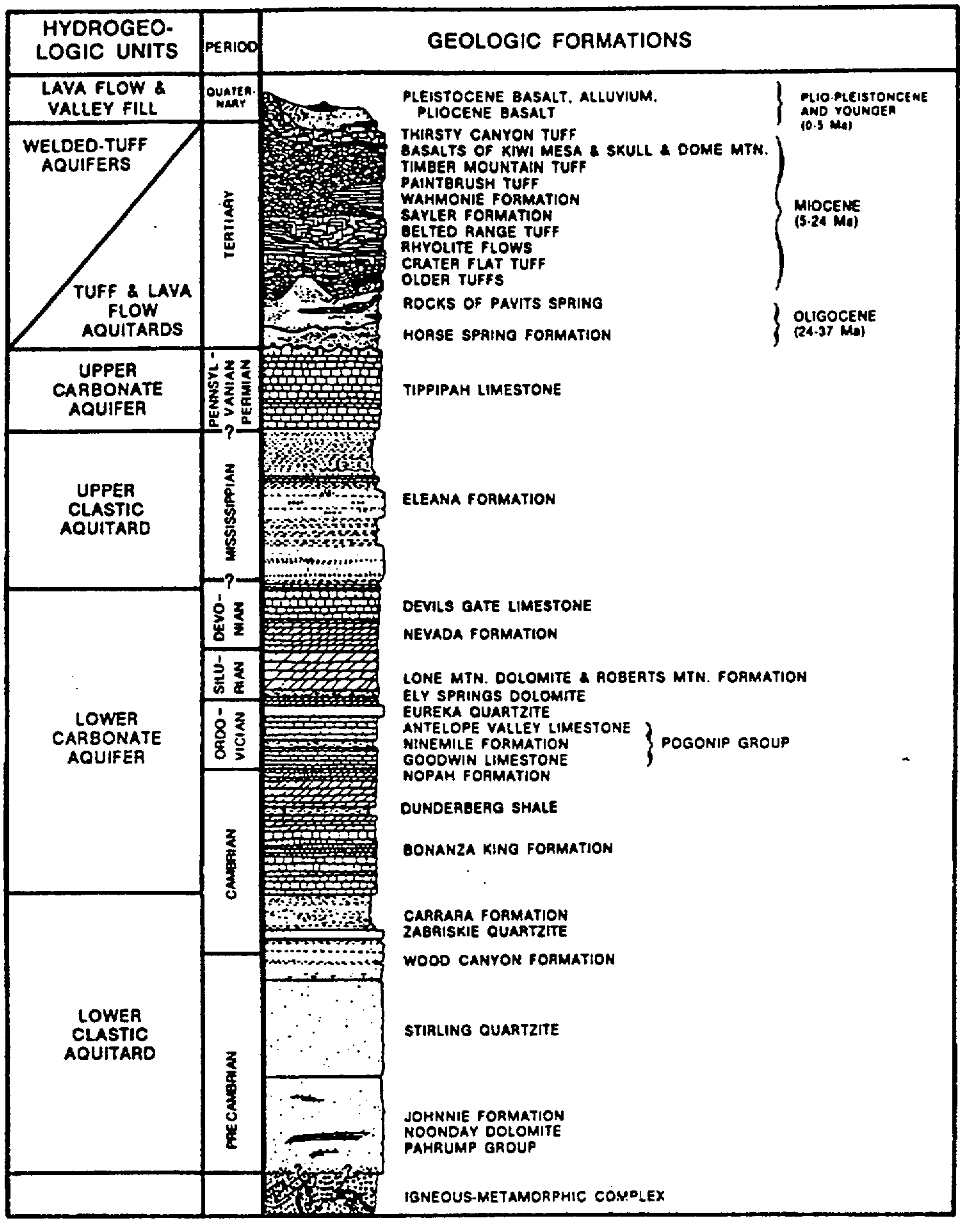

Figure 3.1.1.1.2-1 Generalized Regional Stratigraphic Column Showing Geologic Formations and Hydrogeological Units in the Nevada Test Site Area. Modified from Sinnock (1982) and Carr et al. (1986)

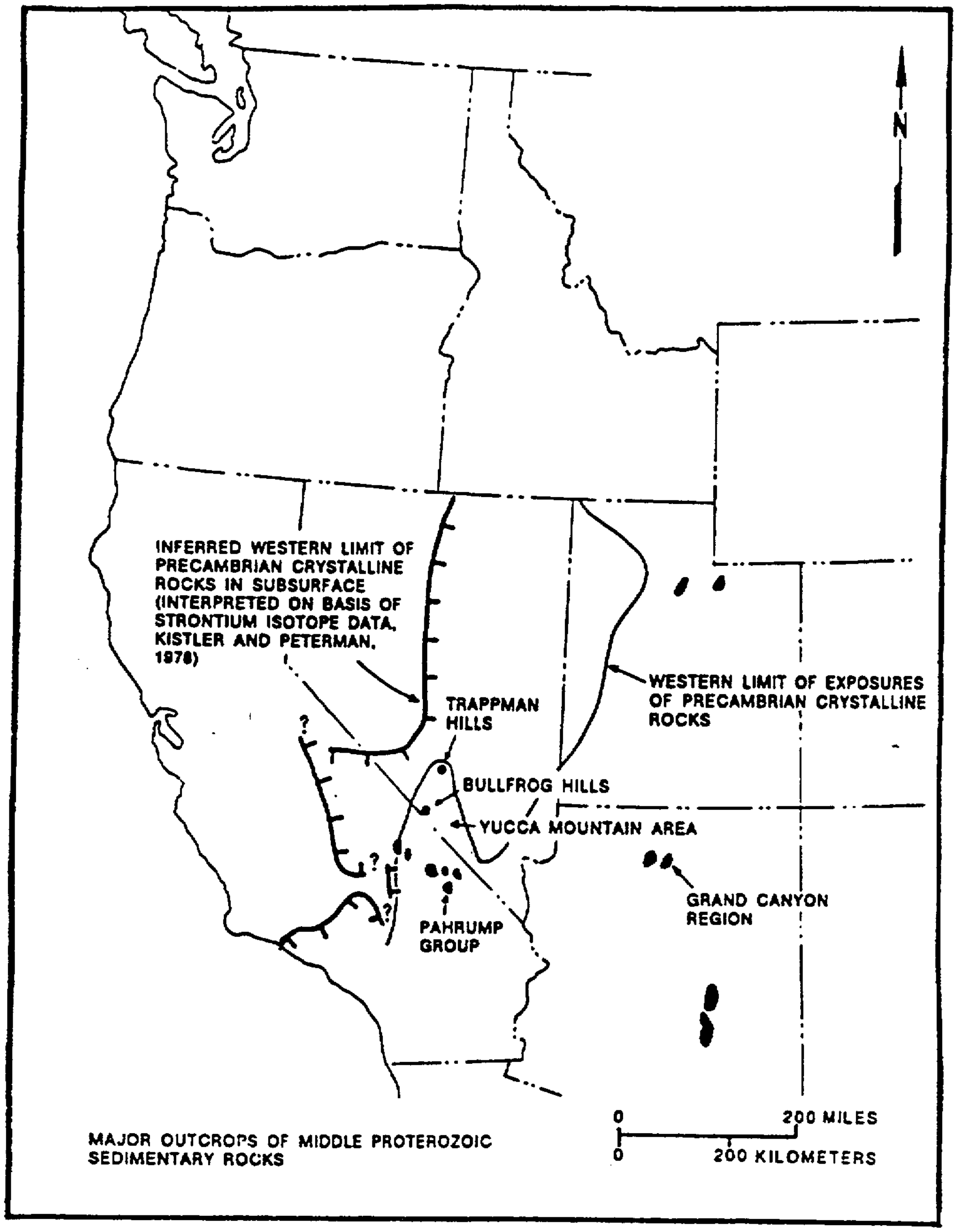

Figure 3.1.1.1.2.1-1 Distribution of Lower and Middle Proterozoic Crystalline Rocks and Middle Upper Proterozoic Restricted Deposits in the Great Basin. Modified from USGS (1984)

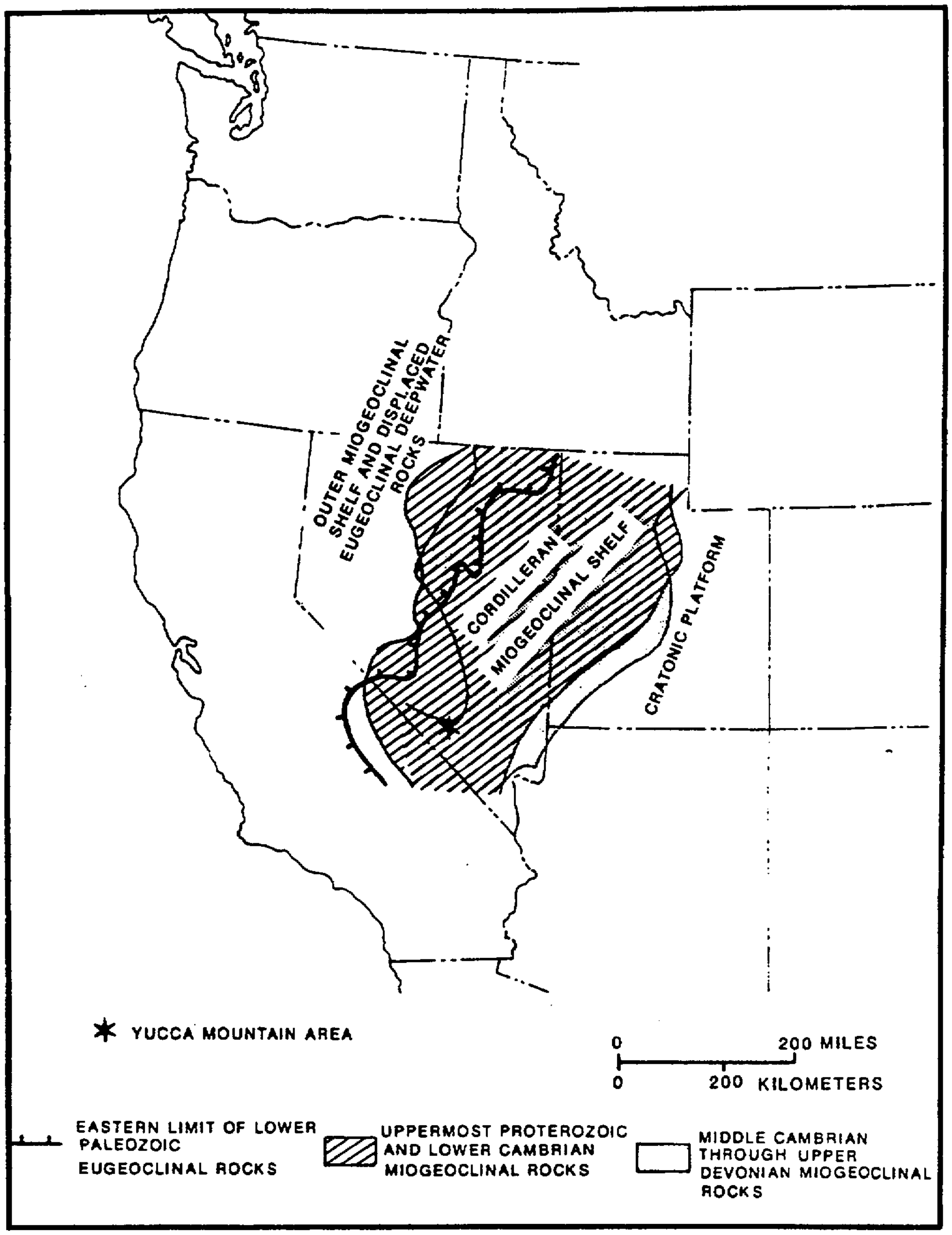

Figure 3.1.1.1.2.2-1 Latest Precambrian Through Mid-Paleozoic Paleogeography of the Great Basin. Modified from USGS (1984)

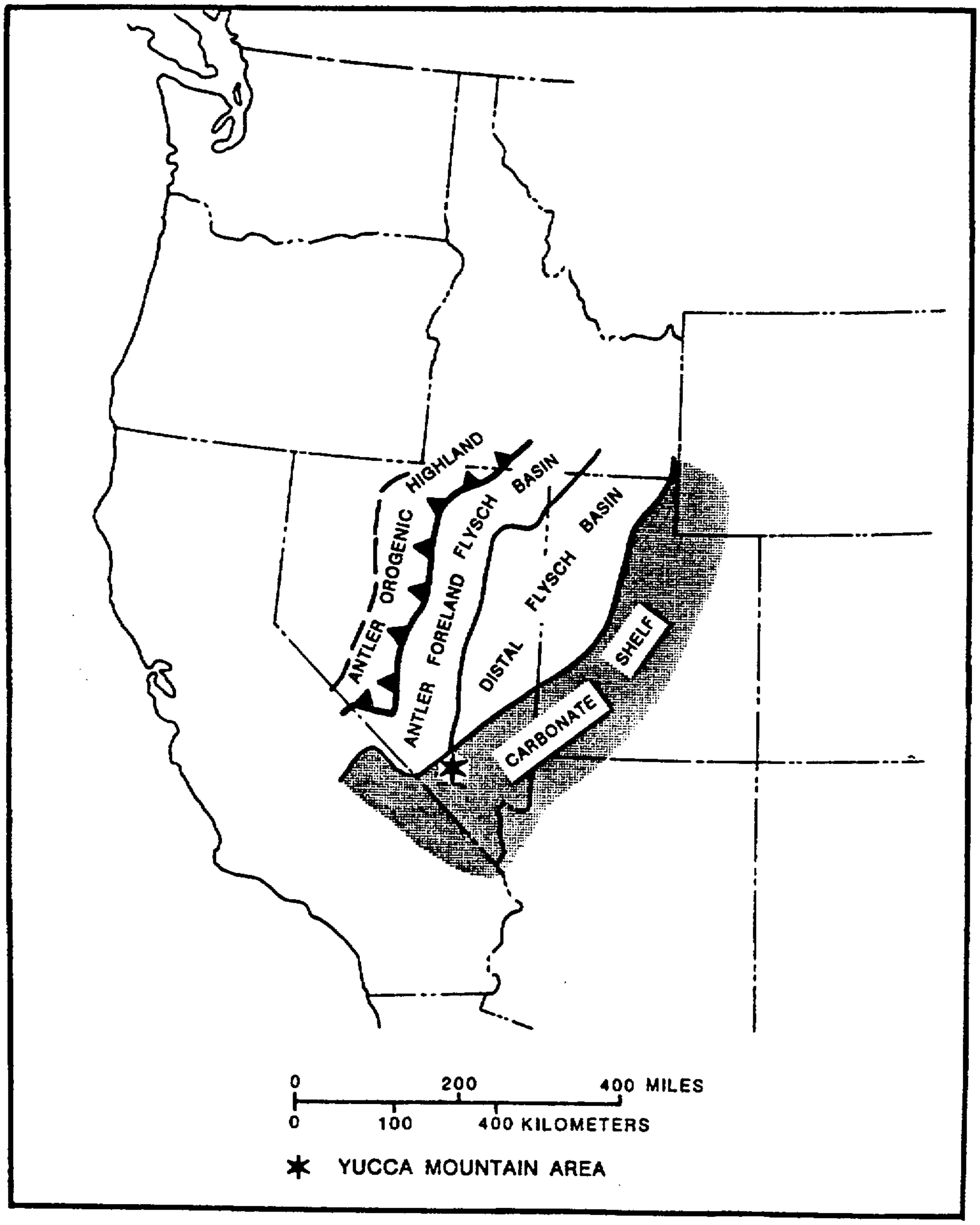

Figure 3.1.1.1.2.4-1 Late Devonian and Mississippian Paleogeography of the Great Basin. Modified from USGS (1984)

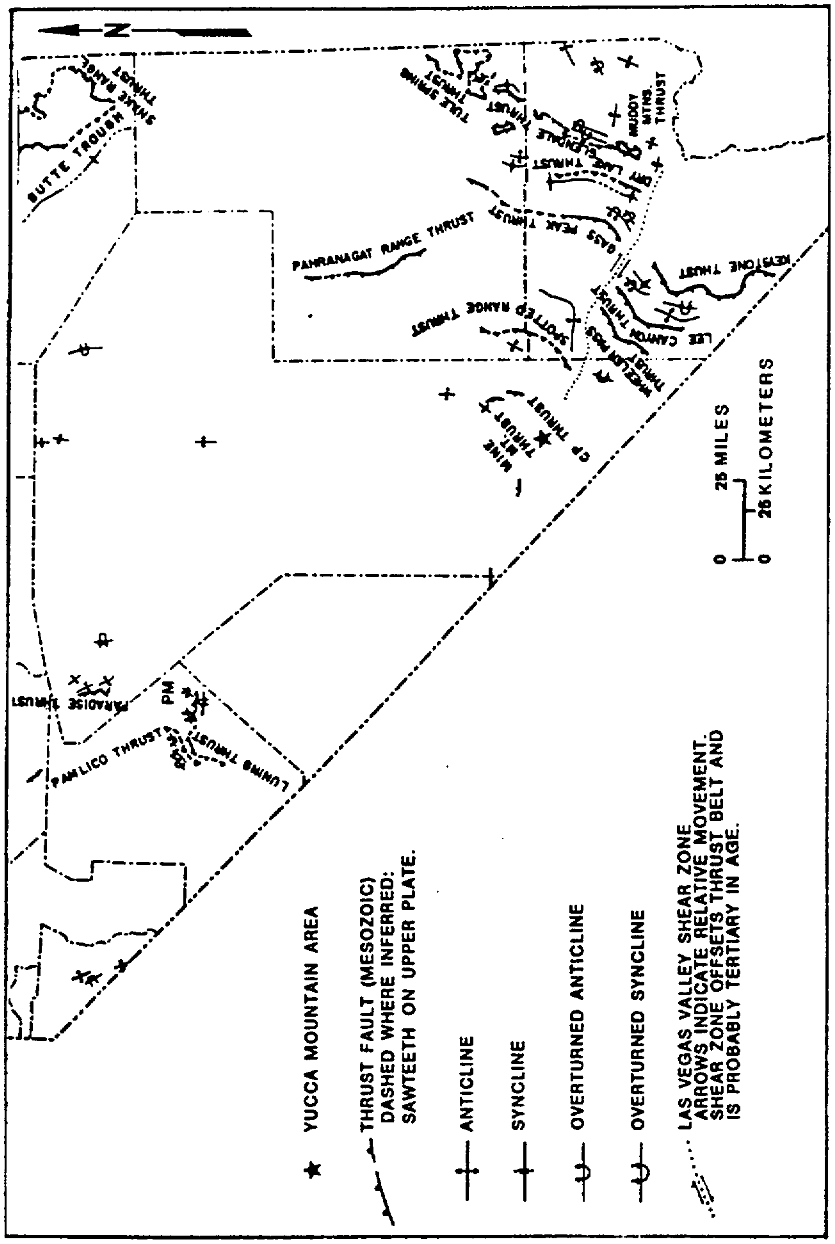

Figure 3.1.1.1.2.5-1 Major Mesozoic Thrust Faults in Southern Nevada. Modified from Stewart (1980a)

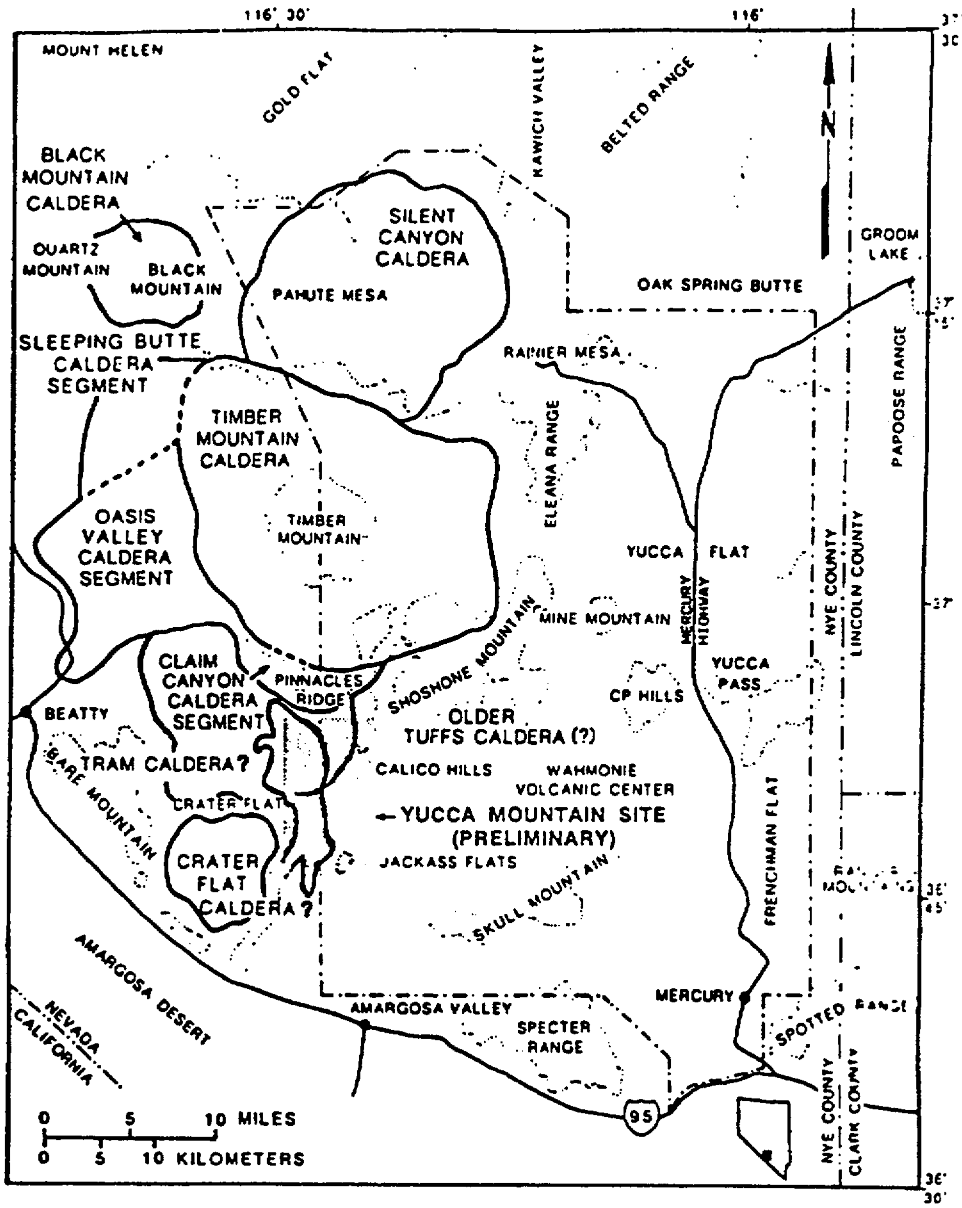

Figure 3.1.1.1.2.7-1 Calderas of the Southwest Nevada Volcanic Field Near Yucca Mountain. Modified from Maldonado and Koether (1983)

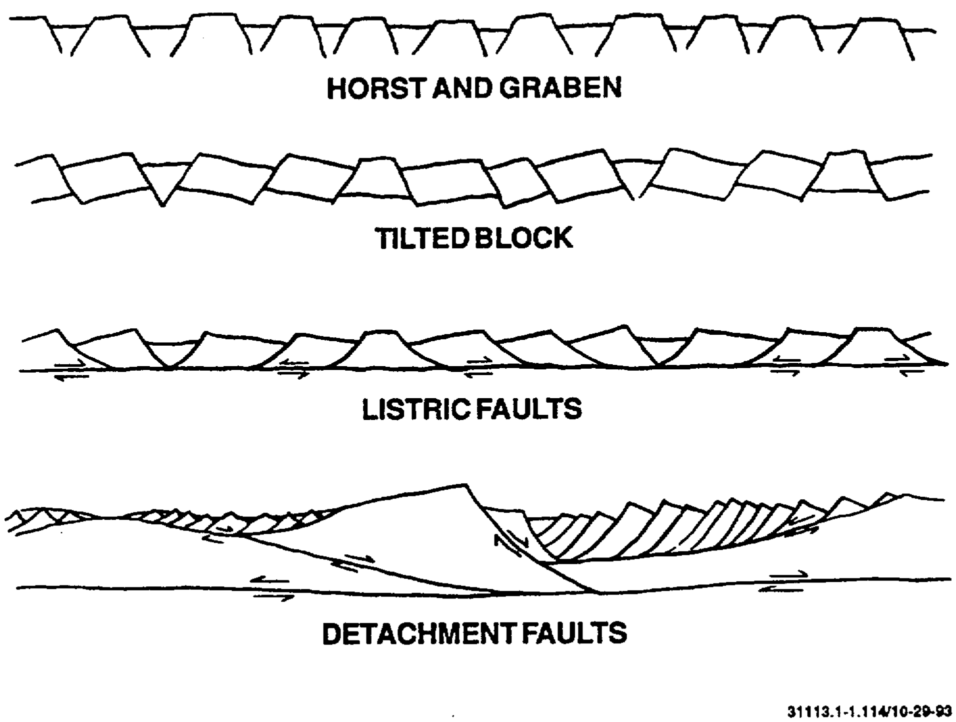

Figure 3.1.1.1.3.1-1 This schematic (modified from Stewart, 1980, and Scott, 1990) illustrates some of the mechanisms and geometric configurations proposed for extensional faulting in the Basin and Range. The geometry of the Horst and Graben and the Tilted Block models allows for fairly limited extension (approximately 15%), while that of the Listric Faults and Detachment Faults models allows for progressively greater amounts of extension. Using detachment models, Wernike et al. (1988) has proposed up to 300% extension for parts of the Basin and Range.

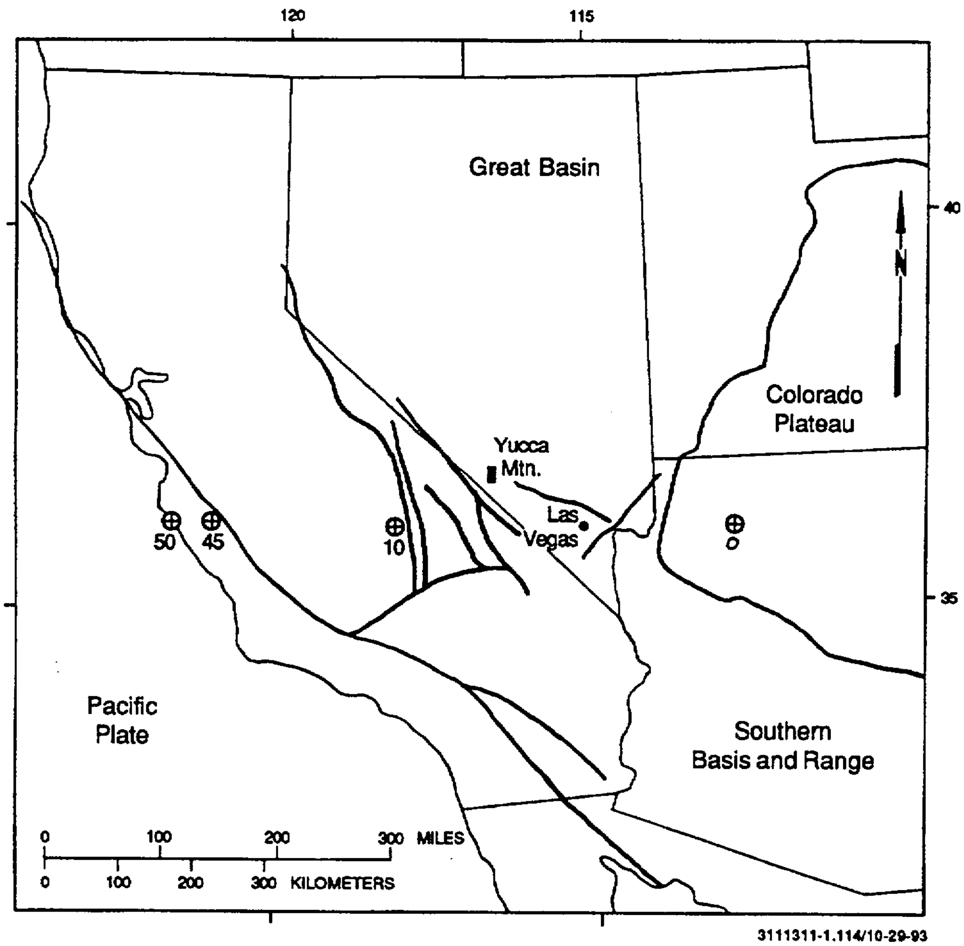

Figure 3.1.1.1.3.1.1-1 Sketch map of the western United States showing some major structural features. Symbols (⊕ 45) at the latitude of Las Vegas give approximate motions toward the NW in mm/yr relative to a "stable North America" (data modified [rounded] from Argus and Gordon, 1991). This interpretation suggests that 10 mm/yr of NW movement occurs between the Colorado Plateau and the crest of the Sierra Nevada Range, 35 mm/yr occurs on the San Andreas Fault, and 5 mm/yr occurs west of the San Andreas Fault. This is consistent with paleoseismic data and historic observations of strike slip faulting in this region.

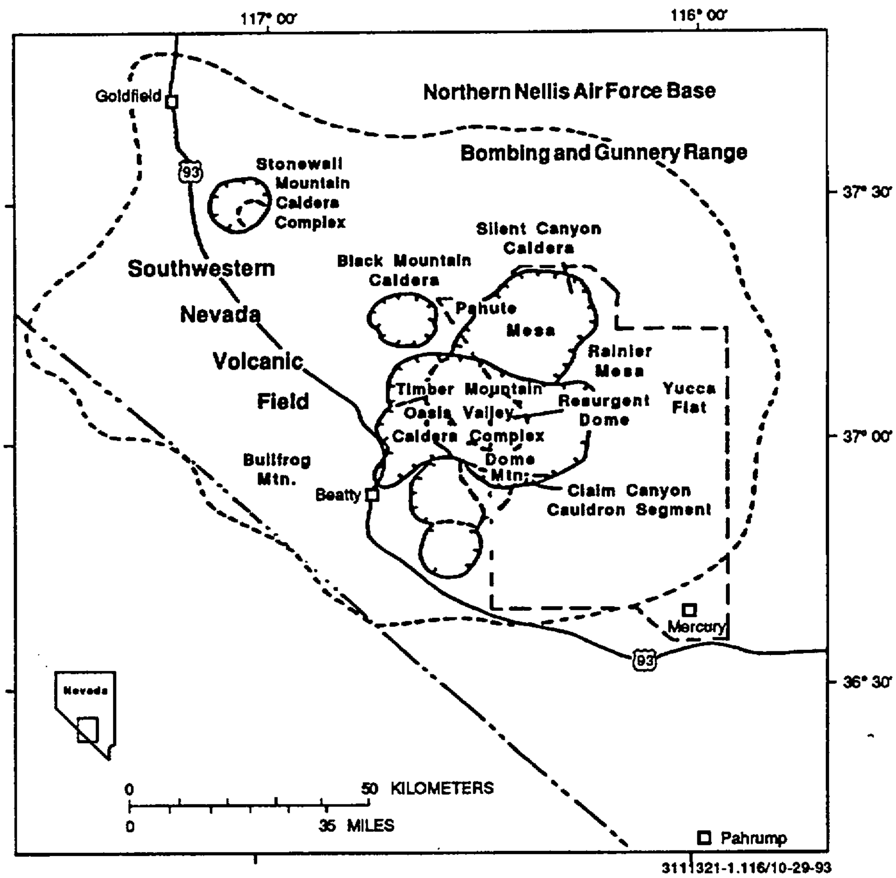

Figure 3.1.1.1.3.2.1-1 The Southwestern Nevada Volcanic Field (from Byers et al. 1989). Yucca Mountain is upheld by a thick sequence of ignimbrites derived from multiple caldera-forming, eruptive cycles of the Claim Canyon and Timber Mountain-Oasis Valley caldera complexes.

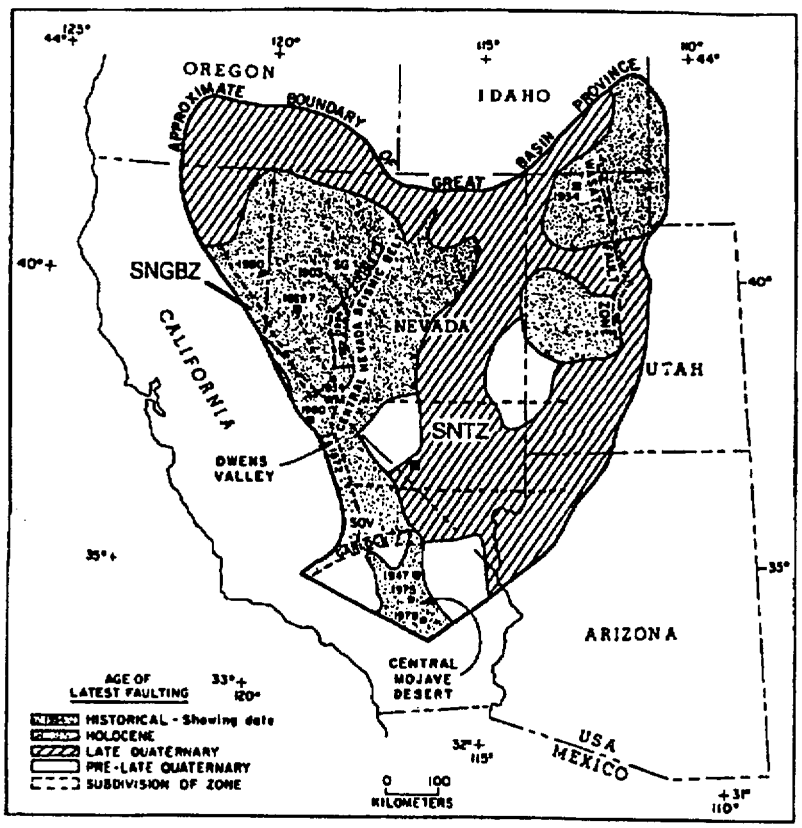

Figure 3.1.1.1.4.1-2 Map of the Great Basin Province Showing Seismic Source Zones. Patterned areas identify regions of coeval Quaternary faulting. Dates refer to historic earthquakes located in the zones. SNGBZ: Sierra Nevada-Great Basin Boundary Zone; SNTZ: Southern Nevada Transverse Zone; SG: Stillwater seismic gap; WM: White Mountains seismic gap; SOV: southern Owens Valley seismic gap. Black square in southern Nevada shows the approximate location of Yucca Mountain. Modified from Wallace (1984)

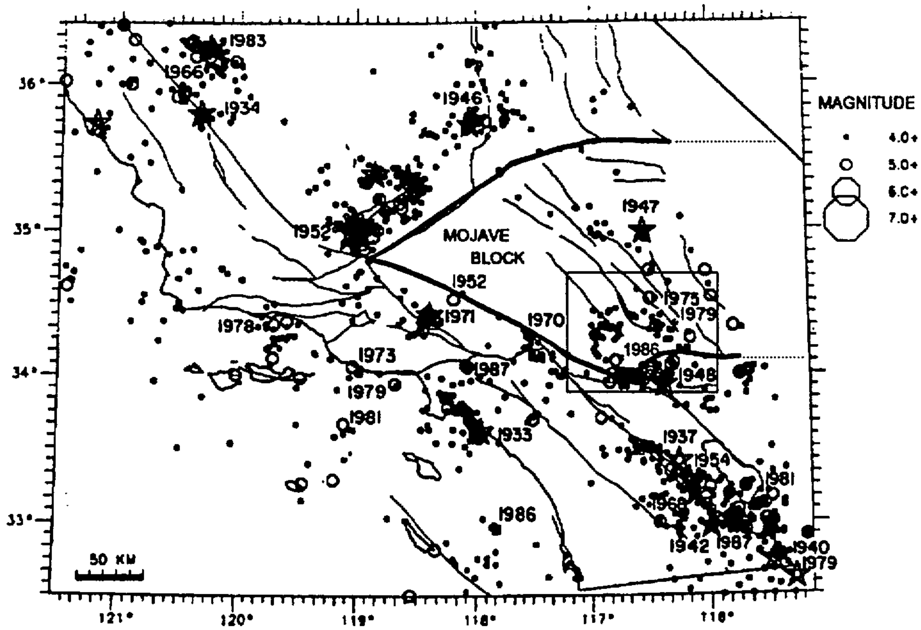

Figure 3.1.1.1.4.1-3 Seismicity in Southern California. Earthquakes ($M_L \geq 4$) recorded by the Southern California Seismic Network (CIT) from 1932 to 1987. Earthquakes of $M_L \geq 6$ are shown by a star and a date. Light lines identify Quaternary faults in the region (Jennings, 1975) and the bold line outlines the Mojave Block discussed in the text. Dashed lines show the projection of the Mojave Block to the state border. The square represents the location of Figure 3.1.1.1.3.2.2-10 showing the events in the 1992 M_S 7.6 Landers earthquake sequence. Modified from Hutton et al. (1991)

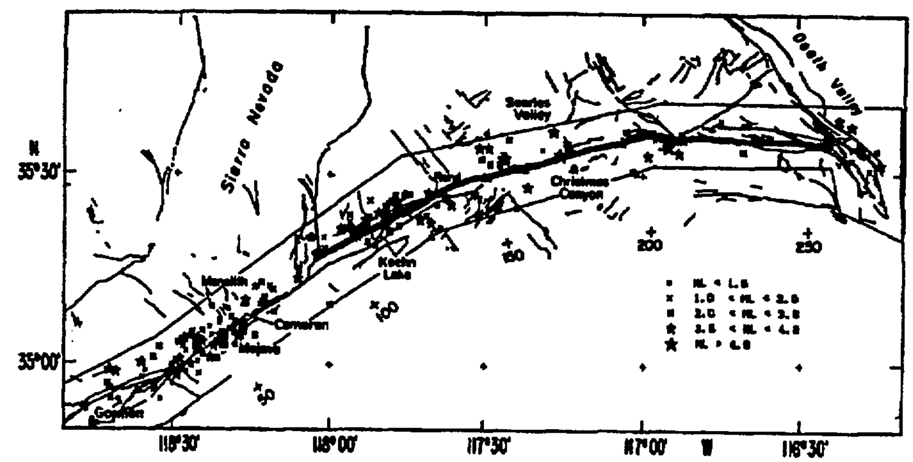

Figure 3.1.1.1.4.2-1 Map of the Garlock Fault Zone. GFZ outlined by light lines; stars represent earthquakes recorded from 1932 to 1981 (Astiz and Allen, 1983). Heavy line identifies the central and eastern segments of the fault considered by Astiz and Allen (1983) to be a seismic gap. Numbers in the figure correspond to distances in kilometers from Gorman near the intersection with the San Andreas fault. Modified from Astiz and Allen (1983)

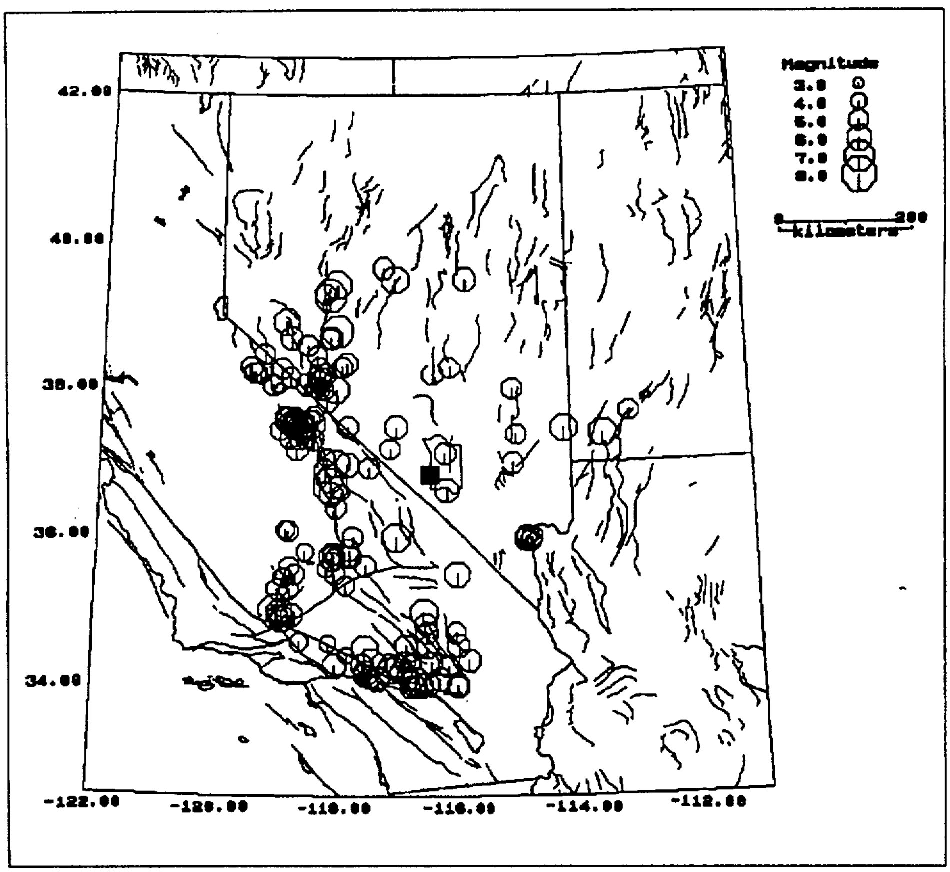

Figure 3.1.1.1.4.2.1-1 Magnitude 5 or Greater Earthquakes within 200 Miles of Yucca Mountain. Octagons represent epicentral location of earthquakes, scaled in size relative to the magnitude. Light lines are Quaternary faults in the region; in California from Jennings (1975). Solid square is approximate location of Yucca Mountain. See text for sources of earthquake data.

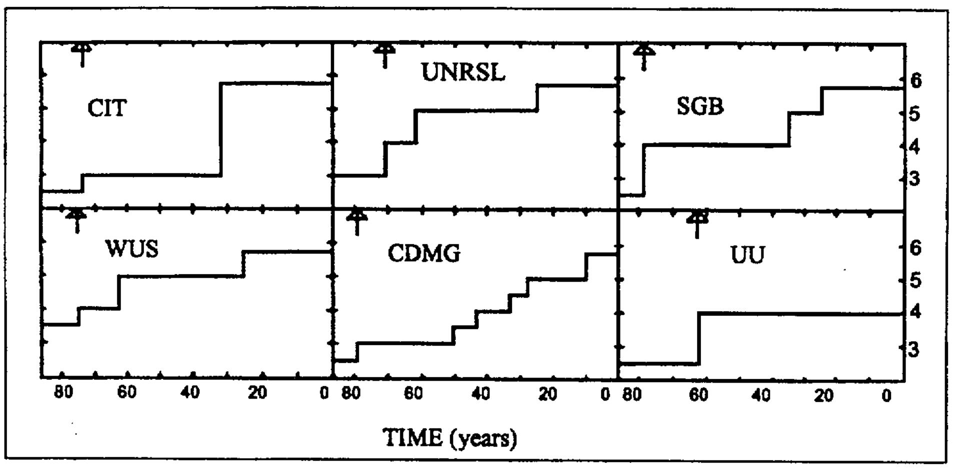

Figure 3.1.1.1.4.2.1-2 Time-Dependent Magnitude Completeness Thresholds for Regional Seismic Networks Covering the Great Basin. The transition from historic data to modern data is shown for each region by the vertical arrows. Horizontal axis represents time in years from 1900. Vertical axis represents earthquake magnitude. Abbreviations in each frame identify the seismic network or the region covered by several networks: CIT = California Institute of Technology; UNRSL = University of Nevada, Reno Seismological Laboratory; SGB = Southern Great Basin network; UU = University of Utah; CDMG = California Division of Mines and Geology; WUS = Western U.S. region covered by several networks. See text for further discussion. Modified from Engdahl and Rinehart (1991)

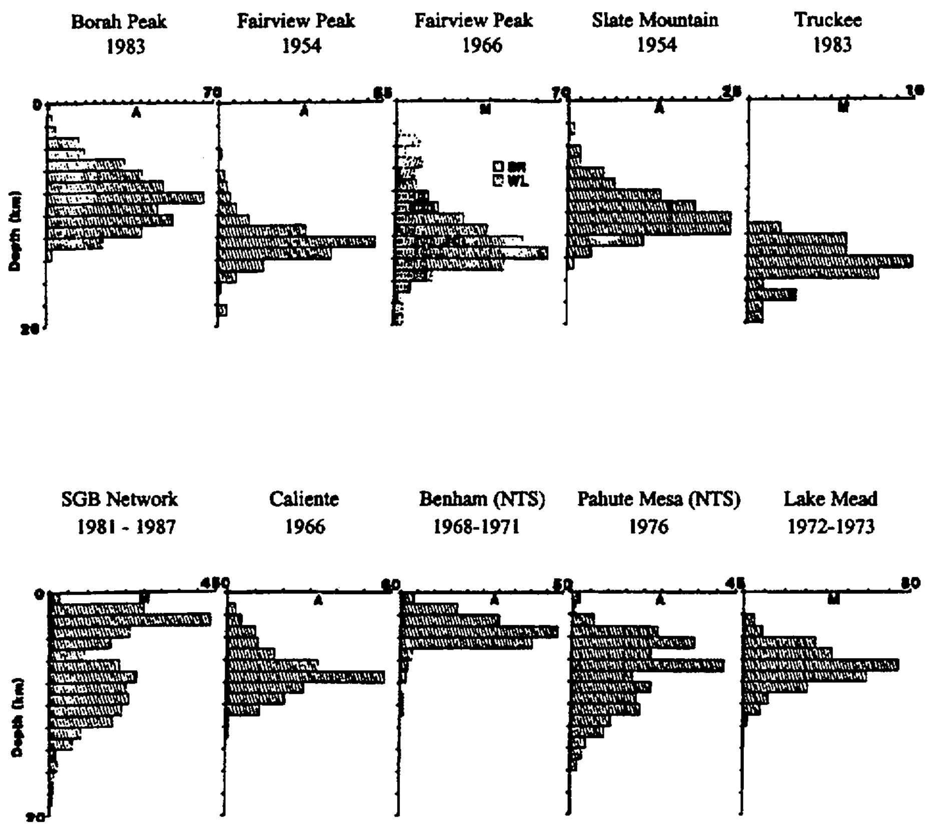

Figure 3.1.1.1.4.2.1-3 Focal Depth Distribution for Various Source Regions in the Great Basin. Data from aftershock studies are denoted by A and include studies of seismicity following nuclear tests (Benham and Pahute Mesa histograms). Data from microearthquake monitoring are denoted by M. Date refers to the year of the mainshock or blast for aftershock studies and monitoring period for microearthquake surveys. The number of earthquakes in each region is shown by the bars and the scale on the abscissa. For 9 out of 10 data sets, less than 1 percent of the events are located below 20 km. For the Fairview Peak region about 8 percent of the events have focal depths greater than 20 km (Westphal and Lange, 1967; WL in the figure). A study by Stauder and Ryall (1967) show a different depth distribution for Fairview Peak events (SR in the figure). Modified from Rogers et al. (1991)

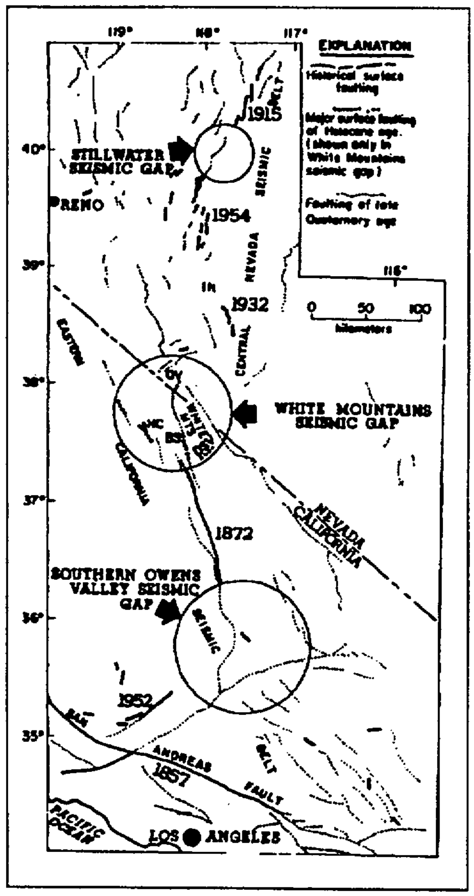

Figure 3.1.1.1.4.2.1-4 Map of a Portion of the Western Great Basin Showing Seismic Gaps Located in the SNGBZ, CNSB, and the GFZ. The eastern California seismic belt is coincident with the SNGBZ between 39° north and the GFZ. Dates and bold lines represent surface ruptures of historic earthquakes larger than M 6.8. Major Holocene surface faults shown in the White Mountains seismic gap are: the Hilton Creek fault (HC); two segments in the White Mountains fault zone (QV and BS); and the Deep Springs Valley fault (DSV). Figure taken from Hill et al. (1985)

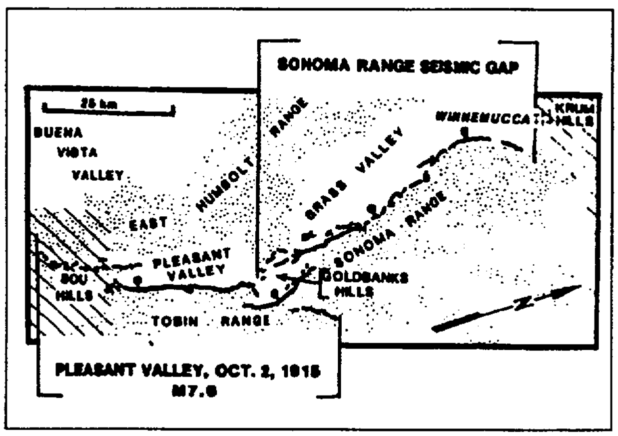

Figure 3.1.1.1.4.2.1-5 Map of Surface Faulting in the Northern CNSB. Surface ruptures of the 1915 Pleasant Valley, Nevada, Earthquake are from Wallace (1979, 1984). Sonoma Range seismic gap (Thenhaus and Barnard, 1989) shows Holocene scarps from Wallace (1979). Ruled regions represent intersection of the central (left side of figure) and northern (right) extensional accommodation zones where they cross the fault zone. Figure taken from Thenhaus and Barnard (1989)

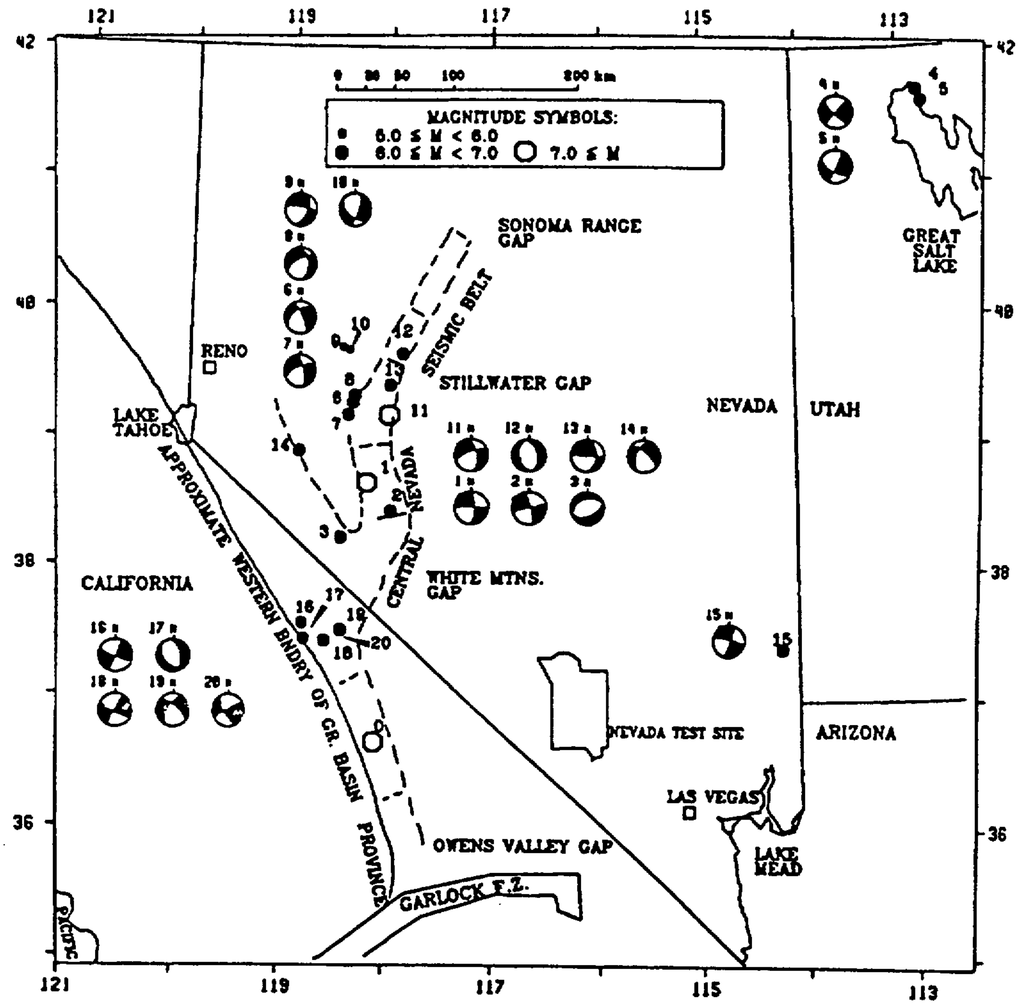

Figure 3.1.1.1.4.2.1-6 Map Showing Earthquake Locations and Their Focal Mechanisms Computed by Body-Waveform Inversion for Great Basin Earthquakes Having M ≥ 5.0 for the Time Period 1932 through 1986. In the case of Mammoth Lakes, the on-double-couple component of the solution is substational (Sipkin, 1986). Focal mechanisms 1 to 14 were computed to Doser (1986, 1987), 15 by Wallace et al. (1983), 16 and 17 by Sipkin (1986), 18 by Barker and Wallace (1986), 19 and 20 by Cockerham and Corbett (1987). Boundaries of Central Nevada Seismic Belt from Wallace (1984a), and Garlock Fault Zone from Astiz and Allen (1983). From Rogers et al. (1991)

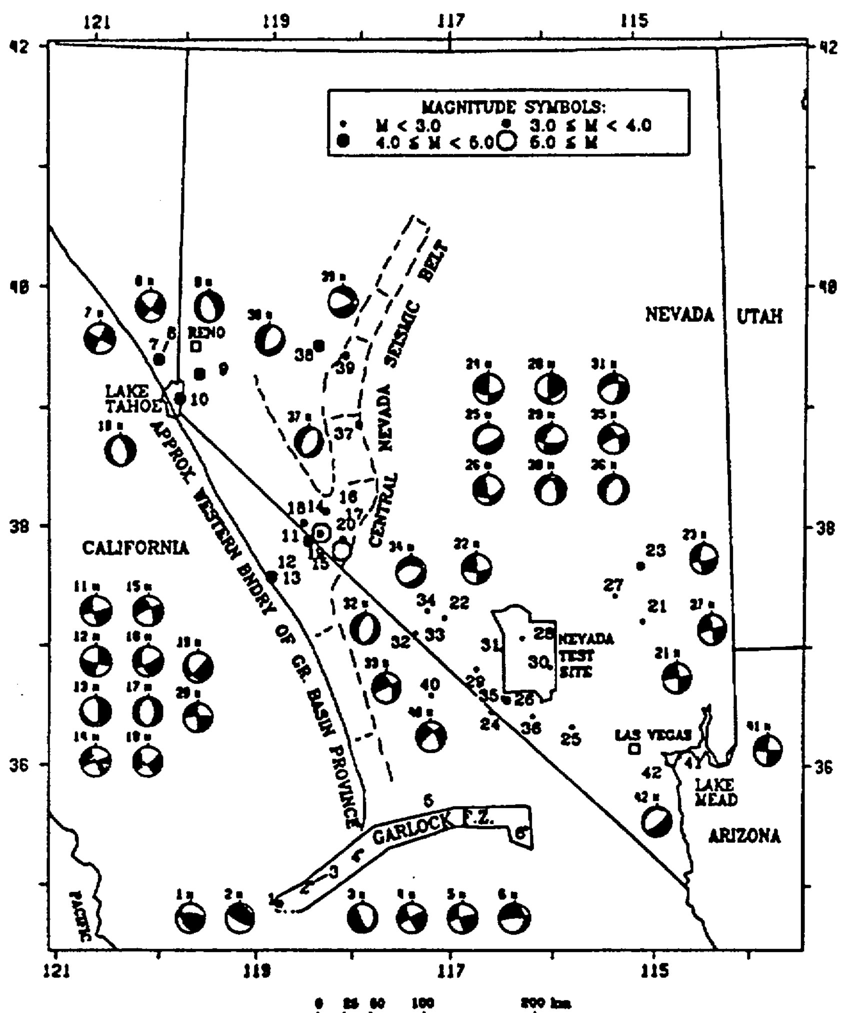

Figure 3.1.1.1.4.2.1-7 Map Showing Earthquake Locations and Their Focal Mechanisms Computed from First-Motion P-Wave Arrivals at Local Seismograph Networks in the Great Basin and Galock Fault Zone. Focal mechanisms 1 through 6 from Astiz and Allen (1983), 7 through 20 and 37 through 39 from Vetter and Ryall (1983) and Vetter (1984), 21 through 24 from Rogers et al. (1987), and 25 through 36 and 40 from Harmsen and Rogers (1987). From Rogers et al. (1991)

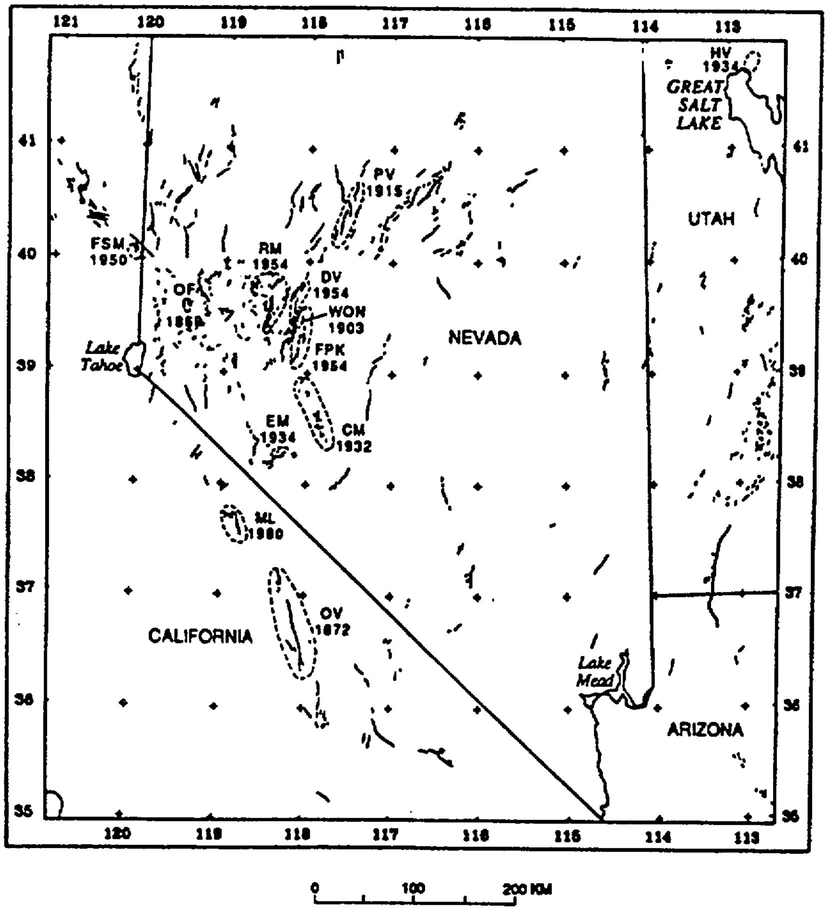

Figure 3.1.1.1.4.2.2-1 Map of Historic (Red), Holocene (Shaded Red), and Late Quaternary (Gray) Faulting in Nevada and Vicinity. Faulting has been adopted from Nakata et al. (1982) and by Thenhaus and Barnard (1989). Symbols are: CM-Cedar Mountain; DV-Dixie Valley; EM-Excelsior Mountain; FPK-Fairview Peak; FSM-Fort Sage Mountain; HV-Hansel Valley; ML-Mammoth Lakes; OV-Owens Valley; OF-Olinghouse; PV-Pleasant Valley; RM-Rainbow Mountain; WON-Wonder.

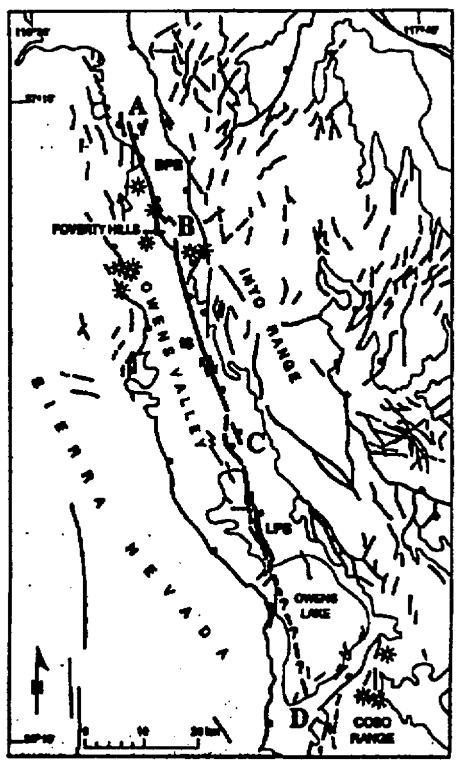

Figure 3.1.1.1.4.2.2-2 Surface Ruptures from the 1872 Owens Valley Earthquake. Bold lines represent ruptures from the 1872 event. Medium weight lines denote other faults. Balls are shown on the downthrown side of faults with normal components. Arrows indicate sense of slip on strike slip segments of the rupture. Stars represent Quaternary volcanic centers. Letters refer to points discussed in the text. Figure taken from dePolo et al. (1991)

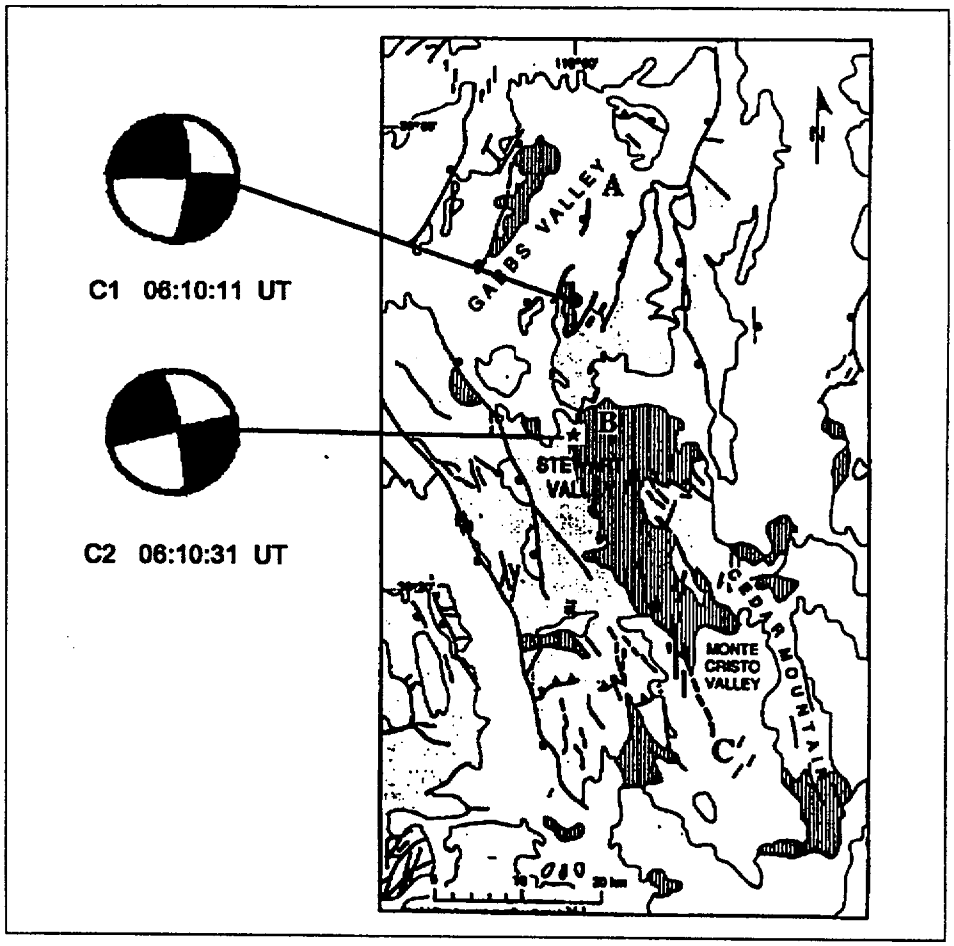

Figure 3.1.1.1.4.2.2-3 Surface Ruptures and Focal Mechanisms from the 1932 Cedar Mountain Earthquake. Vertical patterns are Tertiary sediments. Focal mechanisms are equal-area, lower focal sphere projections; white indicates regions of dilation (from Doser, 1988). Mechanisms C1 is for the first subevent in the mainshock; C2 is for the subevent occurring 20 sec later. The location for C2 (star) follows Doser's hypothesized projection. A, B, and C refer to locations discussed in the text. Modified from dePolo et al. (1991)

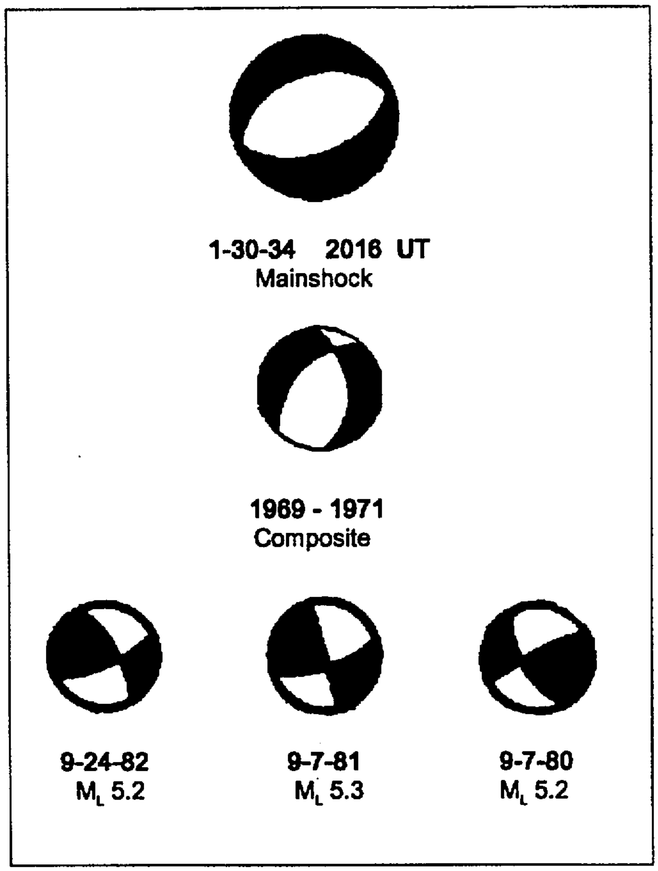

Figure 3.1.1.1.4.2.2-4 Focal Mechanisms for Earthquakes in the Excelsior Mountain Region. Top: 1934 mainshock (Doser, 1988). Middle: composite data from 1969-1971 UNRSL network recordings in the region (Ryall and Priestly, 1975). Bottom: three M 5 earthquakes located southwest of Excelsior Mountain (Vetter, 1990).

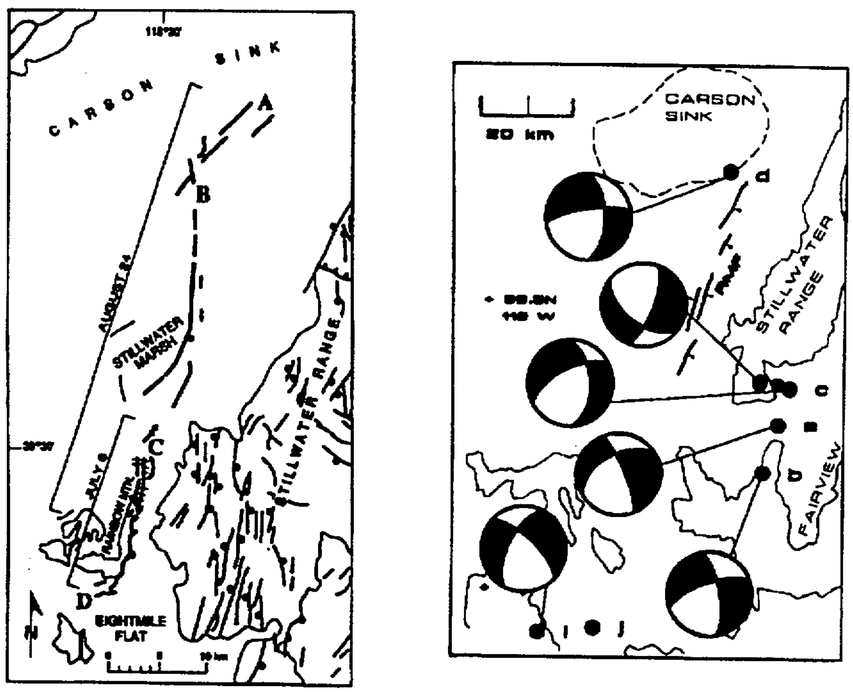

Figure 3.1.1.1.4.2.2-5 Surface Ruptures and Focal Mechanisms for Earthquakes in the 1954 Rainbow Mountain-Stillwater Sequence. The detailed surface ruptures from dePolo et al. (1991) are shown as bold lines in the left frame. The hachured lines show the ruptures that occurred in both the July 6 (Rainbow Mountain) and August 24 (Stillwater) earthquakes. Brackets show the extent of rupture in each event. Letters refer to locations discussed in the text. Left frame from dePolo et al. (1991). Right frame is a larger scale map showing the focal mechanisms from earthquakes in this sequence. Focal mechanisms are based on body-wave inversion by Doser (1986). Events are: 7/6/54 - 1113 UT (a); 7/6/54 - 2207 UT (b); 8/24/54 (c); 8/31/54 (d); 9/1/93 (e); 6/23/59 - 1435 UT (i); 6/23/59 - 1504 UT (j). Right frame modified from Doser (1986)

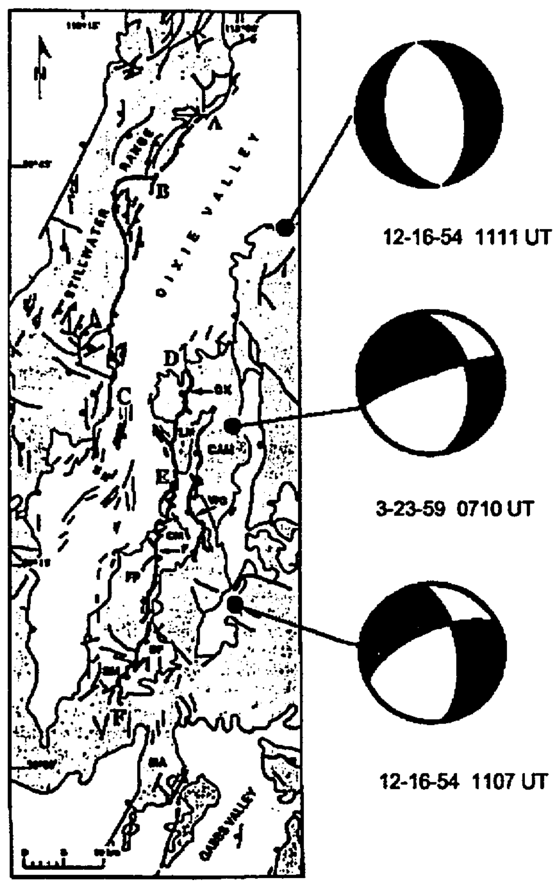

Figure 3.1.1.1.4.2.2-6 Surface Ruptures and Focal Mechanisms for Earthquakes in the Fairview Peak-Dixie Valley Sequence. Surface ruptures from the 1954 Fairview Peak and Dixie Valley earthquakes are shown as bold lines (dePolo et al. (1991)). Letters identify fault segments from dePolo et al. (1991) as follows: GK = Gold King segment; LM = Louderback Mountain; CAM = Clan Alpine Mountains; WG = West Gate segment; CM = Chalk Mountain; MA = Mount Anna. Earthquake epicenters (dark circles) and focal mechanisms are from Doser (1986). Base map modified from dePolo et al. (1991)

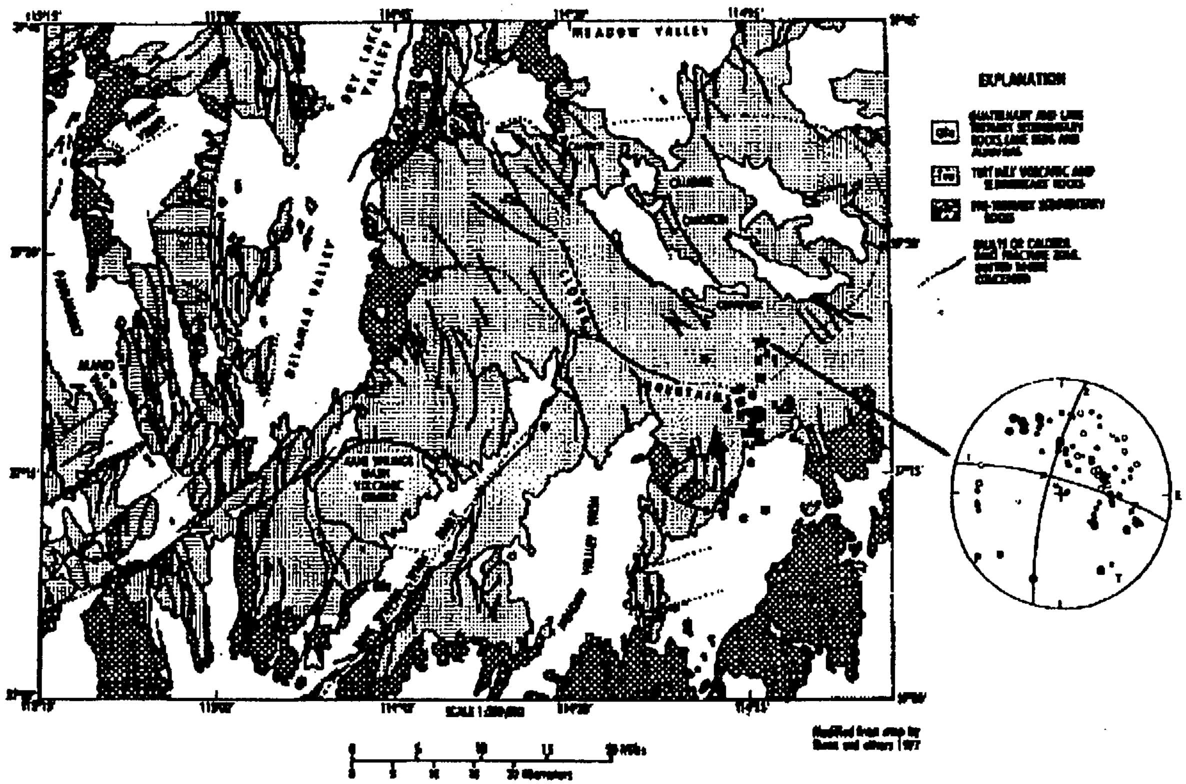

Figure 3.1.1.1.4.2.2-7 Caliente-Clover Mountain Earthquake. Focal mechanism from Smith and Sbar (1974)

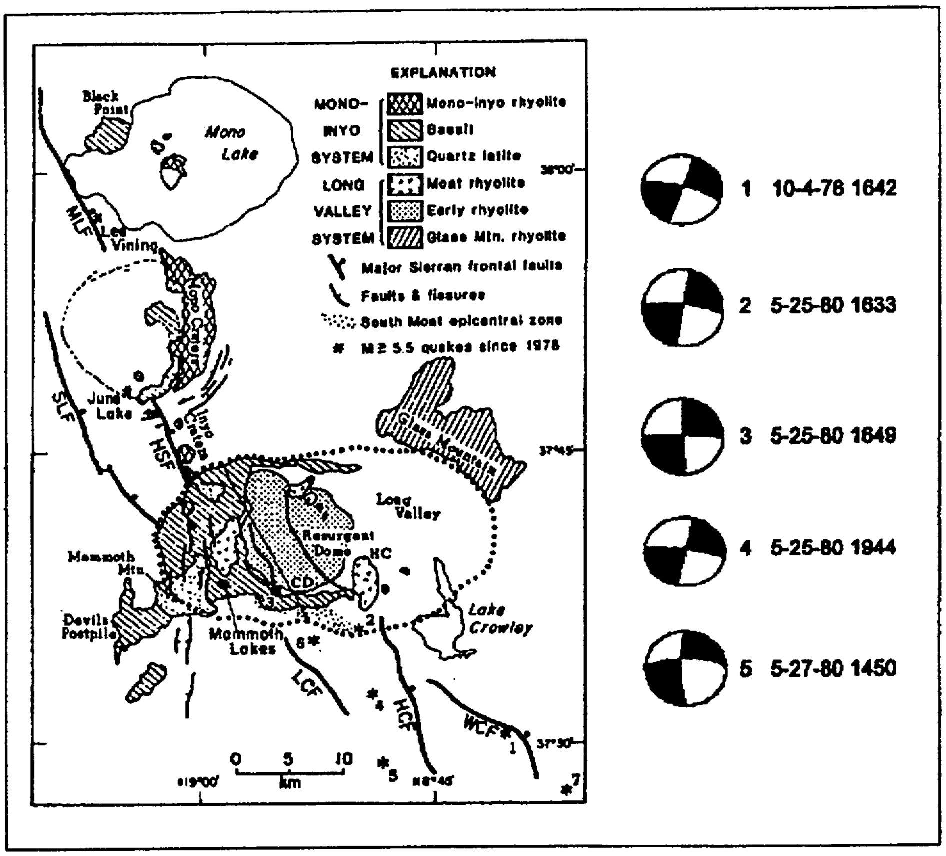

Figure 3.1.1.1.4.2.2-8 Geologic Map of the Long Valley Region with Earthquake Focal Mechanisms. Map shows the distribution of volcanic rocks related to the Long Valley and Inyo/Mono magmatic systems (Hill et al. (1985)). HSF, Hartly Springs fault; HCF, Hilton Creek fault; SLF, Silver Lake fault; WCF, Wheeler Crest fault; CD, Casa Diablo hot spring; HC, Hot Creek hot spring. Focal mechanisms are based on short period data from Cramer and Toppozada (1980). Numbers to the right of focal mechanisms refer to map locations. See Table 3.1.1.1.4.2-1 for magnitudes of the events

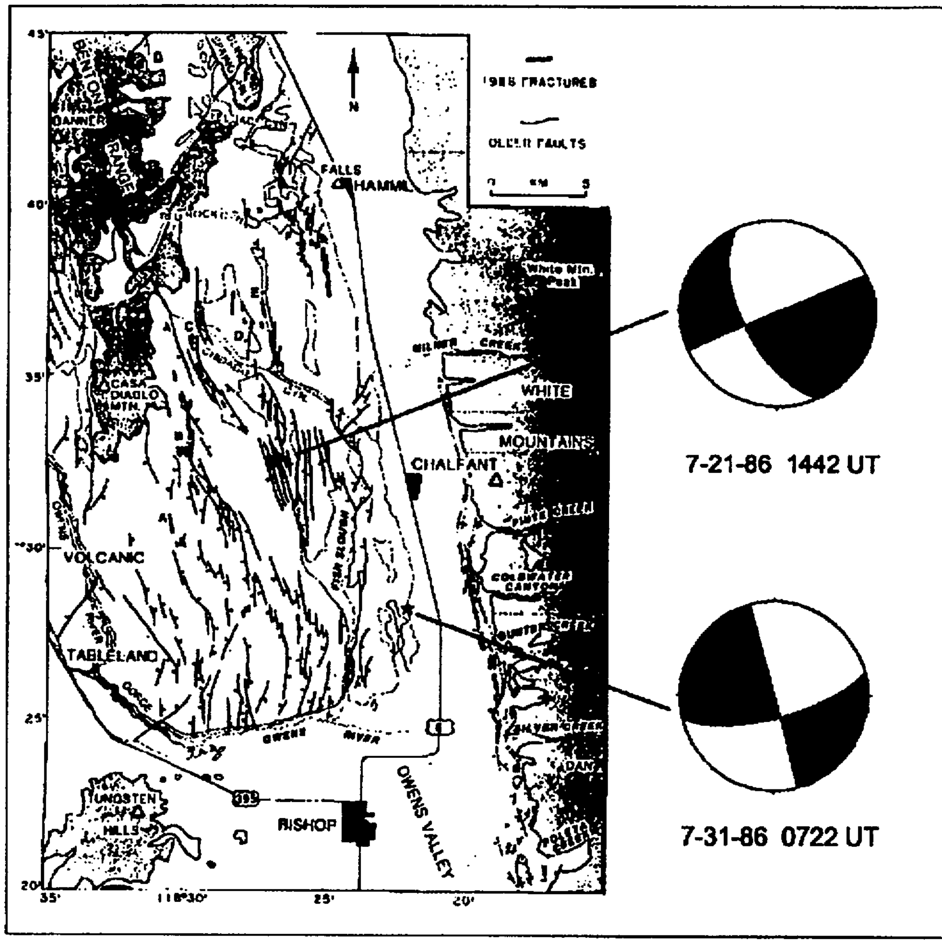

Figure 3.1.1.1.4.2.2-9 Surface Ruptures and Focal Mechanisms for 1986 Chalfant Valley Earthquake Sequence. Surface ruptures shown as bold lines in the Volcanic Tableland and along the White Mountains frontal fault zone (lienkaemper et al. 1987). Letters A - F identify fracture zones in the Volcanic Tableland. Large star indicates the location of the July 21 mainshock (M_w 6.2); small star indicates location of the largest aftershock on July 31 (M_w 5.5). Focal mechanisms from Cockerham and Corbett (1987). Base map from Lienkaemper et al. (1987)

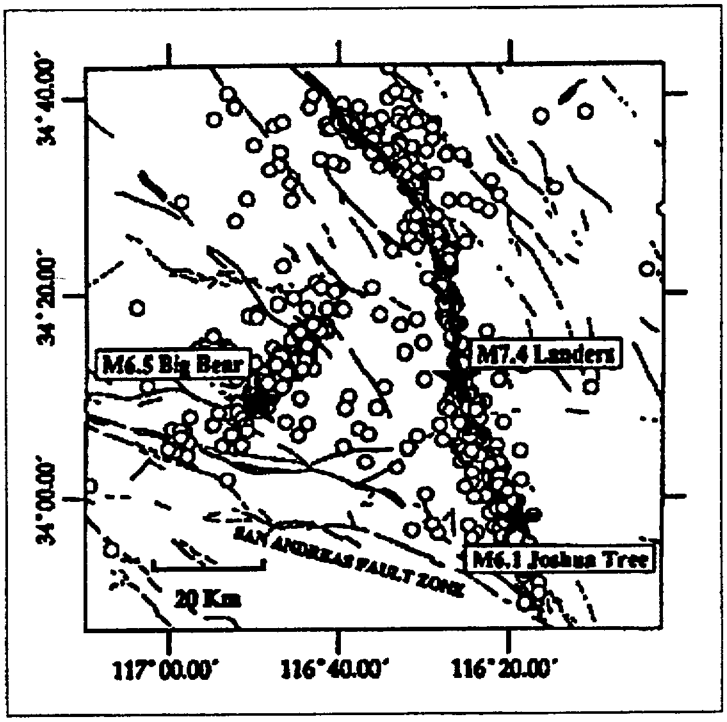

Figure 3.1.1.1.4.2.2-10 Epicentral Region of the 1992 Landers, California, Earthquake. Stars represent significant events in the sequence. Circles are locations of aftershocks. Bold lines denote surface rupture in the mainshock. Light lines are other Quaternary faults. Taken from Campillo and Archuleta (1993)

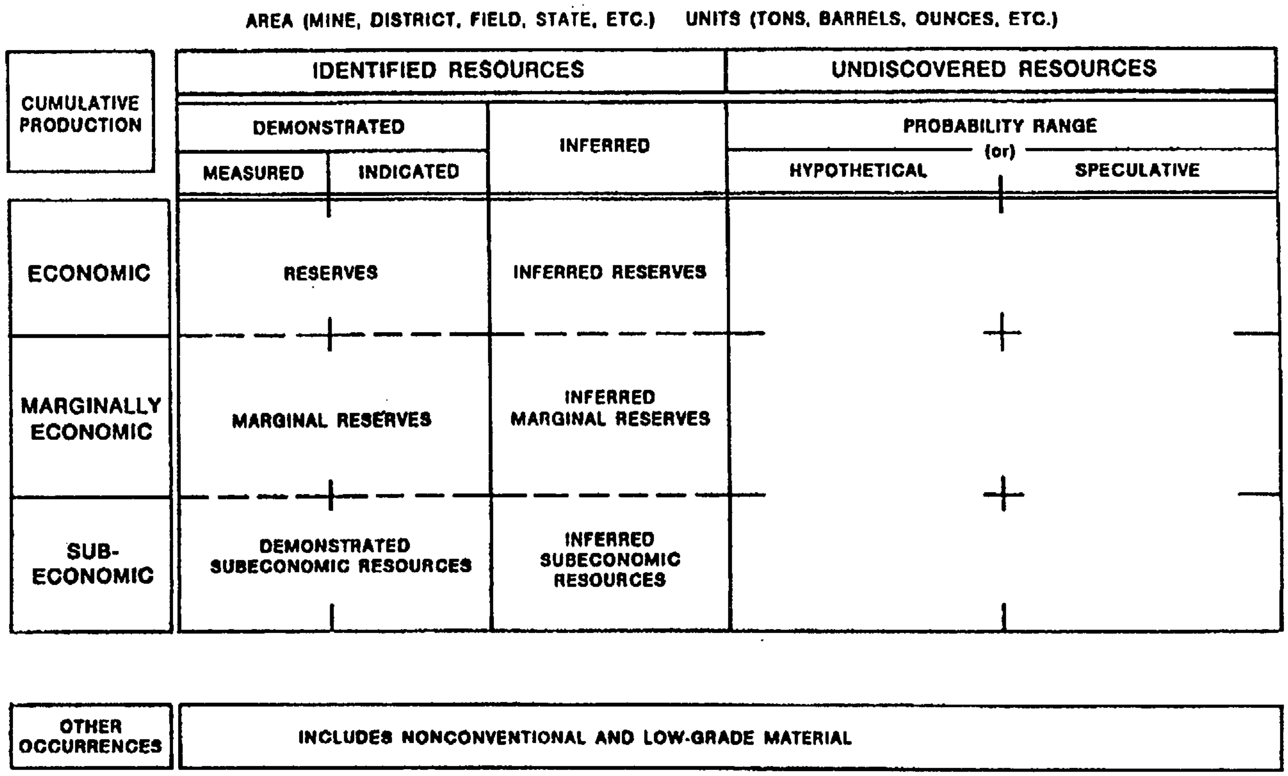

Figure 3.1.1.1.5-1 Major Elements of Mineral-Resource Classification. Modified from USBM/USGS (1980) from the SCP

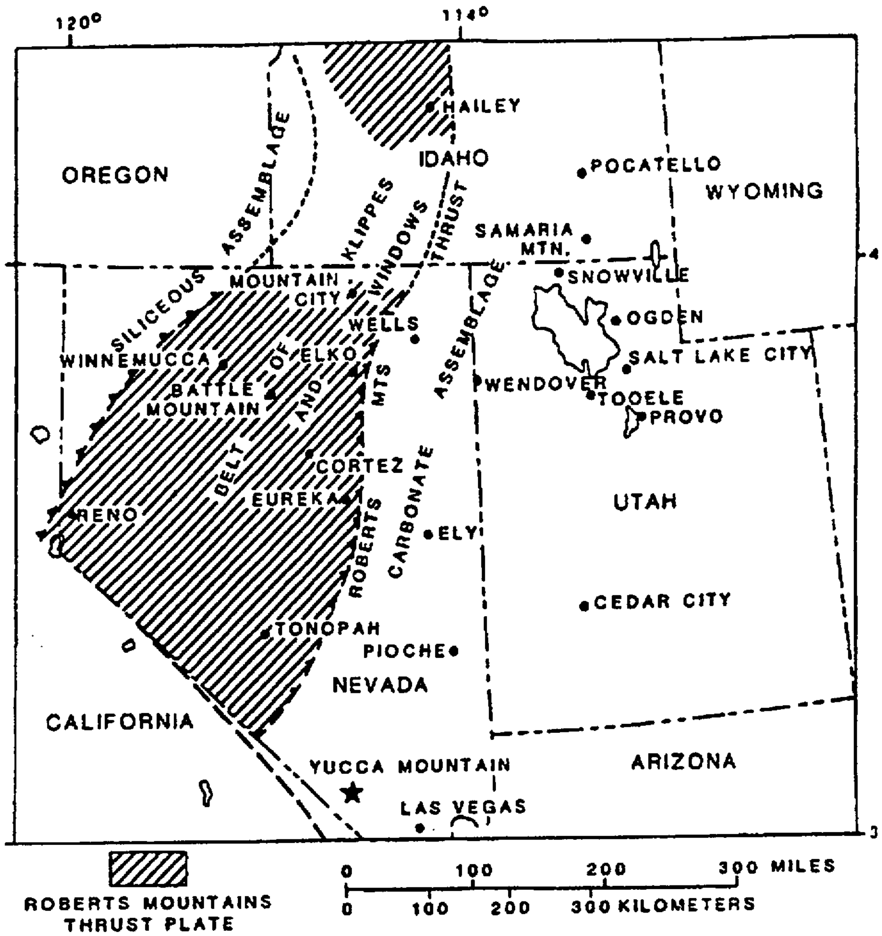

Figure 3.1.1.1.5.2.1-1 Map Showing Distribution of Paleozoic Rocks in Roberts Mountains Thrust Plate After Mississippian Thrusting. Modified from Roberts et al. (1971)

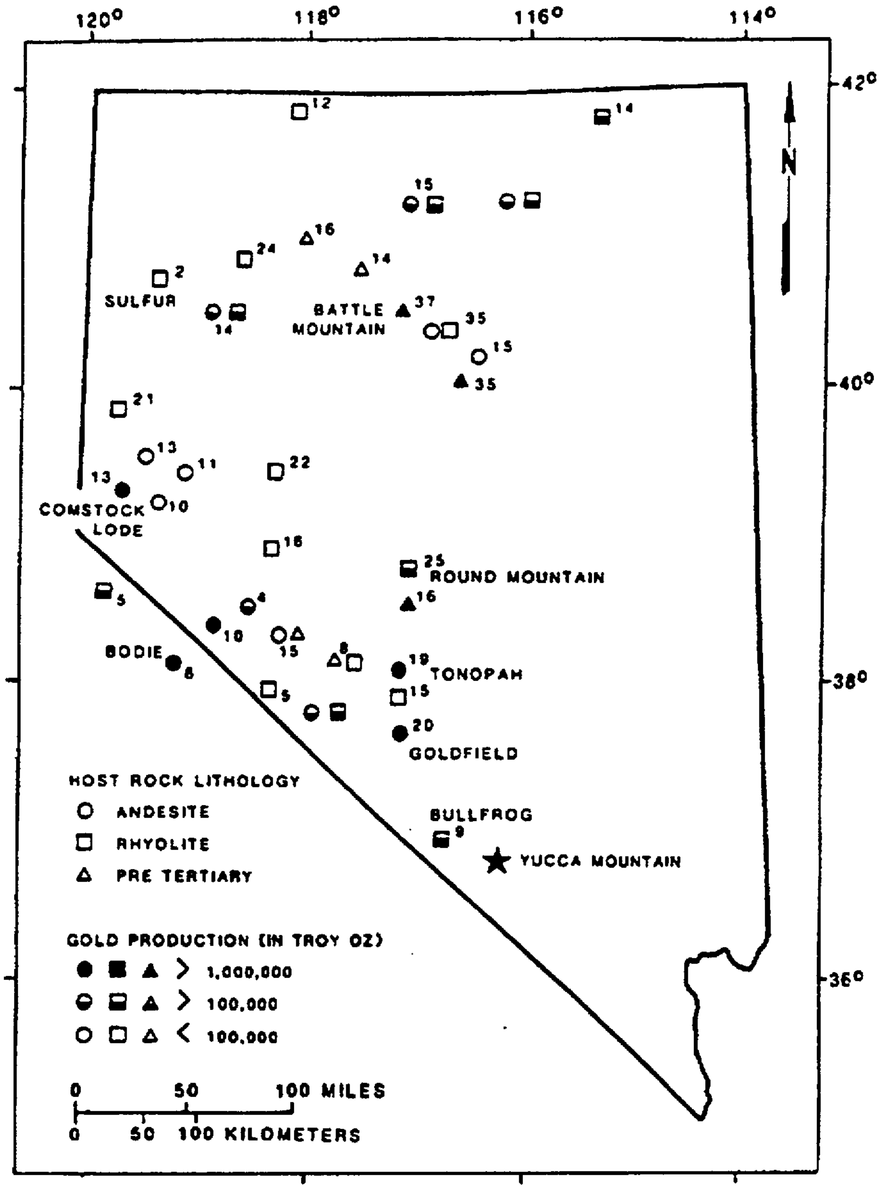

Figure 3.1.1.1.5.2.1-2 Map Showing the Distribution of Ore Deposits Dated by Potassium-Argon Dating Methods, Lithologies of the Host Rock, and Approximate Production of Gold. Potassium-argon dates are mineralization ages and are represented by numbers (million years) next to symbols. Modified from Silberman et al. (1976) and Silberman (1985).

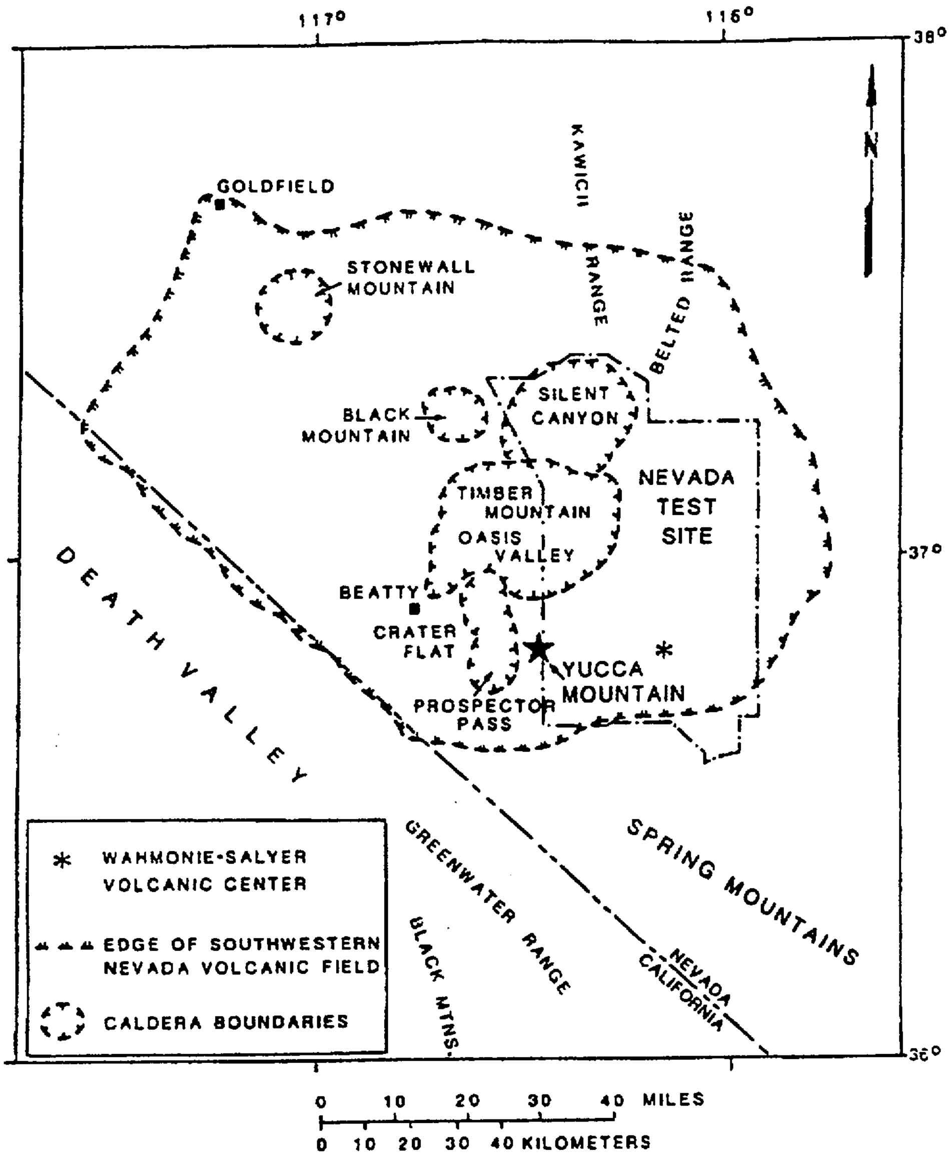

Figure 3.1.1.1.5.2.1-3 Calderas Within the Southwestern Nevada Volcanic Field. Modified from Carr (1984) from the SCP

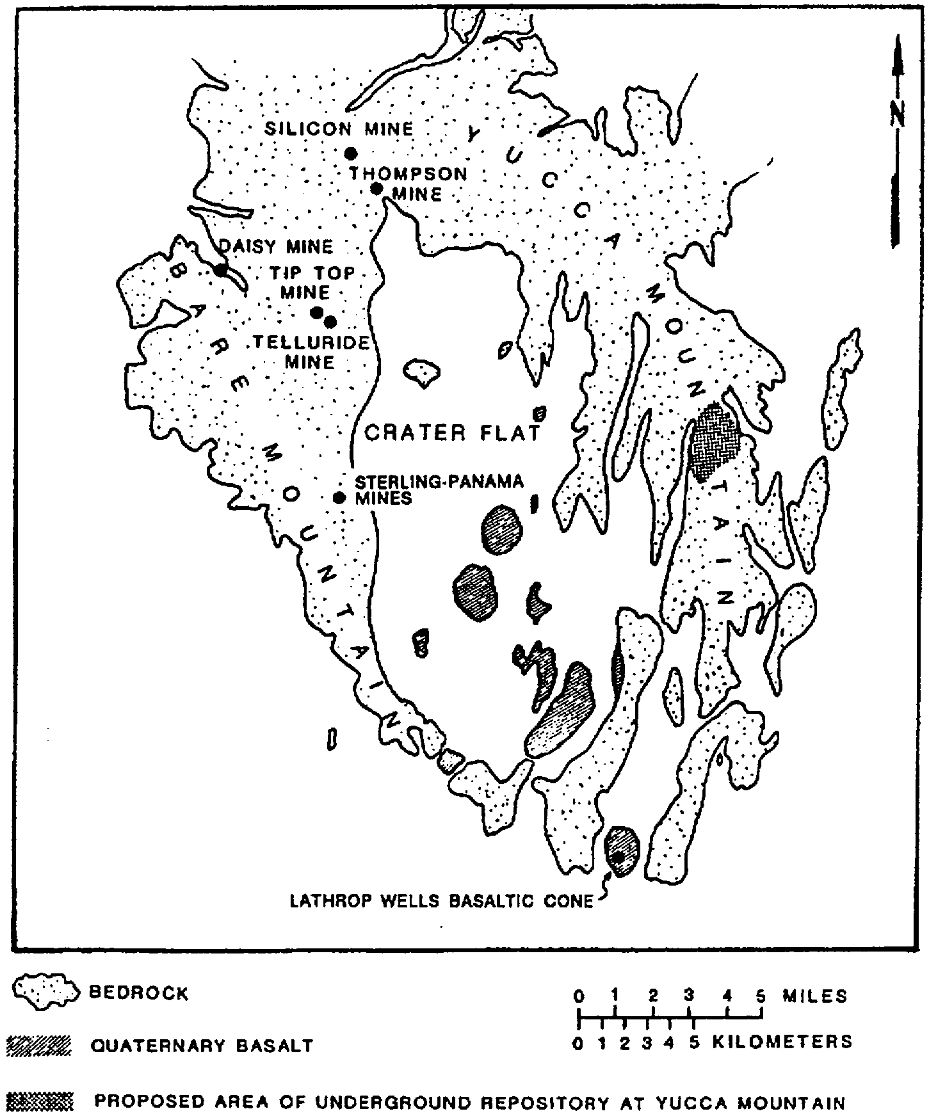

Figure 3.1.1.1.5.2.2-1 Bedrock Map Showing Locations of the Sterling, Daisy, Silicon, Harvey (Telluride), Tip Top, and Thompson Mines Relative to the Proposed Repository Site. Modified from the Geologic Map of Cornwall and Kleinhampl (1964) from the SCP

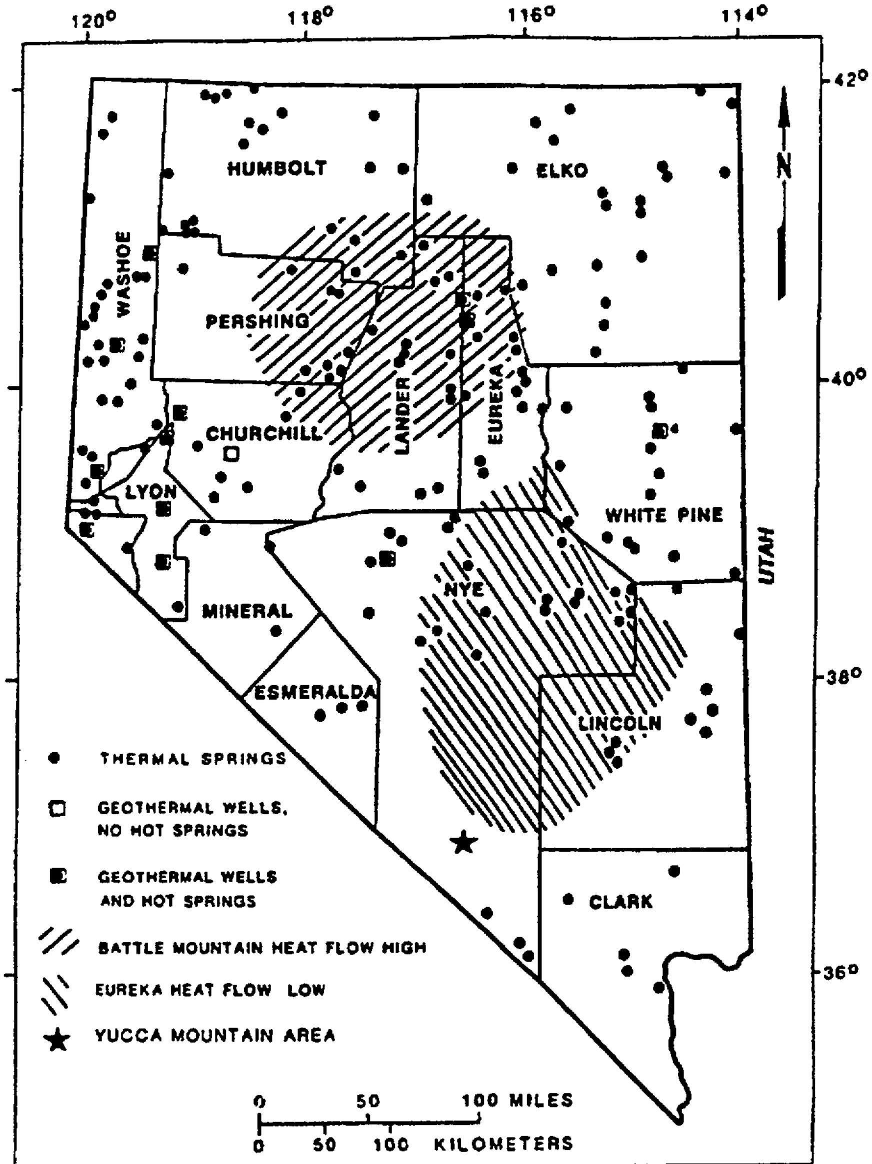

Figure 3.1.1.1.5.3-1 Hot Springs, Geothermal Wells, and Low-Temperature Thermal Resources in Nevada. The Battle Mountain High and the Eureka Low Heat-Flow Regions are also shown. Modified from Garside (1974) from the SCP

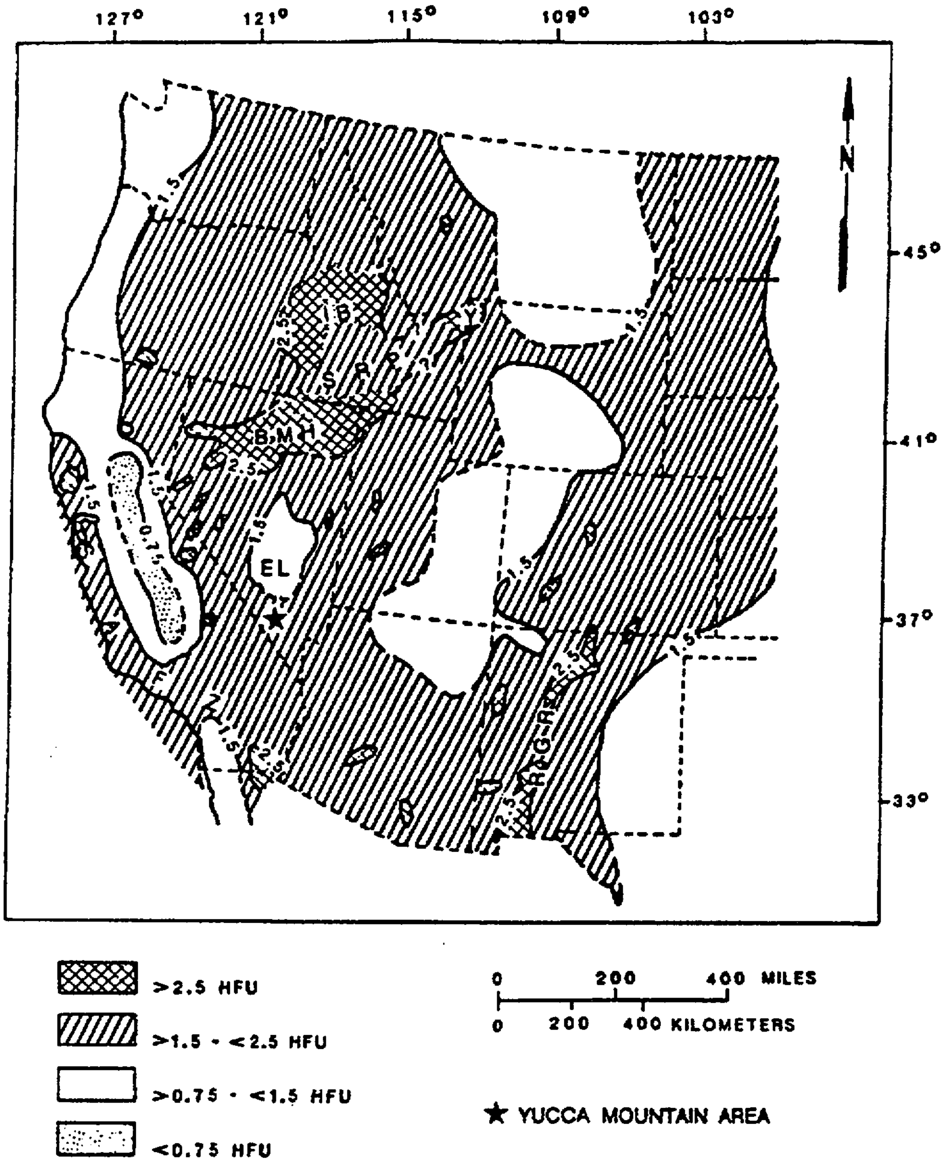

Figure 3.1.1.1.5.3-2 Regional Heat Flow and Distribution of Hydrothermal Systems. Abbreviations are BMH for Battle Mountain High, EL for Eureka Low, IB for Idaho Batholith, SRP for Eastern and Central Snake River Plain, Y for Yellowstone Thermal Area, RGR for Rio Grande Rift, and SAFZ for San Andreas Fault Zone. Modified from Lachenbruch and Sass (1977) from the SCP

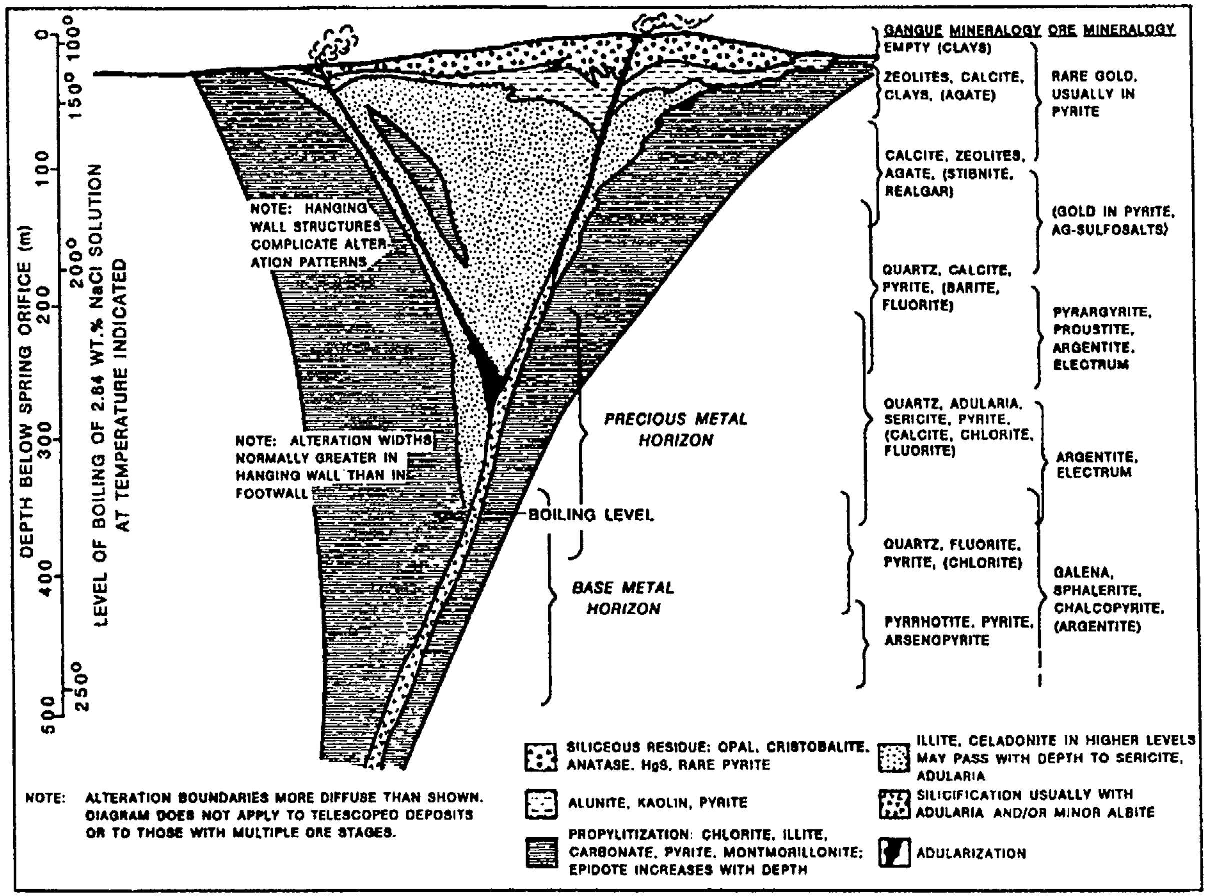

Figure 3.1.1.1.5.5-1 Idealized Model of Epithermal Precious-Metal Deposits. Modified from Buchanan (1981) and Sawkins (1984) from the SCP

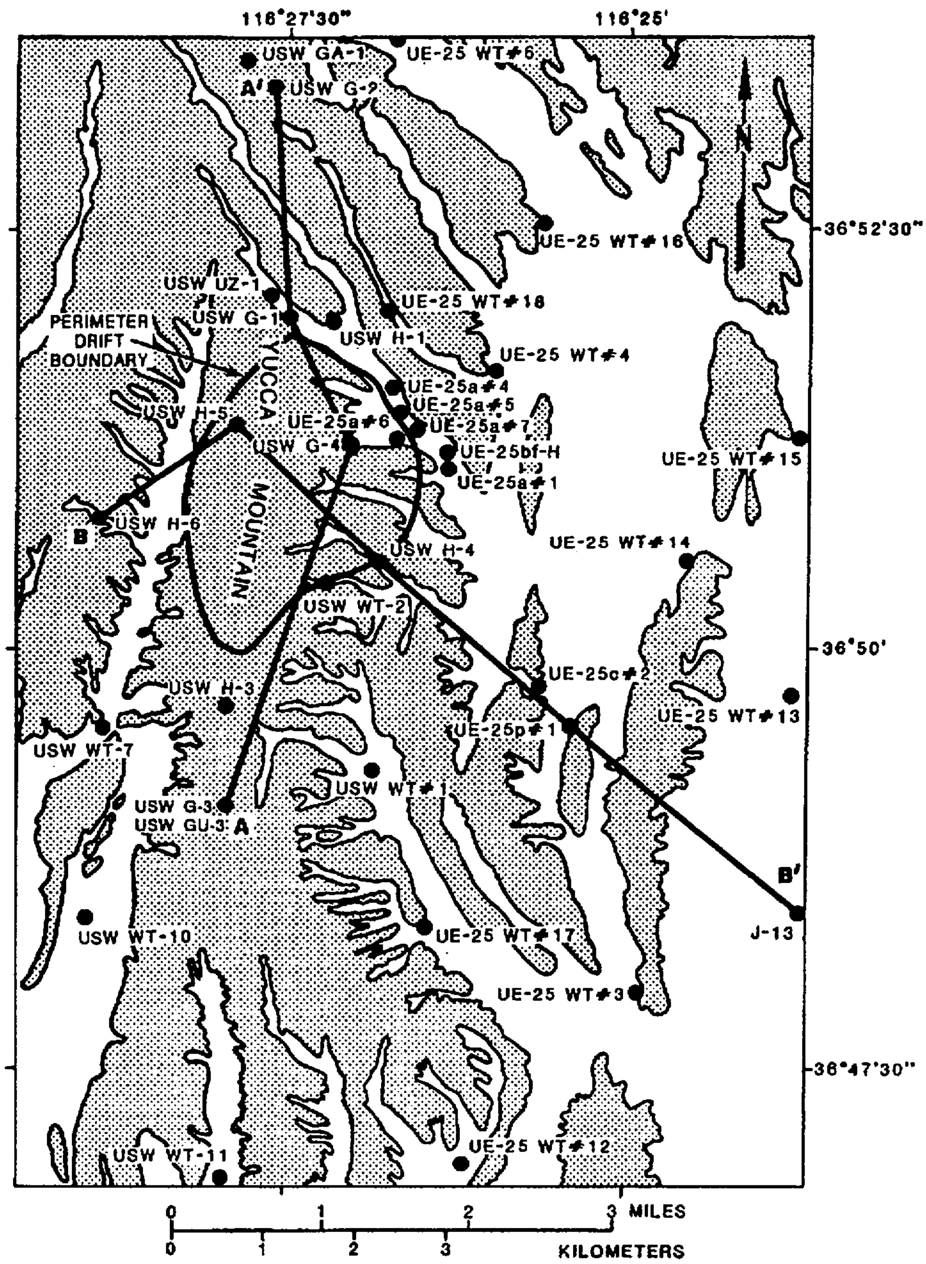

Figure 3.1.1.2.2.3-1 Index Map Showing the Locations of Selected Drillholes in the Vicinity of Yucca Mountain and the Locations of Cross Sections Shown on Figures 3.1.1.2.2.3-2 and 3.1.1.2.2.3-3.

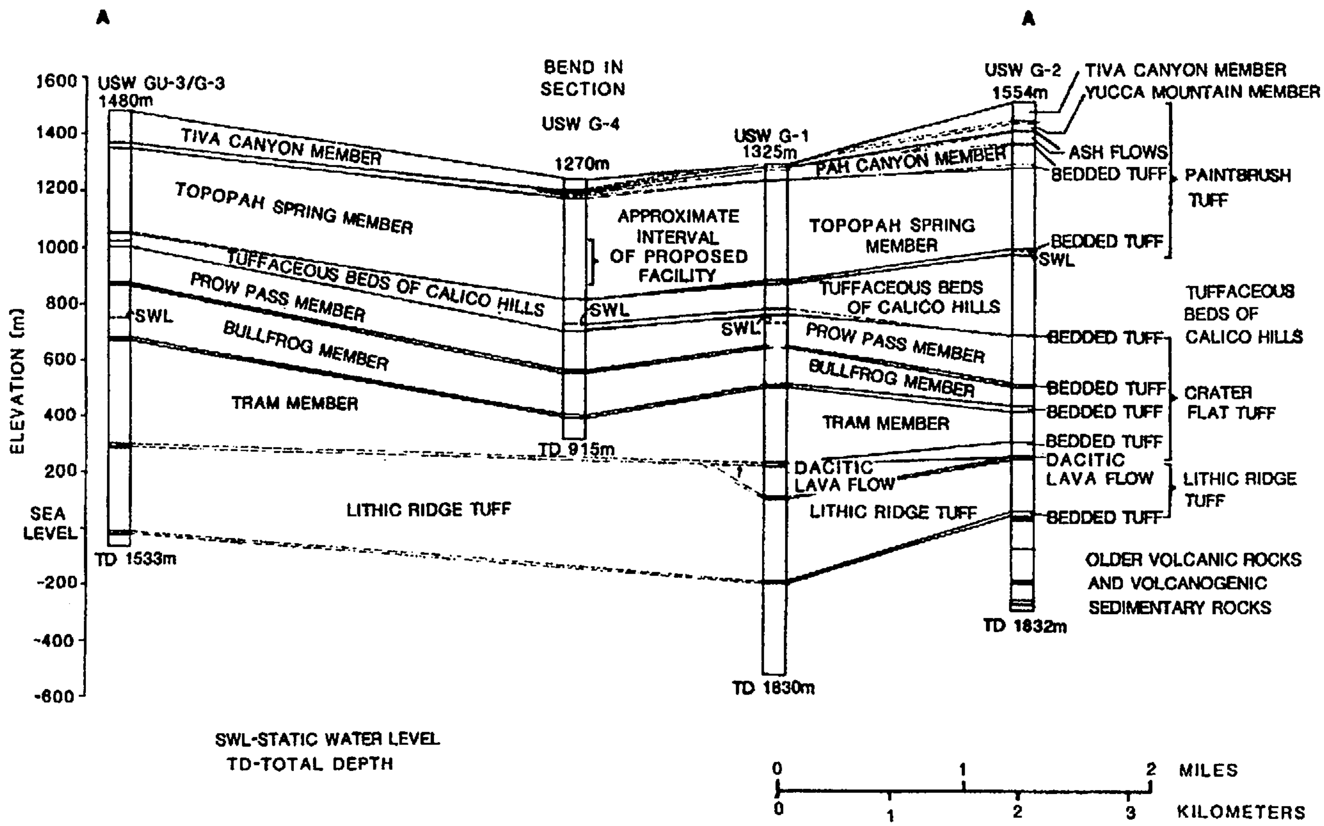

Figure 3.1.1.2.2.3-2 North-South Stratigraphic Cross Section Between Selected Drillholes at Yucca Mountain

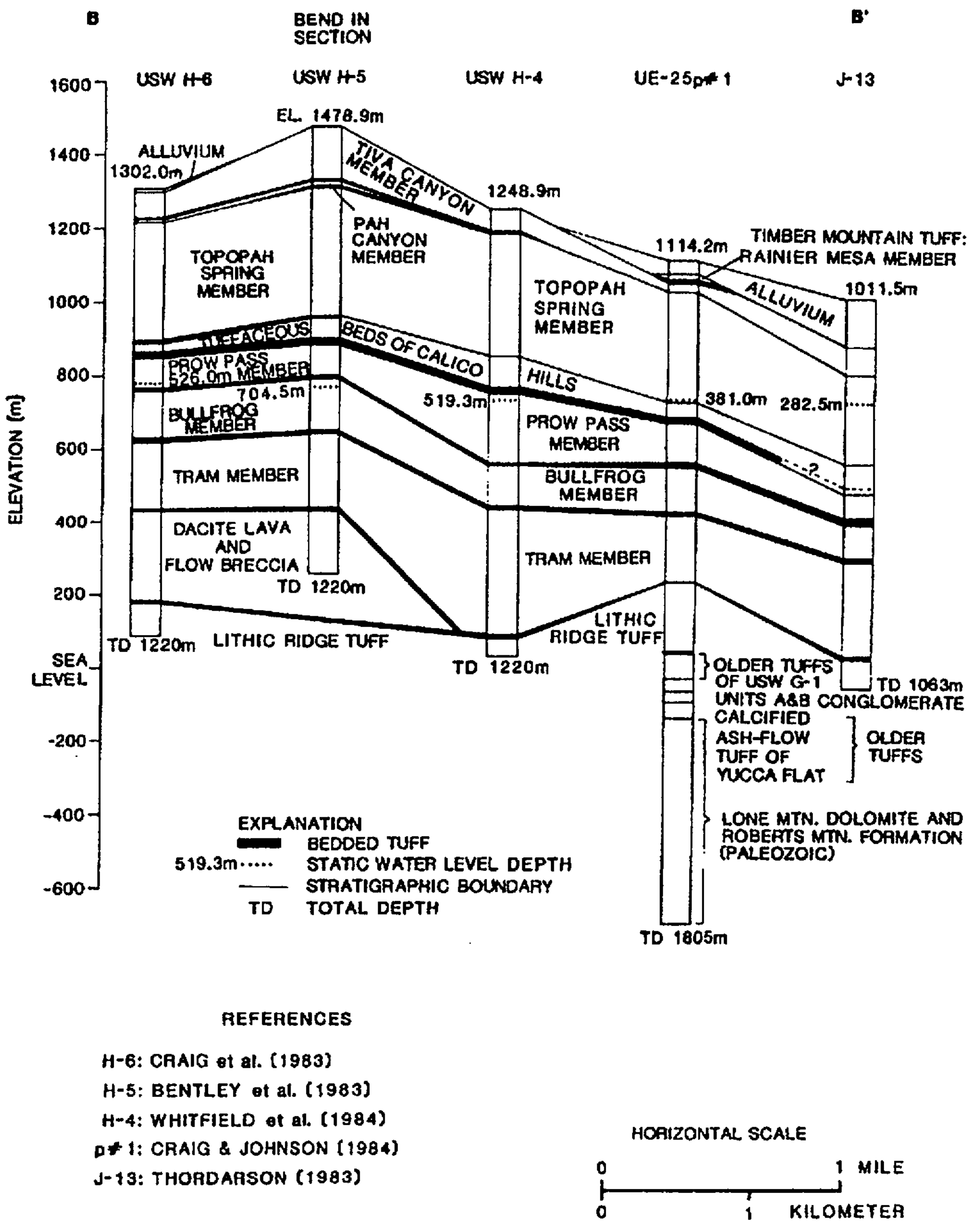

Figure 3.1.1.2.2.3-3 East-West Stratigraphic Cross Section Between Selected Drillholes at Yucca Mountain

0 1 2 MILES

0 1 2 KILOMETERS

PERIMETER DRIFT BOUNDARY

CONTACT

FAULT THAT OFFSETS QUATERNARY DEPOSITS. SHOWN BY LONG DASHES WHERE FAULT EXTENDS INTO TERTIARY ROCKS AND QUATERNARY MOVEMENT IS UNKNOWN. DOTTED WHERE CONCEALED. BAR AND BALL ON DOWNTHROWN SIDE. LETTER SYMBOL REFERS TO DESCRIPTION IN TEXT.

FAULT OF TERTIARY AGE THAT WAS TRENCHED BUT NO EVIDENCE OF QUATERNARY MOVEMENT WAS FOUND. DOTTED WHERE CONCEALED.

TRENCH SITE AND NUMBER

Figure 3.1.1.2.2.5-1 Map of Surficial Sedimentary and Volcanic Deposits in the Yucca Mountain Area. Map units are shown on Figure 3.1.1.2.2.5-2. Modified from Swadley et al. (1984)

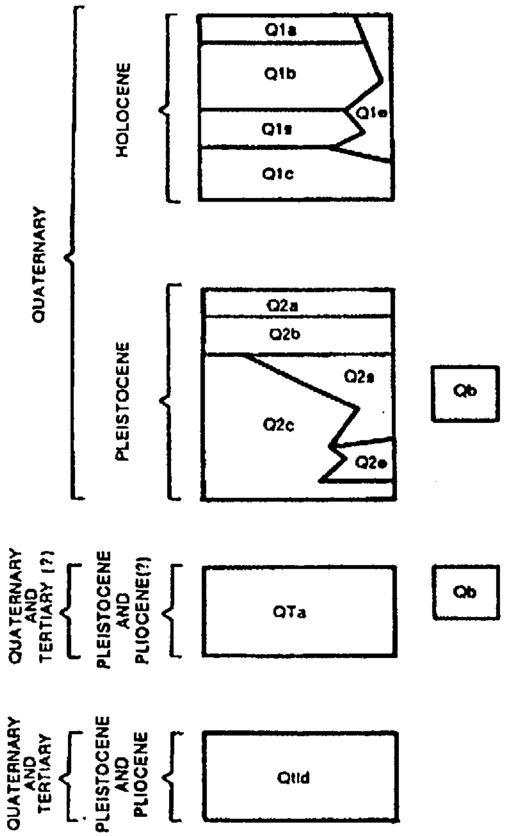

UNIT	ESTIMATED AGE RANGE (IN YEARS)
HOLOCENE DEPOSITS	
Q1a - FLUVIAL DEPOSITS	PRESENT TO 150
Q1b - FLUVIAL DEPOSITS AND DEBRIS FLOWS	150 TO 4,000
Q1e - EOLIAN DUNES AND SAND SHEETS	PRESENT TO 8,000
Q1s - FLUVIAL SAND SHEETS	4,000 TO 7,000
Q1c - COARSE FLUVIAL DEPOSITS	7,000 TO 9,000
MIDDLE AND LATE PLEISTOCENE-PLIOCENE (?) DEPOSITS	
Q2a - LOCAL DEBRIS FLOWS	≈40,000
Q2b - FLUVIAL DEPOSITS	160,000 TO 250,000
Q2s - FLUVIAL SAND SHEETS	270,000 TO 700,000
Qb - BASALT FLOWS AND CINDERS	100,000 TO 300,000
Q2e - EOLIAN DUNES AND SHEETS	700,000 TO 750,000
Q2c - COARSE FLUVIAL DEPOSITS	270,000 TO 800,000
EARLY PLEISTOCENE (?) DEPOSITS	
QTa - DEBRIS FLOWS, MINOR FLUVIAL DEPOSITS	1.1×10^6 TO 2×10^6
Qb - BASALT FLOWS AND CINDERS	1.1×10^6 TO 1.3×10^6
PLIOCENE-PLEISTOCENE DEPOSITS	
QTld - LACUSTRINE DEPOSITS	$< 2 \times 10^6$ TO 4×10^6

Figure 3.1.1.2.2.5-2 Quaternary Units Present in the Yucca Mountain Area and Mapped on Figure 3.1.1.2.2.5-1

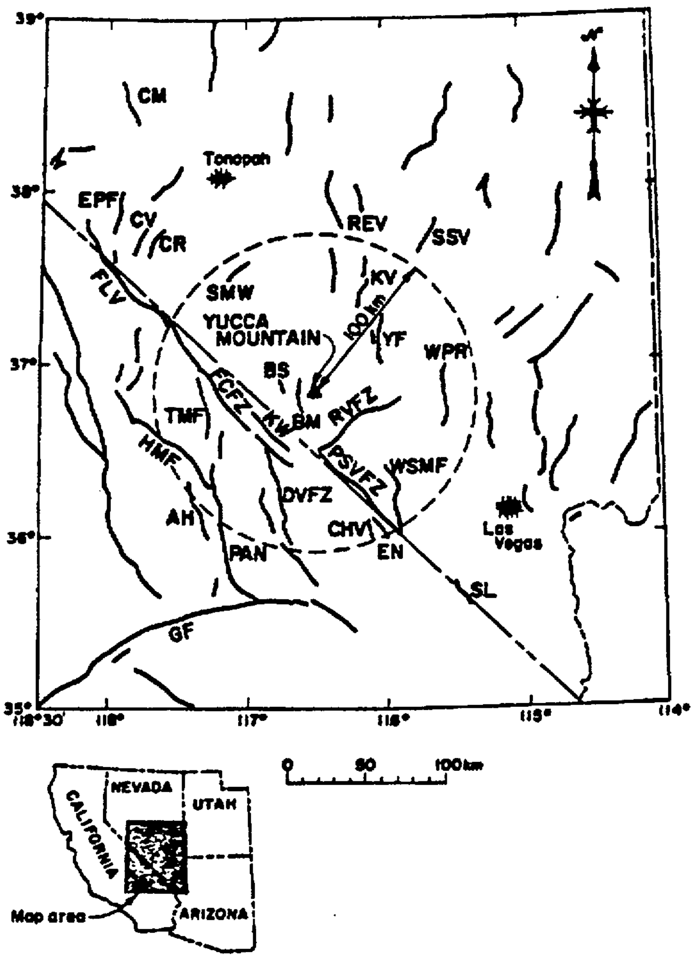

Figure 3.1.1.2.3.2-1 Preliminary Generalized Map of Known and Suspected Quaternary Faults Within 100 km of Yucca Mountain (modified from Piety et al., 1992). Abbreviations are for the following fault names: AH, Ash Hill; BM, Bare Mountain fault zone; BS, Beatty scarp; CHV, Chicago Valley fault; CM, Cedar Mountain fault; CR, Clayton Ridge fault; DVFZ, Death Valley fault zone; EN, East Nopah fault zone; EPR, Emigrant Peak fault; FCFZ, Furnace Creek fault zone; FLV, Fish Lake Valley fault zone; GF, Garlock fault zone; HMF, Hunter Mountain fault; KV, Kawich Valley fault; KW, Keane Wonder fault; PAN, Panamint Valley fault zone; PSVFZ, Pahrump-Stewart Valley fault zone; REV, Reveille Valley faults; RVFZ, Rock Valley fault zone; SL, State Line fault; SSV, Sand Spring Valley fault; SWM, Stonewall Mountain fault; TMF, Tin Mountain fault; WPR, West Pintwater Range fault; WSMF, West Spring Mountains fault; and YF Yucca fault.

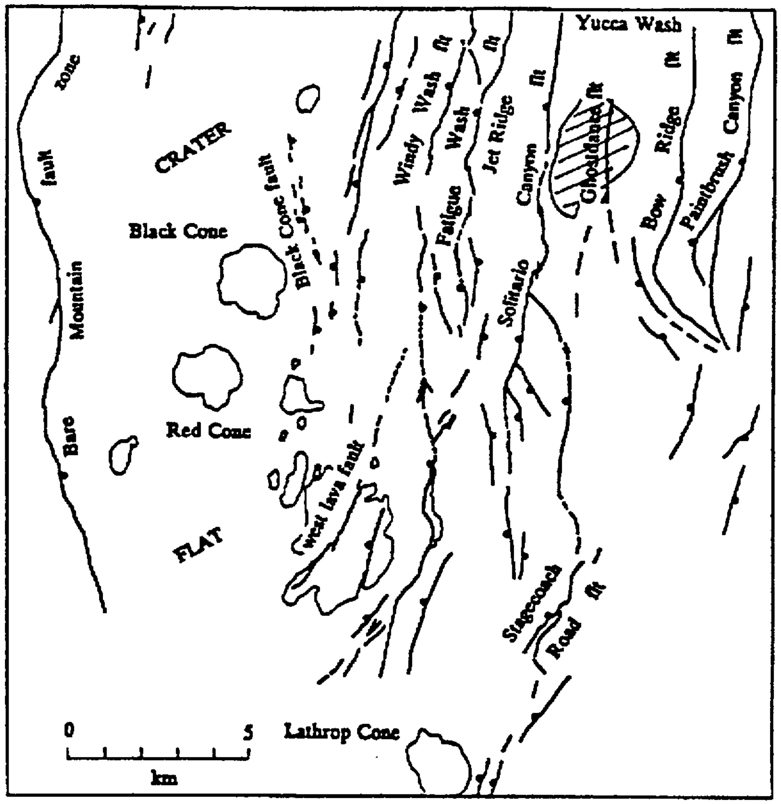

Figure 3.1.1.2.3.2-2 Generalized Map of Quaternary Faults and Pliocene/Quaternary Basalts in the Yucca Mountain Vicinity. Hachures show the location of the proposed repository. Modified after Ramelli et al. (1991)

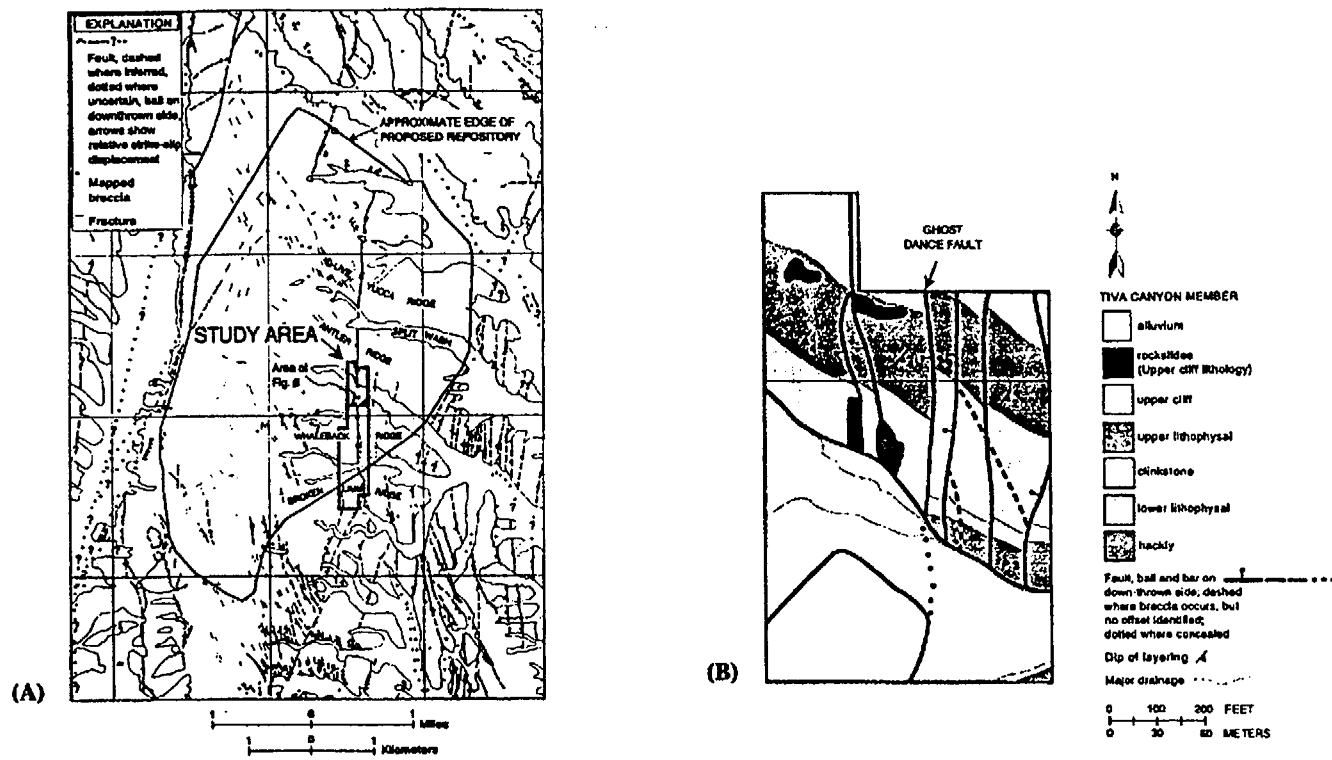

Figure 3.1.1.2.3.2-3 (A) Map of Bedrock Structural Features Within and Surrounding the Proposed Repository at Yucca Mountain; and, (B) Geologic Map of the Antler Ridge Area Along the Ghost Dance Fault Zone. Modified from Spengler et al. (1993)

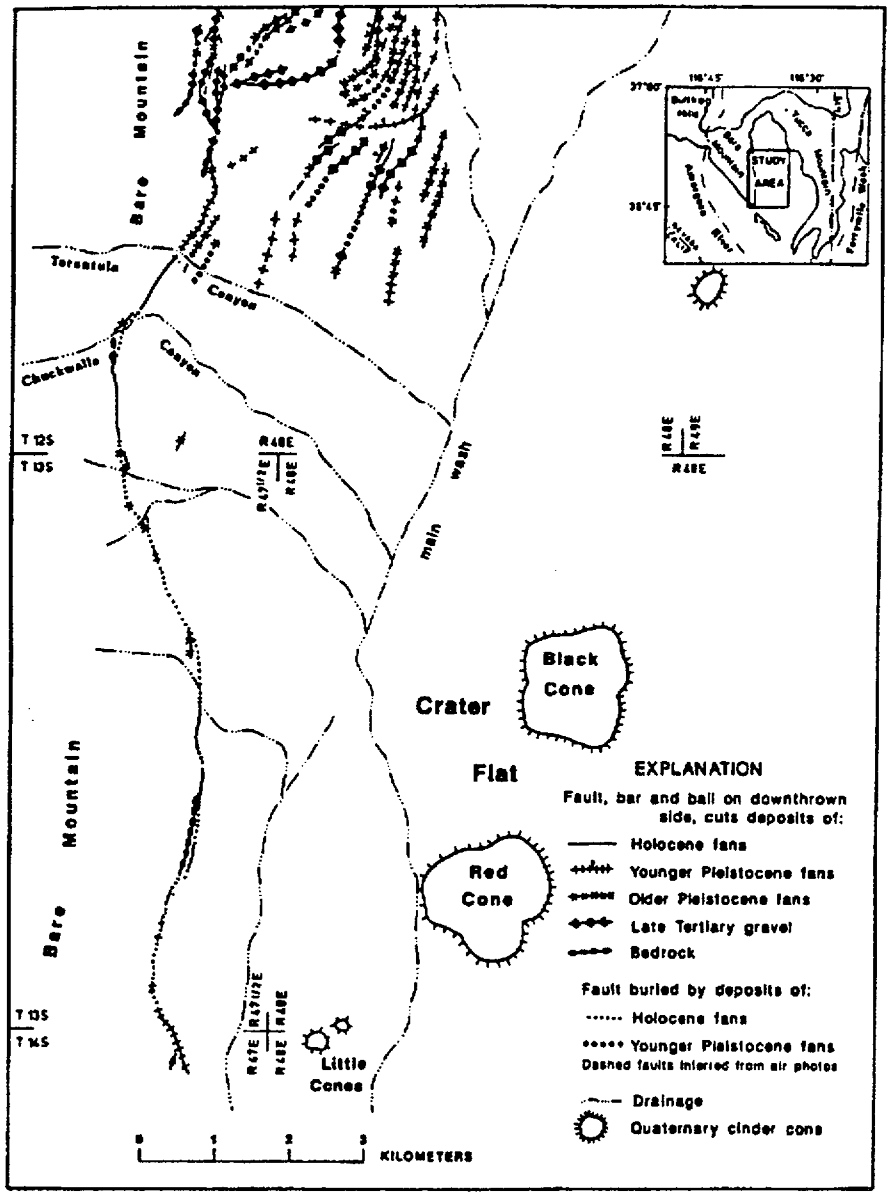

Figure 3.1.1.2.3.2-4 Map of the Bare Mountain Fault on the East Side of Bare Mountain. Modified after Reheis (1988). Faults with no bar and ball are down to the south or east

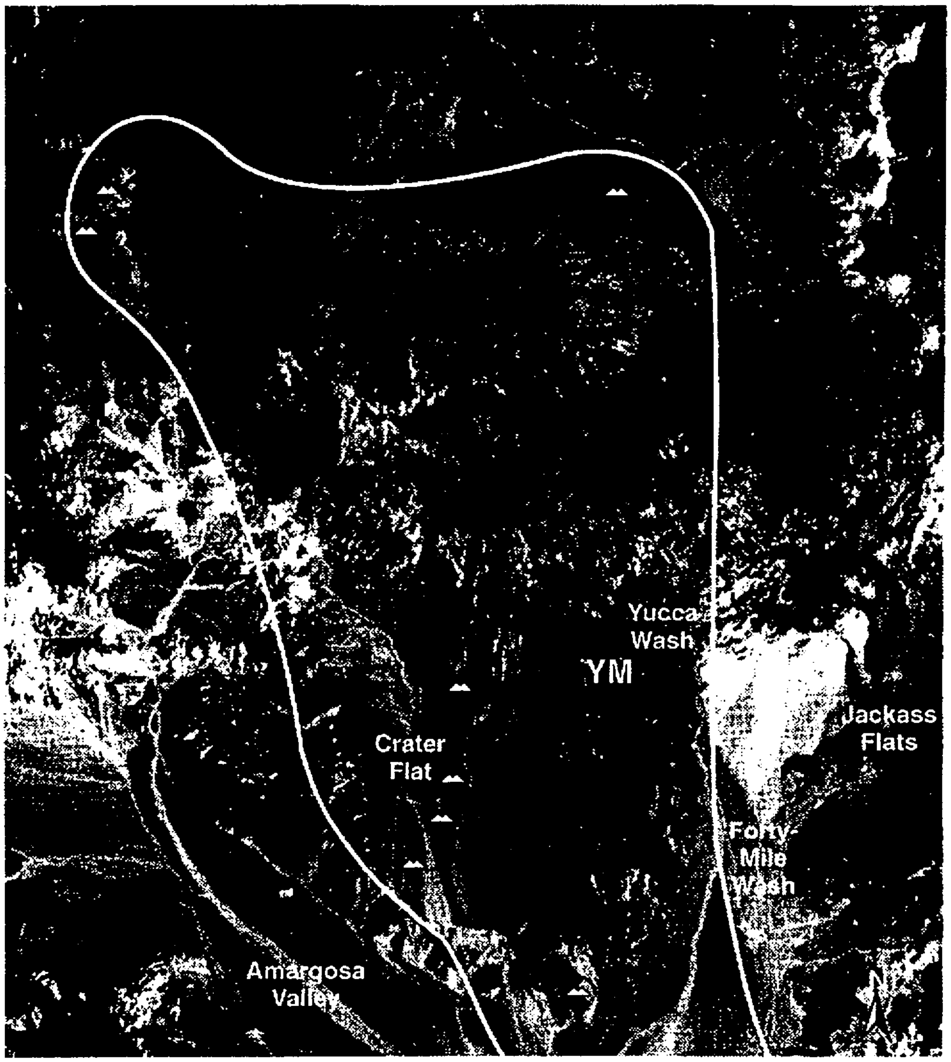

Figure 3.1.1.2.3.5-1 Digital Satellite Image Showing the Location of the Potential Yucca Mountain Site and the Distribution of Quaternary Volcanic Centers in the YMR

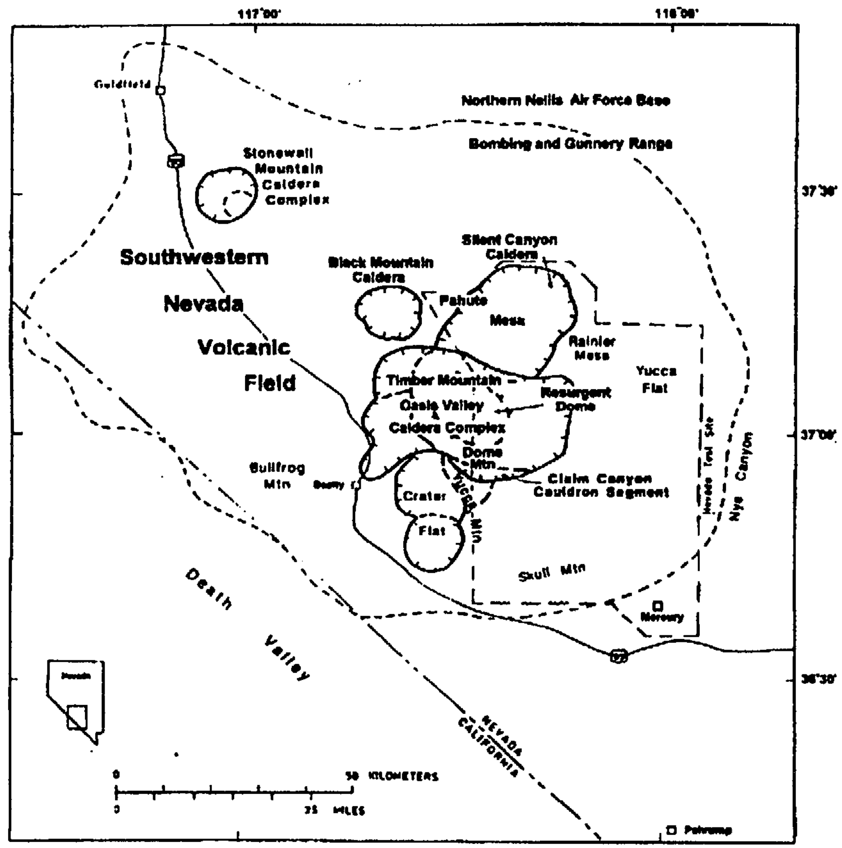

From Byers et al. (1989)

Figure 3.1.1.2.3.5.1-1 The Southwest Nevada Volcanic Field

Magma Gap

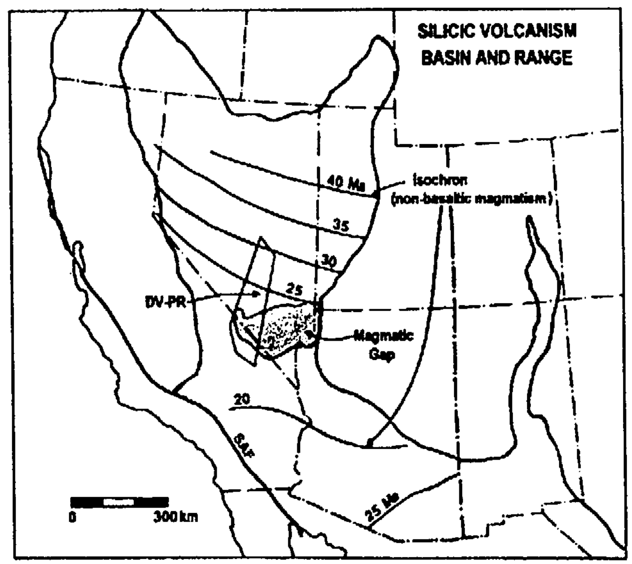

From Farmer et al. (1989)

Figure 3.1.1.2.3.5.1-3 Time Transgressive, Mid-Cenozoic Volcanism of the Basin-Range Province (after Farmer et al., 1989)

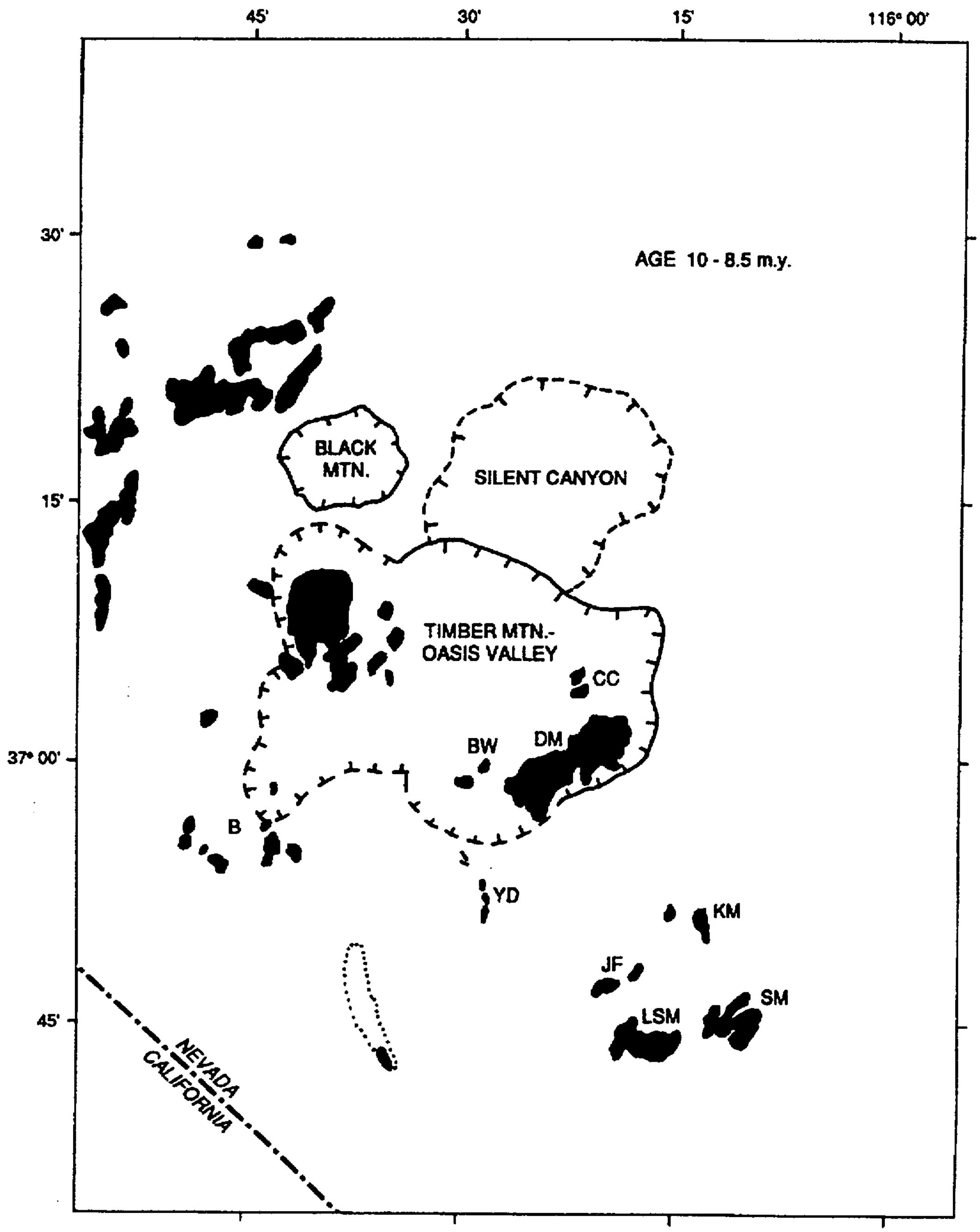

Figure 3.1.1.2.3.5.2.1-2 Distribution of the Basalt of the Silicic Episode

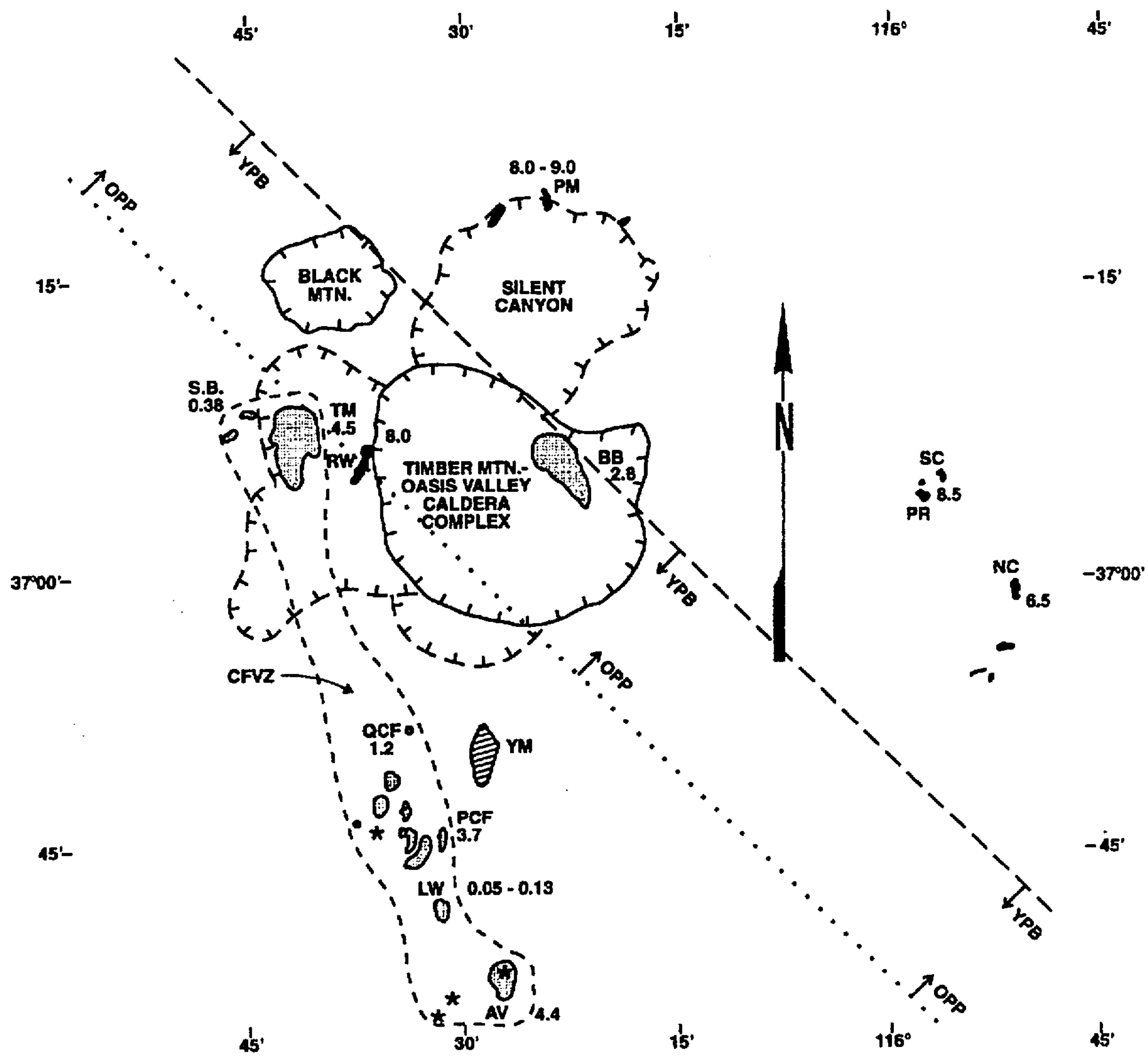

Figure 3.1.1.2.3.5.2.2-1 Post-Caldera Basalt of the YMR

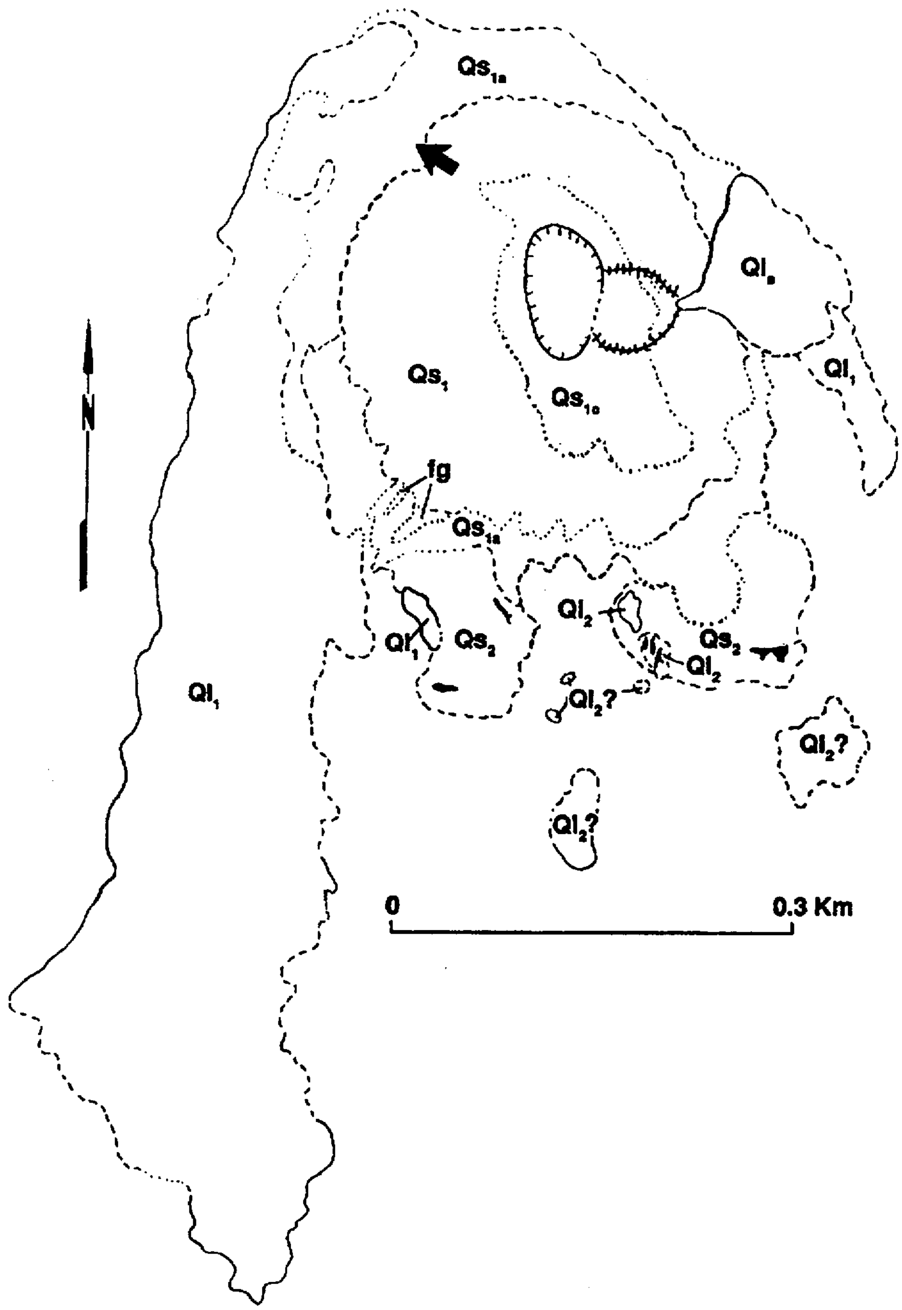

Figure 3.1.1.2.3.5.2.2-3 Generalized Geologic Map of the Little Black Peak Volcanic Center of the Basalt of Sleeping Butte

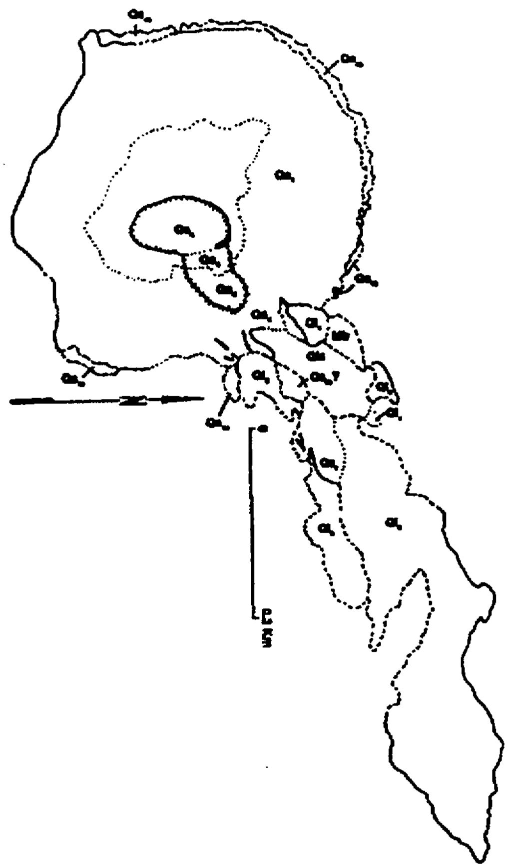

Figure 3.1.1.2.3.5.2.2-4 Generalized Geologic Map of the Hidden Cone Center of the Basalt of Sleeping Butte

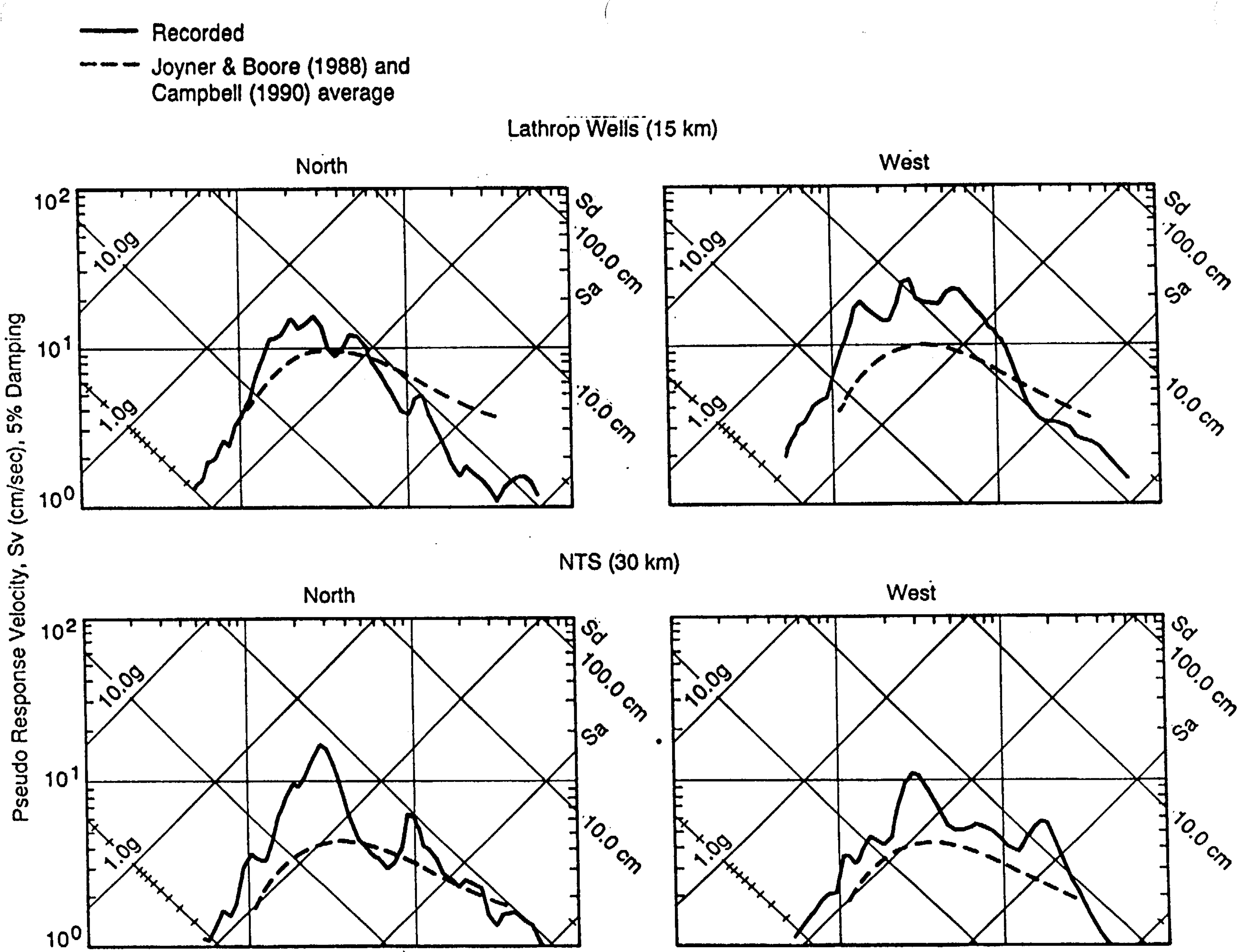

Figure 3.1.1.2.4.2.2-4 Response Spectral Velocity at 5% Damping Recorded at Lathrop Wells (Epicentral Distance 15 km) During the Little Skull Mountain, Nevada Earthquake of 29 June 1992 in Southern Nevada, Compared with the Average of the Estimates Derived from Joyner and Boor (1988) and Campbell (1990). Data Source: URS/Blume & Assoc. (1992)

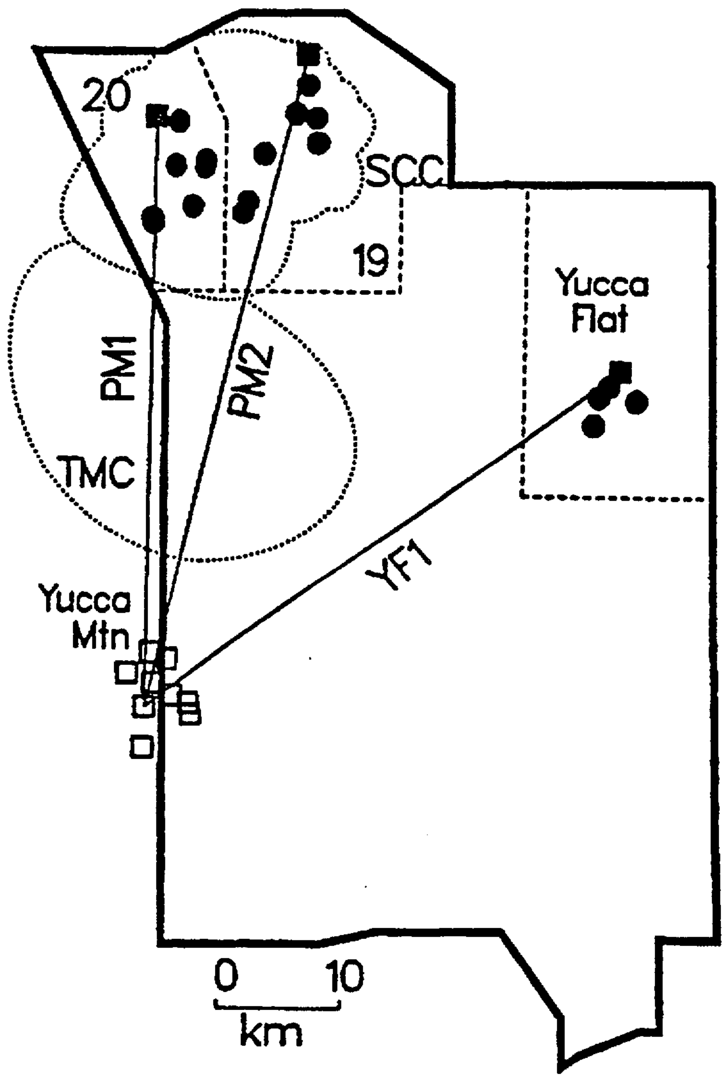

Figure 3.1.1.2.4.2.2-9 Location Map Showing Nevada Test Site, Yucca Mountain Seismic Stations (Open Squares), Explosion Locations (Solid Symbols), and Velocity Profiles PM1, PM2, and YF1. Also denoted are the Timber Mountain Caldera (TMC) and the Silent Canyon Caldera (SCC). Areas 19 and 20 comprise Pahute Mesa. Source: Walck and Phillips (1990)

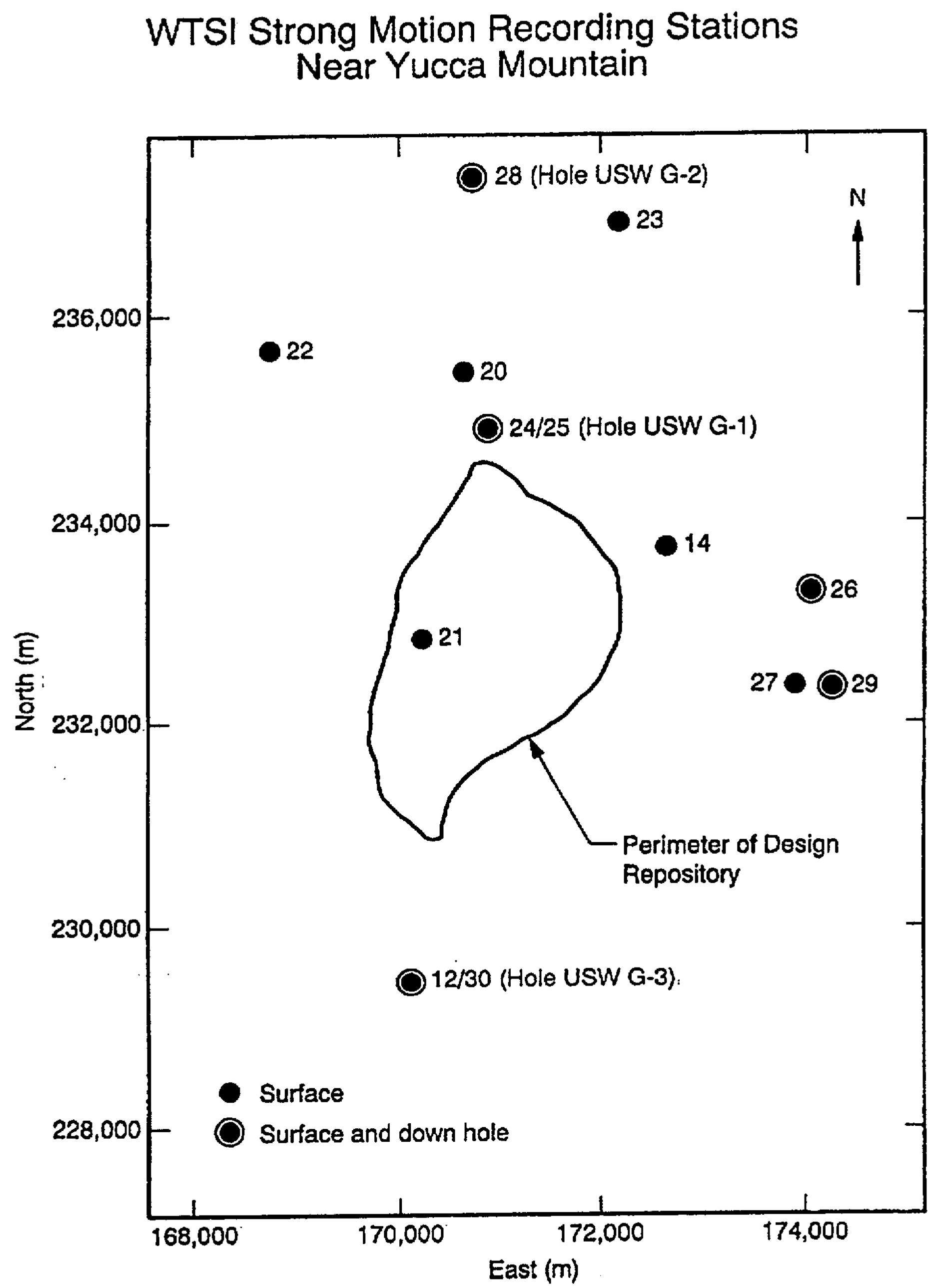

Figure 3.1.1.2.4.2.2-10 Location Map of Strong Motion Recording Stations at Yucca Mountain. Source: Phillips (1991)

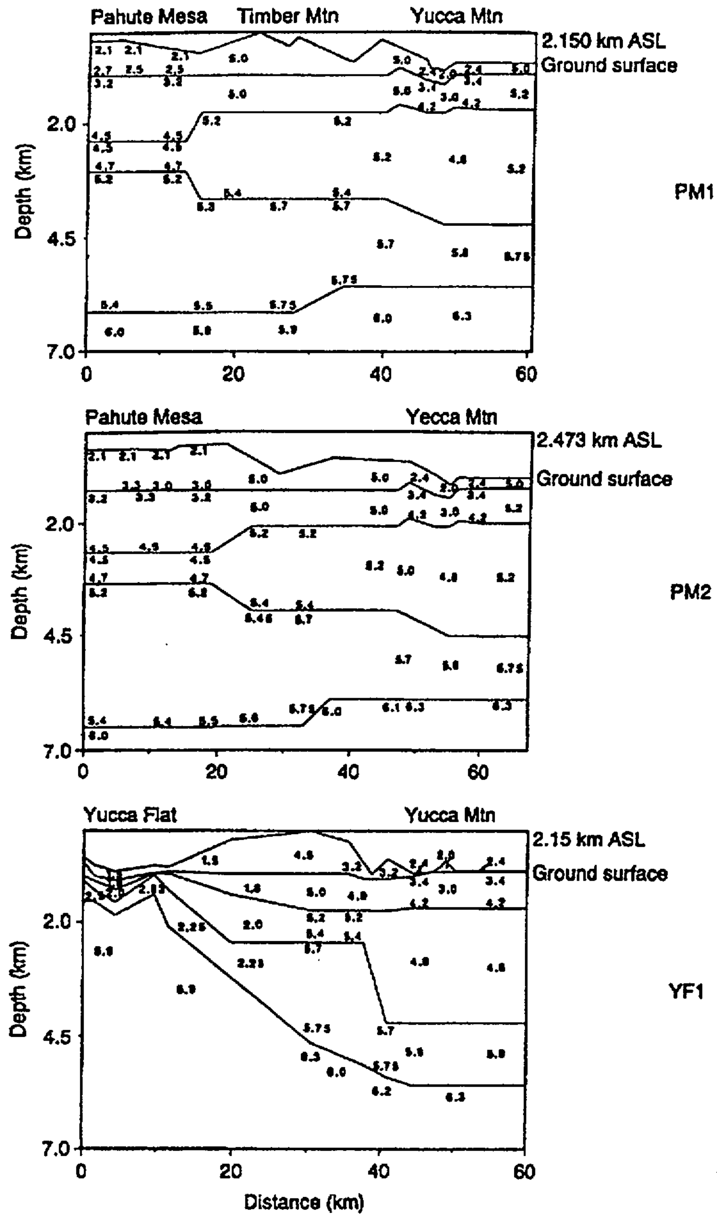

Note: ASL = Above Sea Level

Figure 3.1.1.2.4.2.2-17 Velocity Models for Travel Paths PM1, PM2, and YF1 Shown in Figure 3.1.1.2.4.2.2-9. Source: Walck and Phillips (1990)

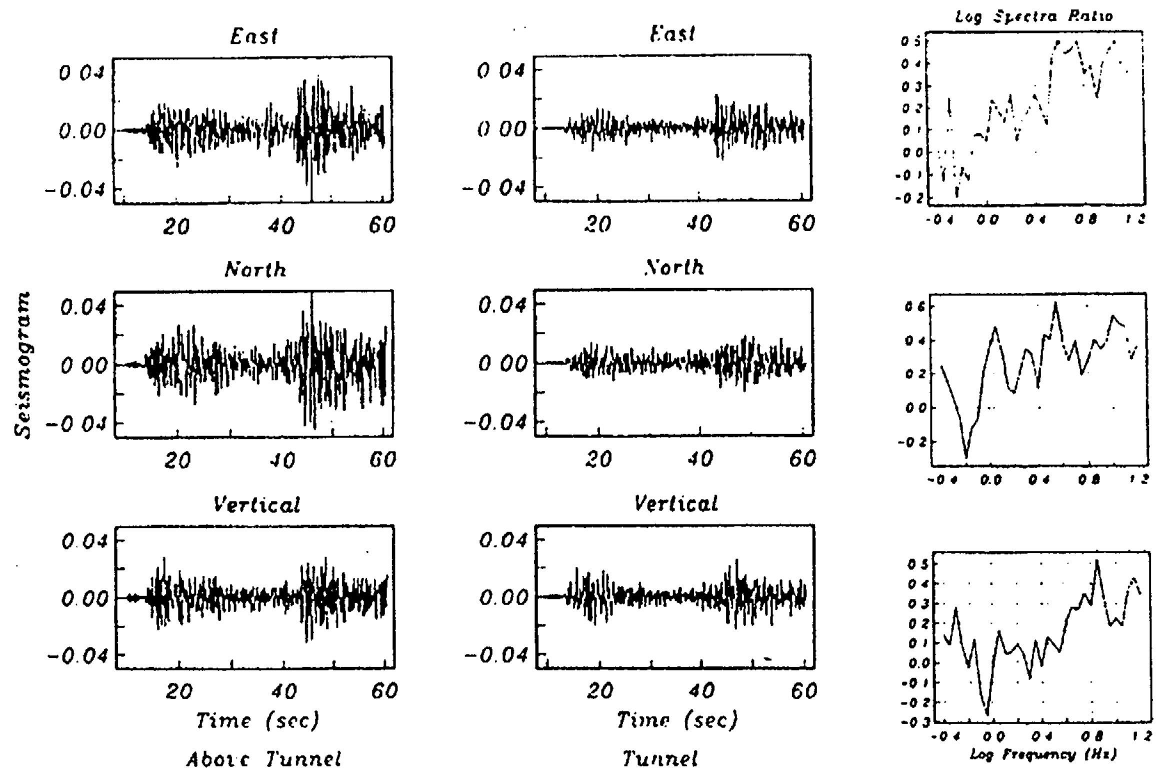

Figure 3.1.1.2.4.3.4-3 Top: Seismograms from the September 2, 1992 Magnitude 5.9 Earthquake in Southern Utah Recorded at Little Skull Mountain Seismic Stations RXTN (Tunnel) and RLSM (Above Tunnel) of the Above Seismograms. Source: Anderson et al. (1993)

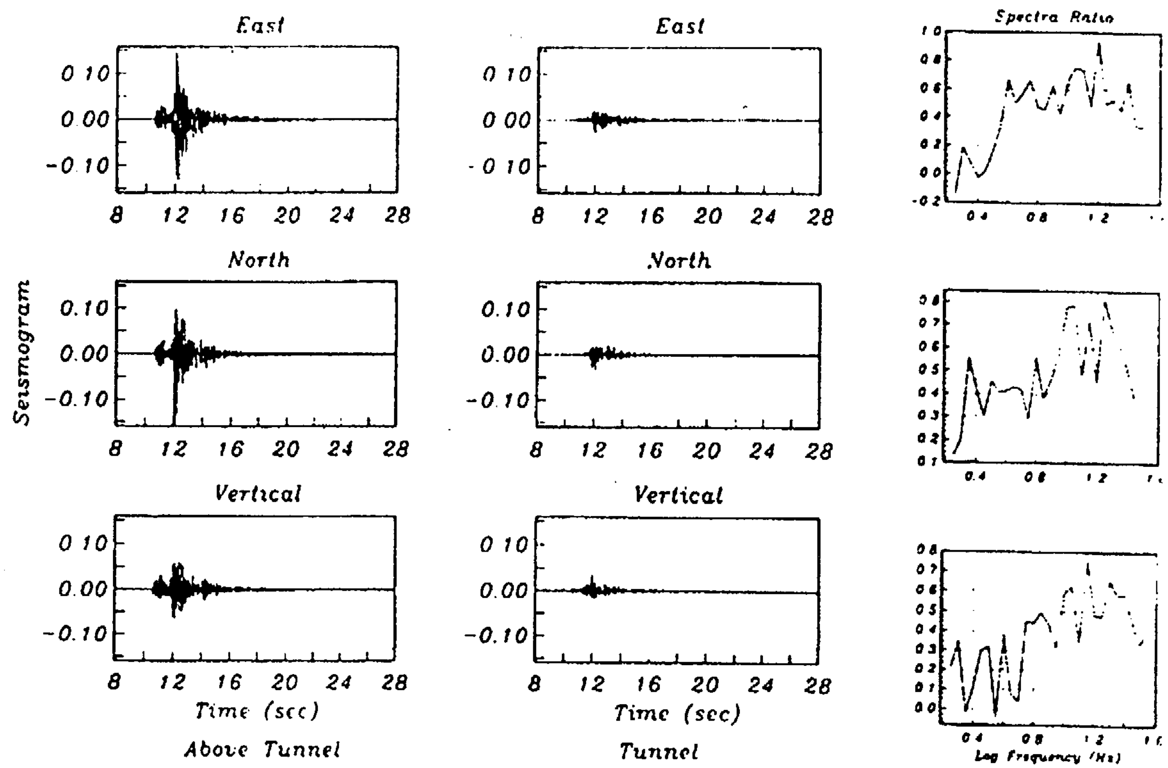

Figure 3.1.1.2.4.3.4-4 Seismograms From a September 7, 1992, M 3.15 Earthquake in Southern Utah Recorded at Little Skull Mountain Seismic Stations RXTN (Tunnel) and RLSM (Above Tunnel). Bottom: Amplitude spectra and spectral ratios (surface/tunnel) of the above seismograms. Source: Anderson et al. (1993)

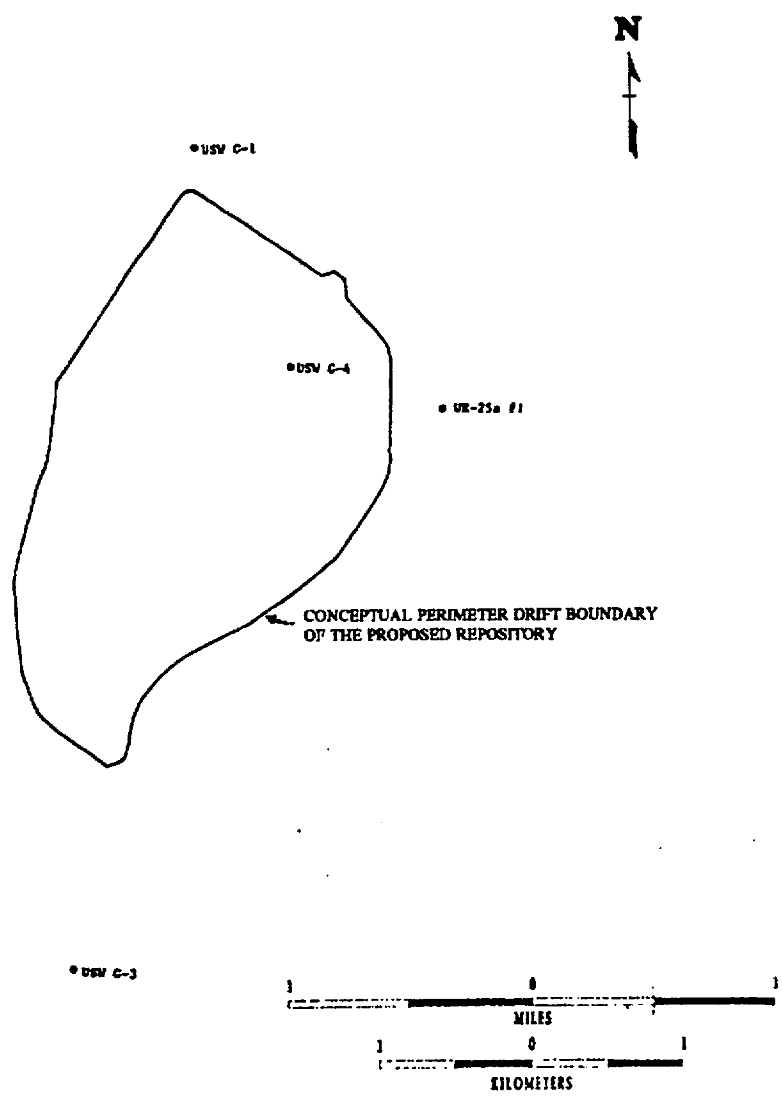

Figure 3.1.1.2.7.1-1 Location of Existing Coreholes for Geoengineering Database

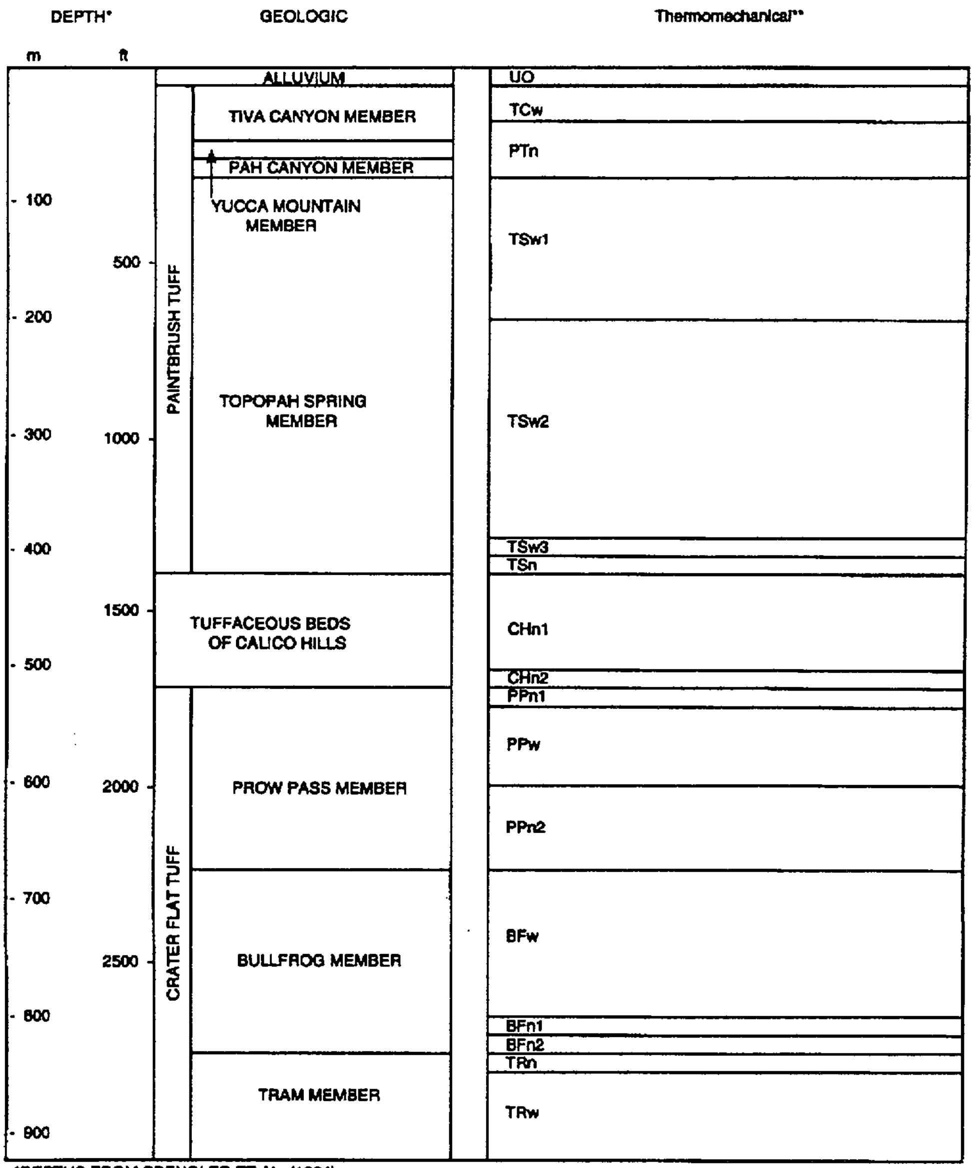

*DEPTHS FROM SPENGLER ET.AL. (1984).
**SEE TABLE 3.1.1.2.7-001 FOR DESCRIPTION OF UNITS.

Figure 3.1.1.2.7.1.1-1 Thermomechanical and Geologic Stratigraphy at Hole USW G-4

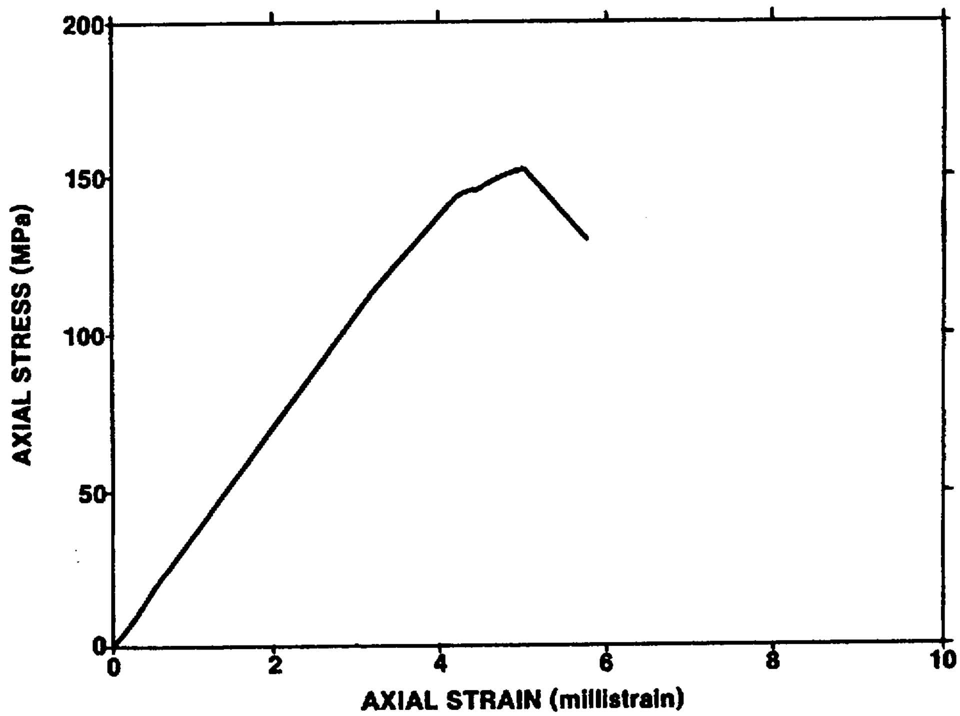

Figure 3.1.1.2.7.3.1-1 Representative Axial Stress-Axial Strain Plot for Welded Devitrified Topopah Spring Member (Test Sample GU-3 1050.4/3; Test Conditions Ambient Temperature and Pressure, Strain Rate 10^{-5}/s). Modified from Price et al. (1984)

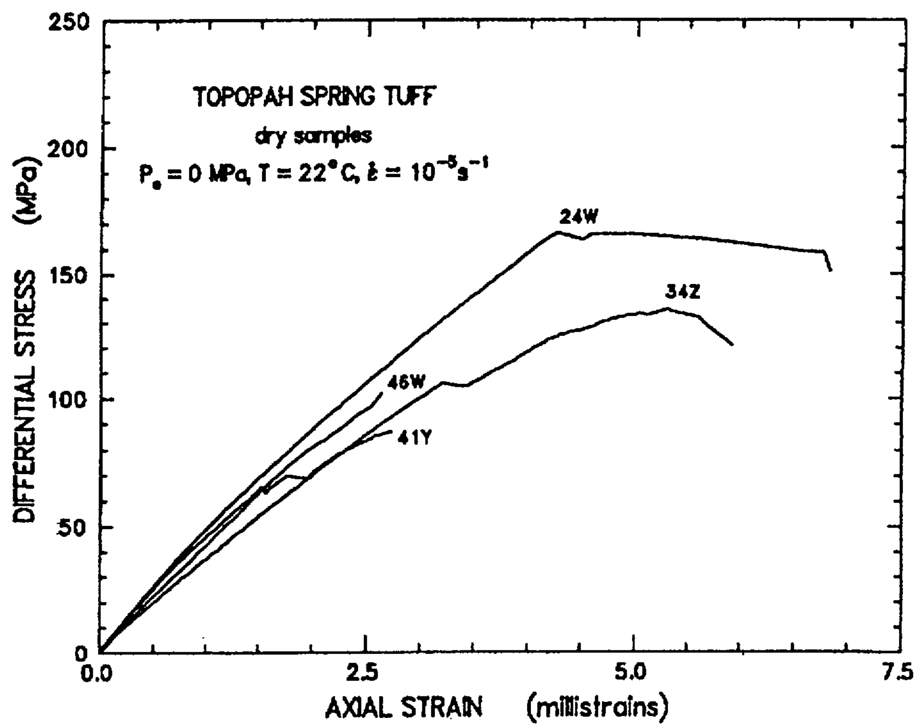

Figure 3.1.1.2.7.3.1-2 Stress-Strain Curves From Compressive Tests on Oven-Dried Samples of Topopah Spring Tuff From Busted Butte at 0 MPa Confining Pressure, 22°C Temperature and 10^{-5} Per Second Strain Rate

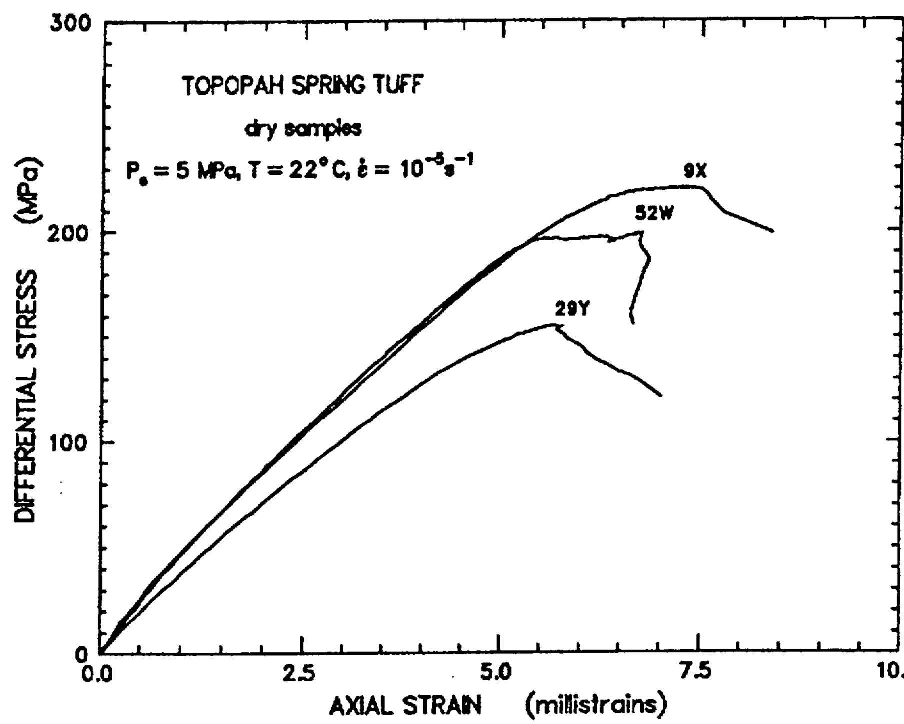

Figure 3.1.1.2.7.3.1-3 Stress-Strain Curves From Compressive Tests on Oven-Dried Samples of Topopah Spring Tuff From Busted Butte at 5 MPa Confining Pressure, 22°C Temperature and 10^{-5} Per Second Strain Rate

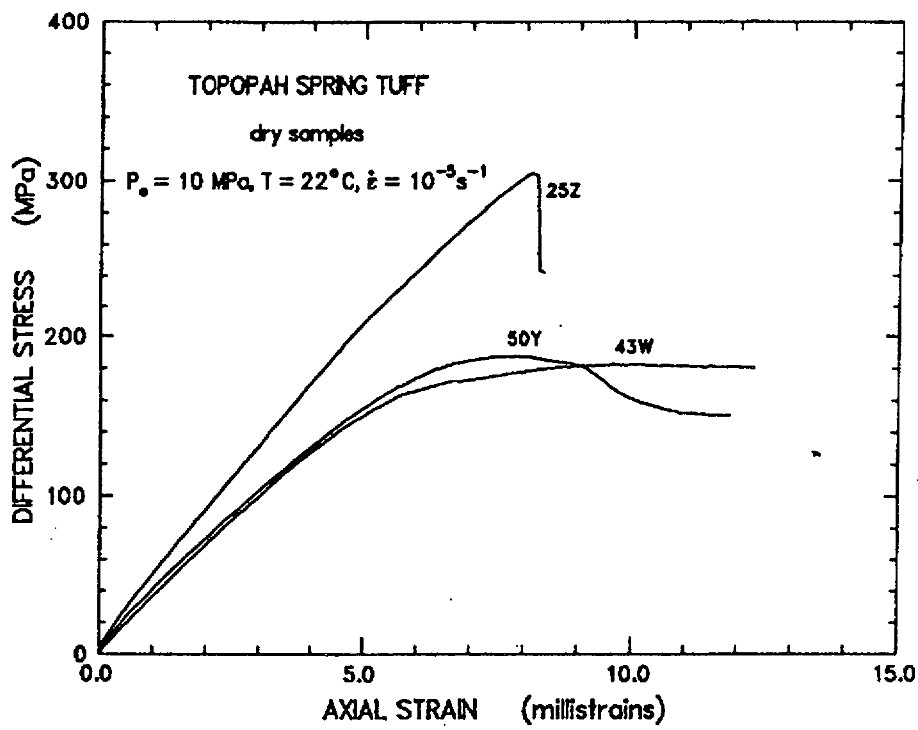

Figure 3.1.1.2.7.3.1-4 Stress-Strain Curves From Compressive Tests on Oven-Dried Samples of Topopah Spring Tuff From Busted Butte at 10 MPa Confining Pressure, 22°C Temperature and 10^{-5} Per Second Strain Rate

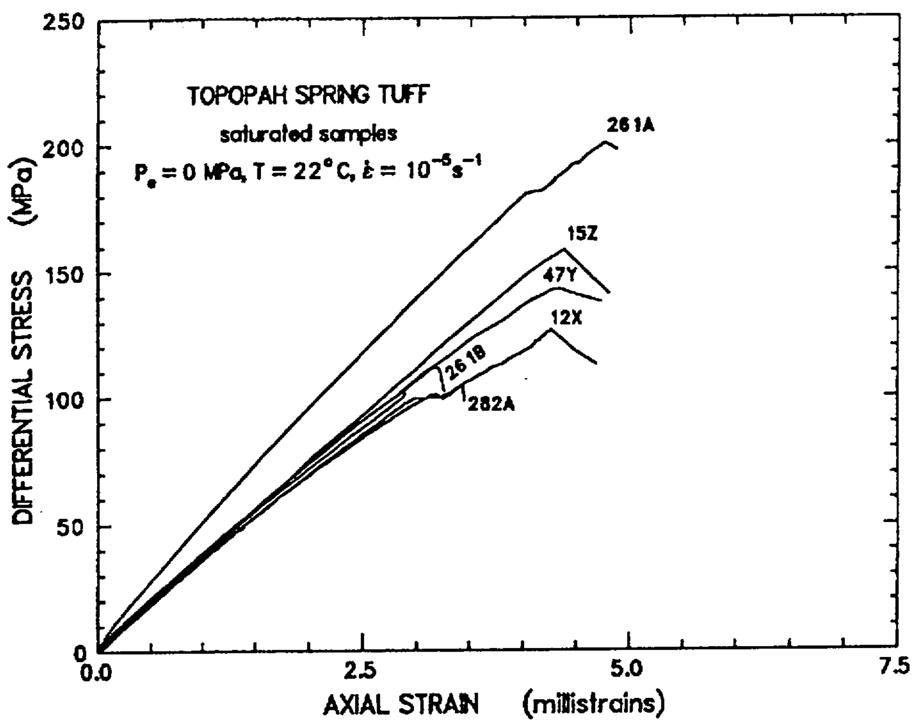

Figure 3.1.1.2.7.3.1-5 Stress-Strain Curves From Compressive Tests on Saturated Samples of Topopah Spring Tuff From Busted Butte at 0 MPa Confining Pressure, 22°C Temperature and 10^{-5} Per Second Strain Rate

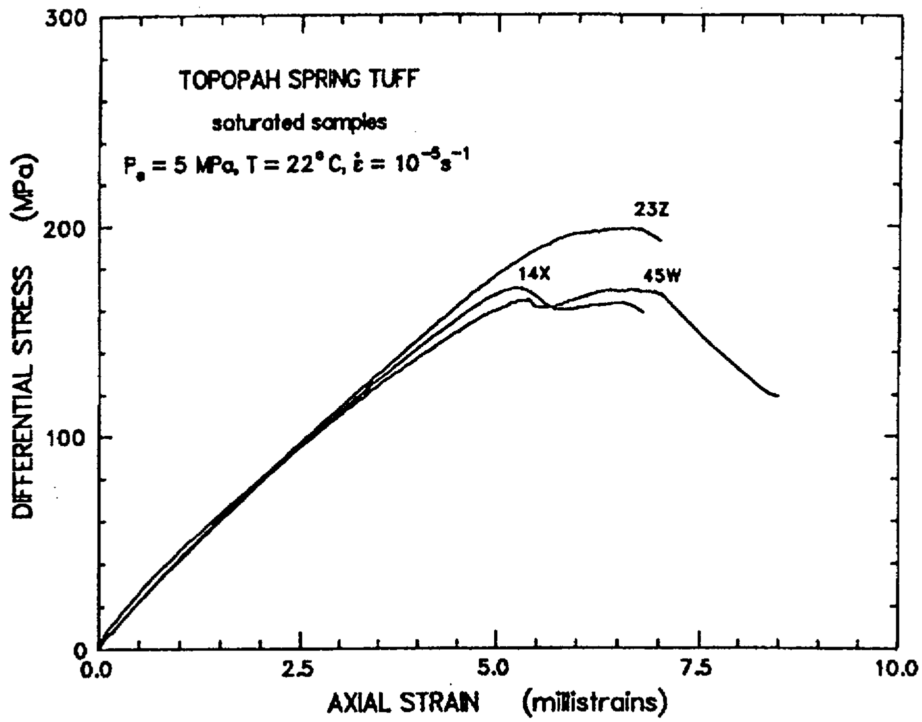

Figure 3.1.1.2.7.3.1-6 Stress-Strain Curves From Compressive Tests on Saturated Samples of Topopah Spring Tuff From Busted Butte at 5 MPa Confining Pressure, 22°C Temperature and 10^{-5} Per Second Strain Rate

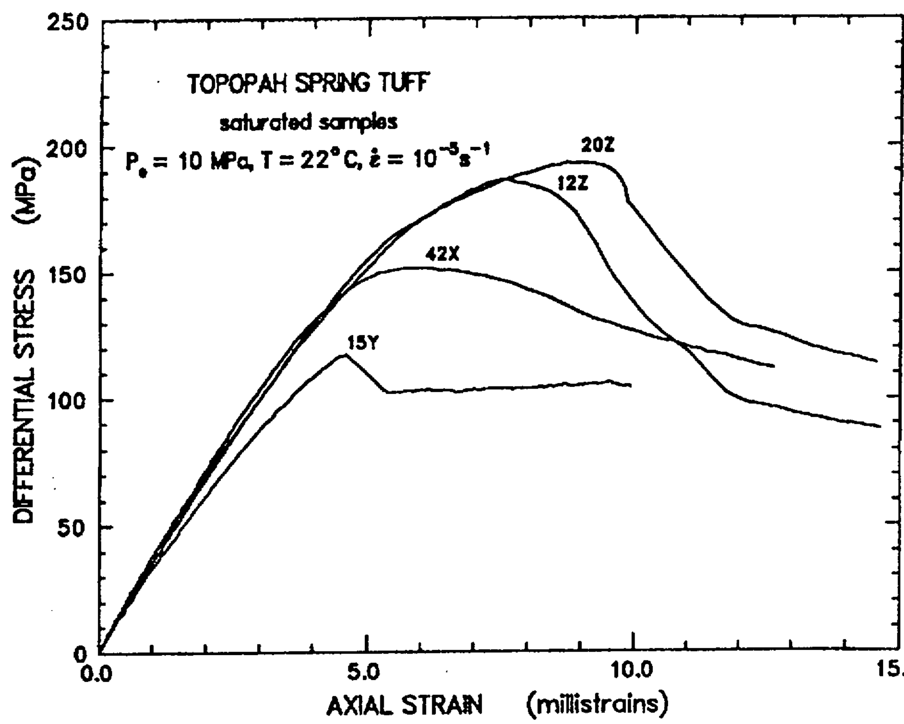

Figure 3.1.1.2.7.3.1-7 Stress-Strain Curves From Compressive Tests on Saturated Samples of Topopah Spring Tuff From Busted Butte at 10 MPa Confining Pressure, 22°C Temperature and 10^{-5} Per Second Strain Rate

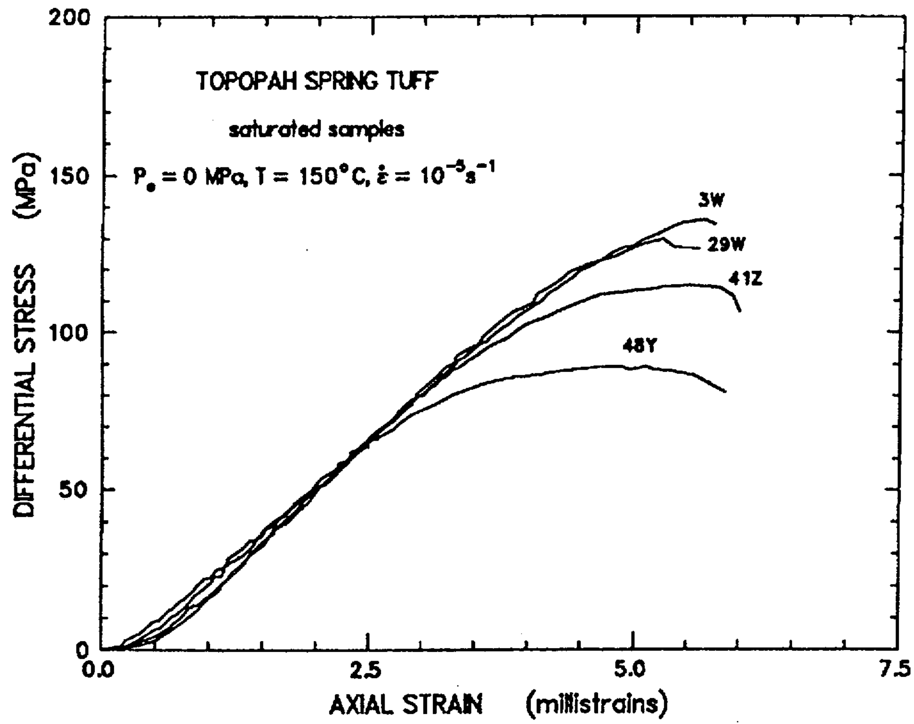

Figure 3.1.1.2.7.3.1-8 Stress-Strain Curves From Compressive Tests on Saturated Samples of Topopah Spring Tuff From Busted Butte at 0 MPa Confining Pressure, 150°C Temperature and 10^{-5} Per Second Strain Rate

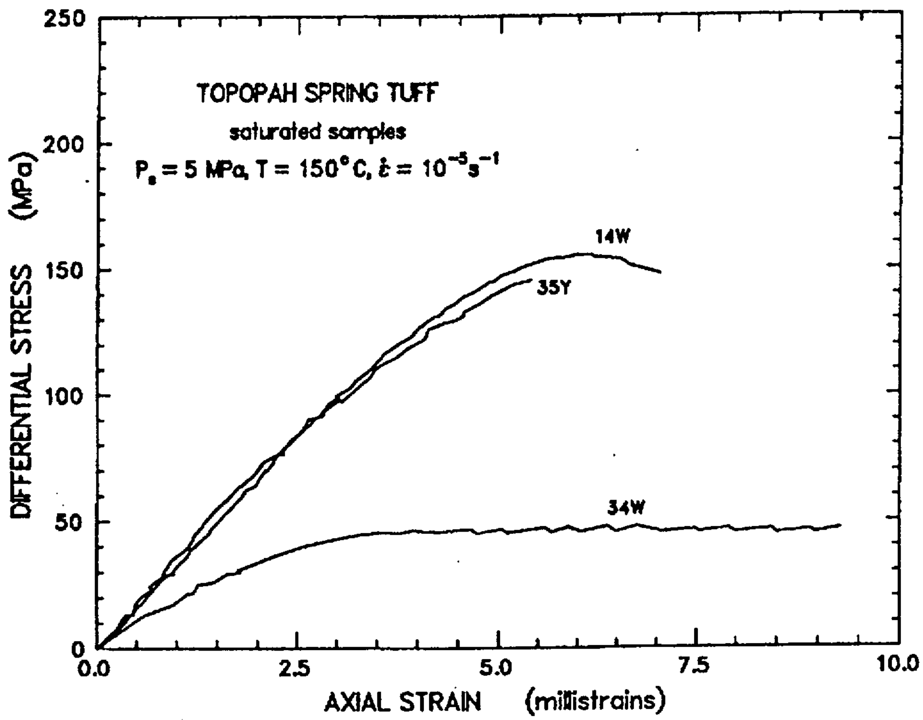

Figure 3.1.1.2.7.3.1-9 Stress-Strain Curves From Compressive Tests on Saturated Samples of Topopah Spring Tuff From Busted Butte at 5 MPa Confining Pressure, 150°C Temperature and 10^{-5} Per Second Strain Rate

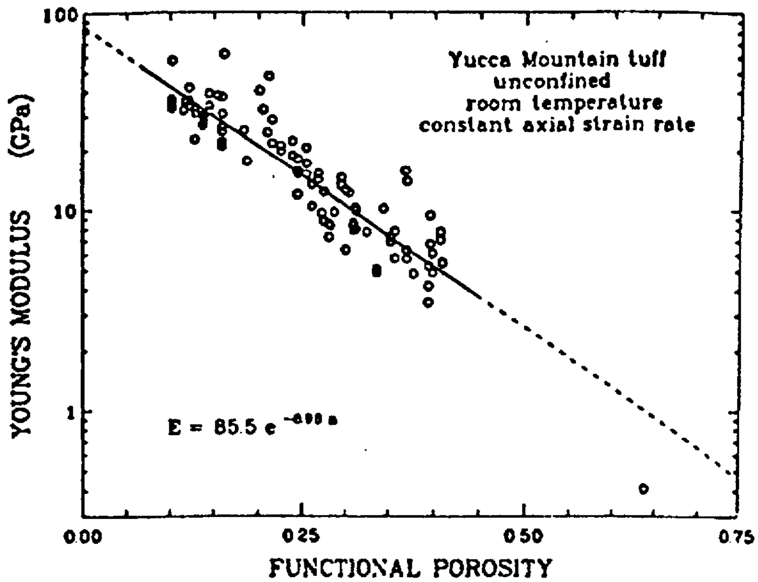

Figure 3.1.1.2.7.3.1-10 Young's Modulus Versus Functional Porosity. After Price and Bauer (1985)

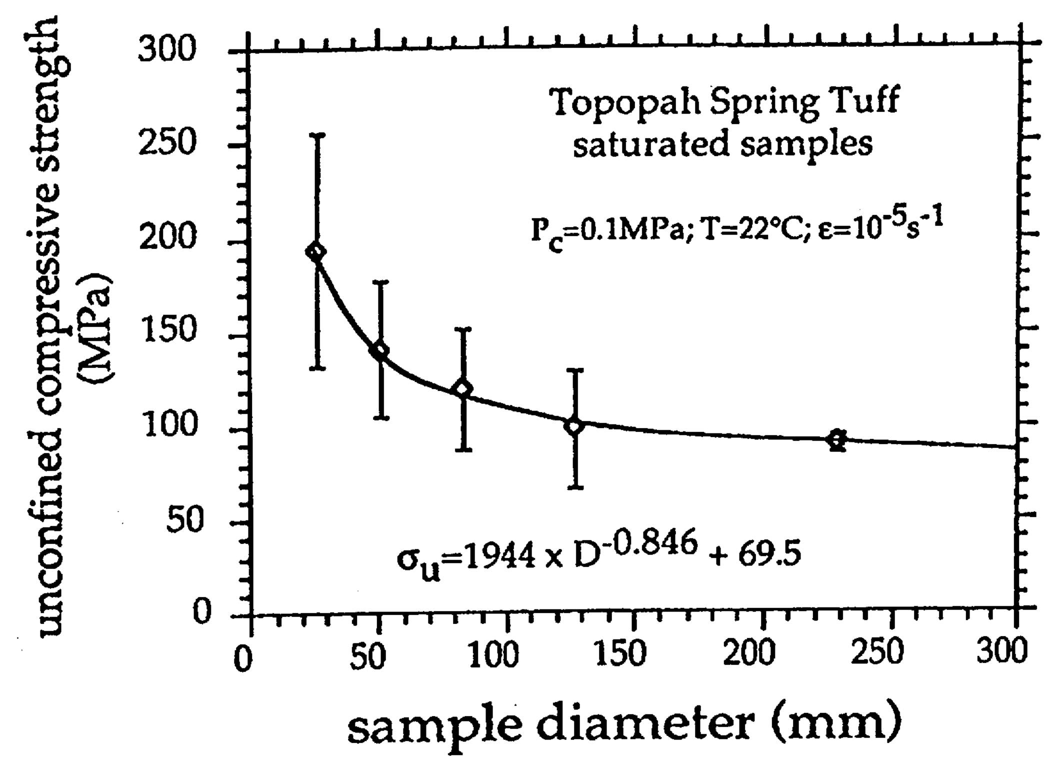

Figure 3.1.1.2.7.3.2-1 Compressive Strength vs. Sample Size

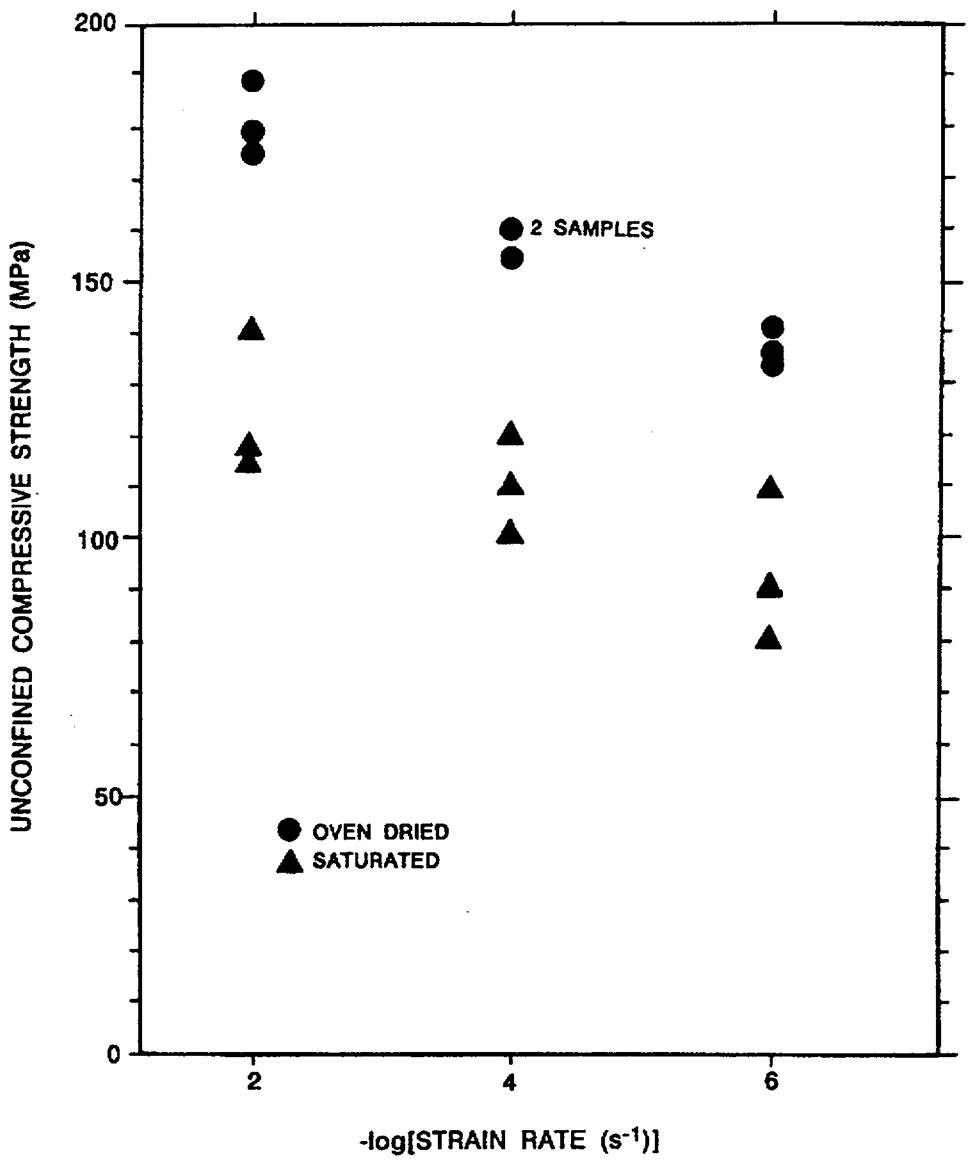

Figure 3.1.1.2.7.3.2-2 Effect of Saturating Samples on Comprehensive Strength

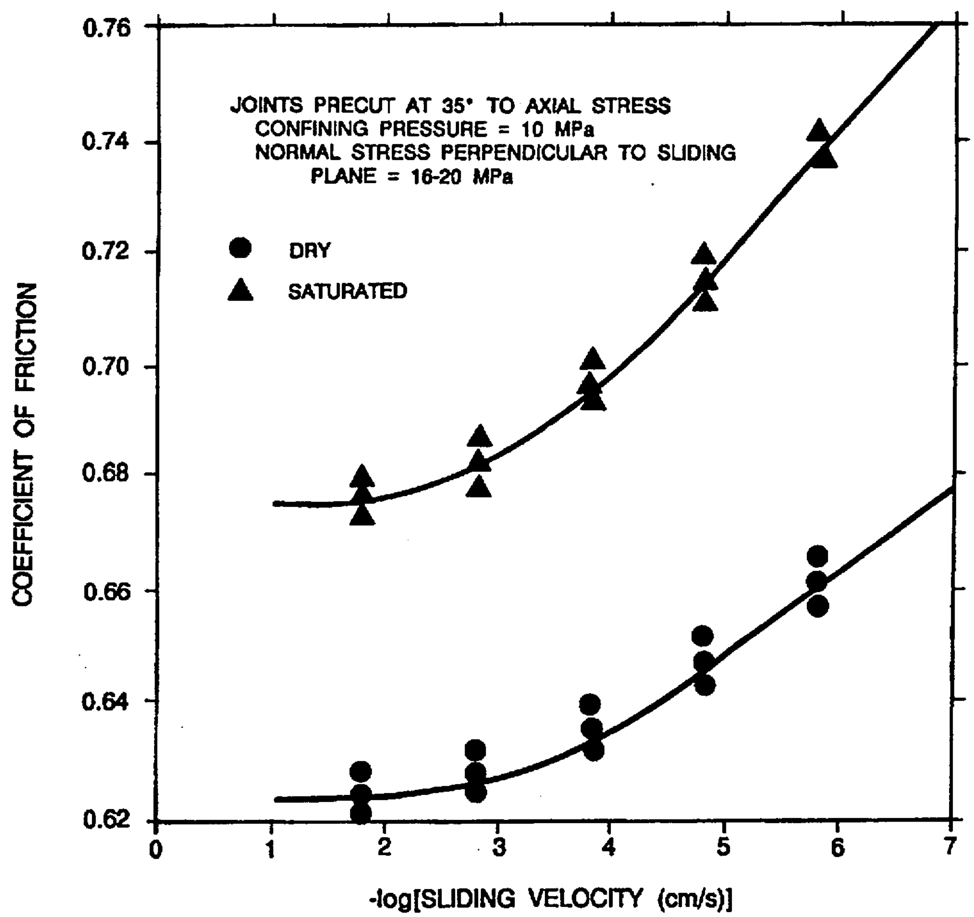

Figure 3.1.1.2.7.4.5-1 Plot of the coefficient of friction against log sliding velocity for oven-dried and water-saturated joints for Grouse Canyon Member welded tuff. Modified from Teufel (1981)

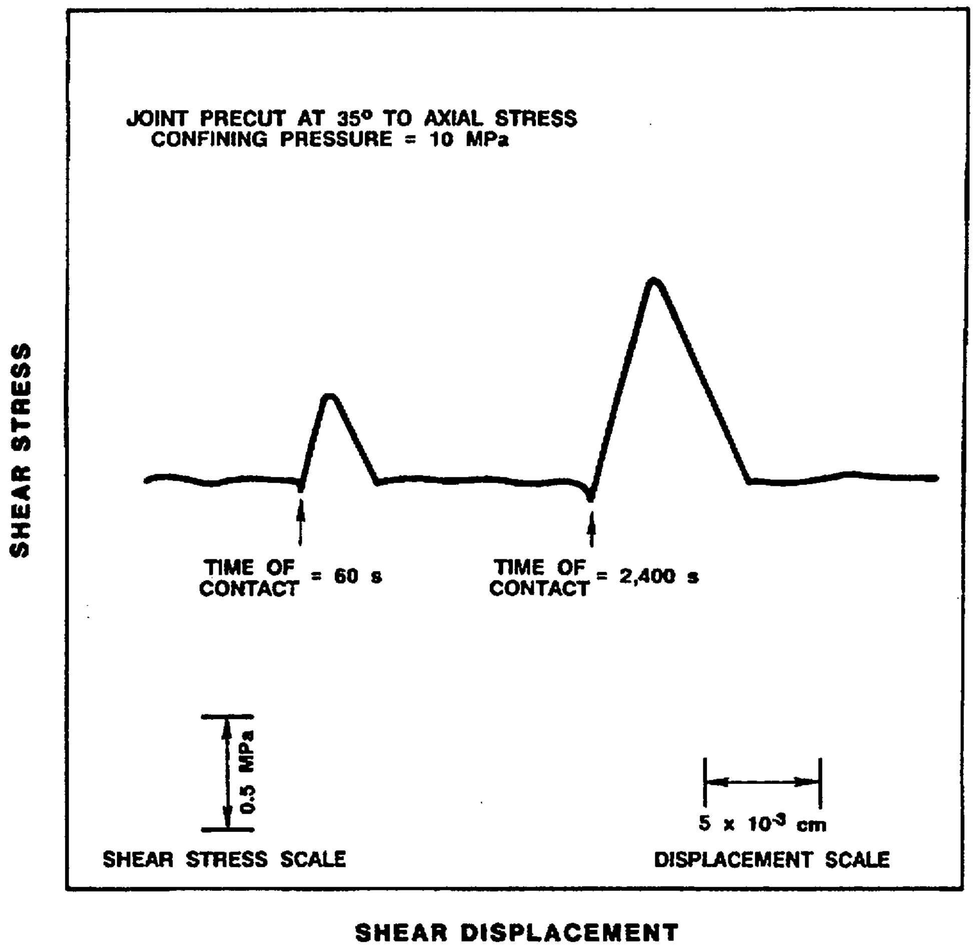

Figure 3.1.1.2.7.4.5-2 Shear stress versus shear displacement for oven-dried Grouse Canyon Member welded tuff sample for 60 and 2,400 s. periods of static contact. Modified from Teufel (1981)

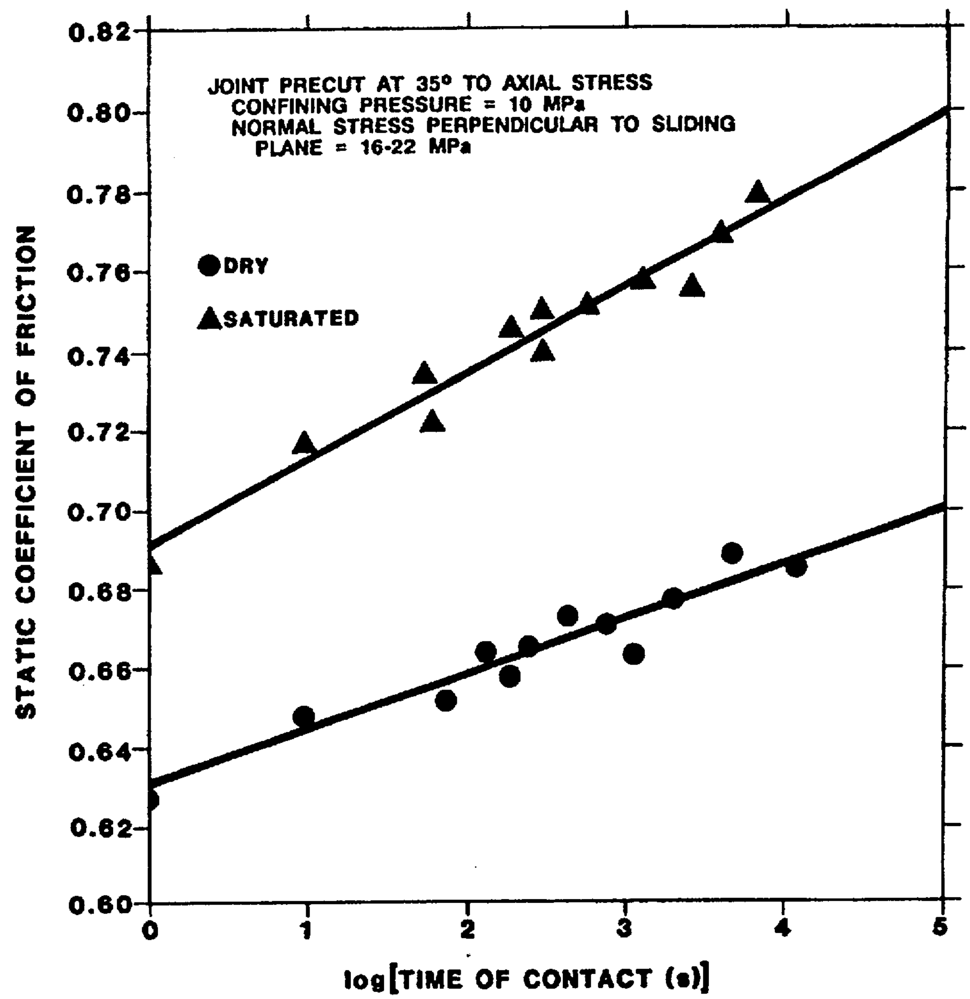

Figure 3.1.1.2.7.4.5-3 Plot of the coefficient of friction against log sliding velocity for oven-dried and water-saturated joints for Grouse Canyon Member welded tuff. Modified from Teufel (1981)

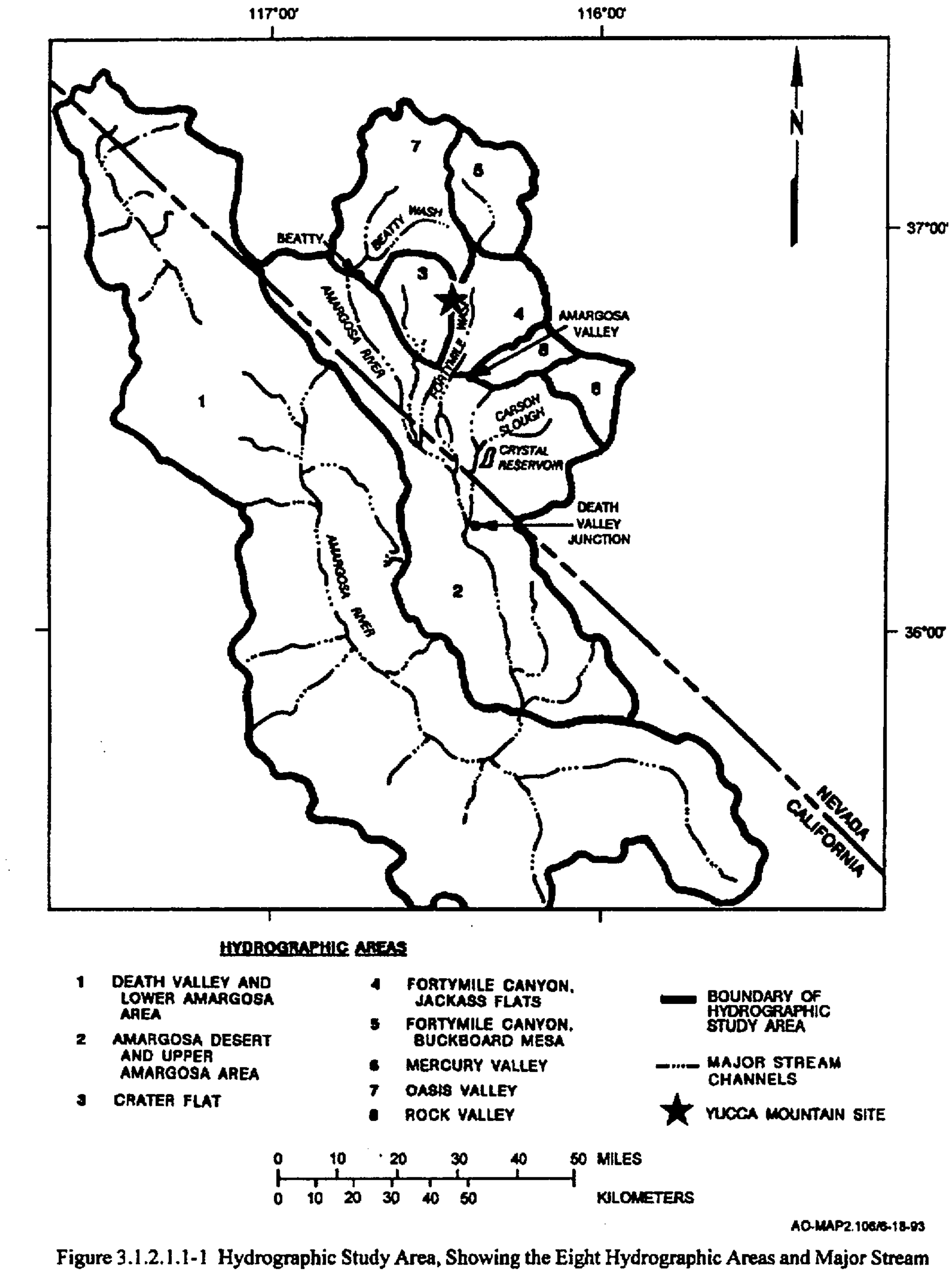

Figure 3.1.2.1.1-1 Hydrographic Study Area, Showing the Eight Hydrographic Areas and Major Stream Channels. Modified from Waddell, et al. (1984)

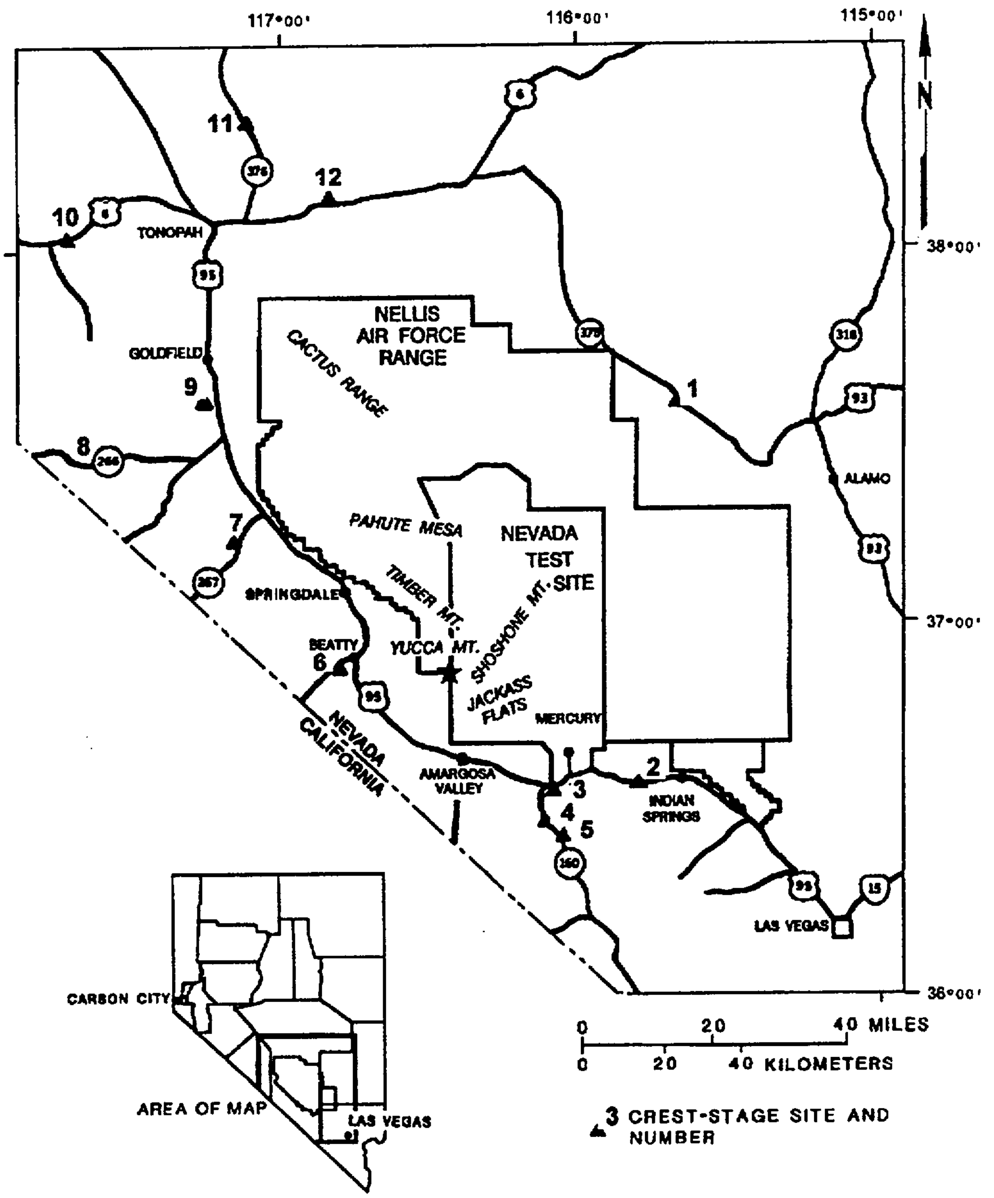

Figure 3.1.2.1.1-2 Locations of Crest-Stage Sites in the Hydrologic Study Area and Adjacent Areas. Modified from Squires and Young (1984)

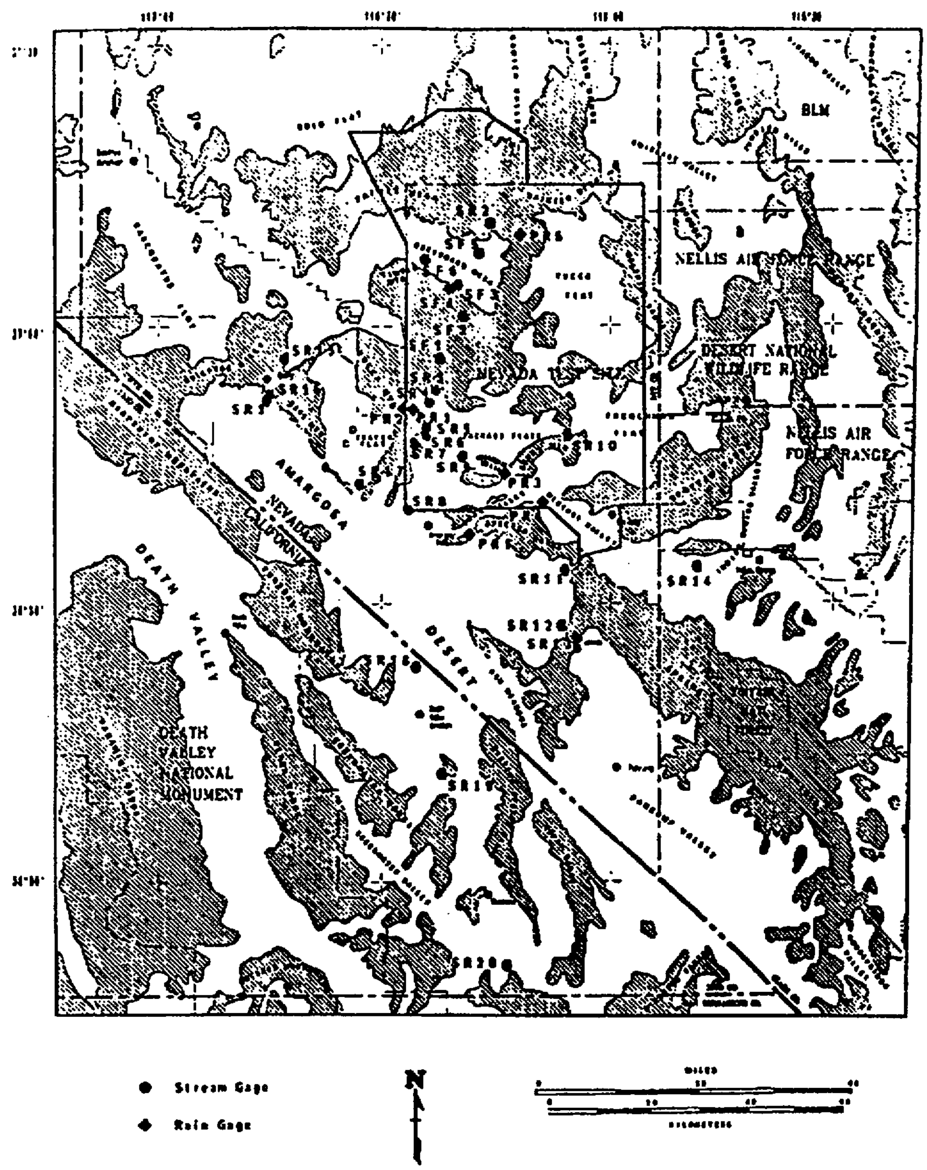

Figure 3.1.2.1.2-1 Regional Surface-Water Monitoring Network

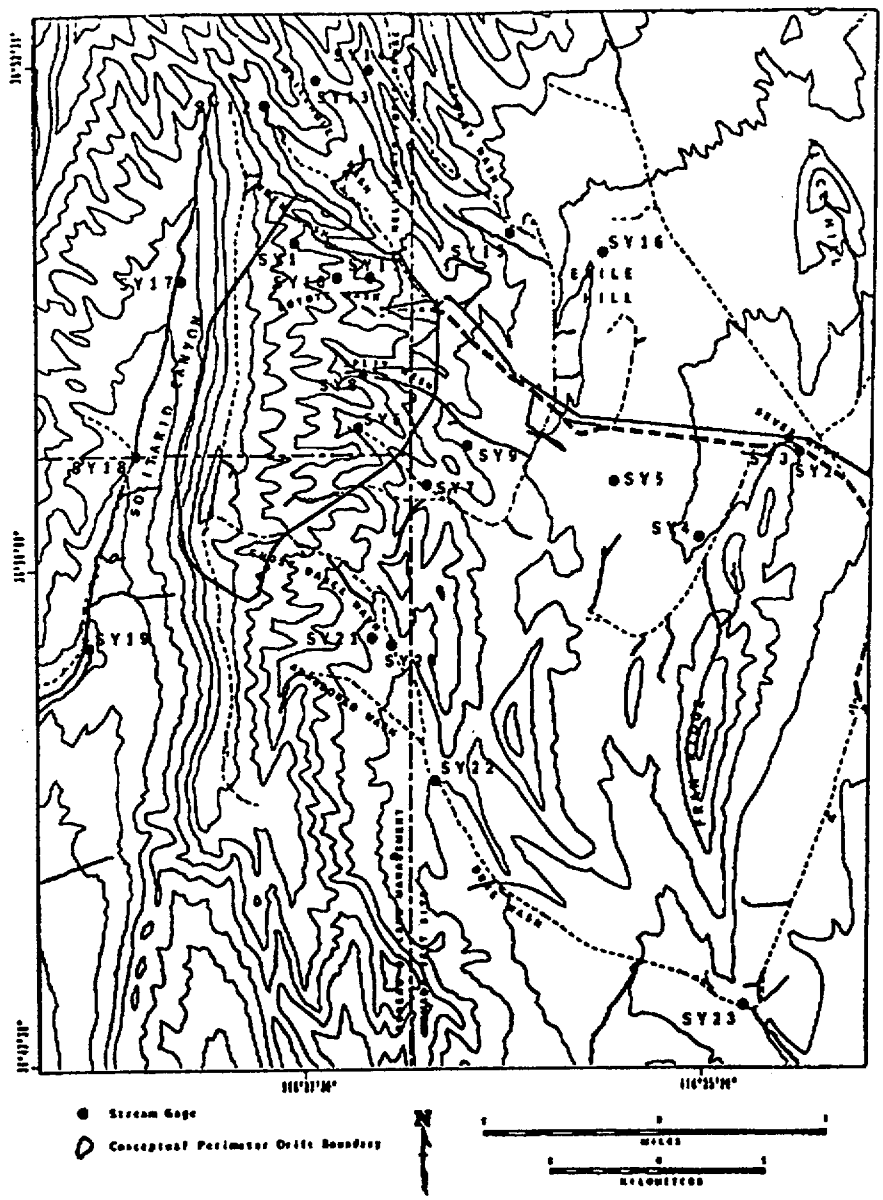

Figure 3.1.2.1.2-2 Site Surface-Water Monitoring Network

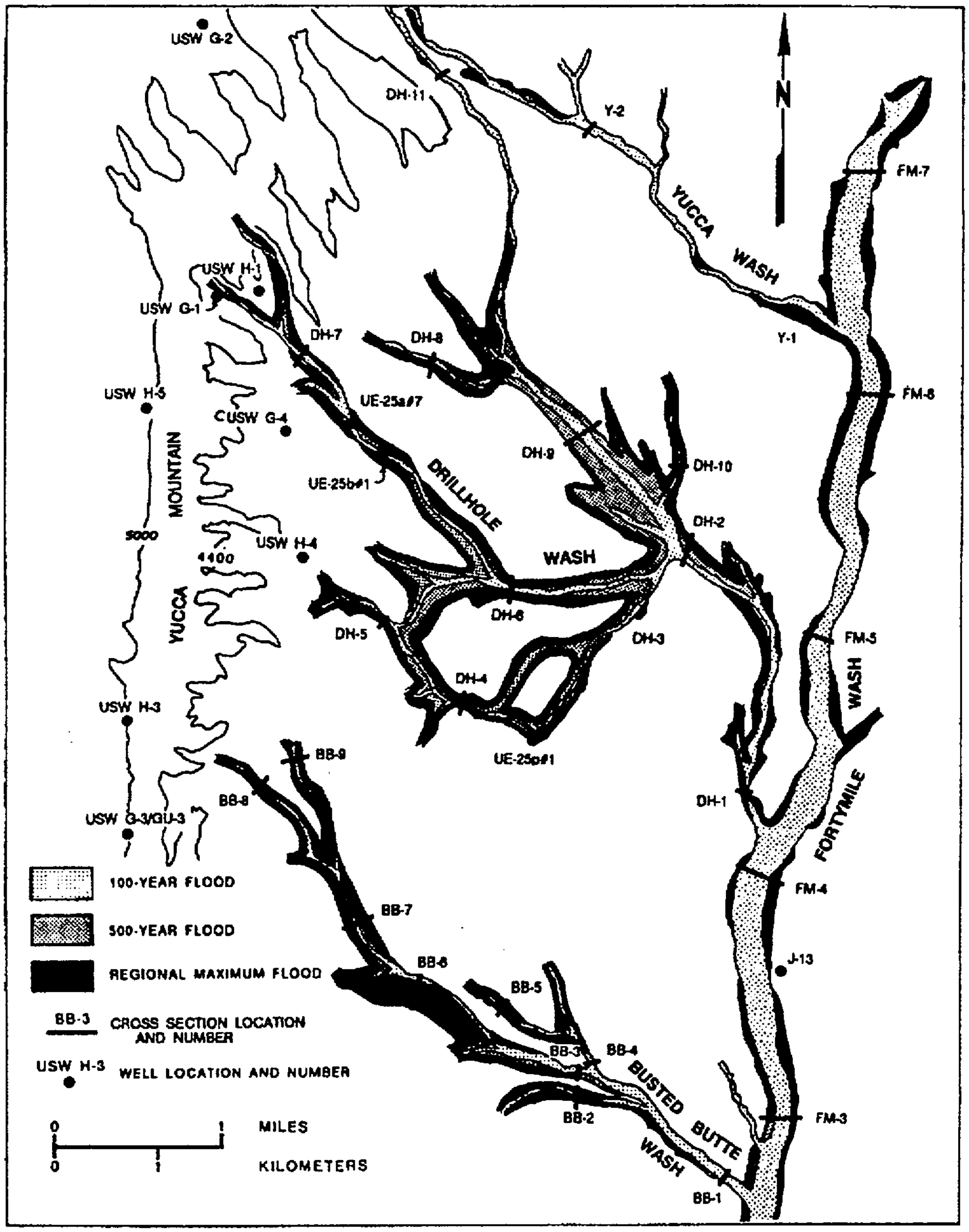

Figure 3.1.2.1.5-1 Flood-Prone Areas in the Vicinity of Fortymile Wash. Modified from Squires and Young (1984)

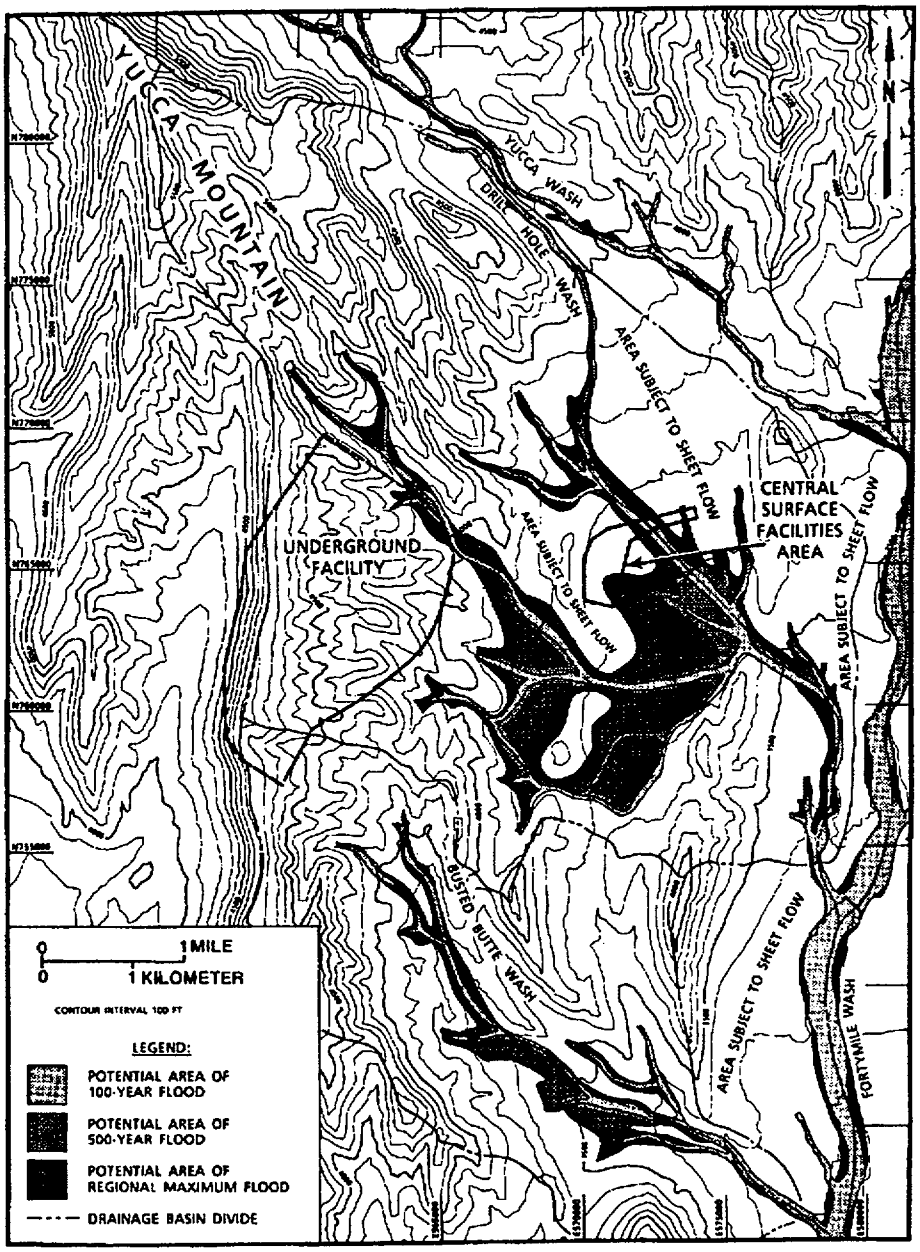

Figure 3.1.2.1.5-2 Site Topography and Flood Potential Areas. Modified from Squires and Young (1984)

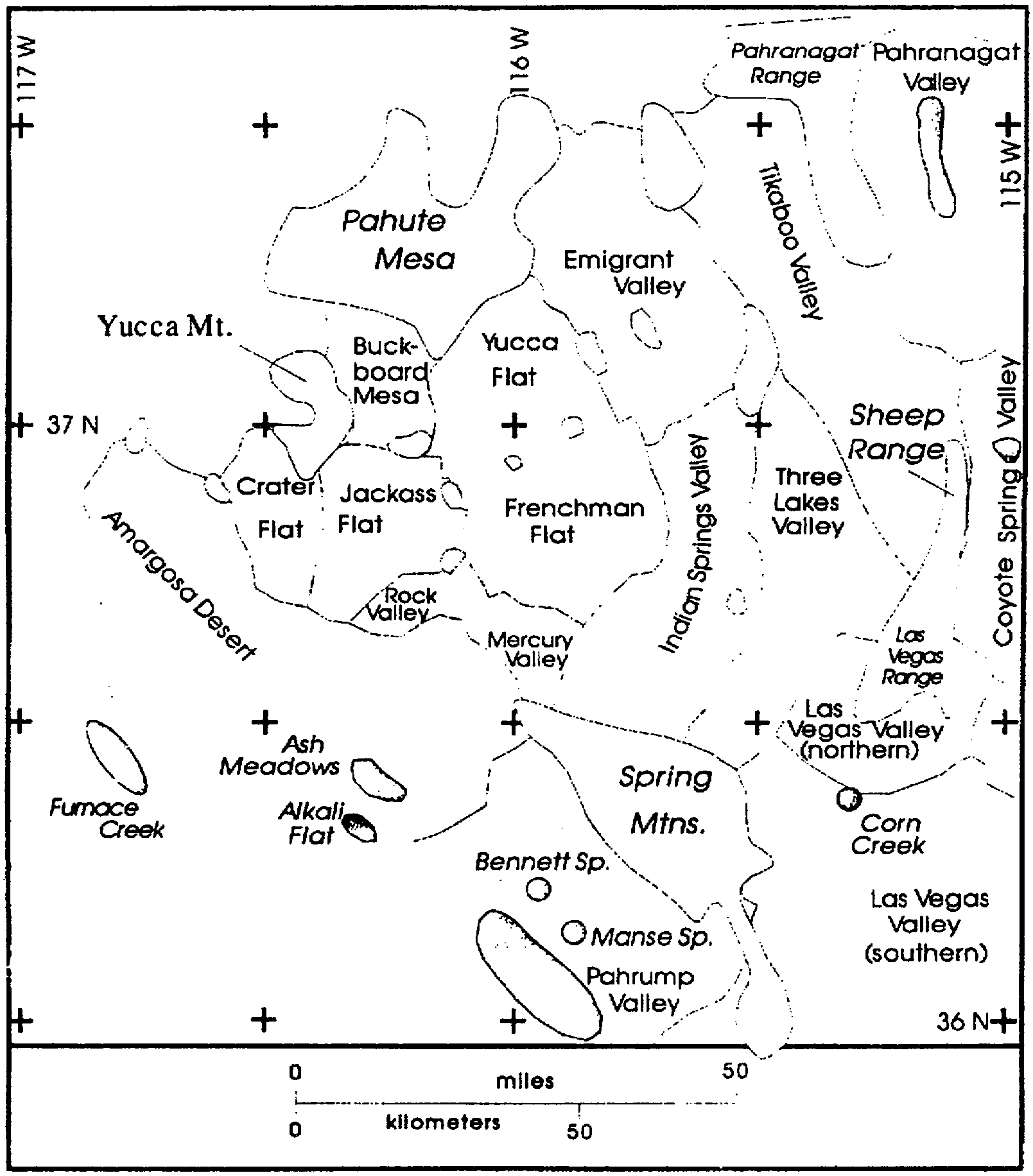

Figure 3.1.2.2.1.2-1 Recharge, Discharge, and Hydrographic Areas. Light shading bounded by solid lines indicates principal recharge areas; dark shading bounded by solid lines indicates principal discharge areas. See Figure 3.1.2.2.1.2-3 for background symbols and related references.

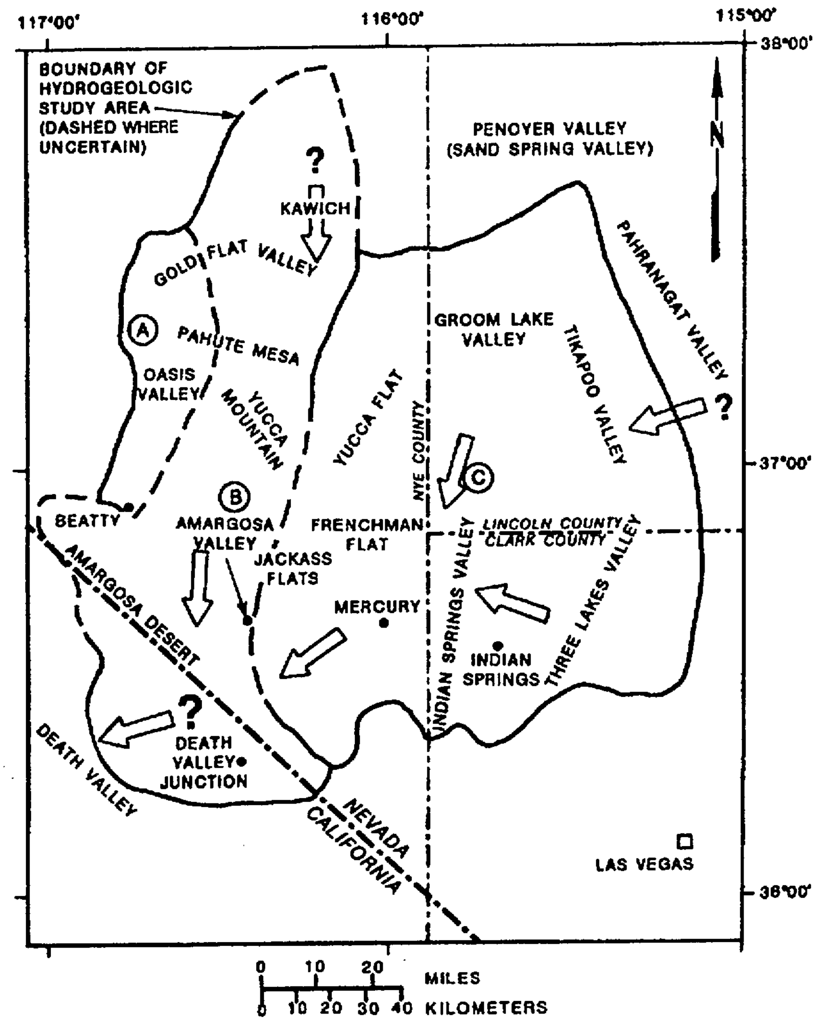

GENERAL DIRECTION OF REGIONAL GROUND-WATER FLOW (QUESTION MARK INDICATES UNCERTAINTY)

A. OASIS VALLEY SUBBASIN
B. ALKALI FLAT-FURNACE CREEK RANCH SUBBASIN
C. ASH MEADOWS SUBBASIN

Figure 3.1.2.2.1.2-2 Hydrogeologic Study Area Showing Three Ground-Water Subbasins. Modified from Rush (1970), Blankennagel and Weir (1973), Winograd and Thordarson (1975), Dudley and Larsen (1976), Waddell (1982), and Waddell et al. (1984). Modified by Dudley - solid arrows--flow in Cenozoic Units. Open arrows--flow in Pre-Cenozoic Units. Added arrows--in Oasis Valley and--to Alkali Flat. From Dudley's Exhibits for J-13 Hearings.

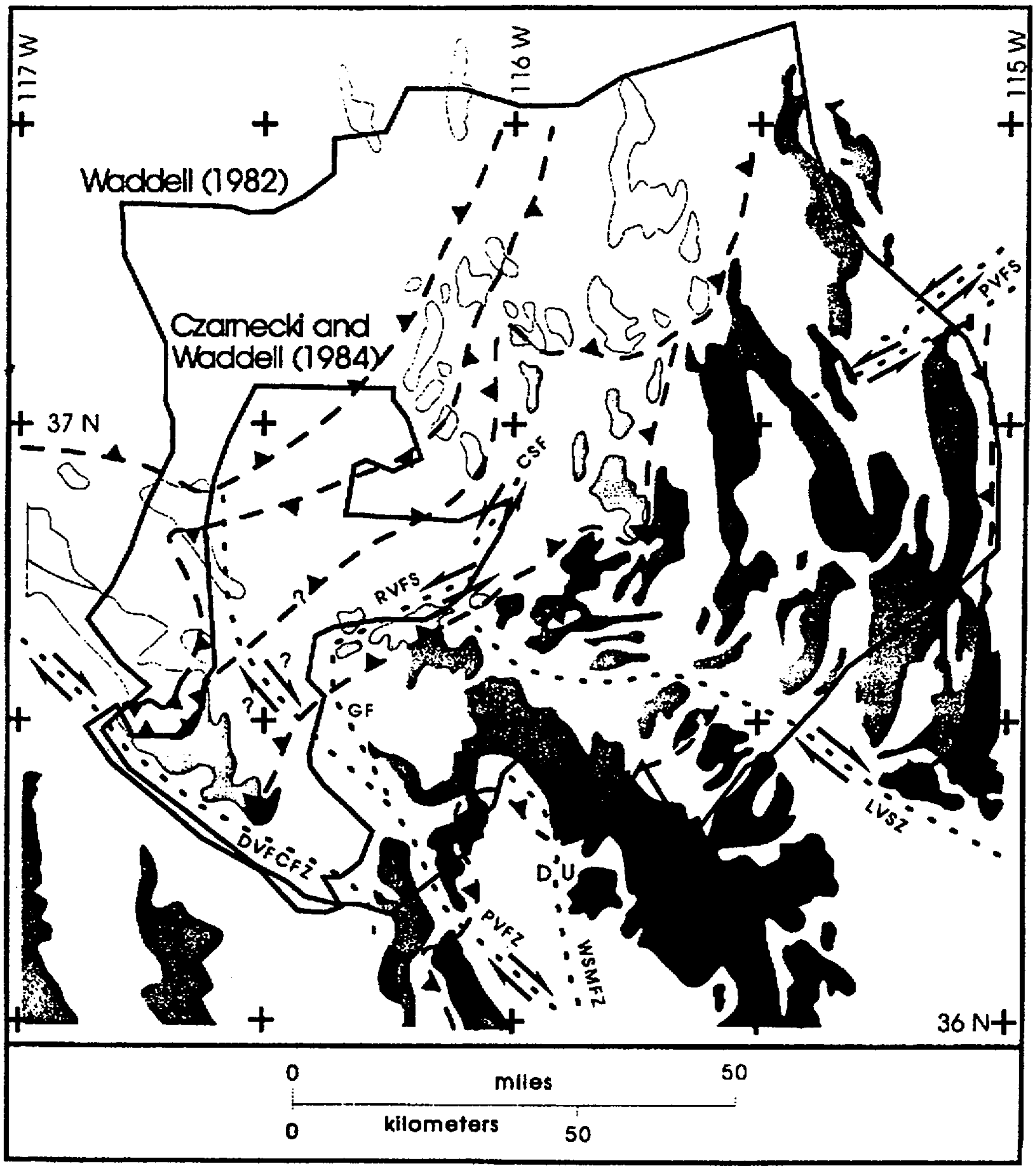

Figure 3.1.2.2.1.2-3 Regional and Sub-regional Hydrologic Model Boundaries. Thrust fault correlations from Wernicke et al. (1988b) and Jayko (1990). High-angle faults shown include Death Valley - Furnace Creek Fault Zone (DVFCFZ), Pahrump Valley Fault Zone (PVFZ), "Gravity Fault" (GF), Western Spring Mountains Fault Zone (WSMFZ), Las Vegas Shear Zone (LVSZ), Pahranagat Valley Fault System (PVFS), Rock Valley Fault System (RVFS), and Cane Spring Fault (CSF).

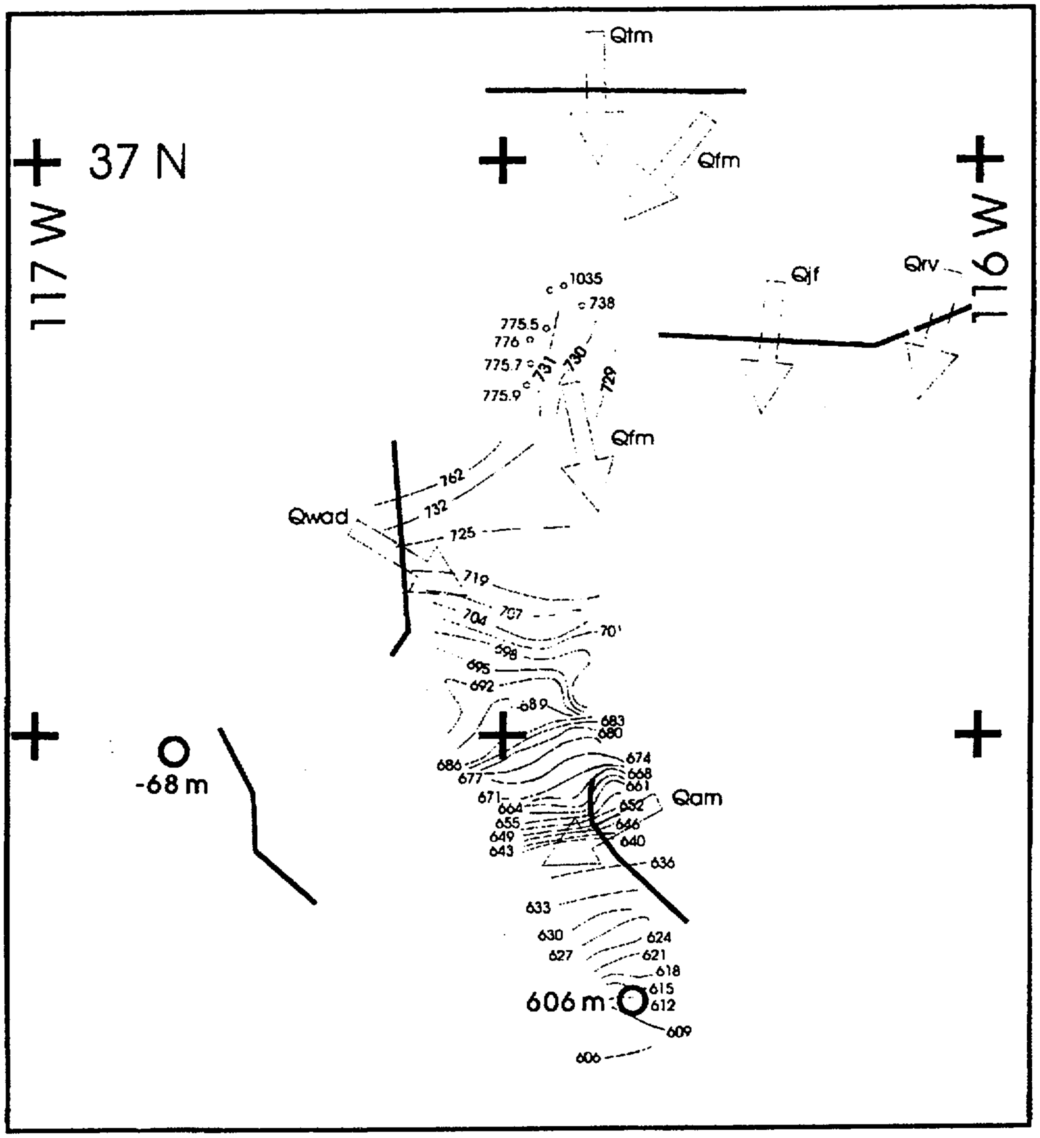

Figure 3.1.2.2.1.2-4 Potentiometric Levels in Cenozoic Rocks and Boundary Conditions for Two-Dimensional, Sub-Regional Model of Ground-Water Flow. Water levels from Ervin et al. (1993) and Czarnecki (1990). Contours in meters AMSL. Arrows and highlighted boundary segments represent boundary conditions prescribed by Czarnecki and Waddell (1984); solid circles represent constant-head nodes.

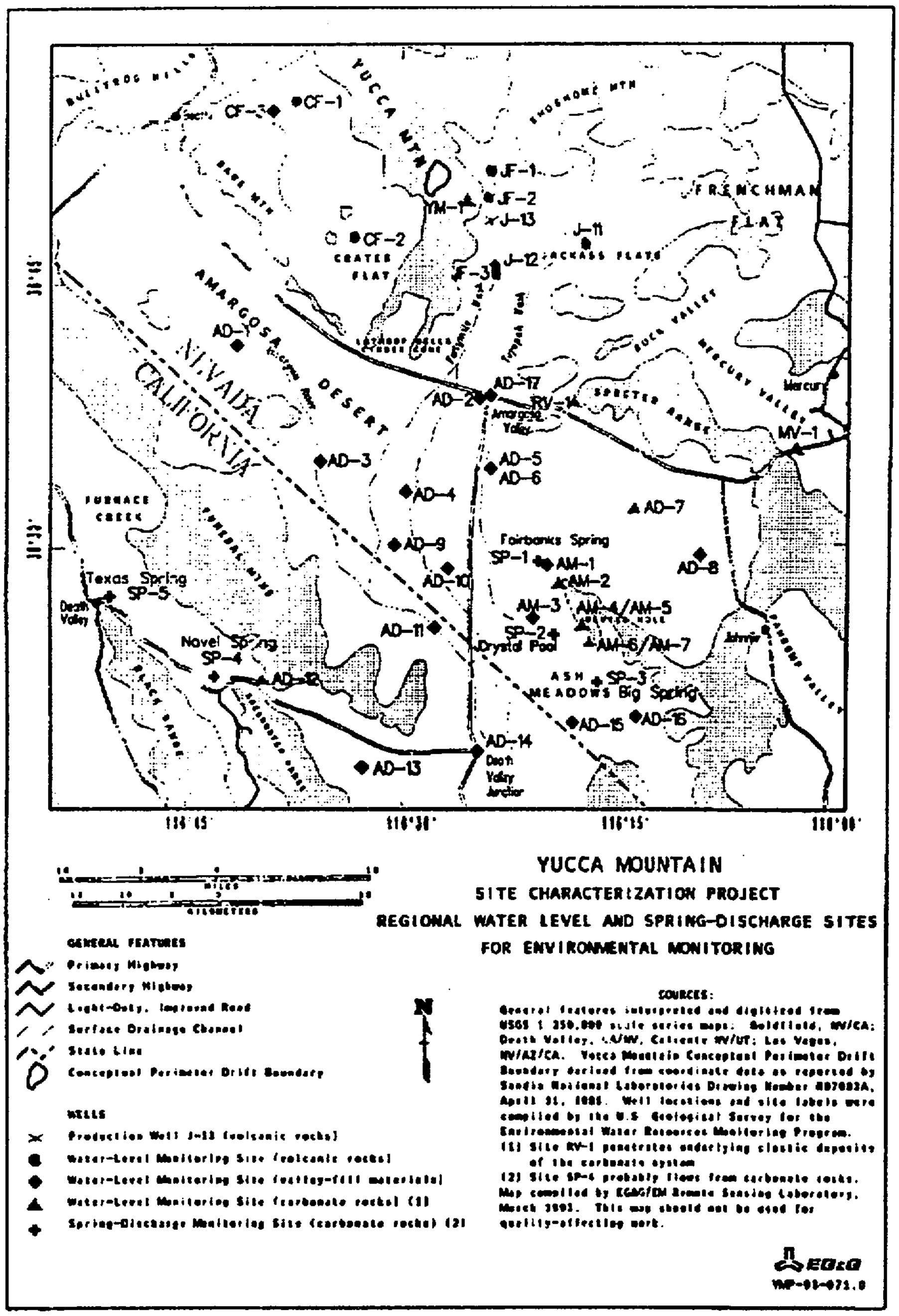

Figure 3.1.2.2.2-1 Yucca Mountain Site Characterization Project Regional Water Level and Spring-Discharge Sites for Environmental Monitoring

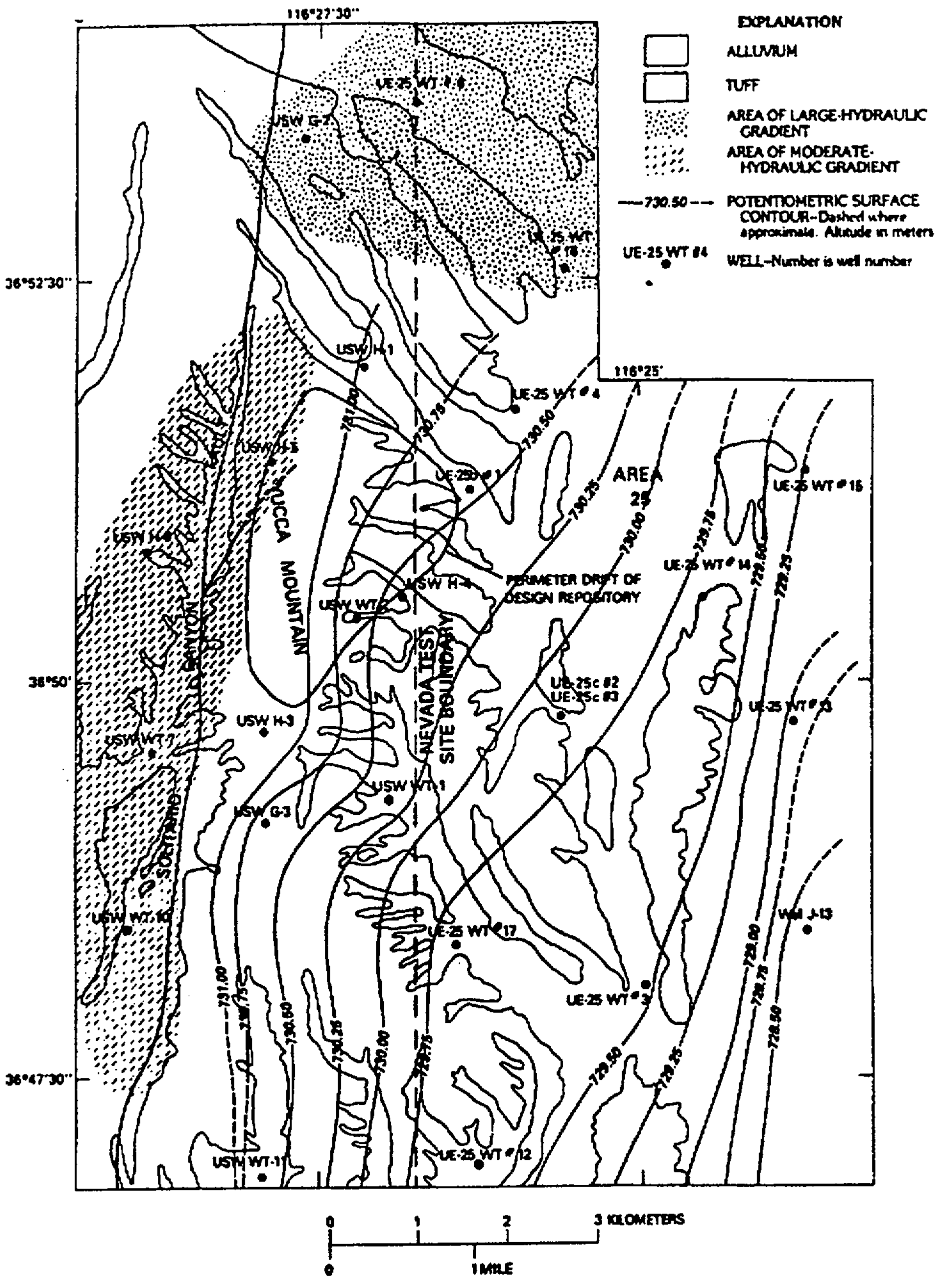

Figure 3.1.2.2.2-2 Potentiometric Surface Map, Yucca Mountain

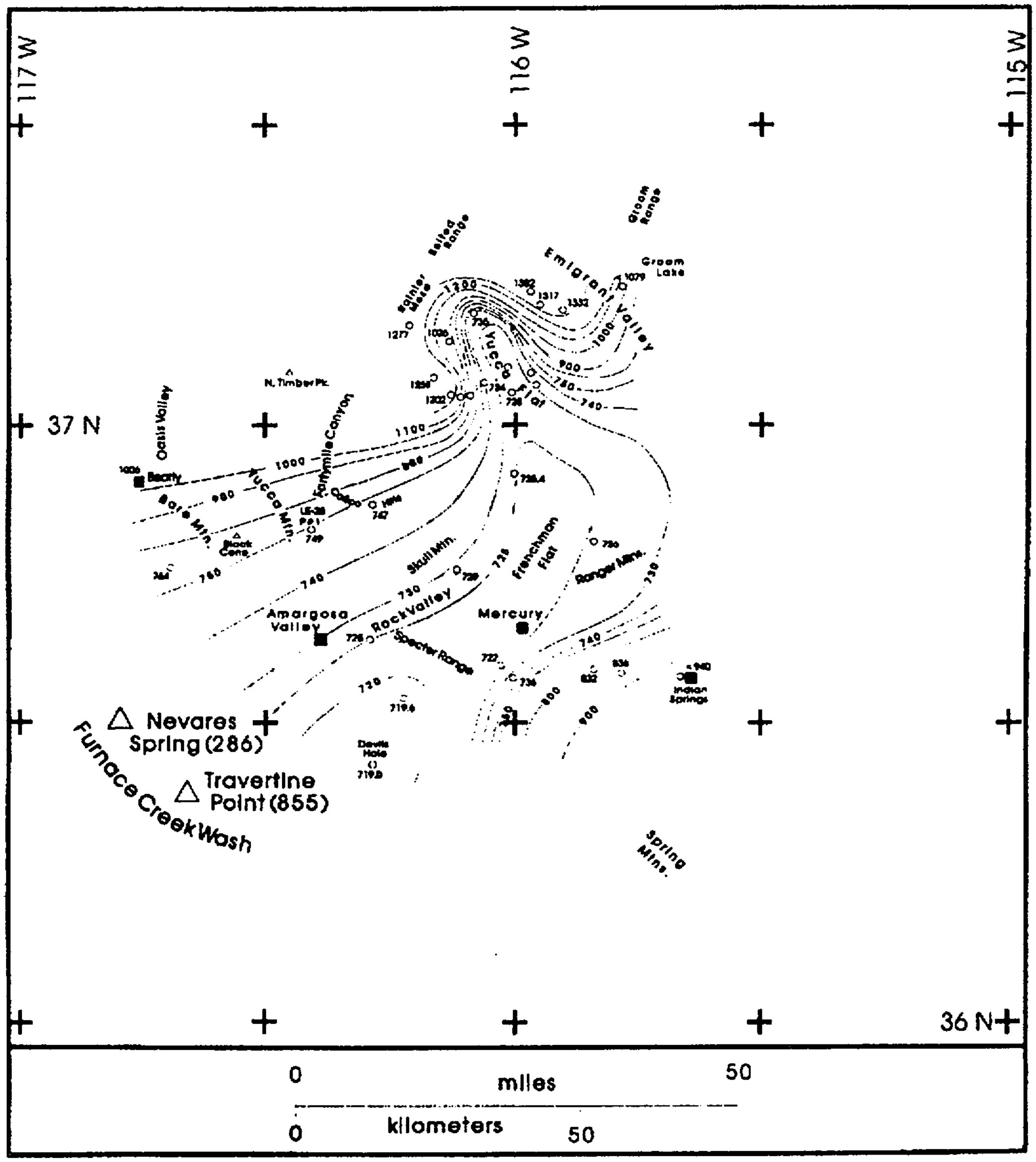

Figure 3.1.2.2.2-3 Potentiometric Levels in Pre-Tertiary Rocks, Yucca Mountain Region. Elevations are given in meters above mean sea level. Contours are conjectural due to sparse data. Heads at Groom Lake, Indian Springs, Beatty, and southwest of Bare Mountain are composite measurements, representing both Cenozoic and Pre-Cenozoic rocks. Travertine Point is a paleodischarge site. Modified after Dudley (1991)

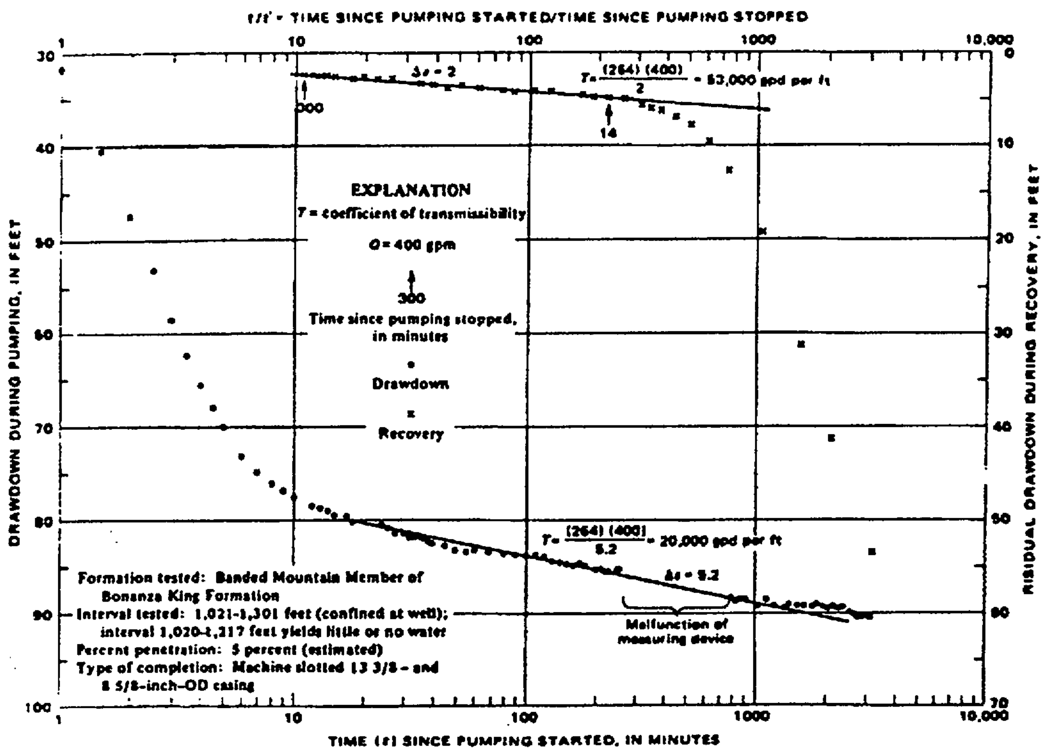

Figure 3.1.2.2.3-1 Semilog Graphs of Drawdown and Residual Drawdown of Water Level During Pumping Testing in Test Well 67-73, February 24-26, 1963

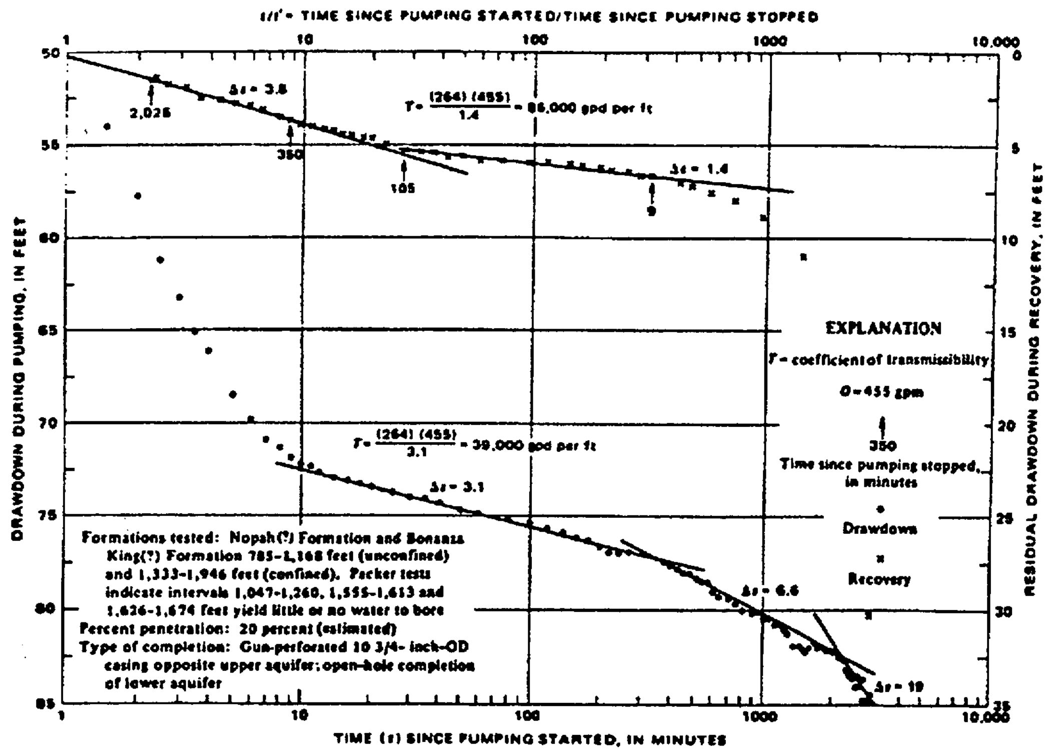

Figure 3.1.2.2.3-2 Semilog Graphs of Drawdown and Residual Drawdown of Water Level During Pumping Testing in Test Well 67-68, September 11-14, 1962

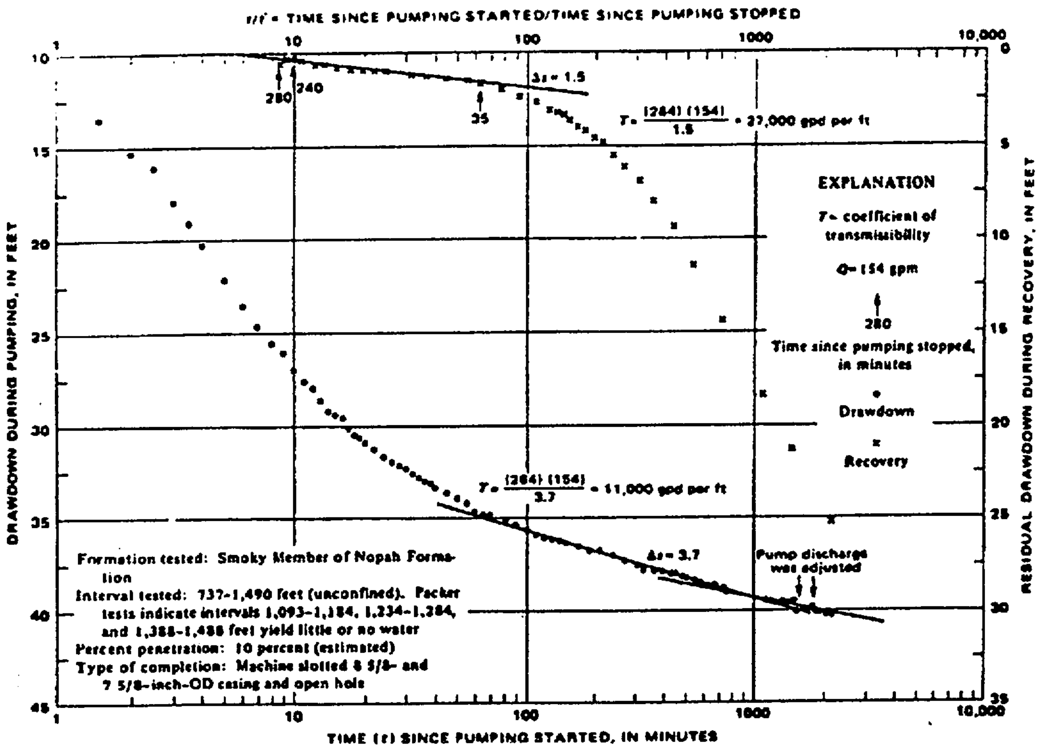

Figure 3.1.2.2.3-3 Semilog Graphs of Drawdown and Residual Drawdown of Water Level During Pumping Testing in Test Well 66-75, September 11-13, 1962

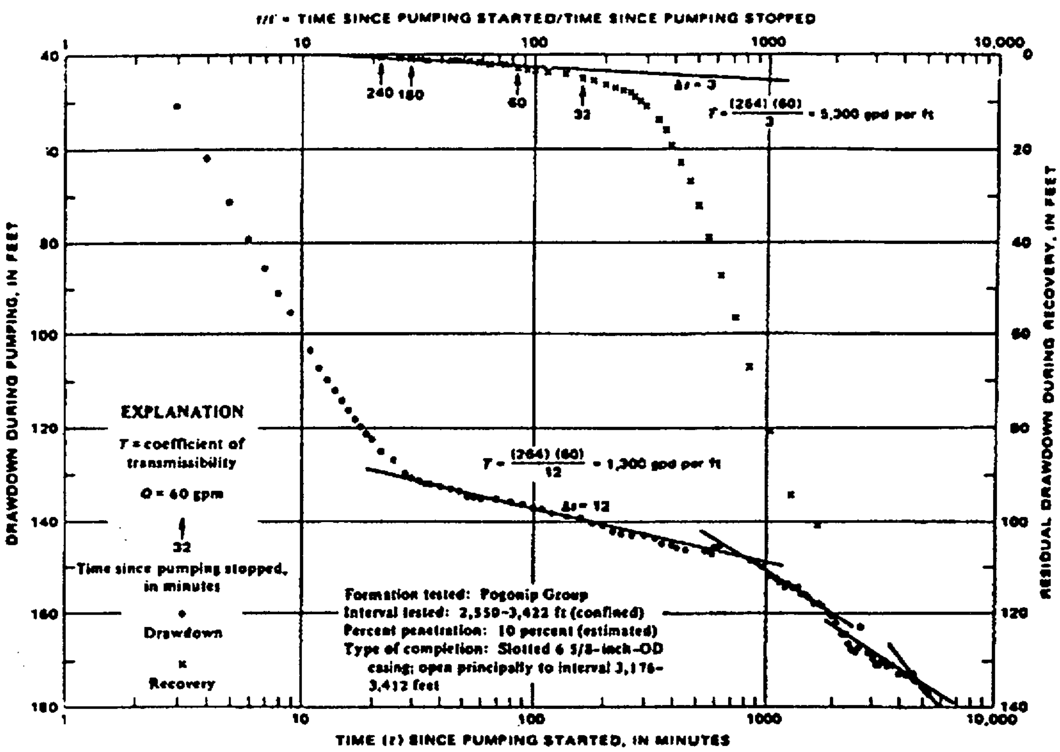

Figure 3.1.2.2.3-4 Semilog Graphs of Drawdown and Residual Drawdown of Water Level During Pumping Testing in Test Well 88-66, March 16-20, 1962

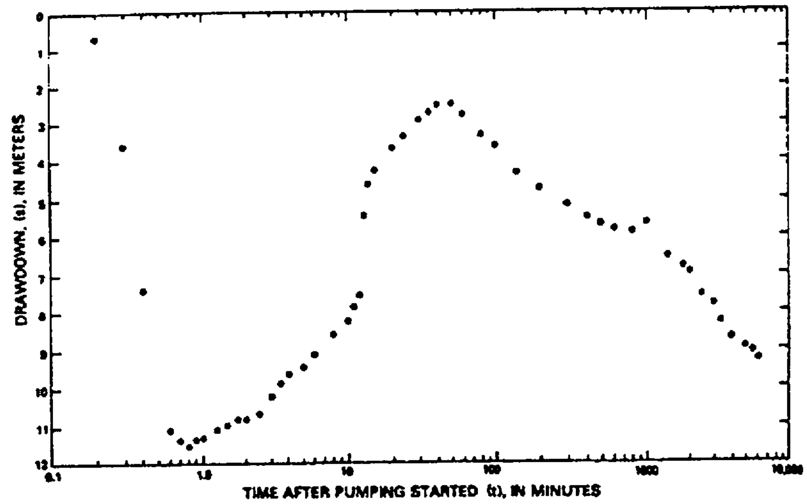

Figure 3.1.2.2.3-5 Water-Level Drawdown, Pumping Test 2, Depth Interval 1,297 to 1,805 Meters

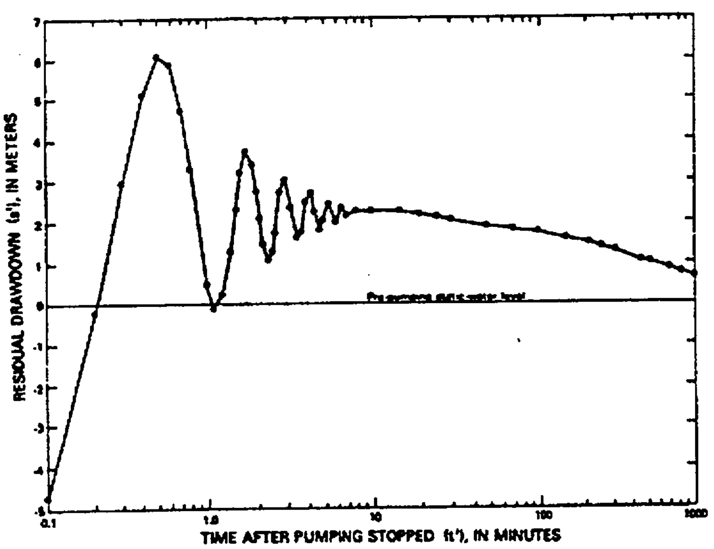

Figure 3.1.2.2.3-6 Residual Drawdown, Recovery Test 2, Depth Interval 1,297 to 1,805 Meters. Craig and Robison (1984)

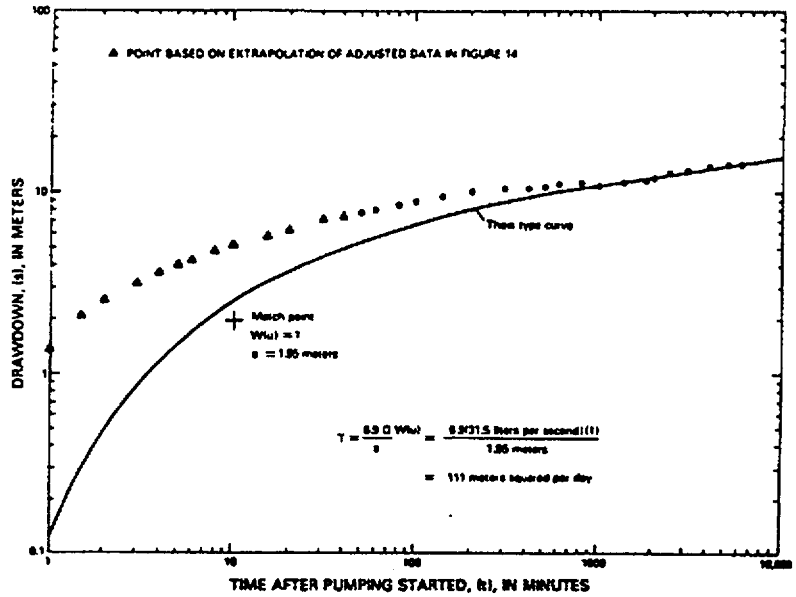

Figure 3.1.2.2.3-7 Analysis of Adjusted Water-Level Drawdown, Pumping Test 2, Depth Interval 1,297 to 1,805 Meters, Theis Method. Craig and Robison (1984

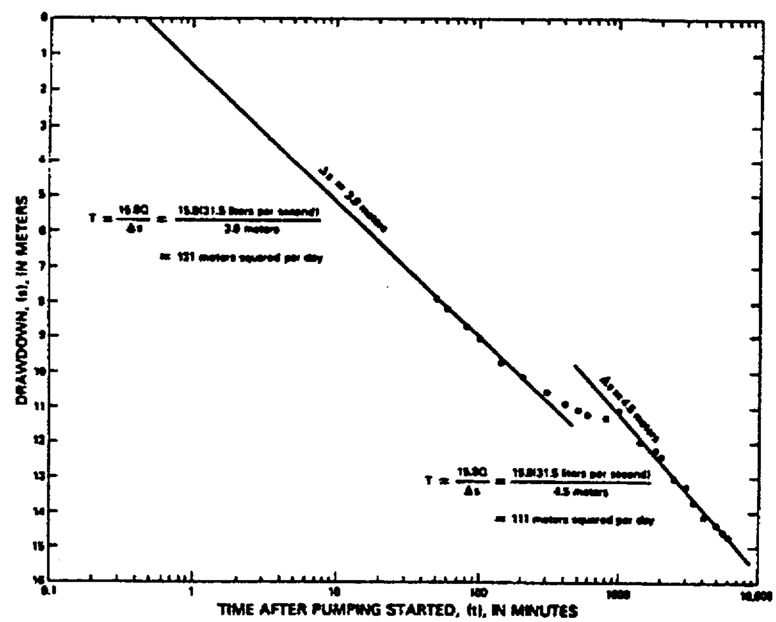

Figure 3.1.2.2.3-8 Analysis of Adjusted Water-Level Drawdown, Pumping Test 2, Depth Interval 1,297 to 1,805 Meters, Straight-Line Method. Craig and Robison (1984

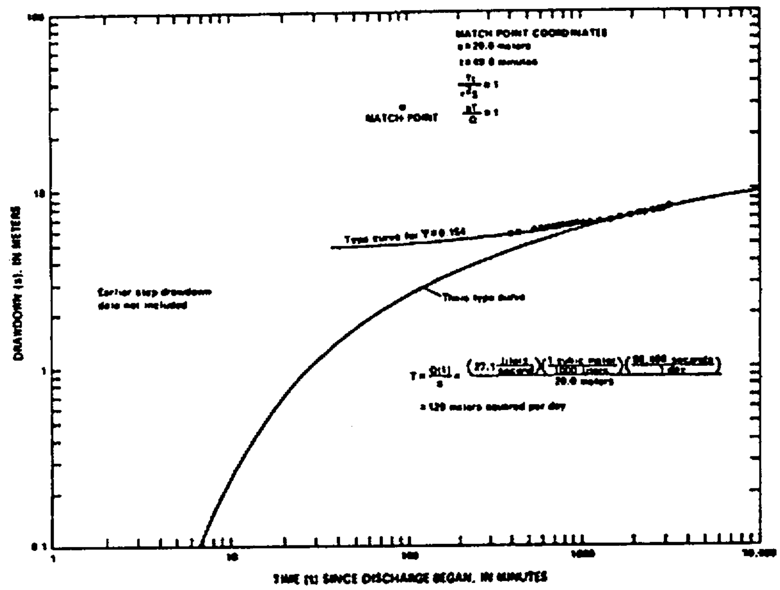

Figure 3.1.2.2.3-9 Drawdown and Analysis of Drawdown During Step-Drawdown Test of Pumping Test 1, Stallman's Method. Thordarson (1983)

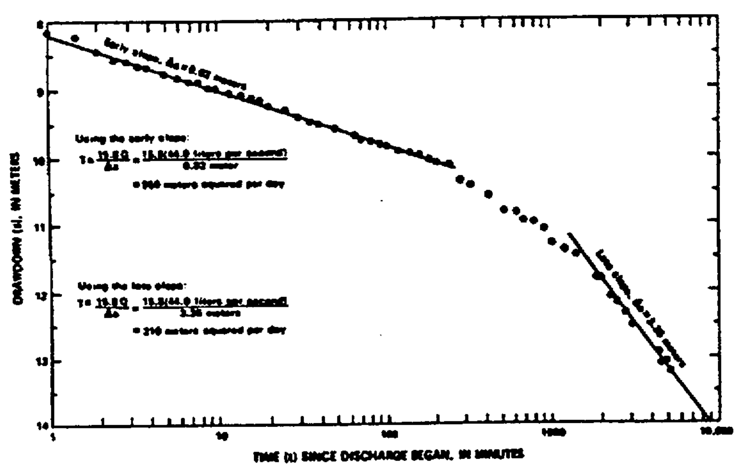

Figure 3.1.2.2.3-10 Drawdown and Analysis of Drawdown During Pumping Test 3, Straight-Line Method. Thordarson (1983)

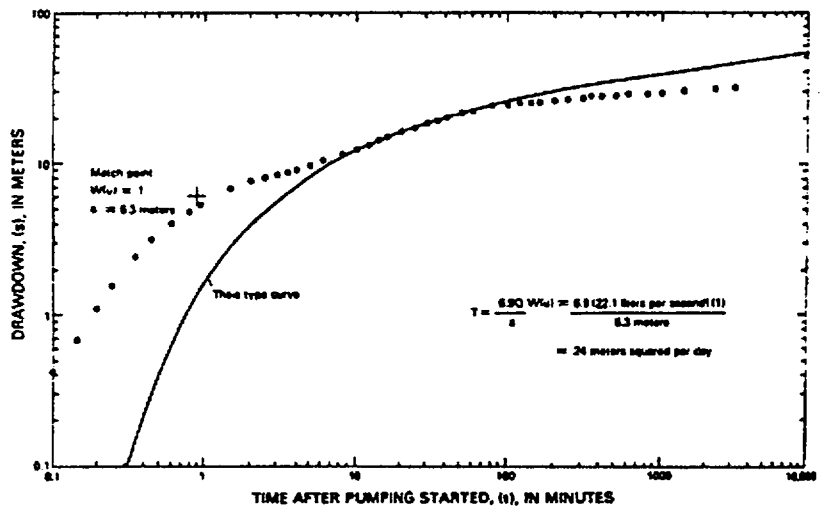

Figure 3.1.2.2.3-11 Analysis of Water-Level Drawdown, Pumping Test 1, Depth Interval 382 to 1,301 Meters, Theis Method. Craig and Robison (1984)

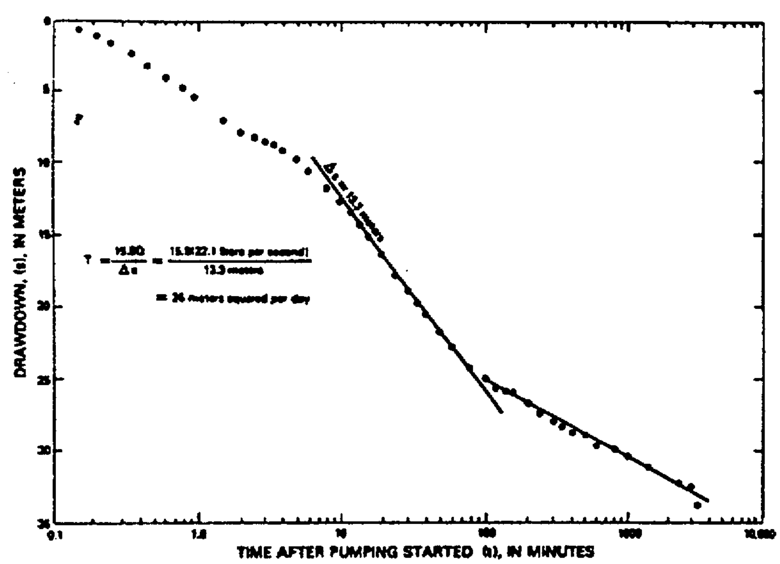

Figure 3.1.2.2.3-12 Analysis of Water-Level Drawdown, Pumping Test 1, Depth Interval 382 to 1,301 Meters, Straight-Line Method. Tuffs

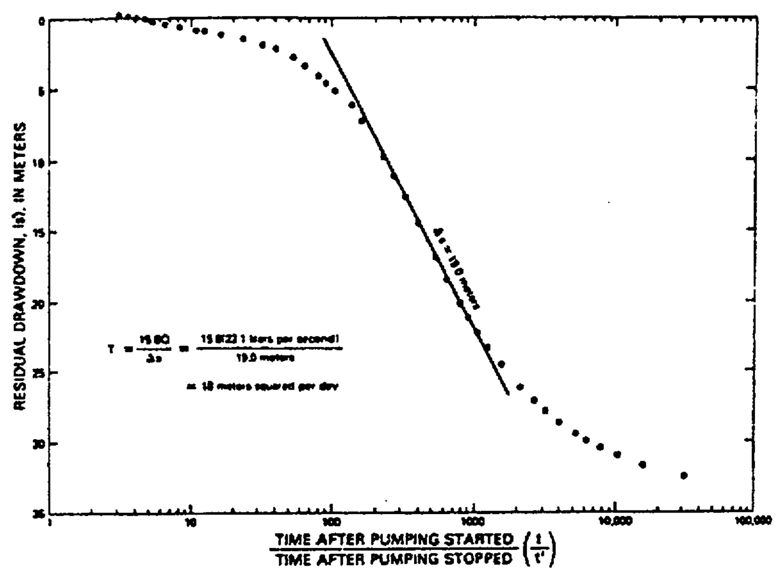

Figure 3.1.2.2.3-13 Analysis of Residual Drawdown, Recovery Test 1, Depth Interval 382 to 1,301 Meters, Straight-Line Method. Craig and Robison (1984)

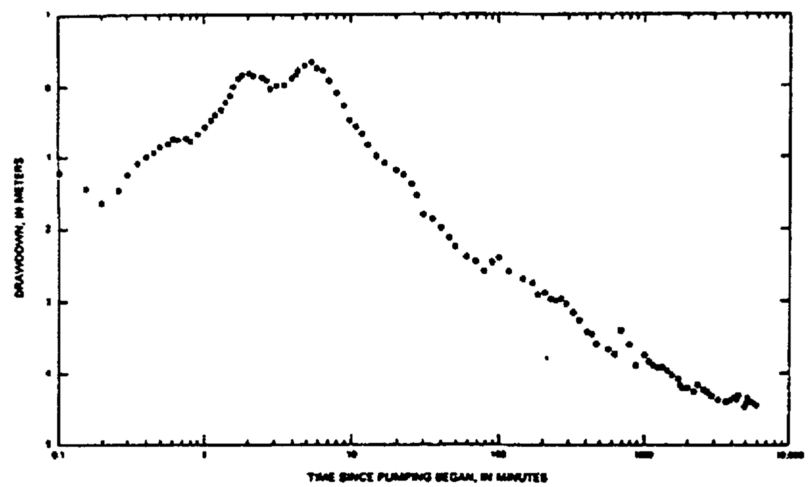

Figure 3.1.2.2.3-14 Drawdown in Well USW VH-1 During Test 3. Thordarson and Howells (1987)

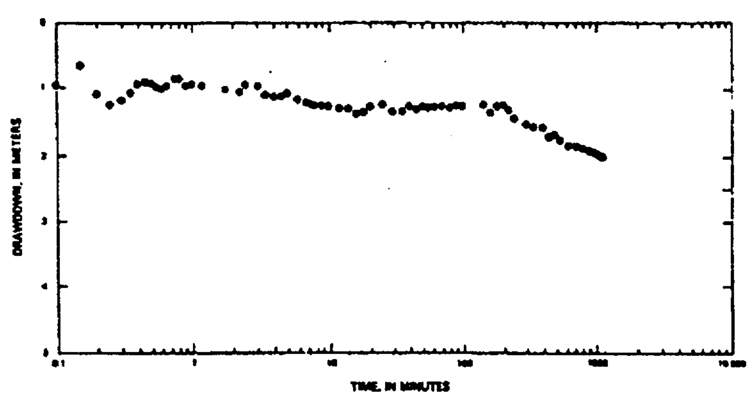

Figure 3.1.2.2.3-15 Drawdown in Well USW VH-1 During Test 5. Thordarson and Howells (1987)

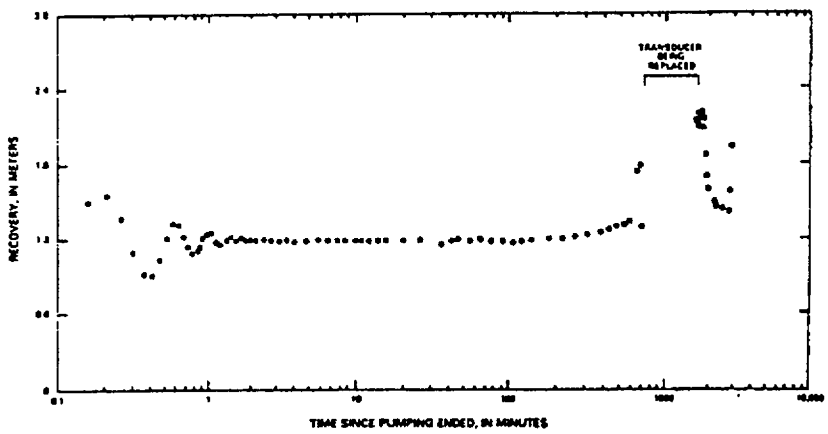

Figure 3.1.2.2.3-16 Recovery in Well USW VH-1 During Test 4. Thordarson and Howells (1987)

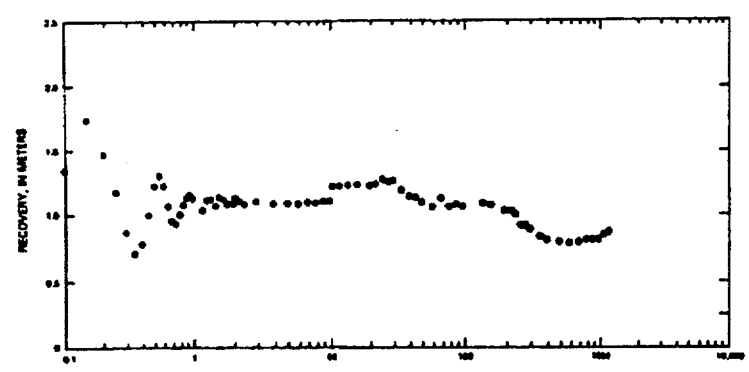

Figure 3.1.2.2.3-17 Recovery in Well USW VH-1 During Test 6. Thordarson and Howells (1987)

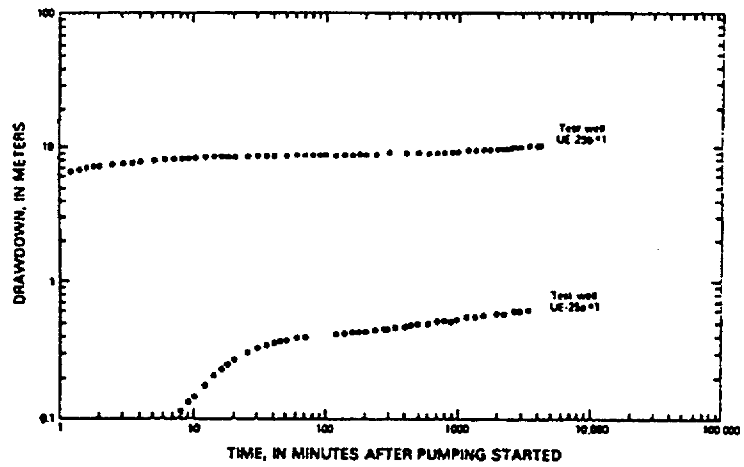

Figure 3.1.2.2.3-18 Drawdown in Test Wells UE-25b#1 and UE-25a#1 During Pumping Test 3. Lahoud et al. (1984)

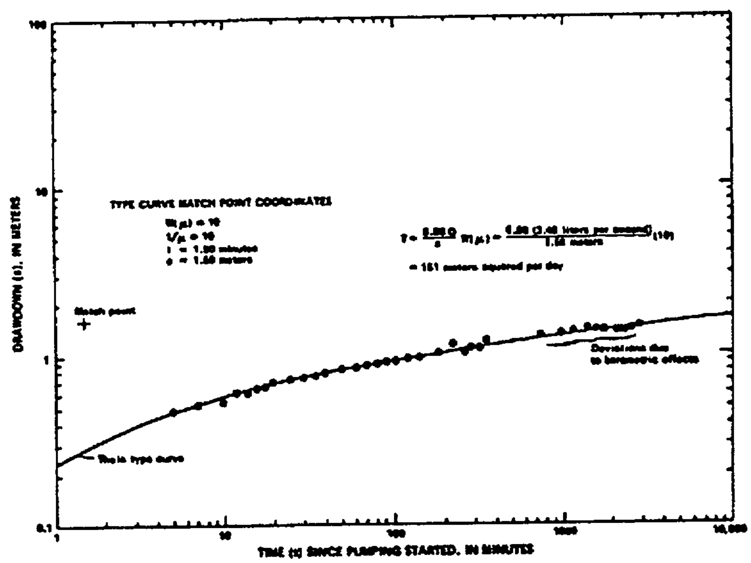

Figure 3.1.2.2.3-19 Analysis in Water-Level Drawdown, Pumping Test 1, Zone from 572 to 688 Meters in the Well, Theis Method. Rush et al. (1984)

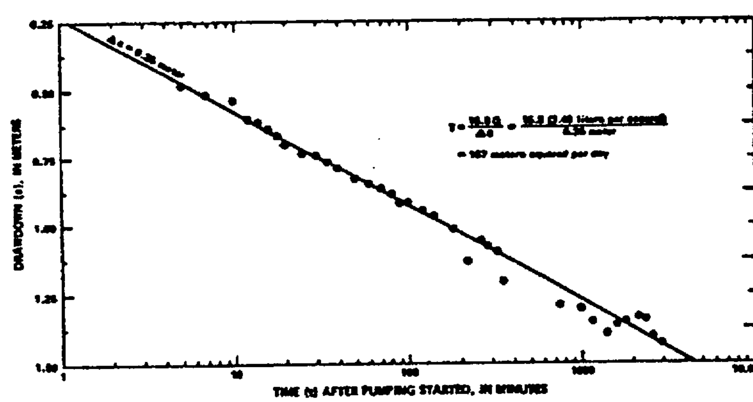

Figure 3.1.2.2.3-20 Analysis of Water-Line Drawdown, Pumping Test 1, Zone from 572 to 688 Meters in the Well, Straight-Line Solution

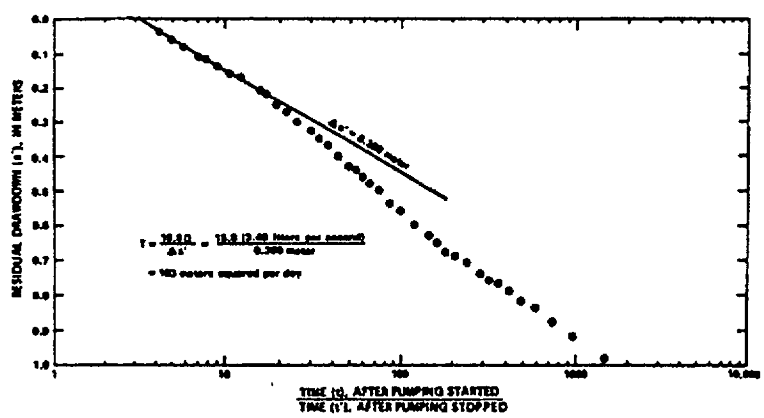

Figure 3.1.2.2.3-21 Analysis of Water-Level Recovery, Pumping Test 1, Zone from 572 to 688 Meters in the Well, Straight-Line Solution

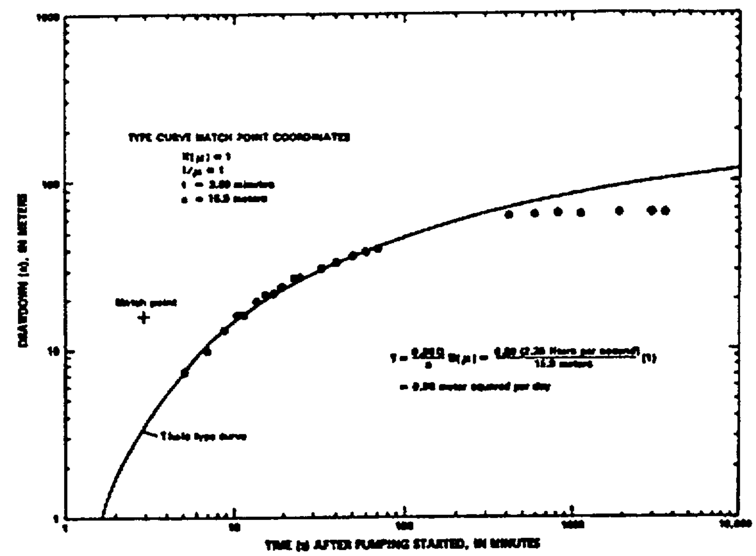

Figure 3.1.2.2.3-22 Analysis of Water-Line Drawdown, Pumping Test 2, Zone from 687 to 1,829 Meters in the Well, Theis Method

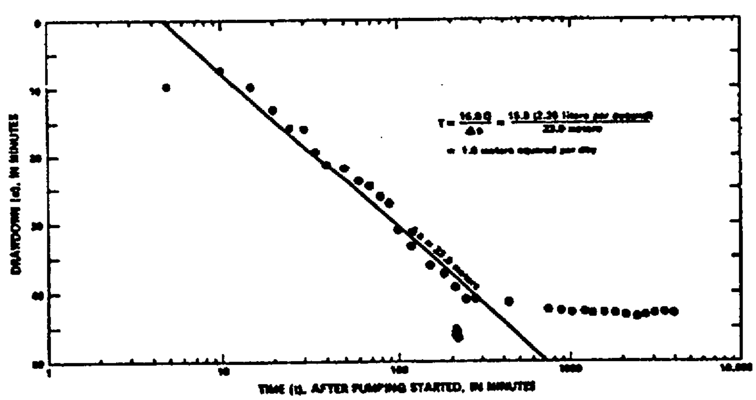

Figure 3.1.2.2.3-23 Analysis of Water-Level Drawdown, Pumping Test 2, Zone from 687 to 1,829 Meters in the Well, Straight-Line Solution. Rush et al. (1984)

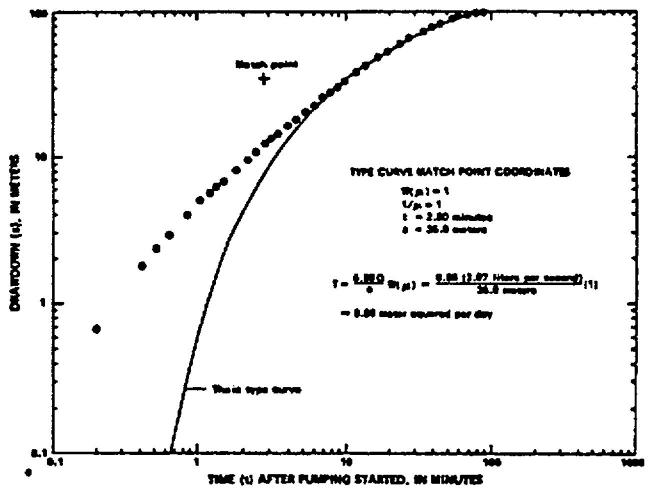

Figure 3.1.2.2.3-24 Analysis of Water-Level Drawdown, Pumping Test 3, Zone from 687 to 1,829 Meters in the Well, Theis Method. Rush et al. (1984)

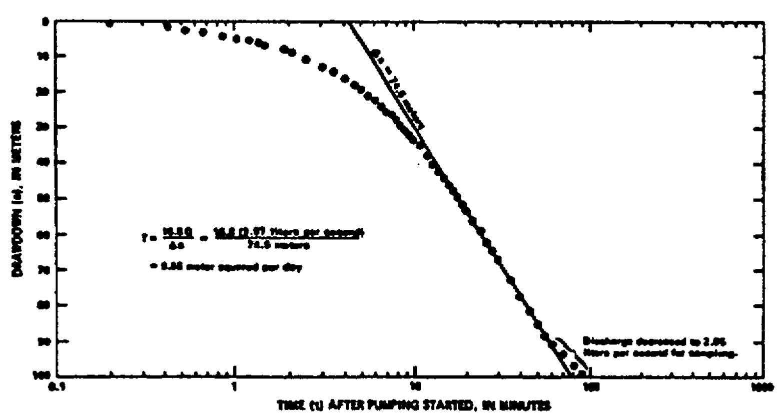

Figure 3.1.2.2.3-25 Analysis of Water-Level Drawdown, Pumping Test 3, Zone from 687 to 1,829 Meters in the Well, Straight-Line Solution

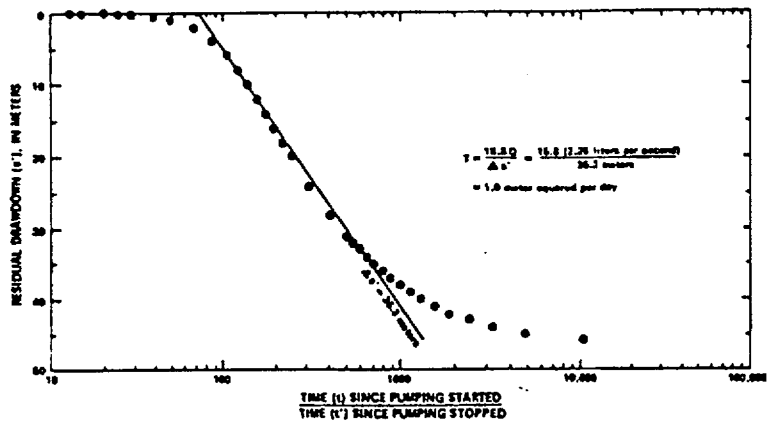

Figure 3.1.2.2.3-26 Analysis of Water-Level Recovery, Pumping Test 2, Zone from 687 to 1,829 Meters in the Well, Straight-Line Solution. Rush et al. (1984)

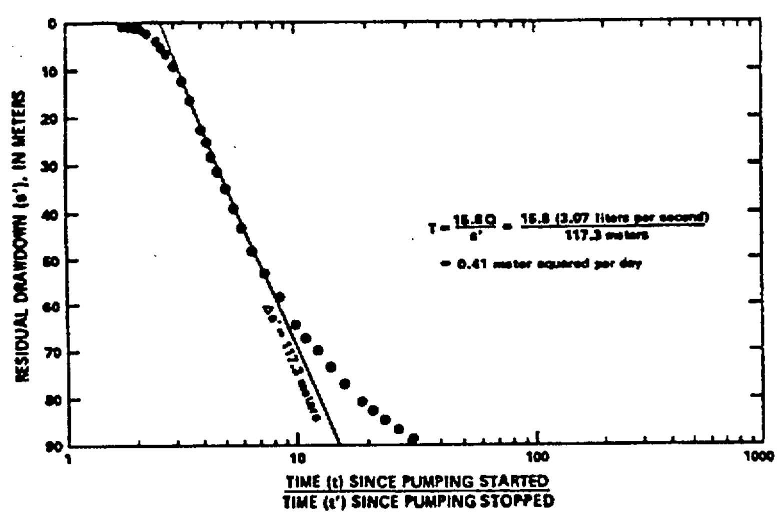

Figure 3.1.2.2.3-27 Analysis of Water-Line Recovery, Pumping Test 3, Zone from 687 to 1,829 Meters in the Well, Straight-Line Method. Rush et al. (1984)

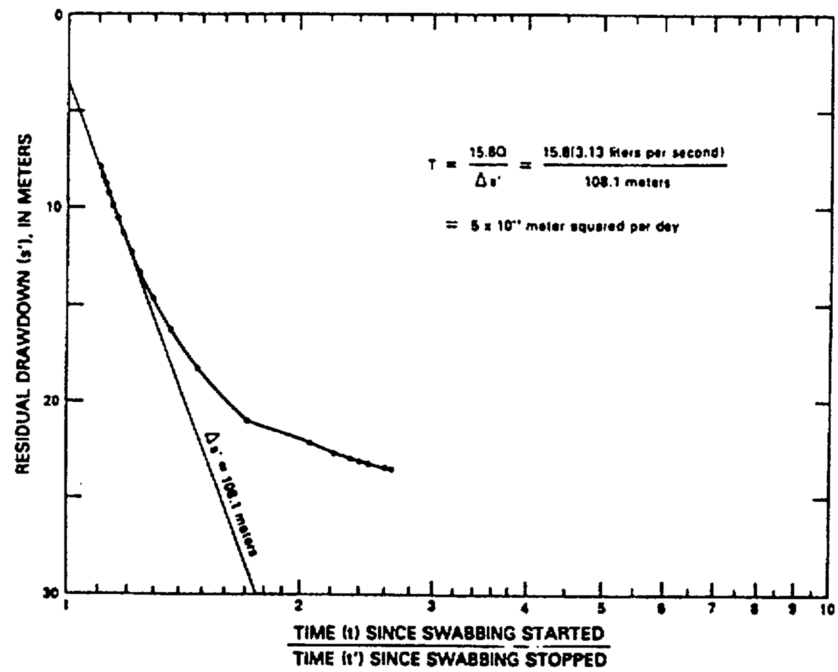

Figure 3.1.2.2.3-28 Analysis of Water-Level Recovery, Following Second Cycle of Pumping of the Interval from 754 to 1,219 Meters, Using the Straight-Line Method

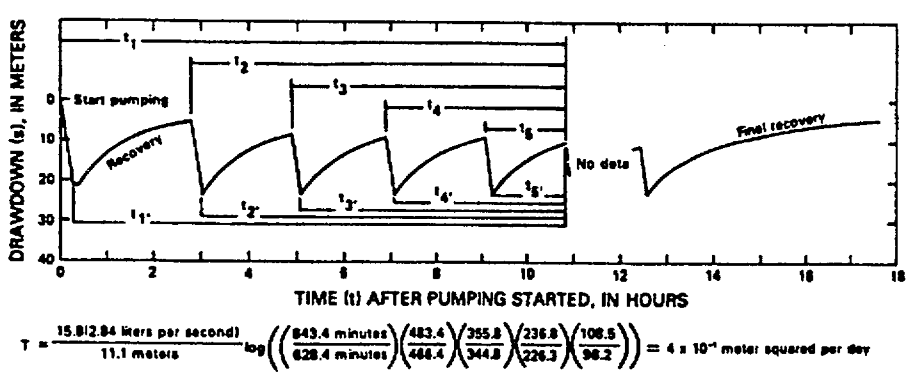

Figure 3.1.2.2.3-29 Analysis of the Pumping Test of the Interval from 754 to 1,219 Meters, Using Brown's Method for a Cyclically Pumped Well. Thordarson et al. (1985)

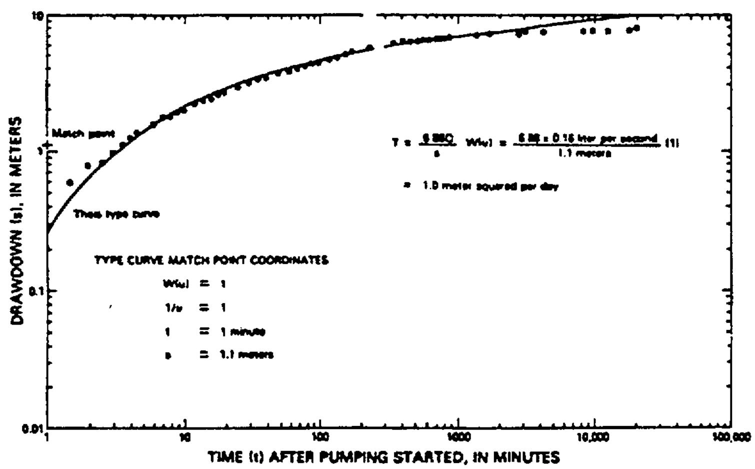

Figure 3.1.2.2.3-30 Analysis of the Water-Level Drawdown of the Interval from 822 to 1.219 Meters, Using Theis Method. Thordarson et al. (1985)

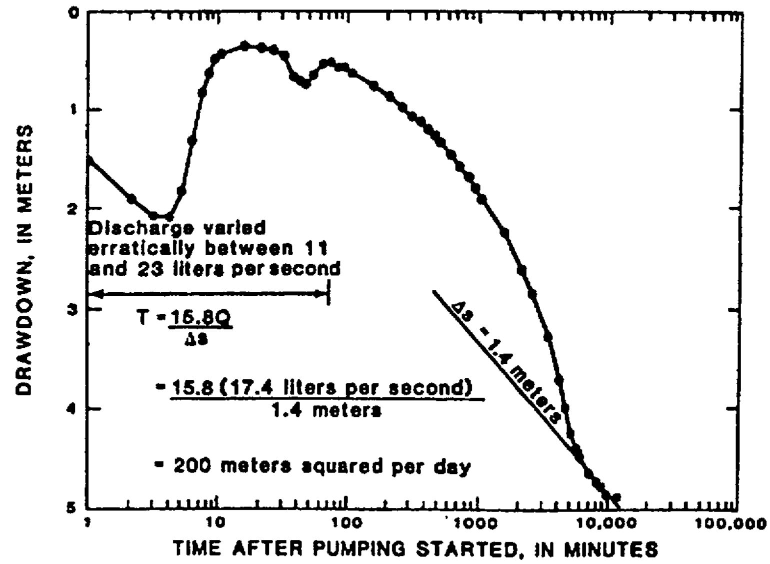

Figure 3.1.2.2.3-31 Analysis of Water-Level Drawdown Versus Time for Pumping Test 6, Depth Interval from 519 to 1,219 Meters, Using the Straight-Line Method of Analysis. Whitfield et al. (1985)

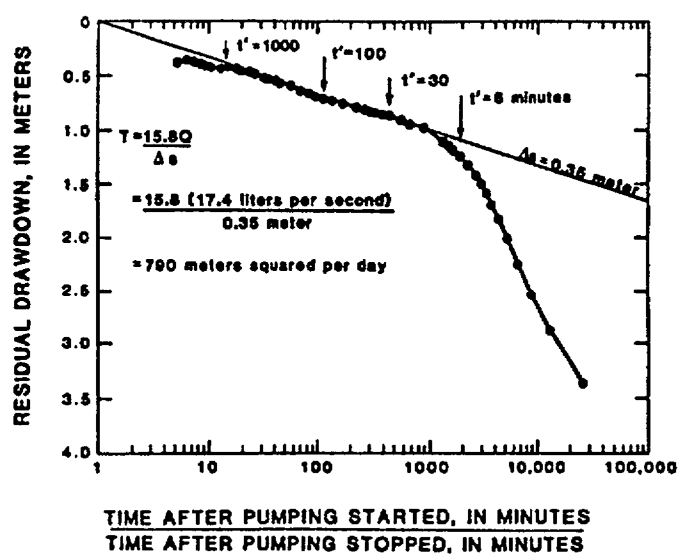

Figure 3.1.2.2.3-32 Analysis of Water-Level Recovery Versus Time for Pumping Test 6, Depth Interval from 519 to 1,219 Meters

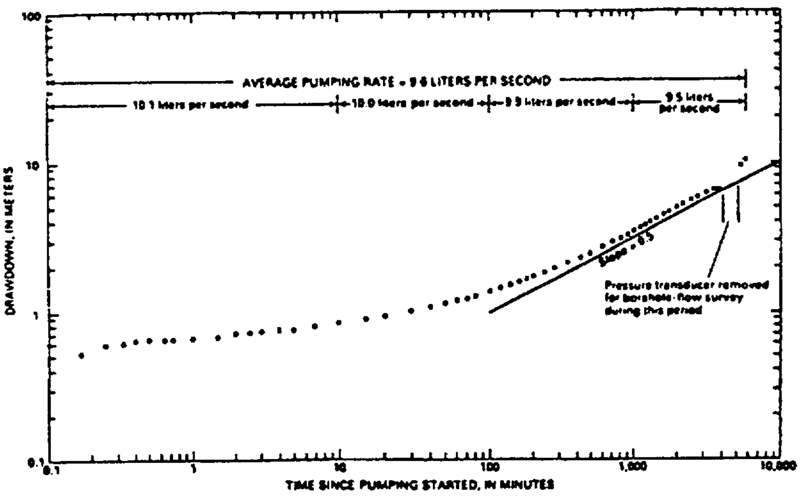

Figure 3.1.2.2.3-33 Water-Level Drawdown, Pumping Test 3, Depth Interval from 704 to 1,219 Meters. Robison and Craig (1991)

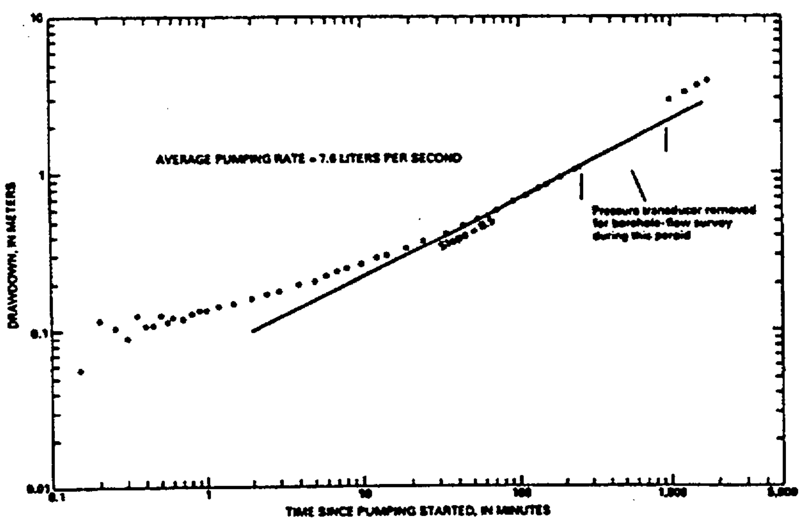

Figure 3.1.2.2.3-34 Water-Level Drawdown, Pumping Test 4, Depth Interval from 704 to 1,219 Meters

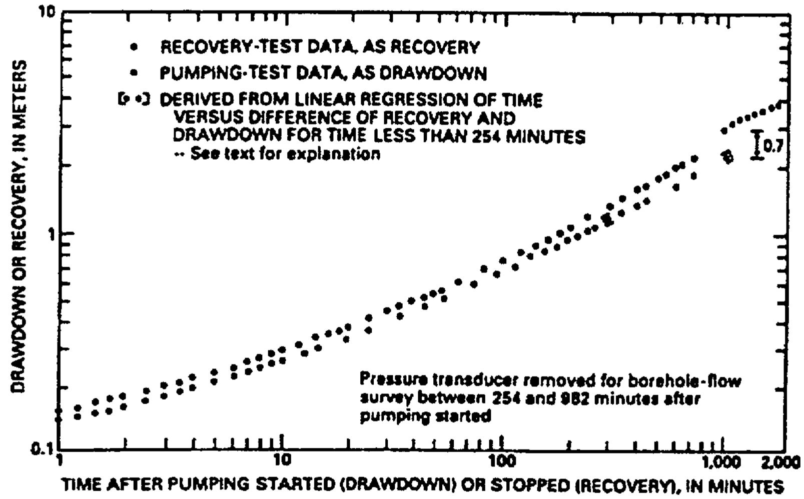

Figure 3.1.2.2.3-35 Data for Pumping and Recovery Tests 4, Depth Interval from 704 to 1,219 Meters

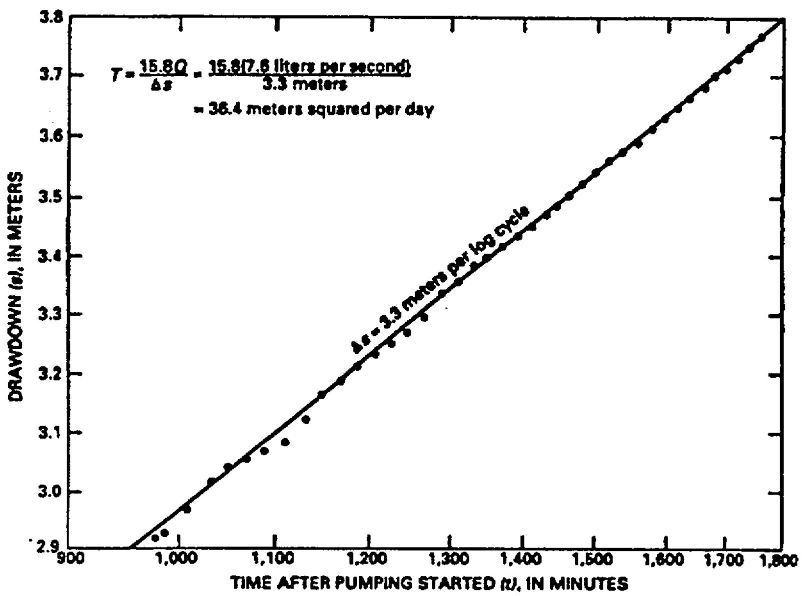

Figure 3.1.2.2.3-36 Analysis of Late-Time Data, Pumping Test 4, Depth Interval from 704 to 1,219 Meters, Straight-Line Method. Robison and Craig (1991)

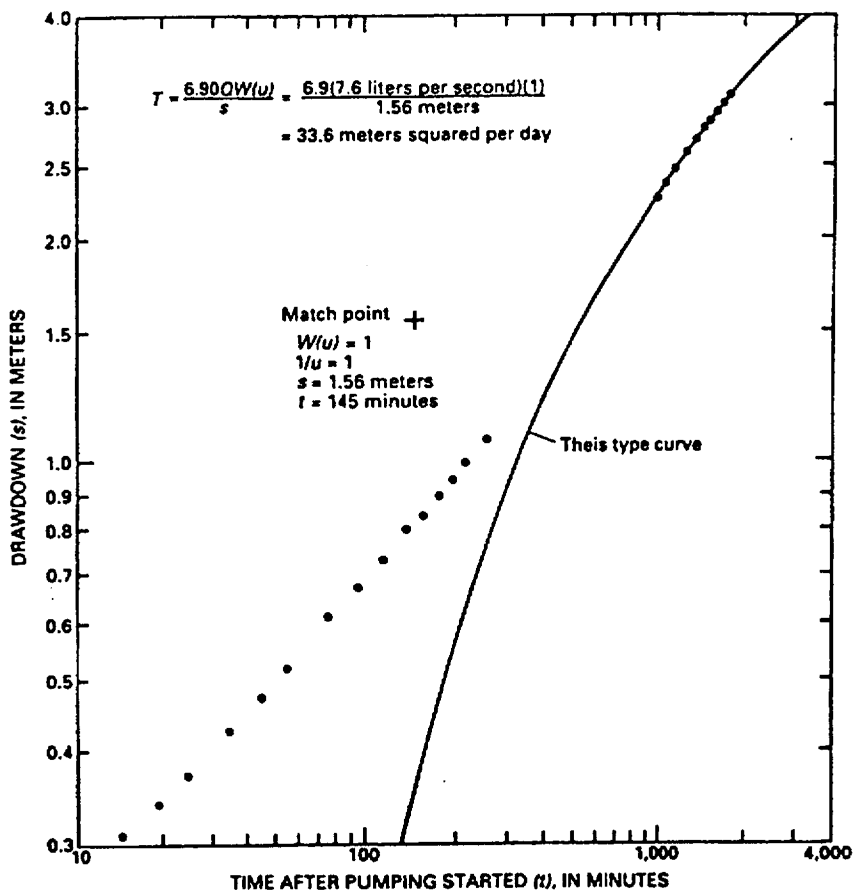

Figure 3.1.2.2.3-37 Analysis of Adjusted Water-Level Drawdown, Pumping Test 4, Depth Interval from 704 to 1,219 Meters, Theis Method (Lohman, 1972). Robison and Craig (1991)

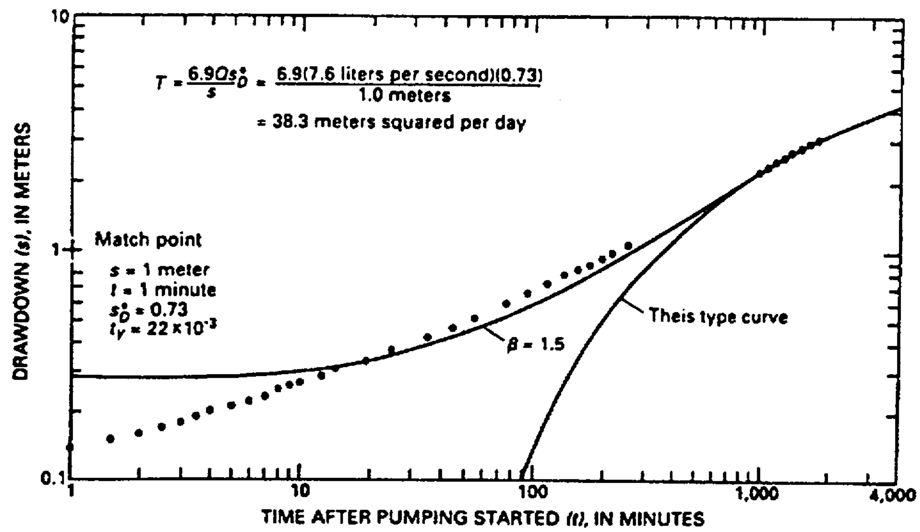

Figure 3.1.2.2.3-38 Analysis of Adjusted Water-Level Drawdown, Pumping Test 4, Depth Interval from 704 to 1,219 Meters, Method of Neuman (1975)

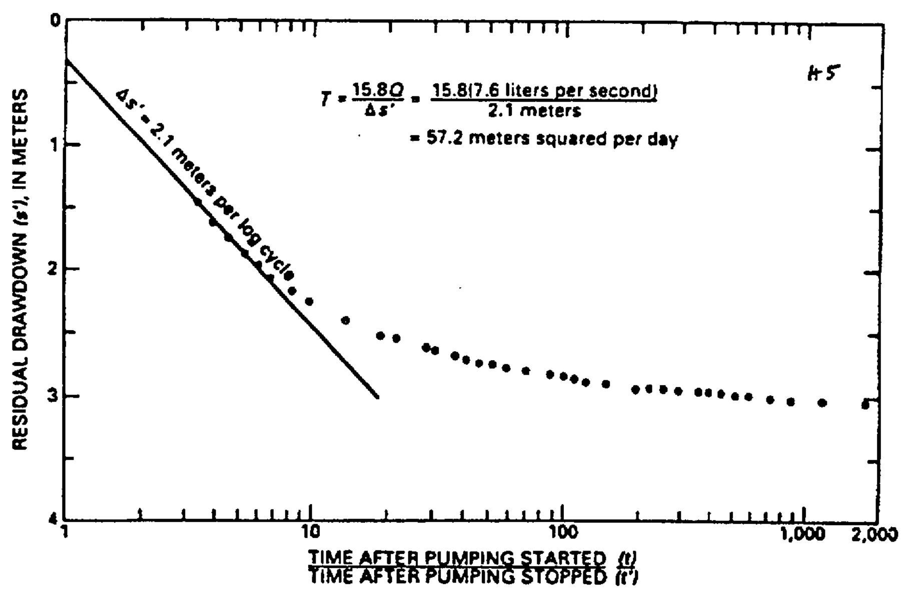

Figure 3.1.2.2.3-39 Analysis of Residual Drawdown, Pumping Test 4, Depth Interval from 704 to 1,219 Meters, Straight-Line Method

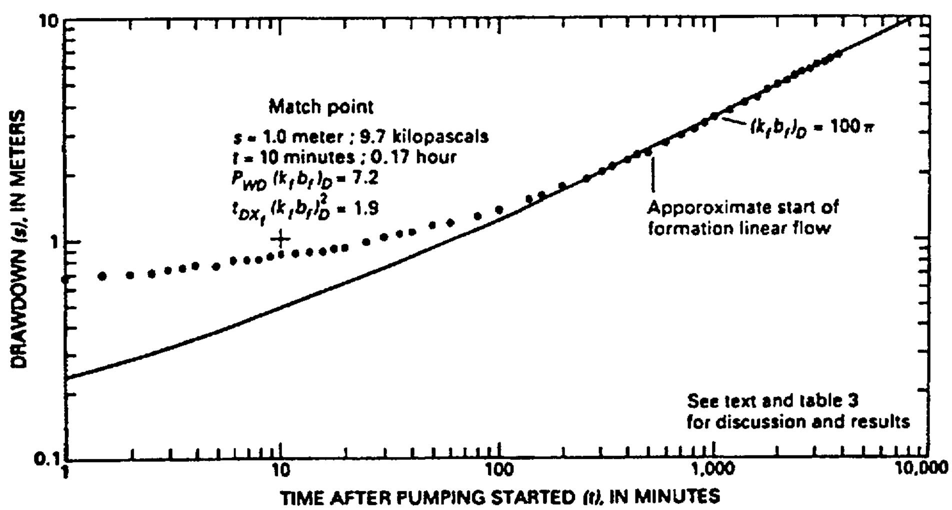

Figure 3.1.2.2.3-40 Analysis of Pumping Test 3, Depth Interval from 704 to 1,219 Meters, Vertical-Fracture Model, Curve-Match Method

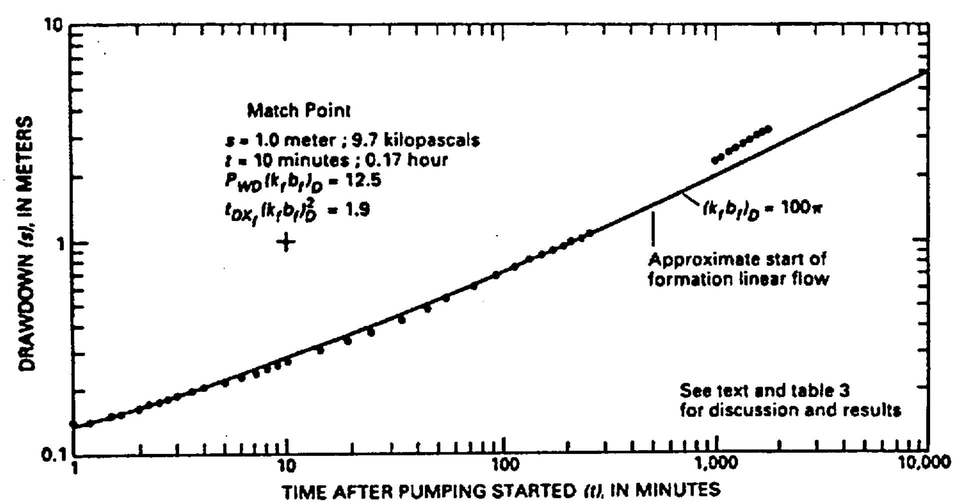

Figure 3.1.2.2.3-41 Analysis of Pumping Test 4, Depth Interval from 704 to 1,219 Meters, Vertical-Fracture Model, Curve-Match Method. Robison and Craig (1991)

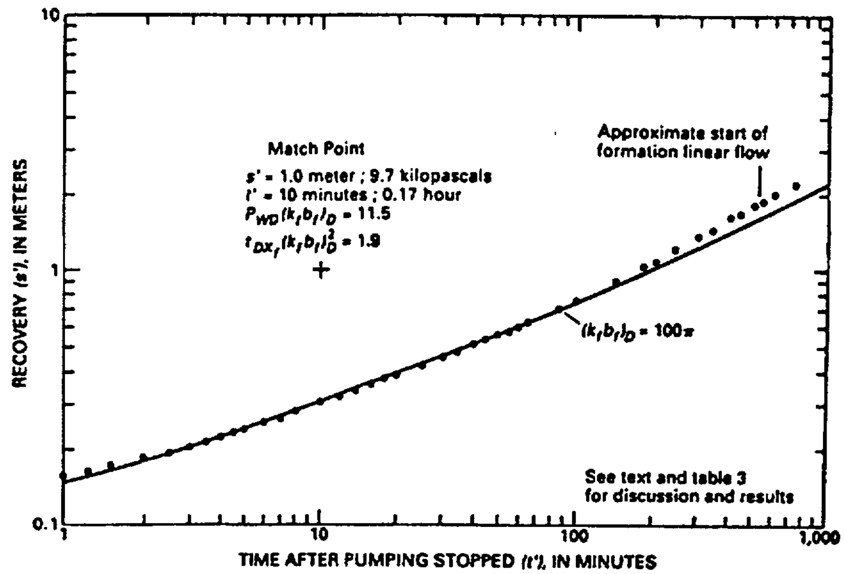

Figure 3.1.2.2.3-42 Analysis of Recovery Test 4, Depth Interval from 704 to 1,219 Meters, Vertical-Fracture Model, Curve-Match Method

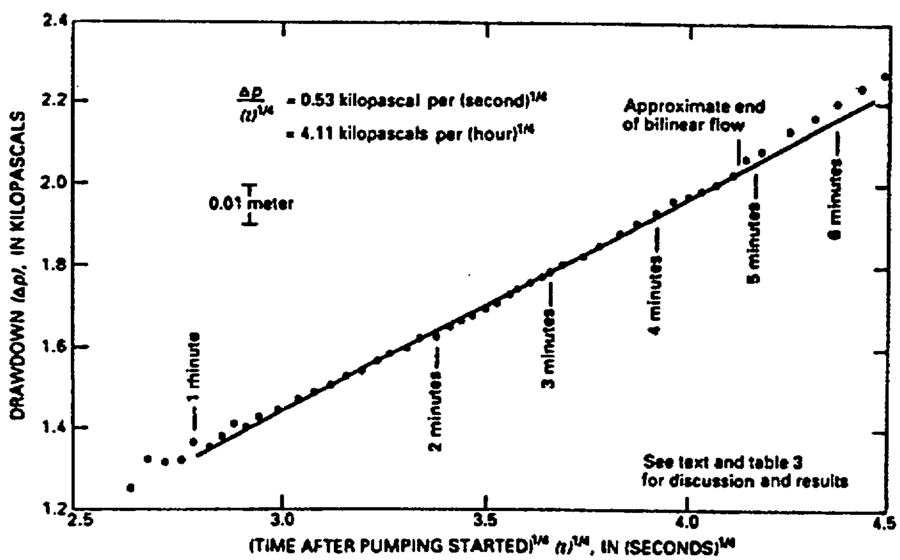

Figure 3.1.2.2.3-43 Analysis of Pumping Test 4, Depth Interval from 704 to 1,219 Meters, Vertical-Fracture Model, Bilinear-Flow Method. Robison and Craig (1991)

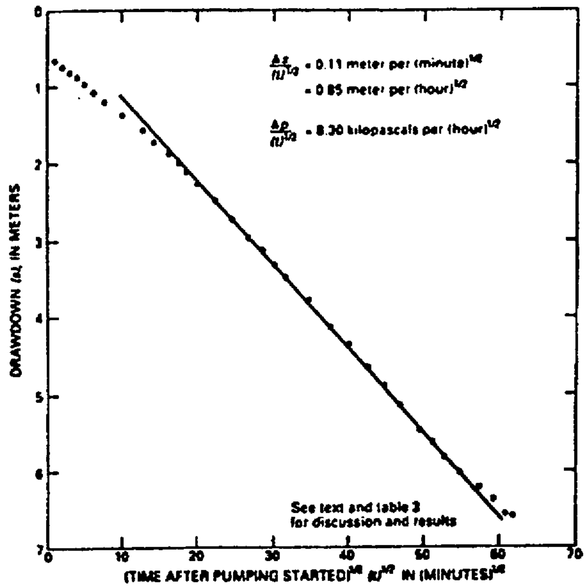

Figure 3.1.2.2.3-44 Analysis of Pumping Test 3, Depth Interval from 704 to 1,219 Meters, Vertical-Fracture Model, Linear-Flow Method

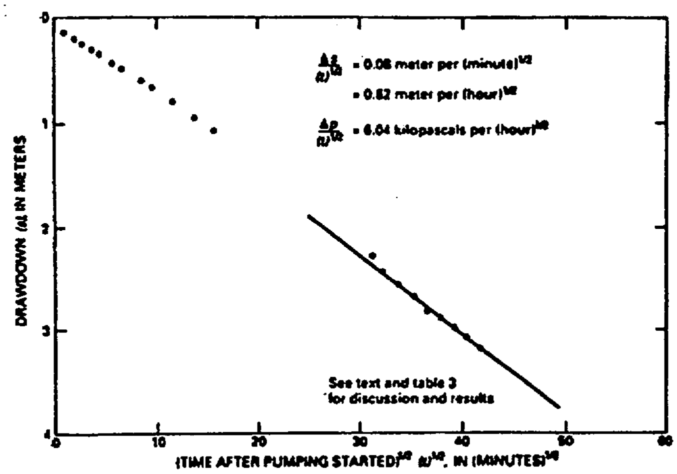

Figure 3.1.2.2.3-45 Analysis of Pumping Test 4, Depth Interval from 704 to 1,219 Meters, Vertical-Fracture Model, Linear-Flow Method. Robison and Craig (1991)

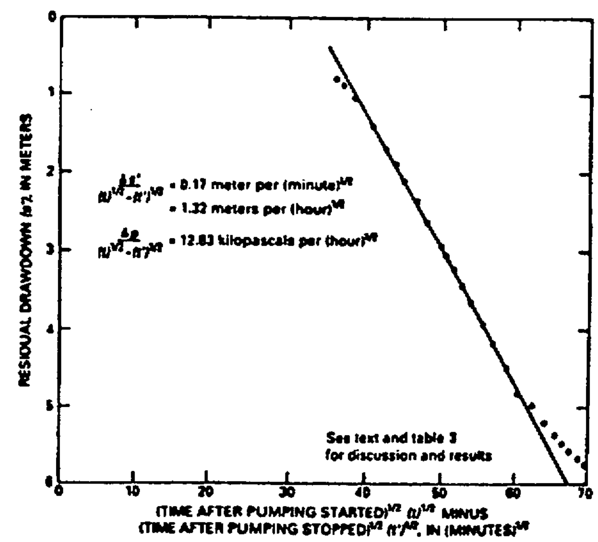

Figure 3.1.2.2.3-46 Analysis of Recovery Test 3, Depth Interval from 704 to 1,219 Meters, Vertical-Fracture Model, Linear-Flow Method

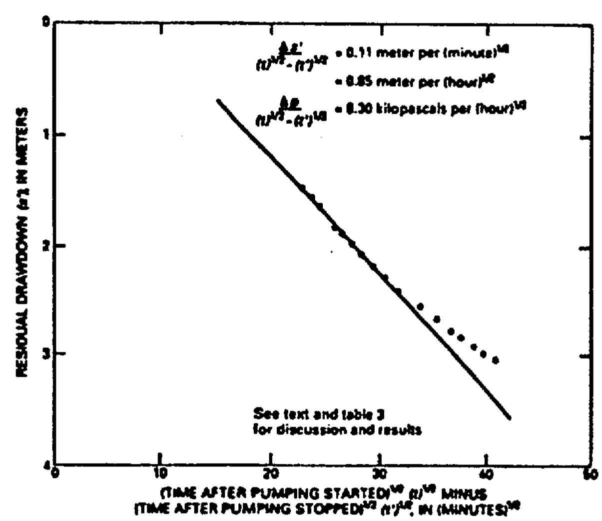

Figure 3.1.2.2.3-47 Analysis of Recovery Test 4, Depth Interval from 704 to 1,219 Meters, Vertical-Fracture Model, Linear-Flow Method. Robison and Craig (1991)

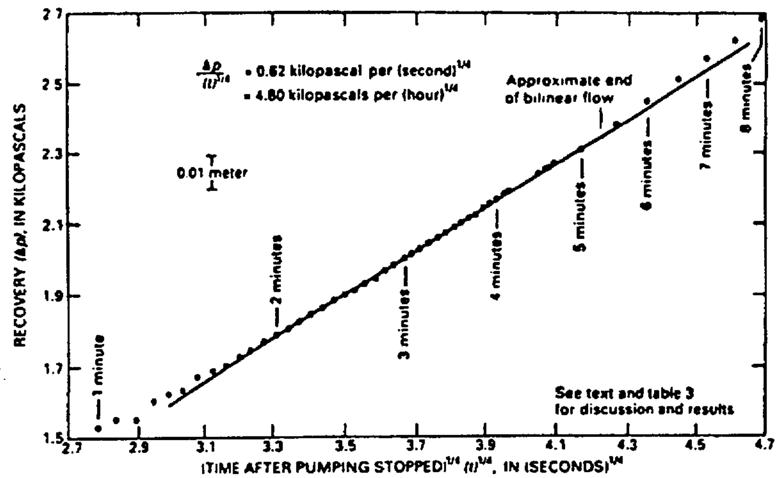

Figure 3.1.2.2.3-48 Analysis of Recovery Test 4, Depth Interval from 704 to 1,219 Meters, Vertical-Fracture Model, Bilinear-Flow Method. Robison and Craig (1991)

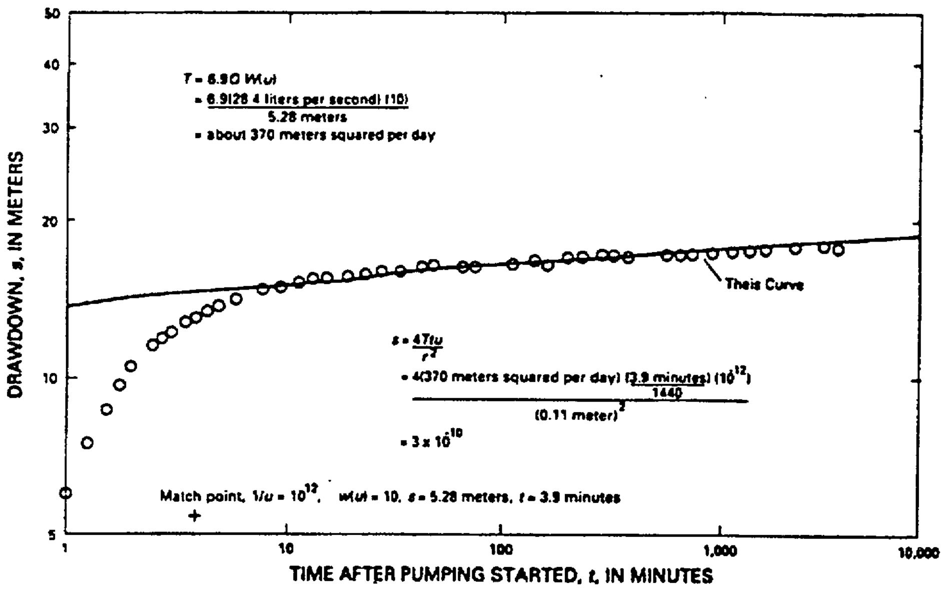

Figure 3.1.2.2.3-49 Analysis of Water-Level Drawdown, Pumping Test 1, Depth Interval from 526 to 1,220 Meters, Theis Method. Craig and Reed (1991)

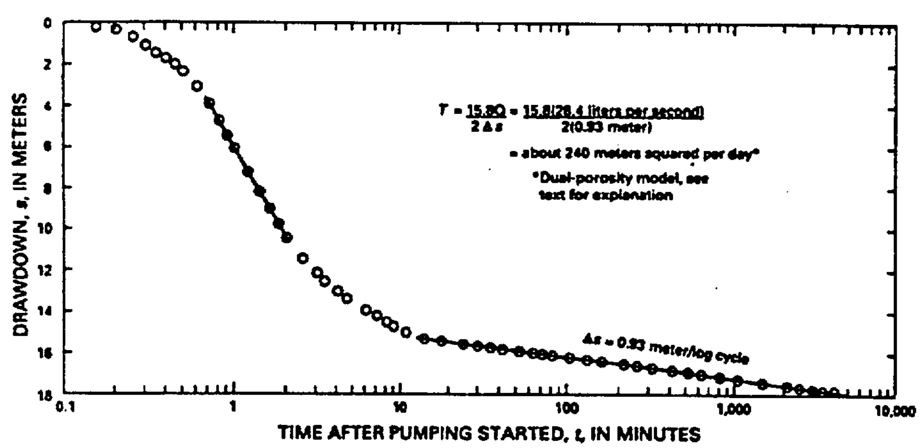

Figure 3.1.2.2.3-50 Analysis of Water-Level Drawdown, Pumping Test 1, Depth Interval from 526 to 1,220 Meters, Straight-Line Solution with Dual-Porosity Model. Craig and Reed (1991)

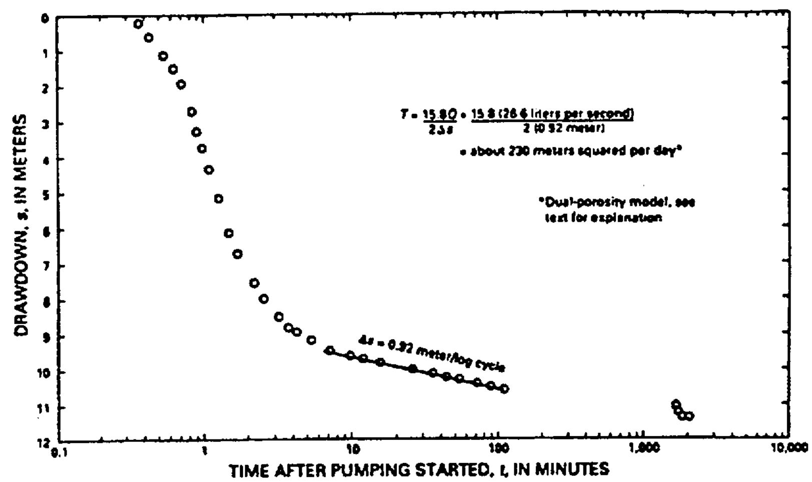

Figure 3.1.2.2.3-51 Analysis of Water-Level Drawdown, Pumping Test 2, Depth Interval from 526 to 1,220 Meters, Straight-Line Solution with Dual Porosity Model

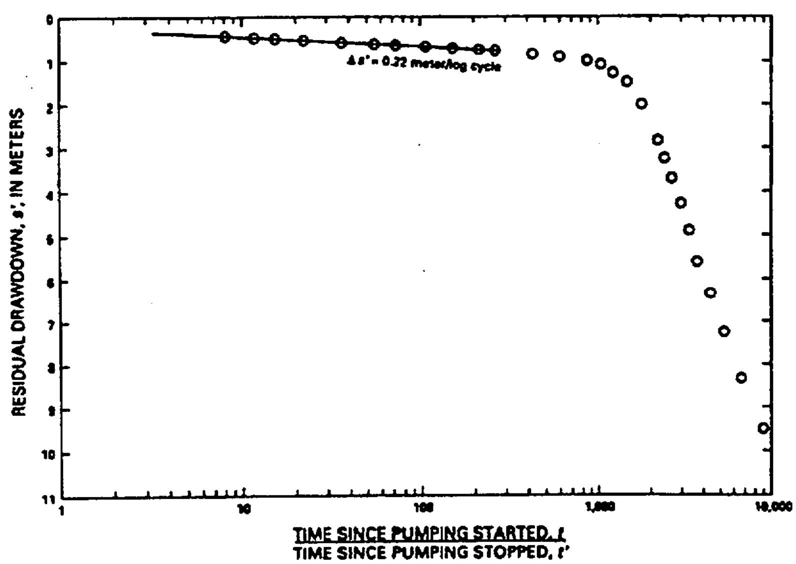

Figure 3.1.2.2.3-52 Water-Level Recovery, Pumping Test 2, Depth Interval from 526 to 1,220 Meters. Craig and Reed (1991)

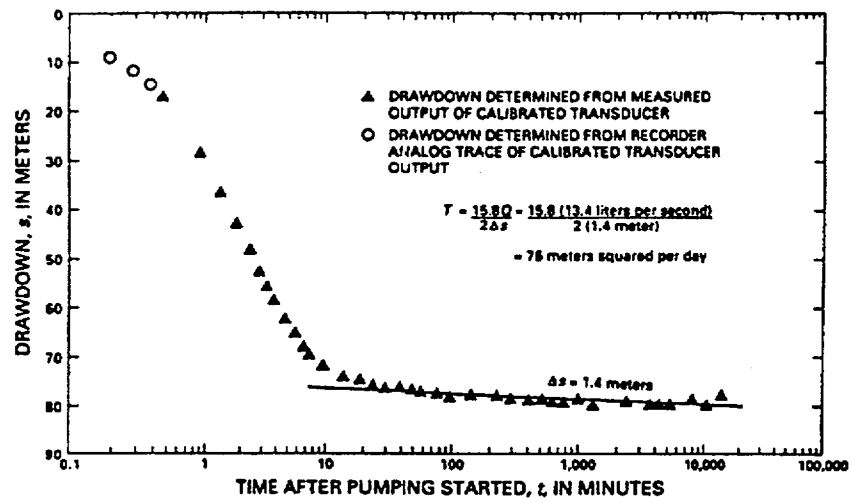

Figure 3.1.2.2.3-53 Analysis of Water-Level Drawdown, Pumping Test 3, Depth Interval from 753 to 834 Meters, Straight-Line Solution with Dual-Porosity Model

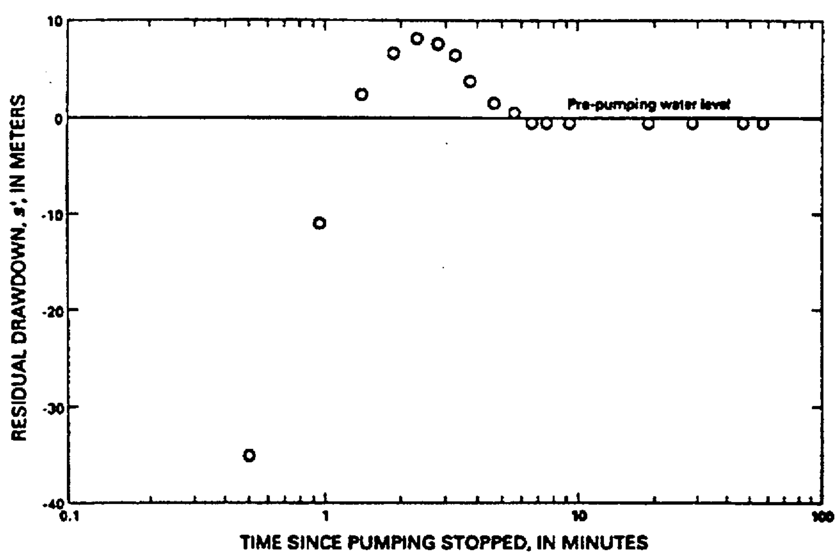

Figure 3.1.2.2.3-54 Residual Drawdown, Recovery Test 3, Depth Interval from 753 to 834 Meters. Craig and Reed (1991)

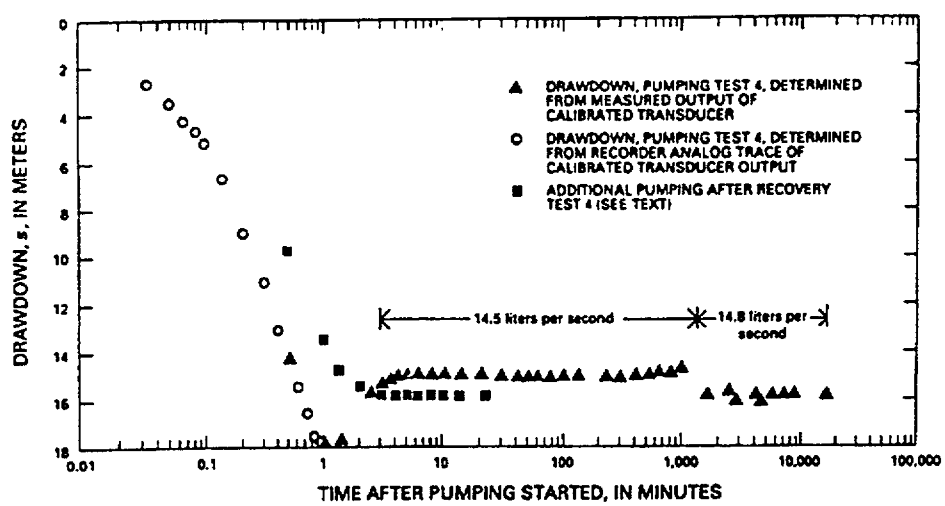

Figure 3.1.2.2.3-55 Water-Level Drawdown, Pumping Test 4, Depth Interval from 608 to 645 Meters

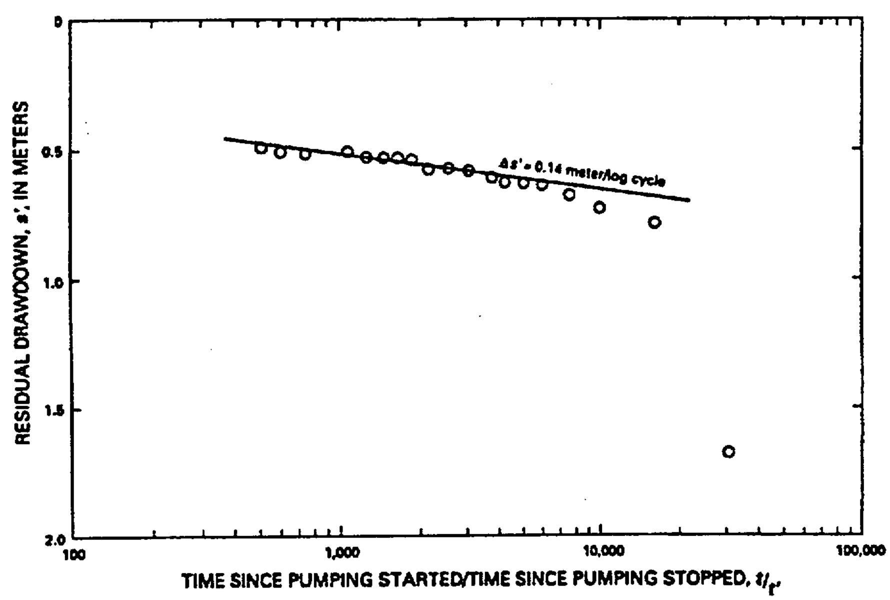

Figure 3.1.2.2.3-56 Water-Level Recovery, Recovery Test 4, Depth Interval from 608 to 645 Meters. Craig and Reed (1991)

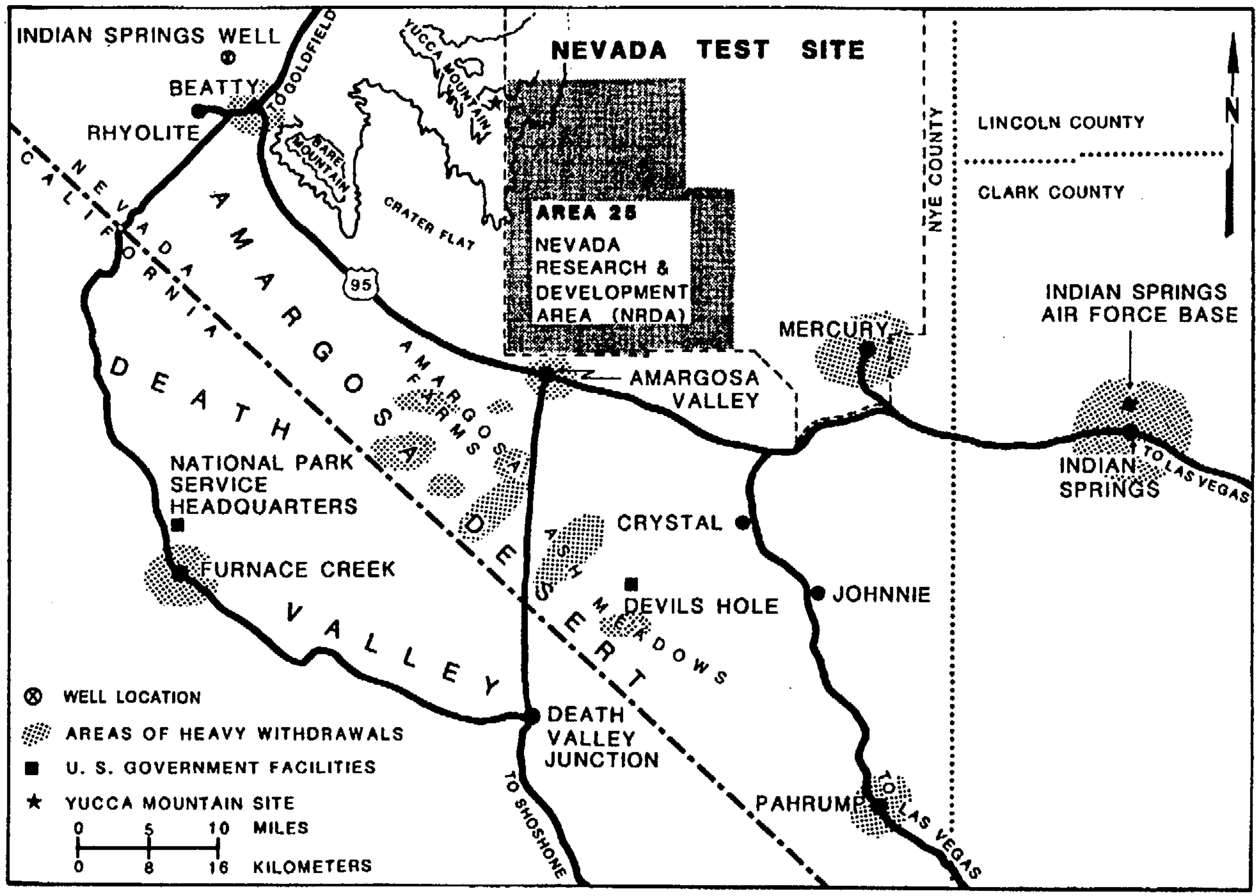

Figure 3.1.2.2.8-1 Map Showing Areas of Heavy Withdrawals Near Yucca Mountain. Modified from French et al. (pg. 3, 1984)

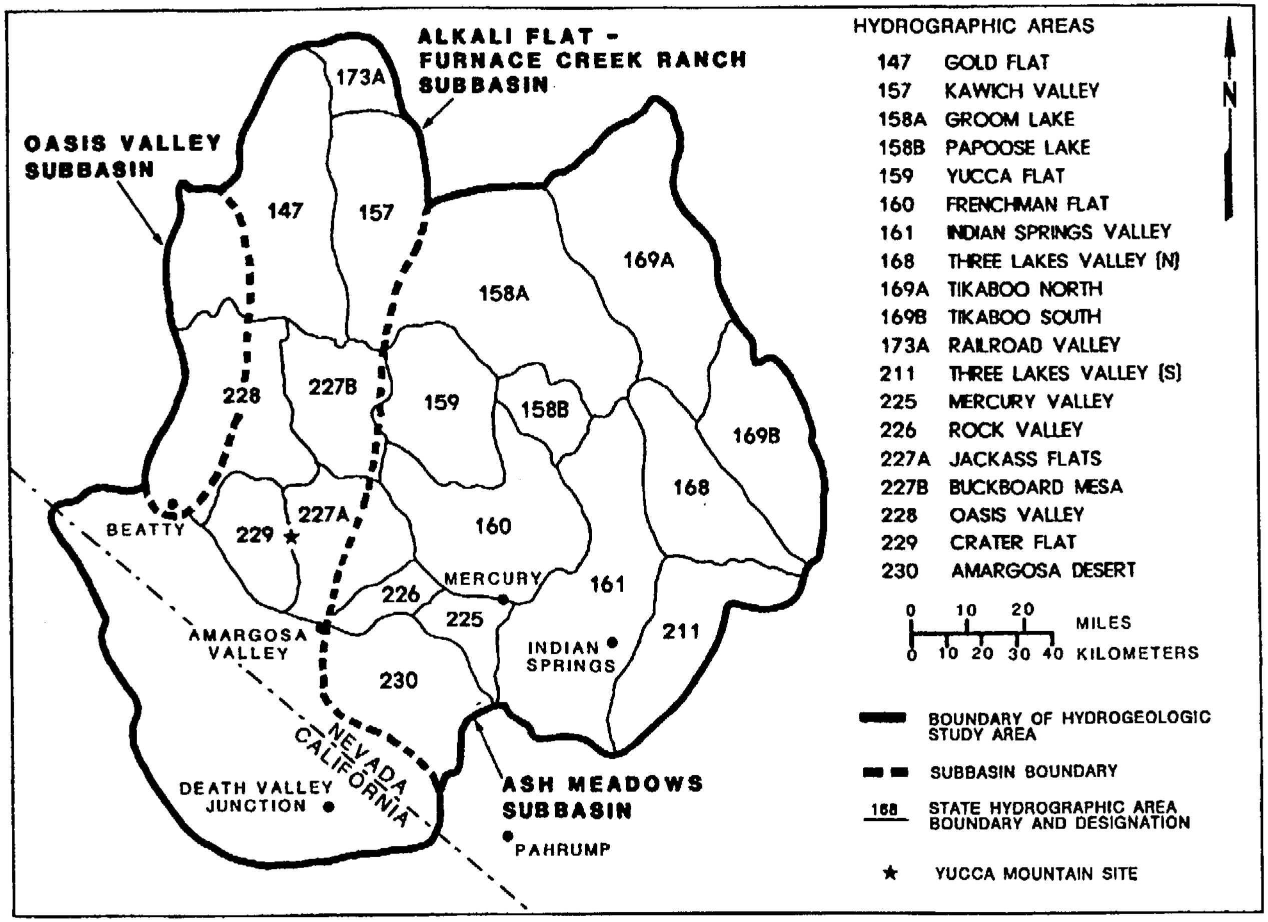

Figure 3.1.2.2.8-2 State Hydrographic Areas Within the Hydrogeologic Study Area

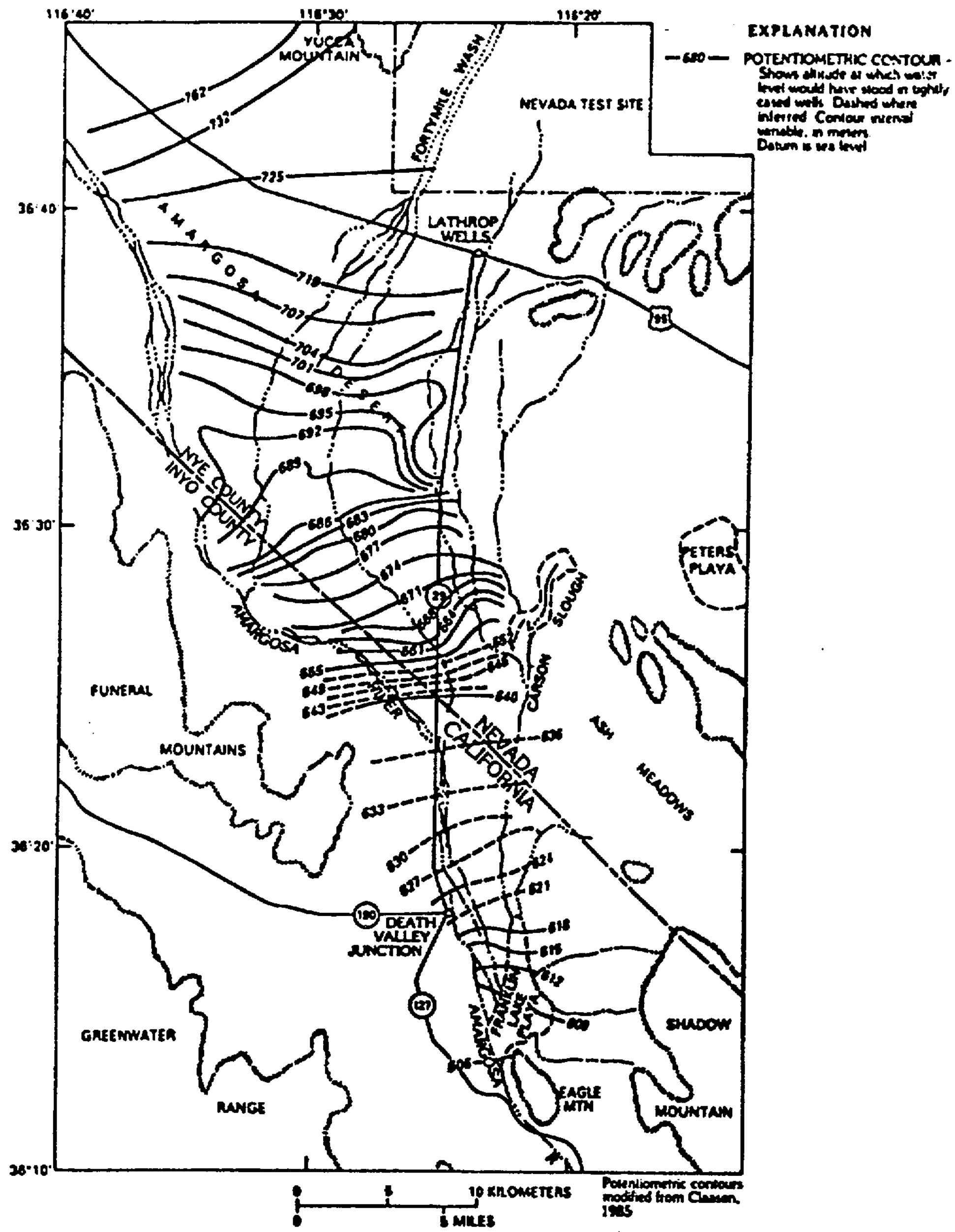

Figure 3.1.2.2.8-3 Potentiometric Surface of the Amargosa Desert

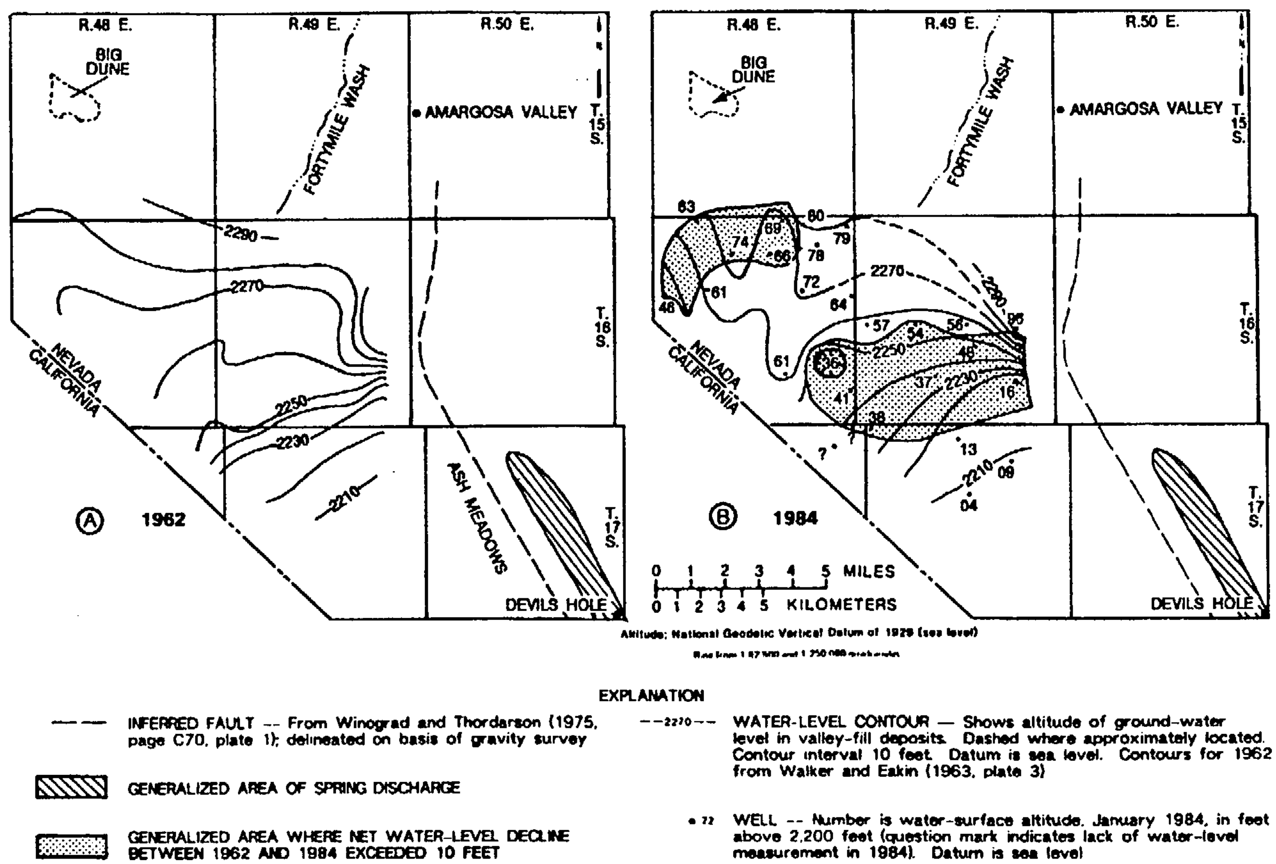

Figure 3.1.2.2.8-4 Potentiometric Maps of the Amargosa Desert (Valley Fill Aquifer) Based on the Well Data from (1962) (A) and 1984 (B). Modified from Nichols and Akers (1985)

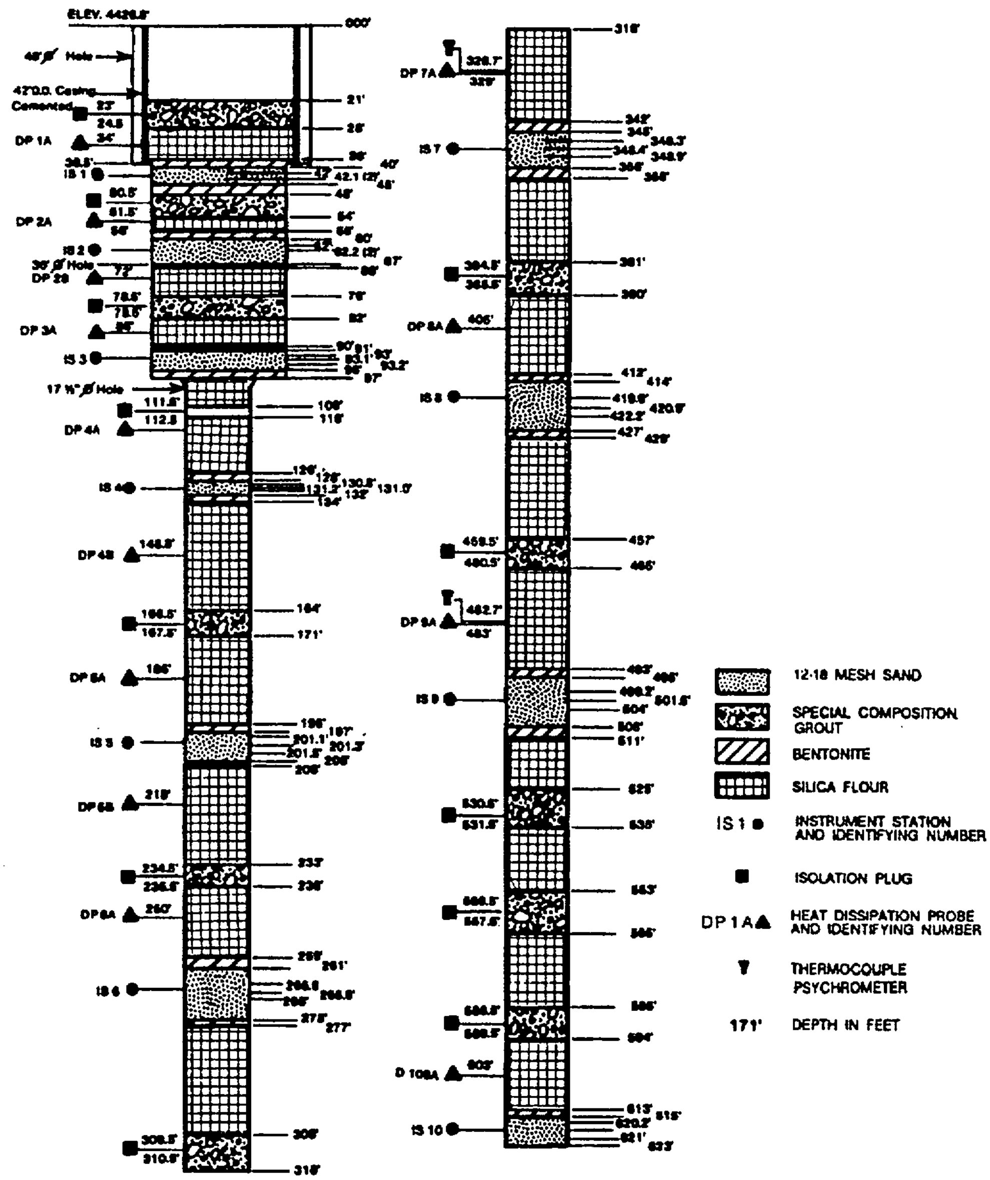

Figure 3.1.2.3.1-1 Instrumentation of Monitoring Borehole USW UZ-1 (0- to 623-feet depth). Modified from Montazer et al. (1986)

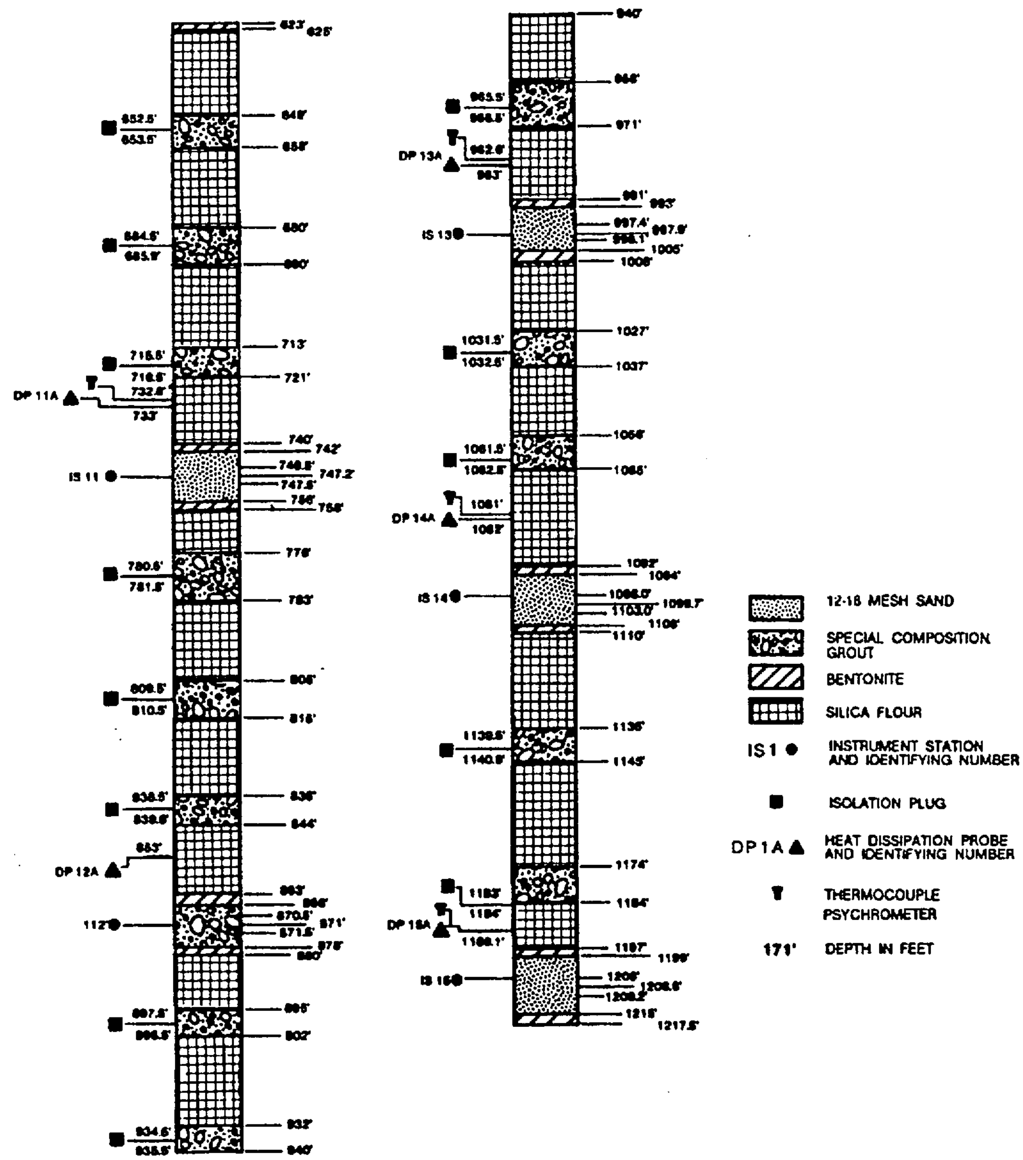

Figure 3.1.2.3.1-1 Instrumentation of Monitoring Borehole USW UZ-1 (623-1217.5 feet depth). Modified from Montazer et al. (1986)(continued)

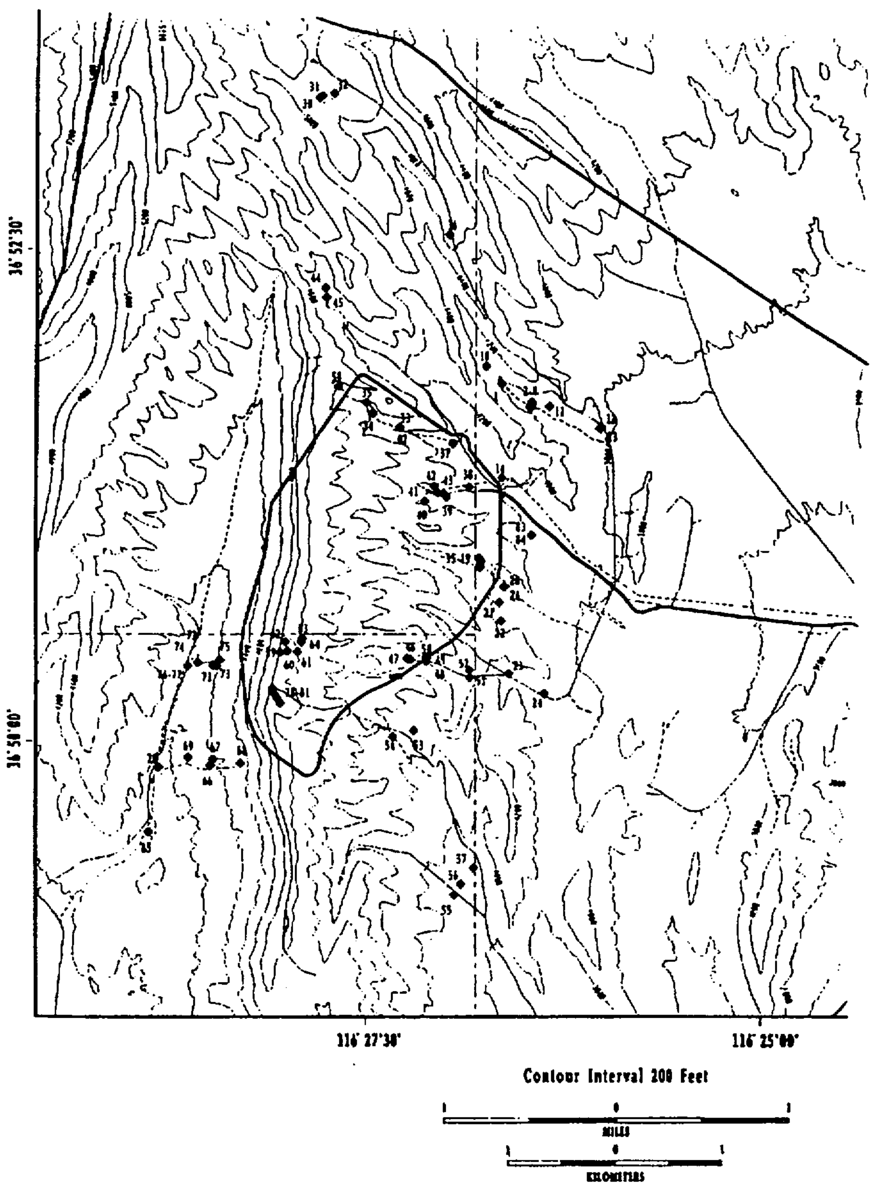

Figure 3.1.2.3.1-2. Unsaturated Zone Moisture Monitoring Sites (DOE, 1992).

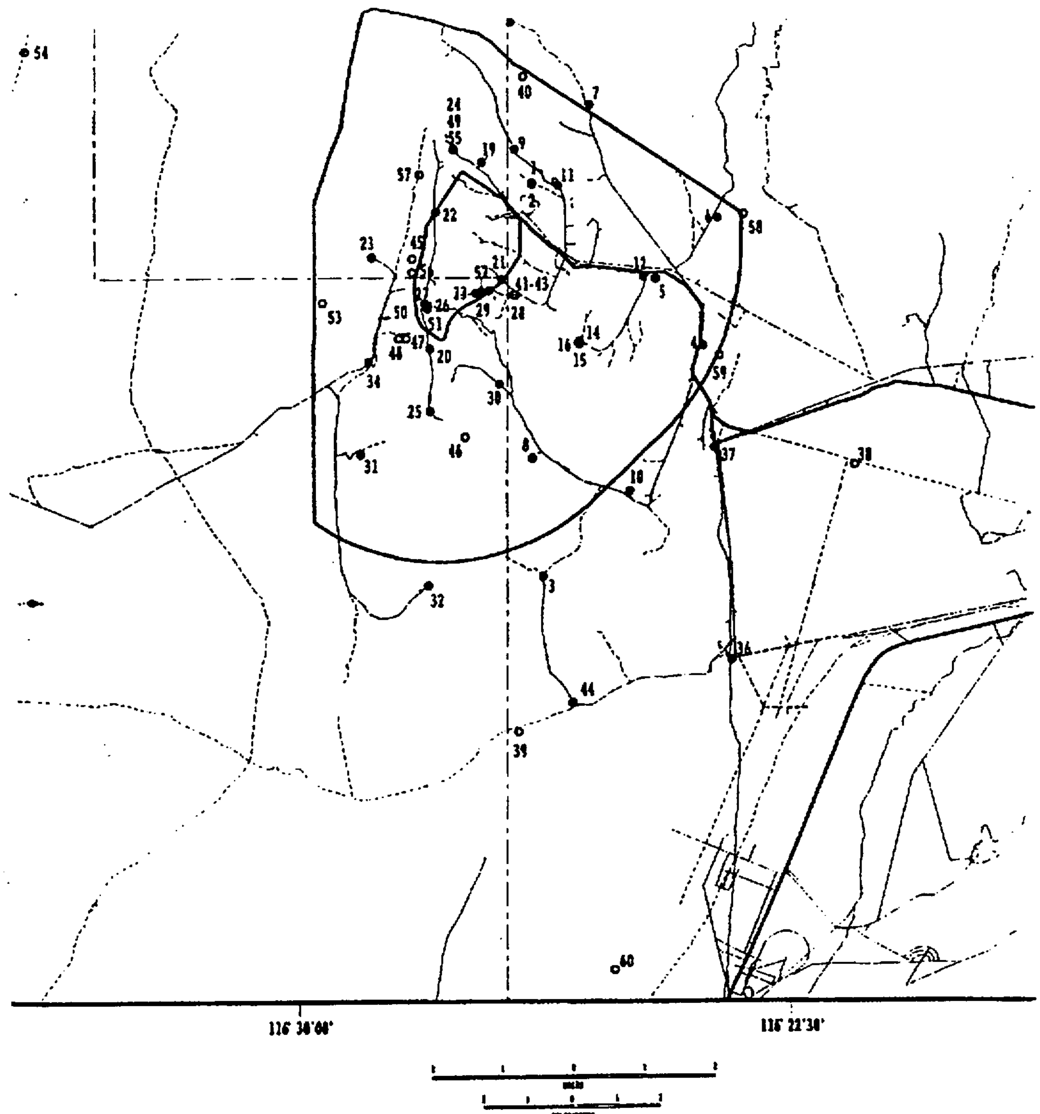

Figure 3.1.2.3.1-3. Saturated Zone Monitoring Sites (DOE, 1992).

	Rock-Stratigraphic Unit	Hydrogeologic Unit [b]	Approximate Range of Thickness (m)	Lithology [c]
	Alluvium	QAL	0-30	Irregularly distributed surficial deposits of alluvium and colluvium
Paintbrush Tuff	Tiva Canyon Member	TCw	0-150	Moderately to densely welded, devitrified ash-flow tuff
Paintbrush Tuff	Yucca Mountain Member; Pah Canyon Member	PTn	20-100	Partially welded to nonwelded, vitric and occasionally devitrified tuffs
Paintbrush Tuff	Topopah Spring Member	TSw	290-360	Moderately to densely welded, devitrified ash-flow tuffs that are locally lithophysae-rich in the upper part, includes basal vitrophyre
	Tuffaceous beds of Calico Hills	CHn: CHnv / CHnz	100-400	Nonwelded to partially welded ash-flow tuffs: Vitric / Zeolitized
Crater Flat Tuff	Prow Pass Member	CHn: CHnv / CHnz		
Crater Flat Tuff	Bullfrog Member	CFu	0-200	Undifferentiated, welded and nonwelded, vitric, devitrified, and zeolitized ash-flow and air-fall tuffs

[a]Sources: Montazer and Wilson (1984) except as noted.

[b]QAL = Quaternary Alluvium, TC_w = Tiva Canyon welded unit, PT_n = Paintbrush nonwelded unit, TS_w = Topopah Spring welded unit, CH_n = Calico Hills nonwelded unit, CH_{nv} = Calico Hills nonwelded vitric unit, CH_{nz} = Calico Hills nonwelded zeolitized unit, CF_u = Crater Flat undifferentiated unit.

[c]Lithology summarized from Ortiz et al. (1985).

Figure 3.1.2.3.2-1 Definition of Unsaturated-Zone Hydrogeologic Units and Correlation with Rock-Stratigraphic Units[a]

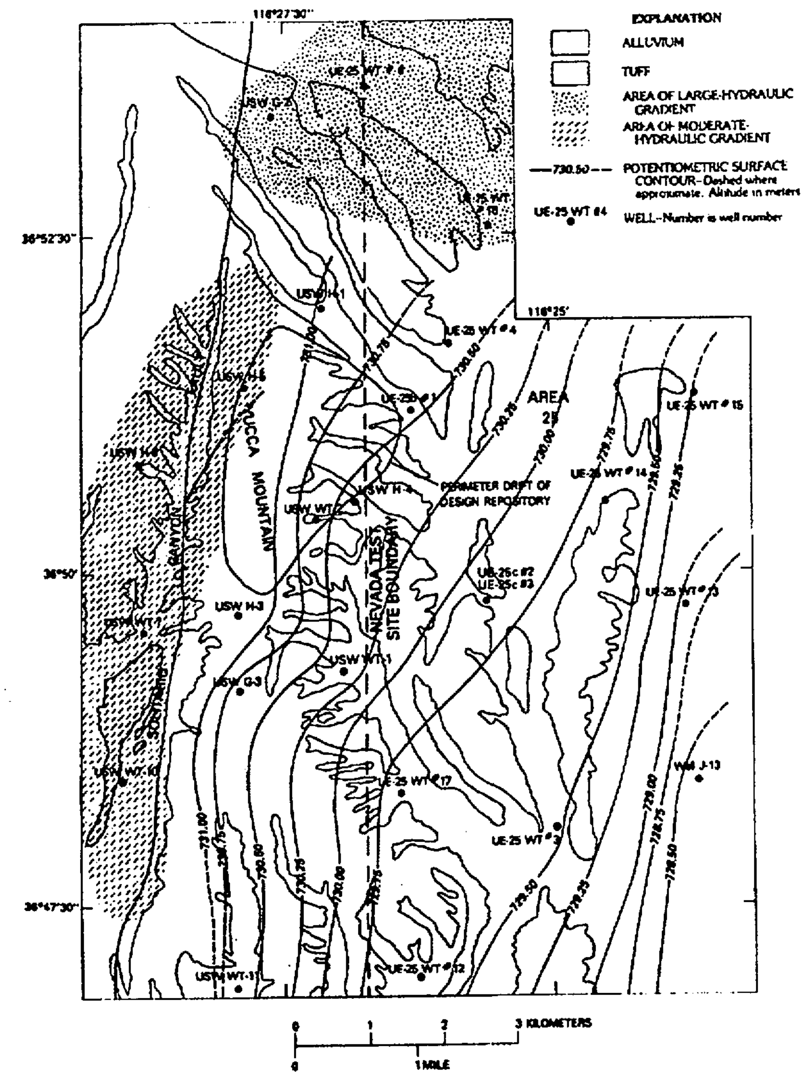

Figure 3.1.2.3.3.2-1 Revised Potentiometric-Surface Map, Yucca Mountain (Constructed From Mostly 1988 Average Water Levels). Ervin et al. (1993)

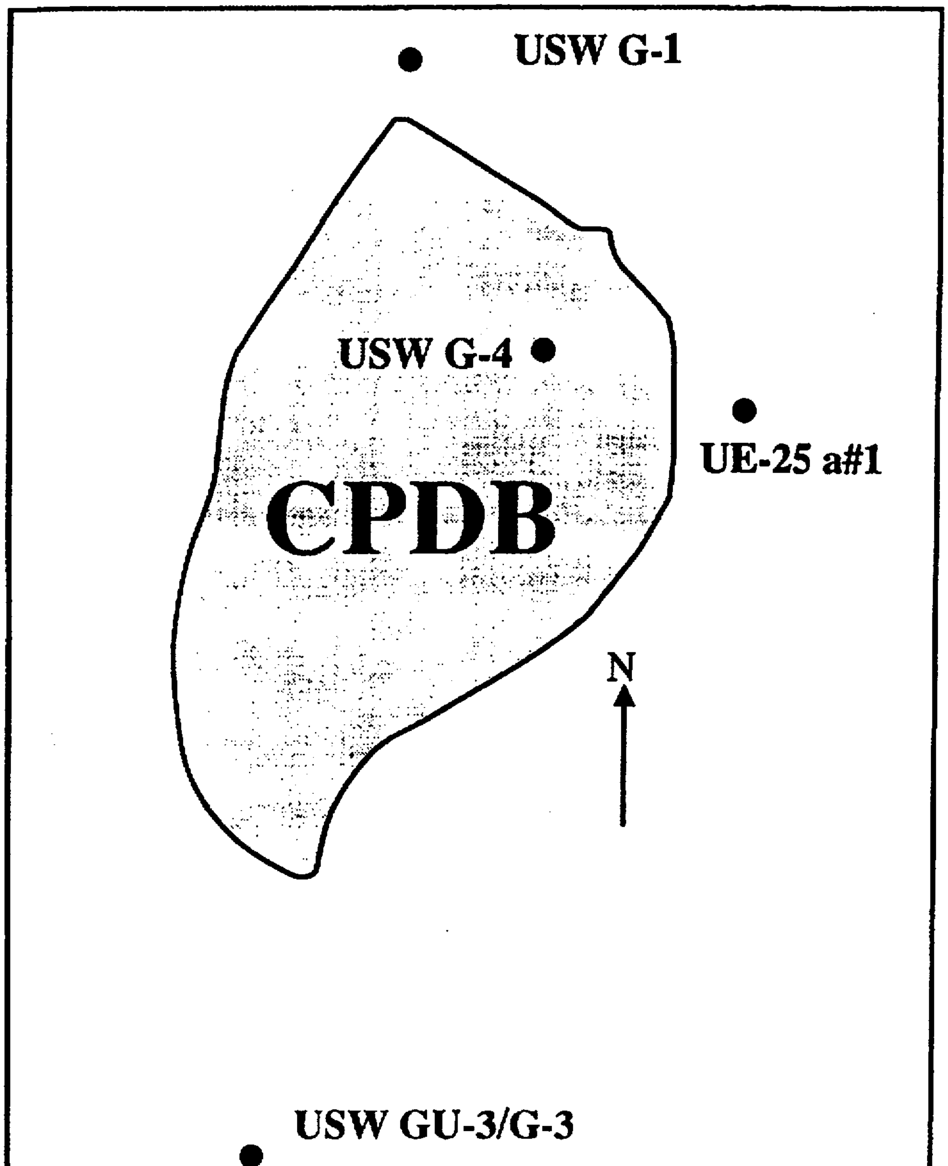

Figure 3.1.3.2.1.1-1 Index Map Showing the Location of Drill Holes in Relation to the CPDB from Which Data Primarily were Derived for this Section of the Annotated Outline

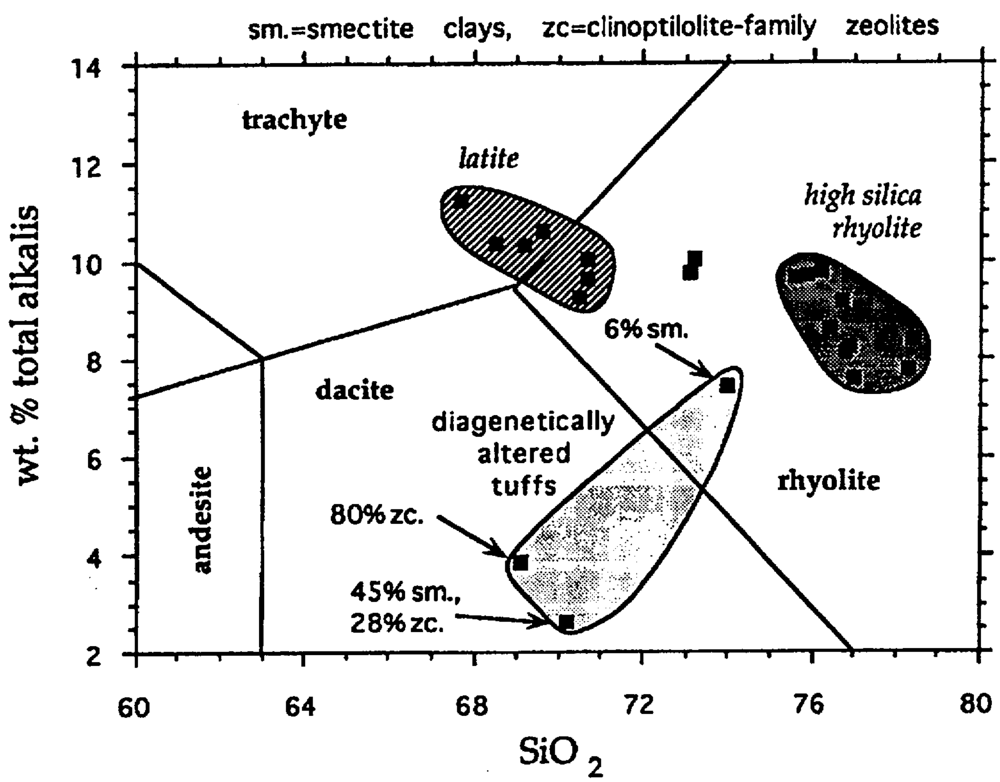

Figure 3.1.3.2.1.1.1-1 Total Alkali Silica Diagram (Le Bas et al. (1986)) for Representative Fresh and Altered Samples of Latite and Rhyolite Tuff of the Topopah Spring Member of the Paintbrush Tuff. Data from Schuryatz et al. (1989), and Broxton et al. (1986)

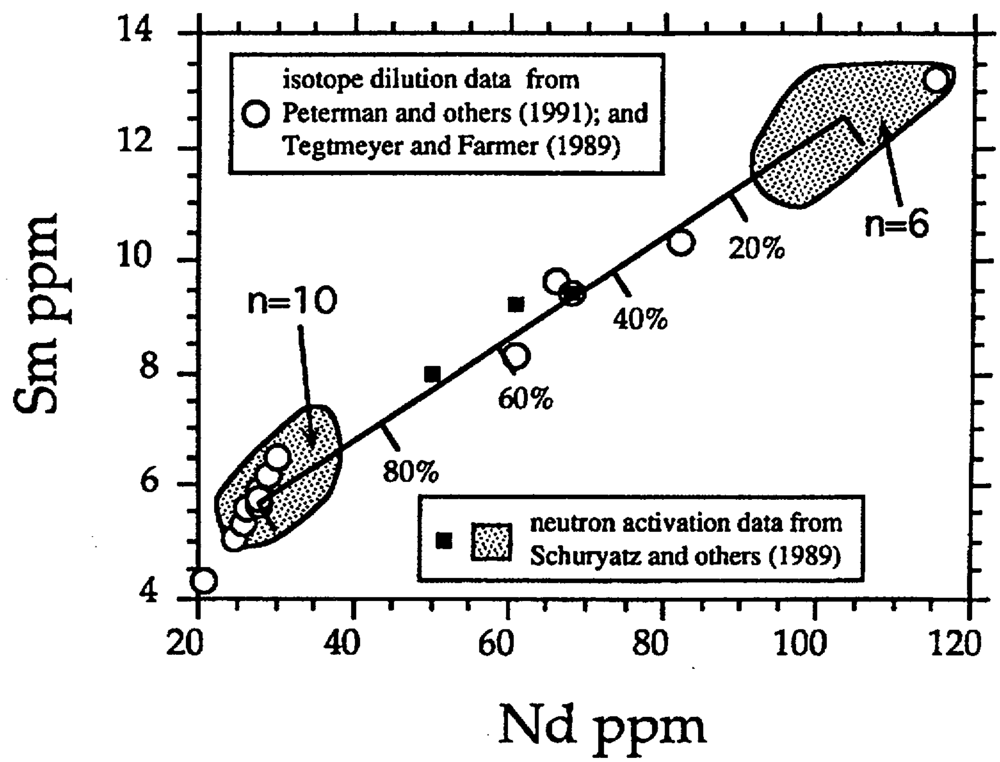

Figure 3.1.3.2.1.1.1-2 Sm-Nd Plot for Representative Samples of the Topopah Spring Member of the Paintbrush Tuff. Note the distinct break between the latites and rhyolites in that the latite has distinctly higher REE abundances and is LREE enriched (lower Sm/Nd ratio). Plotted data from Peterman et al. (1991), and Tegtmeyer and Farmer (1989). Data from Schuryatz et al. (1989) cited for comparative purposes

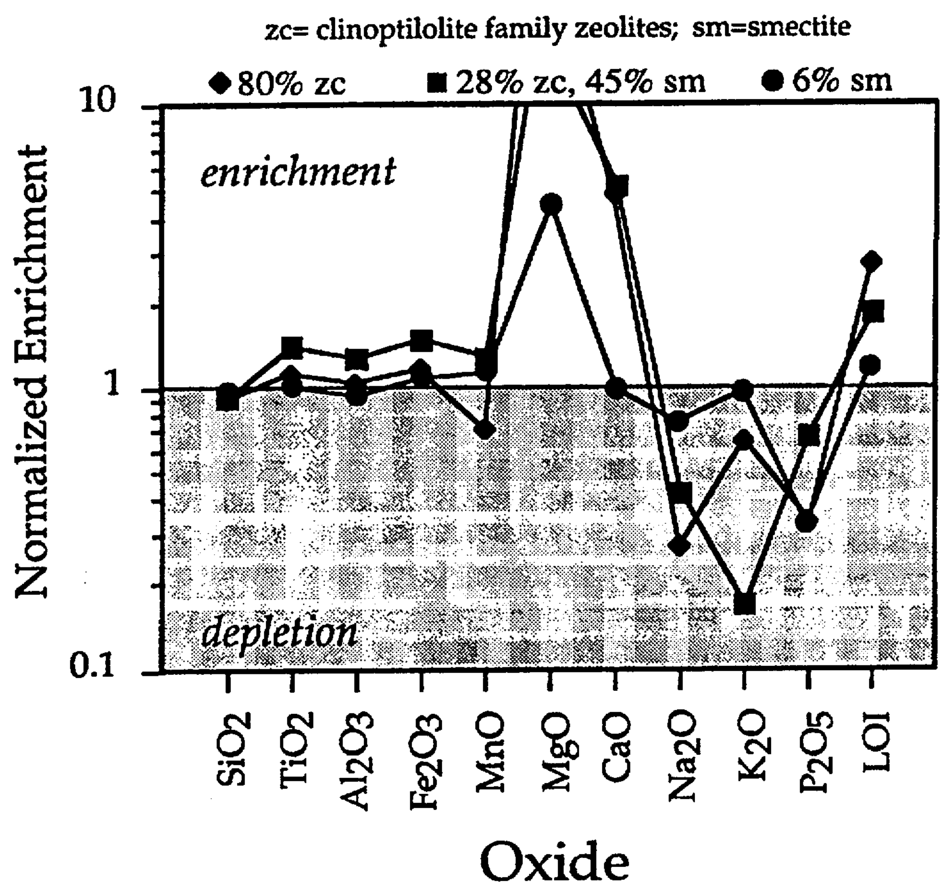

Figure 3.1.3.2.1.1.1-3 Enrichment Diagram for Major Elements in Altered Topopah Spring Rhyolite. Normalization value from sample BB8-85WR of Schuryatz et al. (1989)

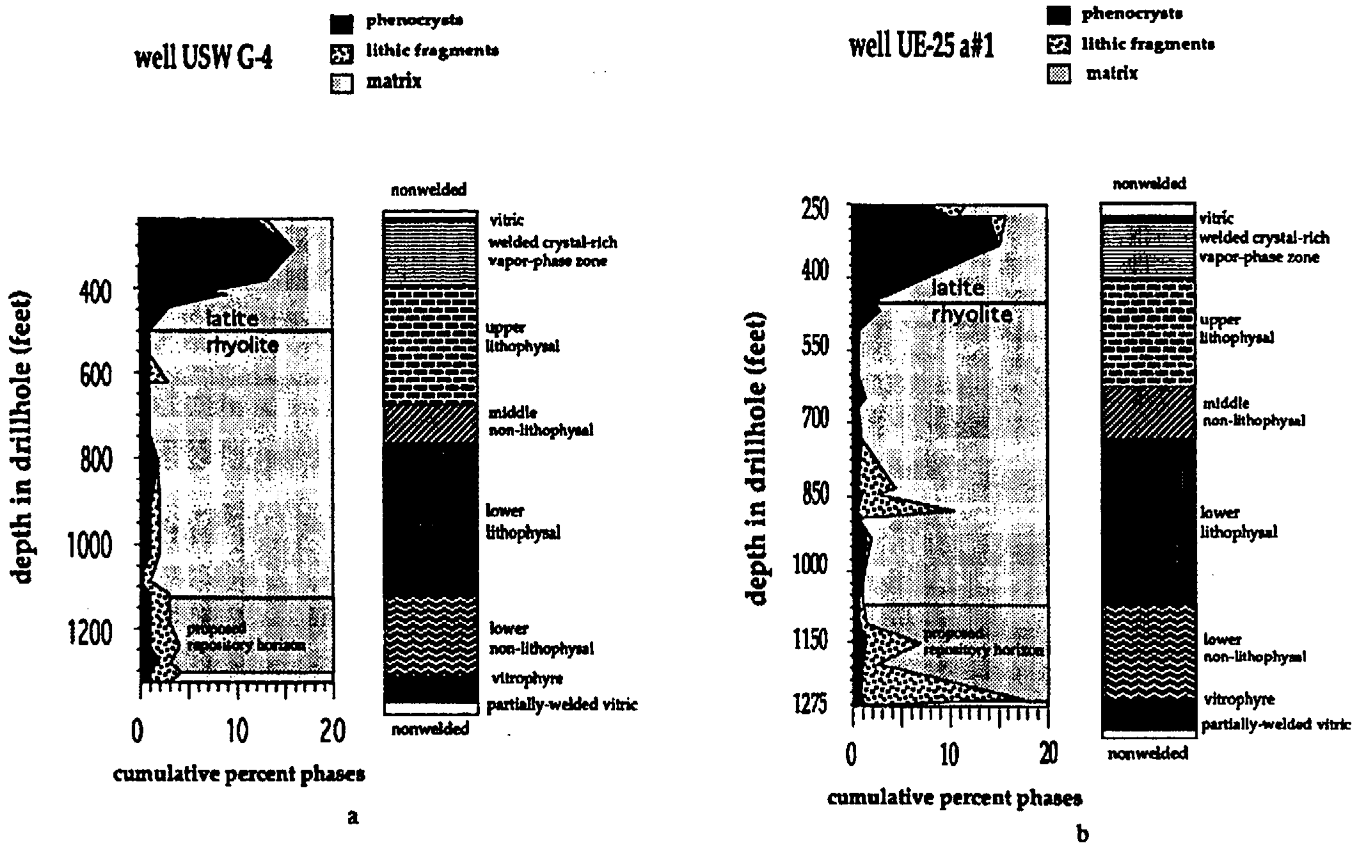

Figure 3.1.3.2.1.1.2-1 Illustration of the Cumulative Percent of Phenocrysts and Lithic Fragments with Depth in the Topopah Spring Member for a) Drill Hole USW G-4 and b) UE-25 a#1. Data from Broxton et al. (1989)

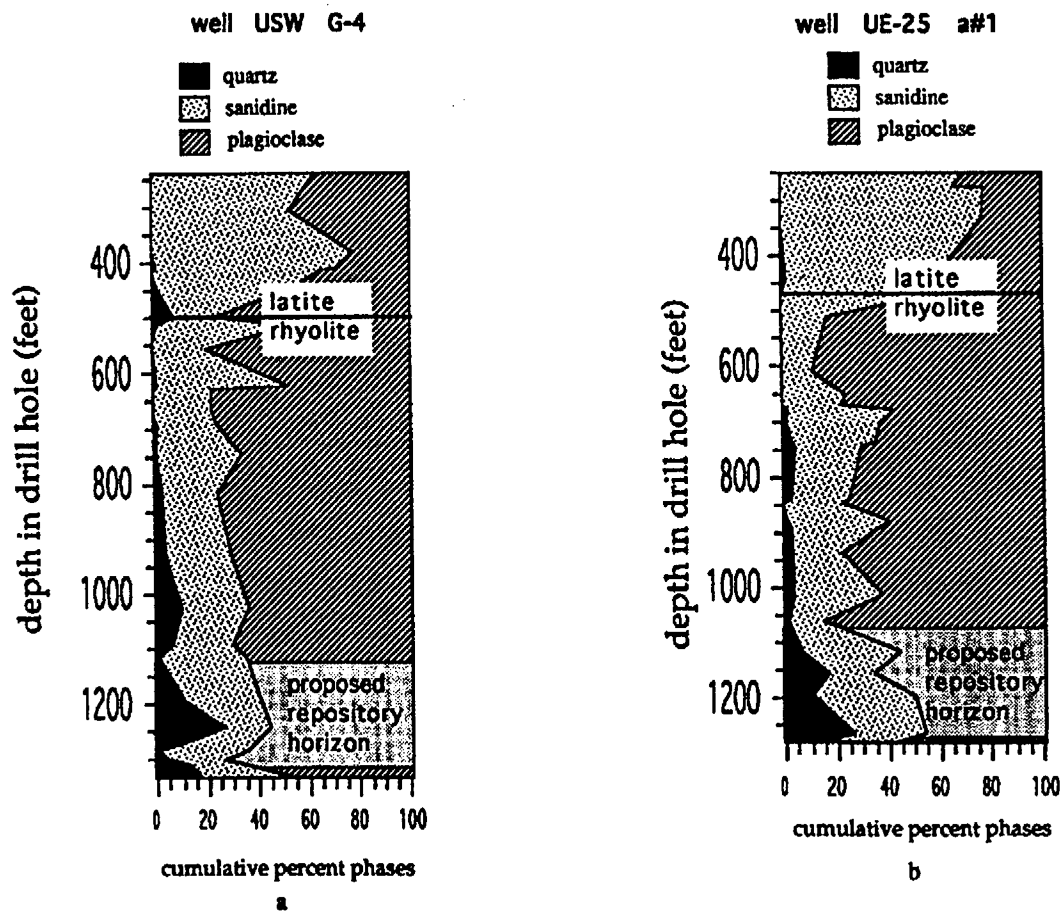

Figure 3.1.3.2.1.1.2-2 Illustration of the Cumulative Percent of Felsic Phenocrysts with Depth in the Topopah Spring Member for a) Drill Hole USW G-4 and b) UE-25 a#1. Data from Broxton et al. (1989)

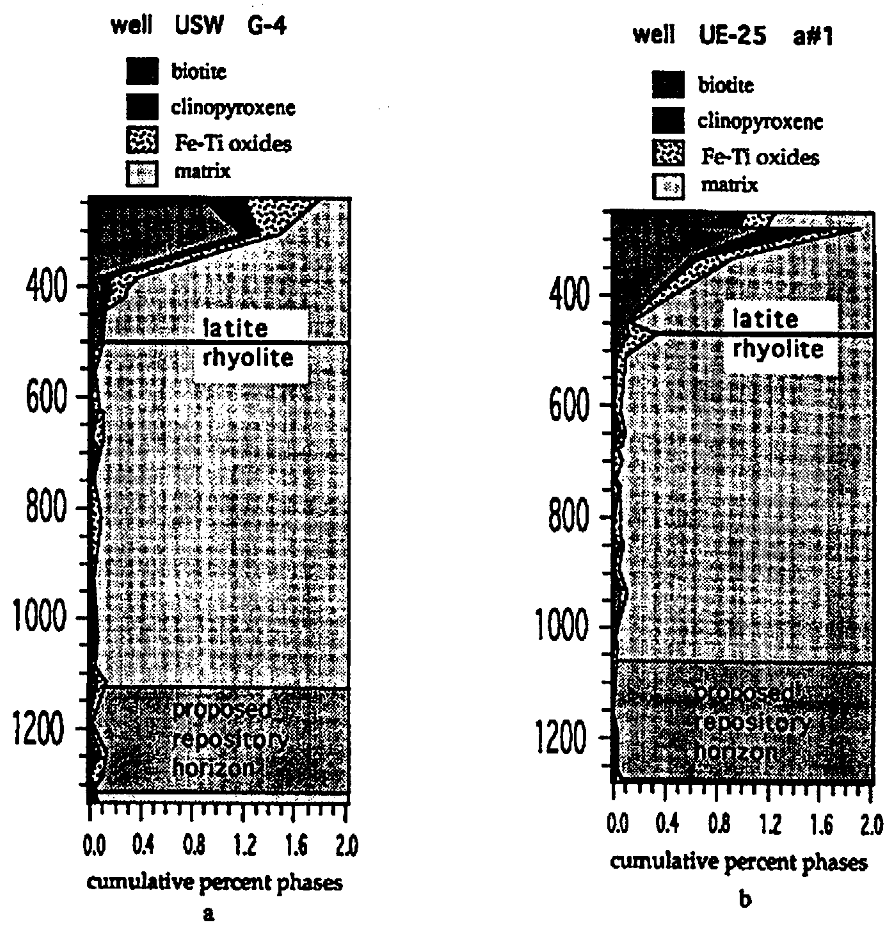

Figure 3.1.3.2.1.1.2-3 Illustration of the Cumulative Percent of Mafic Phenocrysts with Depth in the Topopah Spring Member for a) Drill Hole USW G-4 and b) UE-25 a#1. Data from Broxton et al. (1989)

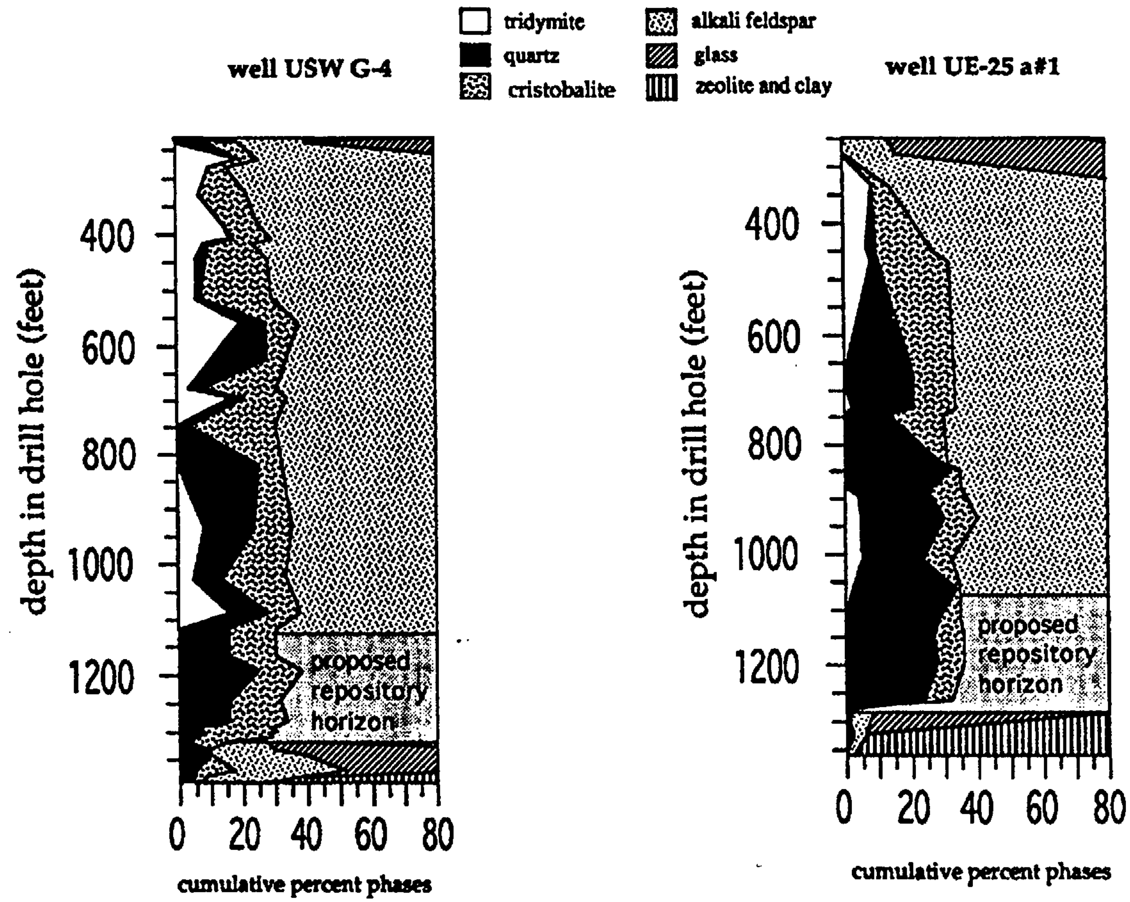

Figure 3.1.3.2.1.1.2-4 Ilustration of the Cumulative Percent Phases as Determined by Quantitative X-Ray Diffraction with Depth in the Topopah Spring Member for: a) Drill Hole USW G-4 and b) UE-25 a#1. Data from Bish and Chipera (1989)

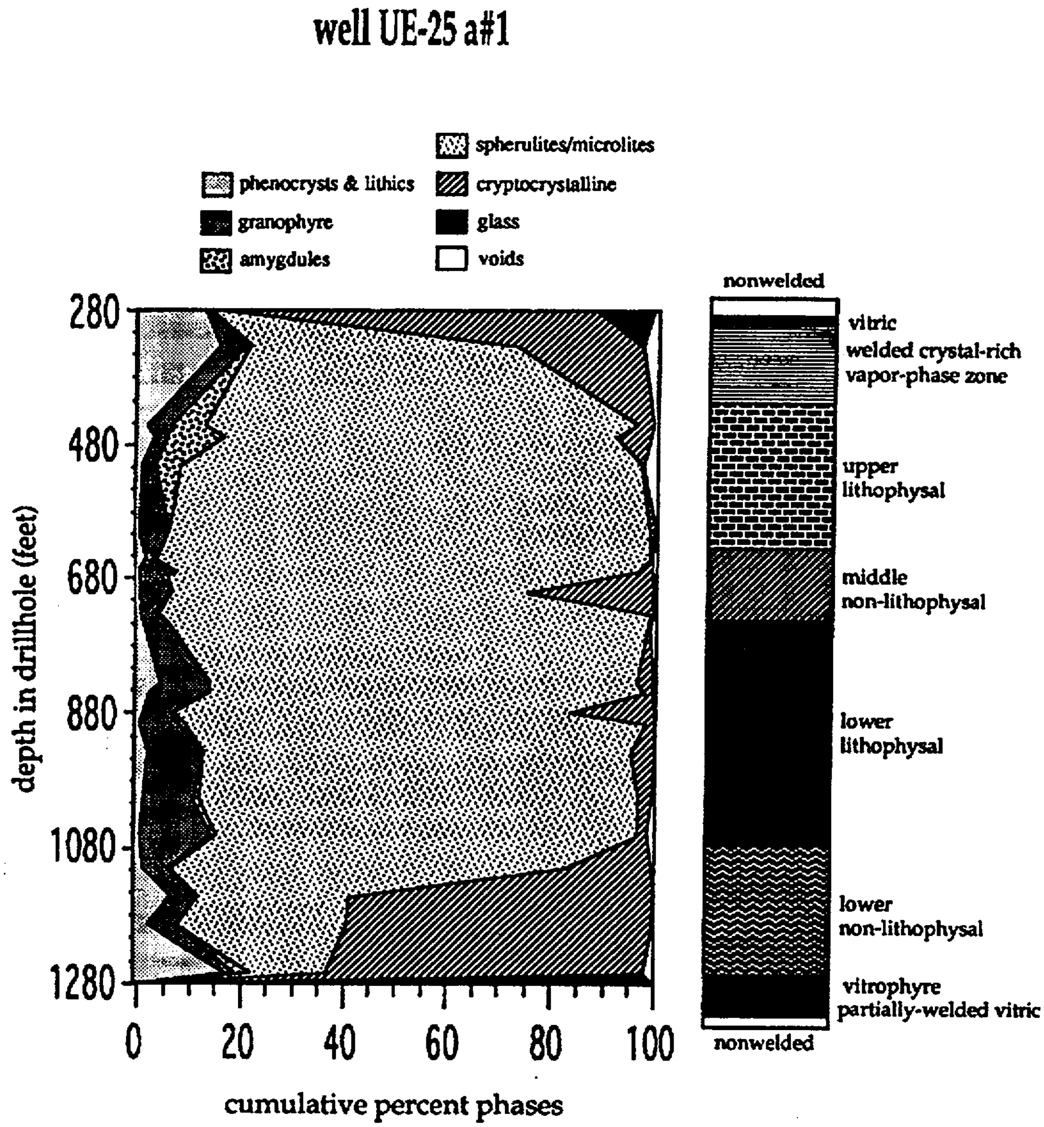

Figure 3.1.3.2.1.1.3-1 Illustration of the Cumulative Percentage of Matrix Textures with Depth in the Topopah Spring Member Compared to Macroscopic Welding Horizons for Drill Hole UE-25 a#1. Data from Byers and Moore (1987)

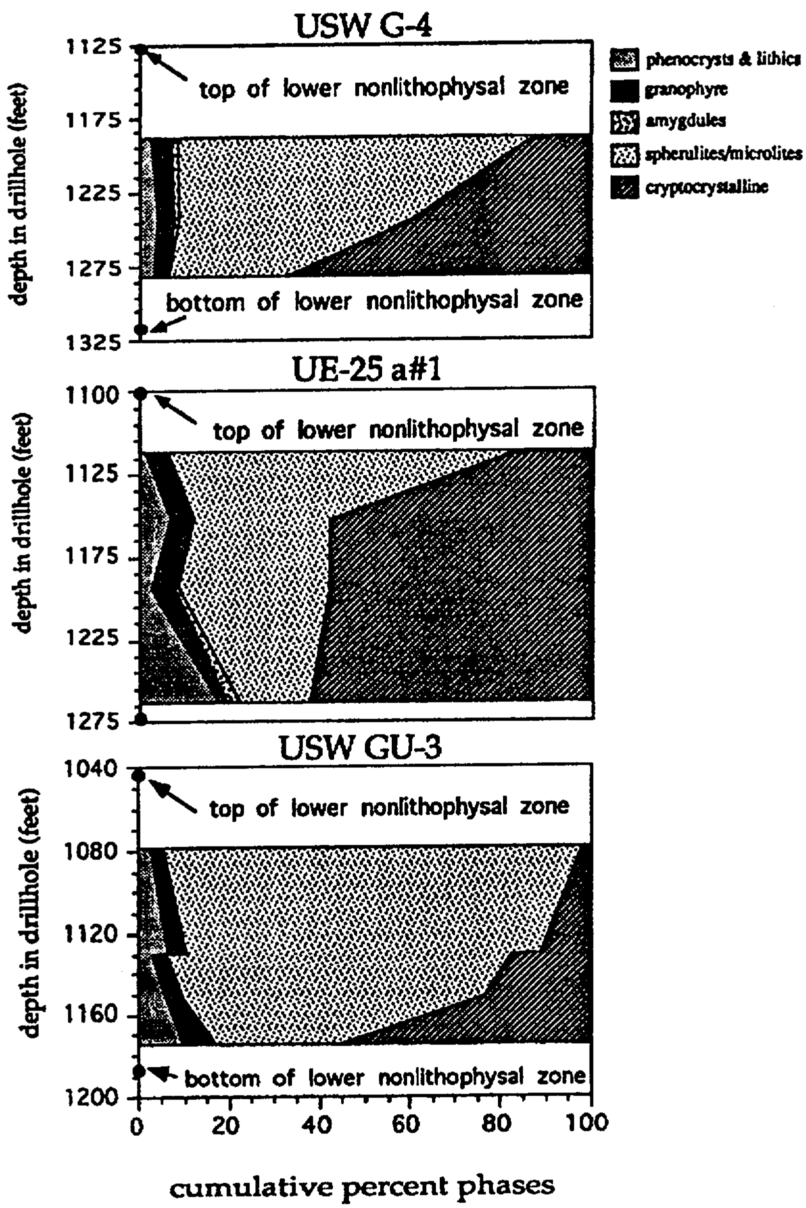

Figure 3.1.3.2.1.1.3-2 Comparison of the Matrix Textures Within the Proposed Repository Horizon for Drill Holes USW G-4, UE-25 a#1, and USW GU-3. Data from Byers and Moore (1987) and Byers (1985)

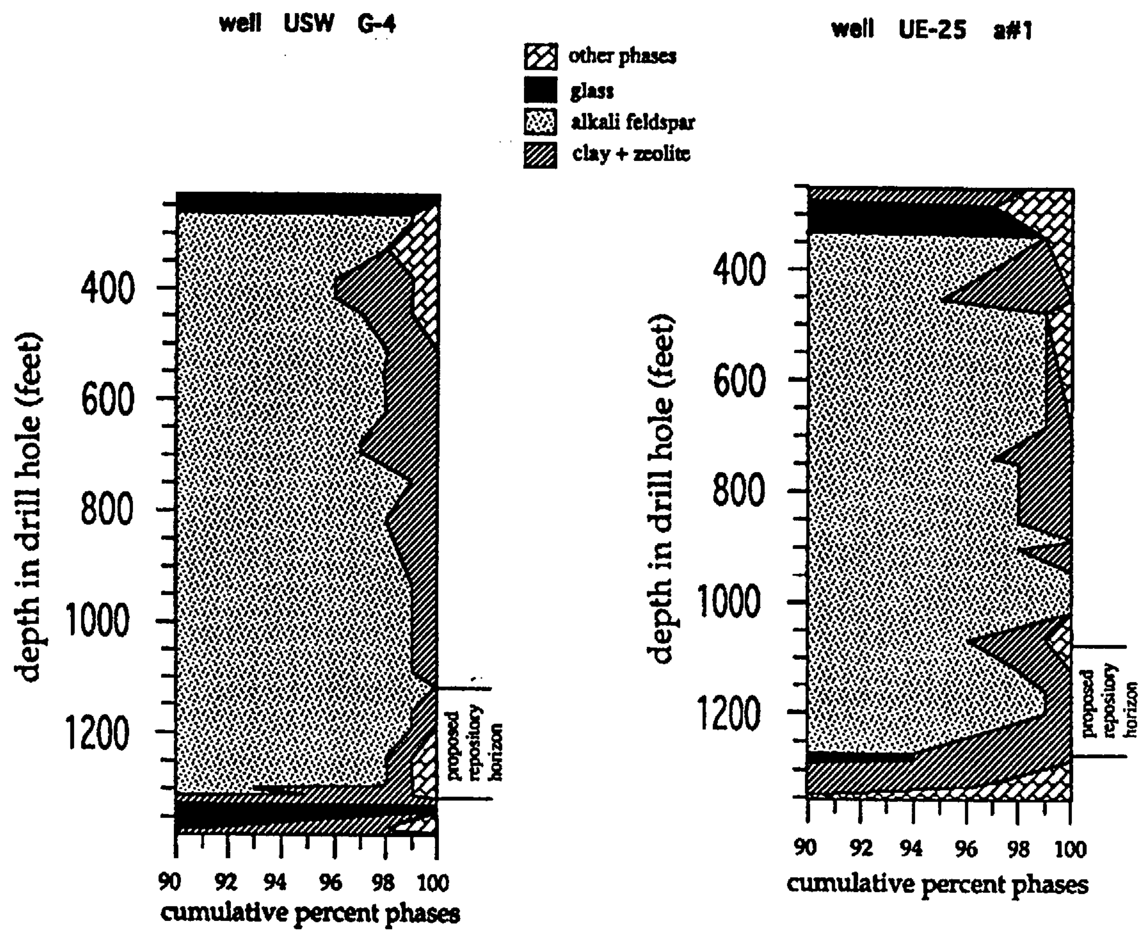

Figure 3.1.3.2.1.1.4-1 These Plots are an Expansion of the Horizontal Scale for Data Not Shown in Figure 8 to Better Illustrate the Distribution of Digenetic Phases in the Topopah Spring Member for a) Drill Hole USW G-4 and b) UE-25 a#1. Data from Bish and Chipera (1989)

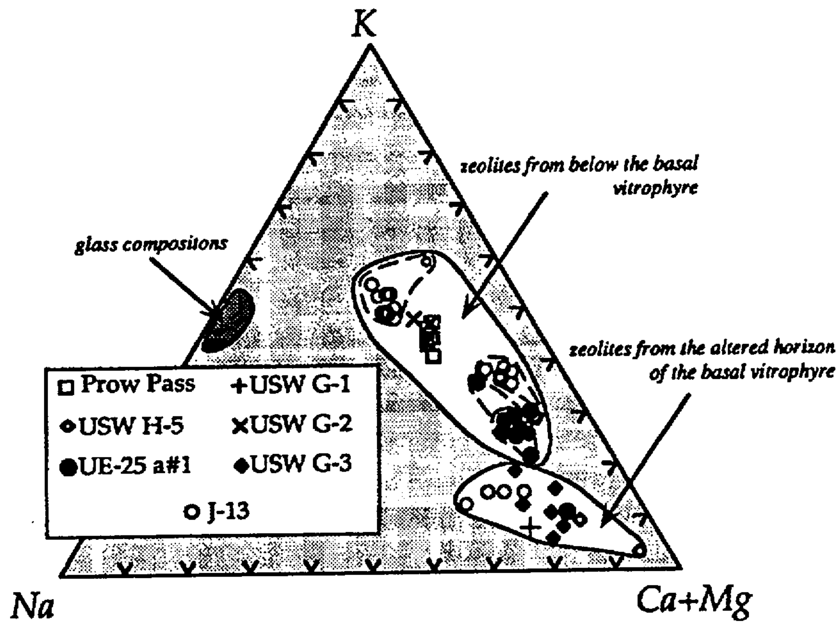

CLINOPTILOLITE-FAMILY ZEOLITES FROM THE TOPOPAH SPRING MEMBER

Figure 3.1.3.2.1.1.4-2 Ternary Plot of Exchangeable Cations in Clinoptilolite and Heulandite Zeolites in the Topopah Spring Member

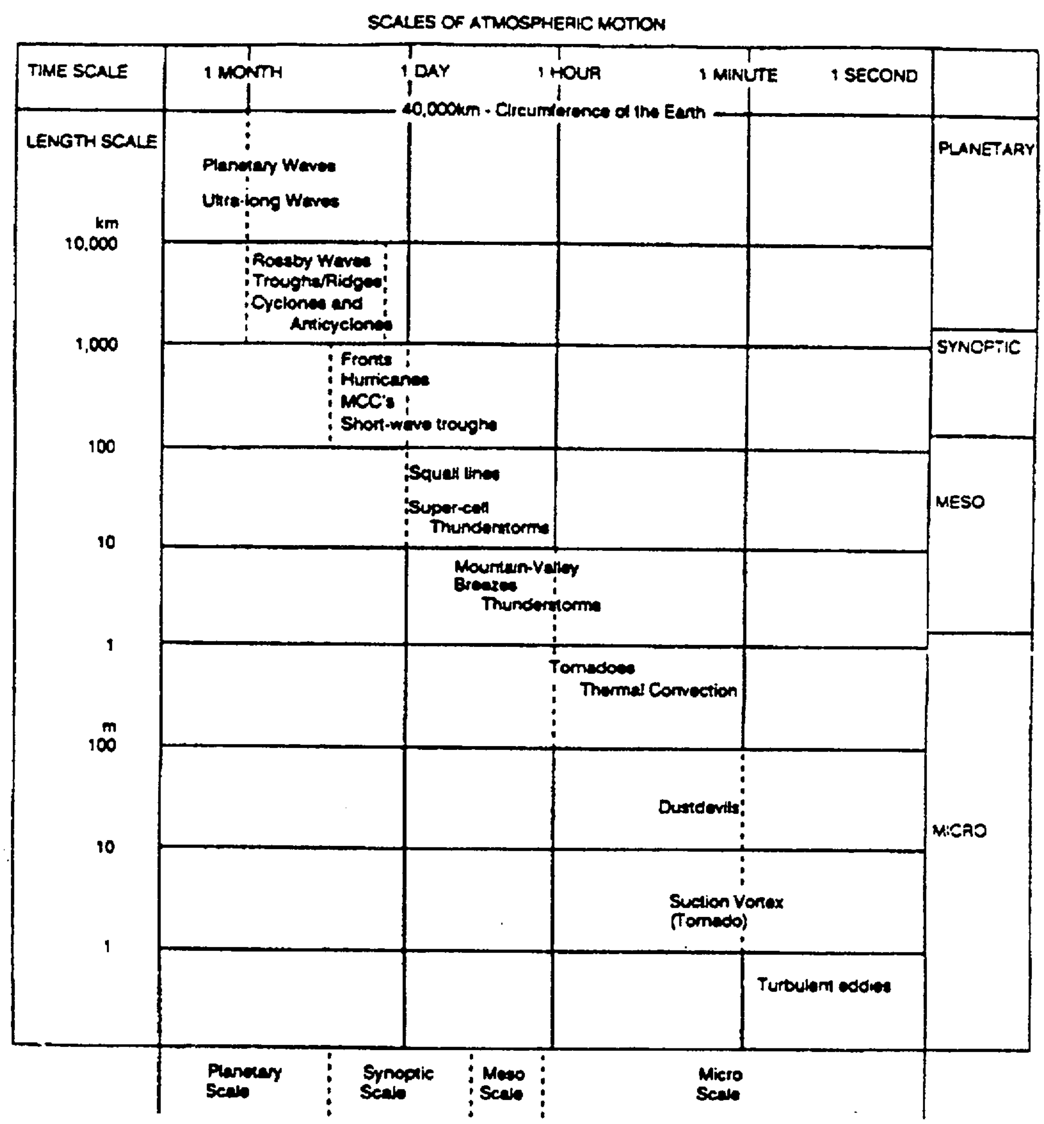

Figure 3.1.4.1.1.1-1 Examples of Atmospheric Motions or "Disturbances" Shown in Context of Their Relationship in Space and Time. The time and length scales measure the duration and wavelength of each disturbance respectively. Modified from Hirschboeck (1987)